Design of P3HT:Fullerene Nanoparticle Dispersions for the Fabrication of Organic Solar Cells

To obtain the academic degree of

Doctor Engineer (Dr.-Ing.)

From the Department of
Electrical Engineering and Information Technology
Karlsruhe Institute of Technology (KIT)

AND

Doctor of Philosophy (Ph.D.)

From the School of Chemistry
University of Melbourne (UoM)

approved
Dissertation
by

M.Sc. Karen Fischer
ORCID ID: 0000-0002-8524-8237
Born in: Freiburg im Breisgau

Date of oral exam:	20.04.2023
First Examiner:	Apl. Prof. Dr. Alexander Colsmann
Second Examiner:	Assoc. Prof. Dr. David Jones
Third Examiner:	Prof. Dr. Thomas Heiser

Design of P3HT:Fullerene Nanoparticle Dispersions for the Fabrication of Organic Solar Cells

Zur Erlangung des akademischen Grades einer

DOKTORIN DER INGENIEURWISSENSCHAFTEN (Dr.-Ing.)

von der KIT-Fakultät für
Elektrotechnik und Informationstechnik
des Karlsruher Instituts für Technologie (KIT)

UND

DOCTOR OF PHILOSOPHY (Ph.D.)

von der Fakultät für Chemie
Universität Melbourne (UoM)

angenommene
DISSERTATION
von

M.Sc. Karen Fischer
ORCID ID: 0000-0002-8524-8237
Geboren in: Freiburg im Breisgau

Tag der mündlichen Prüfung:	20.04.2023
Hauptreferent:	Apl. Prof. Dr. Alexander Colsmann
Korreferenten:	Assoc. Prof. Dr. David Jones
	Prof. Dr. Thomas Heiser

Kurzfassung

Organische Solarzellen bieten viele Vorteile gegenüber herkömmlichen Silizium-Solarzellen. Neben ihren hervorragenden Wirkungsgraden, besonders unter schwacher Beleuchtung, können sie mechanisch flexibel und sogar semitransparent hergestellt werden. Durch ihre geringe Schichtdicke, die im Bereich von wenigen hundert Nanometern liegt, wird eine geringe Menge Material zur Herstellung benötigt, was zu einem geringen Gewicht der Solarzelle führt und zudem eine Energierücklaufzeit von nur wenigen Monaten ermöglicht. Für den industriellen Einsatz überzeugen vor allem die potentiell kostengünstige Herstellung, welche durch Druck- und Beschichtungsverfahren in kontinuierlichen Rolle-zu-Rolle-Verfahren möglich ist. Diese Verfahren erfordern spezielle Tinten, die auf das Druckverfahren und die gewünschten Schichteigenschaften abgestimmt werden müssen. Die meisten organischen Materialien, die in Solarzellen verwendet werden, sind nicht in umweltfreundlichen Lösungsmitteln wie Wasser oder Alkohol löslich, sondern in halogenierten Lösungsmitteln, die oft umweltschädlich und für den Menschen giftig oder krebserregend sind und dadurch aufwendige Gasreinigungen während des Druckprozesses voraussetzen. Mit diesem Verfahren werden aktuelle Laborwirkungsgrade von bis zu 19 % erzielt. Für einen industriellen Prozess wäre der Verzicht auf bedenkliche Lösungsmittel allerdings erstrebenswert. Mit einem alternativen Ansatz, der Nanopartikelfällung, ist es möglich, einen organischen Halbleiter in einer umweltfreundlichen Flüssigkeit zu dispergieren und somit die Verwendung giftiger Lösungsmittel im Druckprozess zu vermeiden.
Die Entwicklung des Wirkungsgrades von 4 % zu Beginn dieser Arbeit auf nun über 10 % durch die Verwendung hocheffizienter Absorbermaterialien und flüchtiger Stabilisatoren unterstreicht das Potential dieses Ansatzes.
Die gebräuchliche Methode zur Herstellung der Nanopartikeldispersionen ist die manuelle Fällung im Becherglas, welche nur eine begrenzte Reproduzierbarkeit ermöglicht. Ausgehend von dem Materialgemisch aus P3HT und $IC_{60}BA$, mit dem die Herstellung von stabilen Nanopartikeldispersionen möglich ist, wird in dieser Arbeit eine Methode der kontinuierlichen Fällung mittels Mikrofluidik untersucht. Zunächst wird ein geeigneter Aufbau umgesetzt. Anschließend werden die Einflussfaktoren auf den Fällungsprozess identifiziert und qualifiziert. Durch die gezielte Kontrolle der Einflussfaktoren können Dispersionen mit maßgeschneiderter Nanopartikelgröße hergestellt werden, die eine hoch reproduzierbare Fällung ermöglichen. Diese Dis-

persionen weisen eine herausragende Stabilität von über einem Jahr auf. Zur Qualifizierung dieses Prozesses werden organische Solarzellen mit einer Absorberschicht aus Nanopartikeln hergestellt, die den Wirkungsgrad der Solarzellen mit einer Absorberschicht aus der bekannten Becherglasfällung im direkten Vergleich übertreffen.
Während P3HT gemeinsam mit dem Akzeptor $IC_{60}BA$ stabile Dispersionen bildet, flocken viele andere Akzeptoren aus. Daher konzentriert sich der zweite Teil dieser Arbeit auf die erforderlichen Voraussetzungen für die Bildung von Nanopartikeln aus P3HT:Akzeptor-Mischungen. Dafür wird die bekannte Gruppe der Fullerene untersucht, wobei die Mischbarkeit von P3HT und Akzeptor als einer der wichtigsten Faktoren identifiziert wird.
Aufbauend auf diesen Erkenntnissen wird die Verwendung einer dritten Komponente untersucht, um P3HT:Akzeptor-Gemische, mit denen vorher keine stabilen Dispersionen möglich waren, zu stabilisieren. Dafür werden Akzeptoren wie das Fulleren $PC_{71}BM$ oder Donatoren wie regiorandom P3HT untersucht. Mit der Mischbarkeit als Prozesskriterium konnten erste vielversprechende Ergebnisse erzielt werden.
Mit den aus dieser Arbeit gewonnenen Erkenntnissen ist ein skalierbares Konzept für die Herstellung von ungiftigen Tinten für die Fertigung von organischen Solarzellen umsetzbar, das einen reproduzierbaren Prozess ermöglicht. So können in Zukunft hocheffiziente Solarzellenmaterialien gezielt für die Schichtherstellung mittels Nanopartikeldispersionen entwickelt werden, welche die umweltfreundliche Herstellung organischer Solarzellen weiter vorantreibt.

Abstract

Organic solar cells have many advantages, compared to conventional silicon solar cells. Besides their excellent low-light performance, especially under low light conditions, they can be mechanically flexible and even semi-transparent, depending on their fabrication. Because the light-harvesting layer thickness is typically in the range of a few hundred nanometers, only a small amount of material is required for the production, resulting in a low weight of the solar cell cell and enabling an energy payback time of only a few months. For industrial use, the potential of low-cost production, which can be achieved via printing and coating processes in continuous roll-to-roll machines, is the most important factor. These processes require special inks that match the printing process and the desired film properties. Most organic semiconductors used in solar cells are not soluble in eco-friendly solvents such as water or alcohol, but in halogenated solvents, which are often harmful to the environment and toxic or carcinogenic to humans, thus requiring costly gas purification during the printing process. With this process, current laboratory efficiencies of up to 19 % are achieved. For an industrial process, however, the elimination of solvents of concern is desirable. With the alternative approach of the nanoprecipitation, it is possible to disperse an organic semiconductor inside an eco-friendly liquid agent hence omitting the use of toxic solvents in the printing process.

The development of the efficiency from 4 % in the beginning of this work to over 10 % mainly due to the use of high efficient absorber materials and volatile stabilizers underlines the potential of this approach.

The common method of synthesizing nanoparticle dispersions is the manual nanoprecipitation inside a beaker, allowing only limited reproducibility. Starting with the blend of P3HT and $IC_{60}BA$, which enables the synthesis of stable nanoparticle dispersions, the production of nanoparticle dispersions by the continuous flow nanoprecipitation via microfluidics is examined in this work.

First, a suitable setup is implemented. Then, the influencing parameters on the nanoprecipitation process are identified and qualified. By controlling the influencing factors, dispersions with tailored nanoparticle sizes can be produced, allowing a highly reproducible nanoprecipitation. These dispersions exhibited an outstanding stability of over one year. To qualify this process, organic solar cells with light-harvesting layers from nanoparticle dispersions are fabricated. In

direct comparison, they outperformed the efficiency of solar cells with a light-harvesting layer from the common beaker precipitation.
While the blends of P3HT and $IC_{60}BA$ form stable dispersions, when blended with P3HT, many other acceptors flocculate. Therefore, the second part of this thesis focuses on the crucial requirements for the nanoparticle formation of P3HT:acceptor blends. Hence, the well-known group of fullerene derivatives is examined, and the miscibility of P3HT and the acceptor is identified as one of the most important factors.
From these results, the use of a third component is investigated to stabilize P3HT:acceptor blend that did not form stable dispersions. For this purpose, acceptors such as the fullerene $PC_{71}BM$ or donors such as regiorandom P3HT are investigated. With miscibility as a relevant factor, fist promising results could be obtained.
With the knowledge gained from this work, a scalable concept for the production of non-toxic inks for the fabrication of organic solar cells can be implemented, enabling a reproducible process. Thus, in the future, highly efficient solar cell materials can be specifically designed for layer production using nanoparticle dispersions, which will further promote the eco-friendly production of organic solar cells.

Publications

Published Articles

- F. Manger, K. Fischer, P. Marlow, H. Röhm, C. Sprau, A. Colsmann. *Iodine-stabilized Nanoparticle Dispersions for the Fabrication of 10% Efficient Non-Fullerene Organic Solar Cells*, Advanced Materials Technologies **2022**, *13*, 2202820.
- F. Manger, P. Marlow, K. Fischer, C. Sprau, A. Colsmann. *Organic Solar Cells: Electrostatic Stabilization of Organic Semiconductor Nanoparticle Dispersions by Electrical Doping*, Advanced Functional Materials **2022**, *32*, 2202566.
- P. Marlow, F. Manger, K. Fischer, C. Sprau, A. Colsmann, *Eco-friendly fabrication of organic solar cells: Electrostatic stabilization of surfactant-free organic nanoparticle dispersions by illumination,* Nanoscale **2022**, *14*, 5569.
- K. Fischer, P. Marlow, F. Manger, C. Sprau, A. Colsmann. *Microfluidics: continuous-flow synthesis of nanoparticle dispersions for the fabrication of organic solar cells*, Advanced Materials Technologies **2022**, *7*, 2200297.

Articles in preparation

- K. Fischer, P. Marlow, F. Manger, C. Sprau, A. Colsmann. *On the formation of polymer:fullerene nanoparticle dispersions: The role of miscibility*, in preparation.
- K. Fischer, J. Armleder, C. Sprau, A. Colsmann. *The use of ternary blends in nanoprecipitation for organic solar cells*, in preparation.

Presentation at international conference

- K. Fischer, P. Marlow, F. Manger, C. Sprau, A. Colsmann. *Microfluidics – a continuous flow synthesis of nanoparticle dispersions for organic solar cells*, E-MRS Spring Meeting **2021**, May 31 - June 4, Poster presentation. – awarded with the *Young Researcher Award* –

Supervised scientific work

Theses

- Hanna Bletzinger, *Einfluss der Regioregularität von P3HT auf die Bildung von Nanopartikeln*, Bachelor thesis in Mechatronics, 2023.
- Peer Große Hokamp, *Einfluss des Fulleren-Anteils auf die Bildung von P3HT:Fulleren Nanopartikeln*, Bachelor thesis in Electrical Engineering and Information Technology, 2022.
- Kilian Bitsch, *Einfluss von Fulleren-Derivaten auf die Bildung von P3HT:Fulleren Nanopartikeln*, Bachelor thesis in Material Sciences, 2021.
- Florian Mintel, *Organische Solarzellen: P3HT:ICBA Nanopartikel für maßgeschneiderte Absorberschichten*, Bachelor thesis in Electrical Engineering and Information Technology, 2021.
- Ayse Ardelt, *Fällung von P3HT:ICBA Nanopartikeldispersionen mittels Mikrofluidik*, Bachelor thesis in Electrical Engineering and Information Technology, 2019.

Contents

1 Introduction

One of the most important challenges of the 21st century is a sustainable energy supply. Currently, our society is highly dependent on oil and gas. In winter 2022, due to a huge increase in oil and gas prices and the fear of insufficient oil and gas, many households in Germany transitioned to electrical heating, resulting in an increased demand for electrical energy.
For the French, the situation was worse. 35 % of the French heat their homes with electricity, mostly from nuclear power plants.[1] But half of the nuclear power plants were shut down due to maintenance. Because of the realistic possibility of a blackout, during the cold period, plans for rationing energy, like heating only at night to save electricity, were made by the government. But also the hot summers, such as the summer 2022, show the need for a sustainable energy supply and the limitations of nuclear power plants for the supply of electricity. Because of low water levels and critical water temperatures over 26 °C, cooling water from the Rhine was missing, resulting in a shut down of nuclear power plants in France.[2] Therefore, other european countries, such as Germany, had to compensate by burning their gas instead of filling their storage, which again resulted in a scarcity of gas for the winter.[3]
A viable solution to meet the increasing demand of electrical energy is a massive expansion of renewable energies. In Germany, in 2022, 46.2 % of the generated electricity came from renewable energies, with a total of 10.9 % from photovoltaics. Compared to 2021, 1.7 % more electricity is generated by photovoltaics. Although this seems like a huge increase, the use of hard coal and lignite also increased by 2.1 % and 1 %, respectively, while the energy from nulear power plants decreased.[4]
Although more and more houses are equipped with solar panels, there is insufficient space on rooftops to cover the future electrical demand. Therefore, utilizing new areas, like windows and house facades, will play an important role in the future. For this purpose, new technologies, such as organic solar cells, provide several advantages.
Organic solar cells have many advantages compared to commonly used silicon solar cells. Besides their excellent low-light performance, they can be lightweight, mechanically flexible and even semi-transparent.[5] Because the light-harvesting layer thickness is typically on the order of a few hundred nanometers, only smallest amounts of the photoactive material are needed. By depositing these thin films on a plastic foil, the solar cells become mechanically flexible. The

optional semi-transparency depends on the architecture and the choice of materials.
Those advantages can be a unique selling point, but for industrial use, the potential for low-cost fabrication and an energy payback time of only a few months is most important.[6, 7] The low-cost fabrication is achieved via printing and coating processes like screen-printing and spray coating in continuous roll-to-roll processes. These processes require special inks that suit the printing process and produce good film quality. Most of the common inks use halogenated solvents that are often harmful to the environment, toxic or carcinogenic. Using those inks for large-scale printing leads to additional costs in waste gas purification and is therefore less environmentally sustainable. Most of the organic semiconductors that are used in organic photovoltaic (OPV) are not soluble in eco-friendly solvents like water or alcohol. By using nanoprecipitation, it is possible to disperse organic semiconductors in an eco-friendly liquid agent, hence omitting the use of toxic solvents in the printing process.
In 2014, Gärtner et al. showed that efficient solar cells can be fabricated from P3HT:ICBA nanoparticle dispersion, yielding a PCE of 4 %.[8] Sankaran et al. ink-jet-printed light-harvesting layers of organic solar cells from such inks, yielding an efficiency of 2.9 %. They also built all-ink-jet printed solar cells with an efficiency of 1.9 %. This shows that upscaling is possible, yet challenging.[9]
Since then, many groups have tried to achieve stable nanoparticle dispersions. The two main goals are the synthesis of nanoparticle dispersions for the fabrication of high-efficient organic solar cells and the ability to achieve a reproducible, scalable production of dispersions with consistent quality and nanoparticle size, that can be used for upscaling concepts.
The performance of solar cells from nanoparticle dispersions was enhanced through the years from 3.8 % to 10 % by using highly efficient absorber materials and volatile stabilizers.[10, 11, 12, 13, 14] Concepts without using a stabilizer do not obtain solar cells with such a high efficiency.
Even though great improvements in the efficiency of solar cells with a nanoparticulate light-harvesting layer were made, reports on the reproducibility of inks from a scalable process are still lacking. A continuous flow nanoprecipitation like microfluidics is a well established way for a scalable, reproducible production of nanoparticle dispersions. In drug manufacturing, imaging and bioanalysis, microfluidics is the state of the art process.[15] Microfluidics offer the advantage of rapid mixing of small amounts of fluids on the microscale and excellent process control for best reproducibility.[16] By parallelization of microfluidic chips and syringe pumps, up-scaling of this process and hence the production of large amounts of ink in a short period of time will be possible.
Starting with a blend of P3HT and $IC_{60}BA$, the only blend that forms nanoparticles without the addition of a dopant, with a dispersion stability of several weeks, this work will examine the

production of nanoparticle dispersions by continuous flow nanoprecipitation in a microfluidic setup. First, the influencing parameters on the nanoprecipitation process will be investigated, and both stability and reproducibility will be examined. The resulting dispersions will be characterized for the fabrication of organic solar cells, while the solar cells will be compared to solar cells from the well-known batch nanoprecipitation.

While P3HT and $IC_{60}BA$ form stable dispersions, many other acceptors flocculate. Therefore, the second part of this thesis will focus on the requirements for the nanoparticle formation of P3HT:acceptor blends and will identify the underlying mechanisms. Hence, a group of well-known fullerene derivatives will be evaluated as acceptors. The stabilization of blends of P3HT:acceptor that do not form stable dispersions will be investigated by adding a third component.

The knowledge gained from this work supports a scalable concept for the production of non-toxic inks for the fabrication of organic solar cells with high reproducibility. The deep understanding on the stabilization of nanoparticle blends enables the synthesis of nanoparticles for the fabrication of future high-efficient solar cells.

2 Fundamentals

In this chapter, the fundamentals of organic materials needed for further understanding, are discussed, starting with the hybridization of carbon and the introduction of the molecular orbitals. After the introduction of organic semiconductors, the key characteristics of solar cells are described, followed by the basics of nanoparticle formation.

2.1 Organic semiconductors

Organic semiconductors refer to a class of organic materials with semiconducting properties. Since they are based on carbon molecules, with mostly hydrogen and sometimes oxygen, nitrogen or sulfur atoms, the electronic structure of carbon is decisive for the properties of organic compounds. The basic electronic properties of carbon-based compounds can be explained by the molecular orbital (MO) theory. Their characteristics are based on the delocalization of electrons over large parts of the molecule.

2.1.1 Molecule orbitals

Carbon has four valence electrons, with the ground state configuration $1s^2\ 2s^2\ 2p^2$. In this configuration, the 2s-orbitals are fully occupied, while the 2p-orbitals contain two unbound electrons. In theory, this would enable carbon to form only two covalent bonds. In reality, through bonding with, for example, another carbon atom and some hydrogen atoms, the formation of hybrid orbitals occurs. In doing so, two carbon atoms may form a single, double, or triple bond, which corresponds to ethane, ethene, or ethyne, respectively. The corresponding hybridizations are illustrated in Figure 2.1. The released binding energy compensates the required energy for the hybridization and enables the formation of hybrid orbitals. Due to the fact that the hybridization is energetically more favorable, carbon exists exclusively in bound form and the ground state is not found in nature.[17, 18]
The linear combination of the wavefunctions from the 2s- and 2p-orbitals describes the formation of hybrid orbitals, and each orbital is occupied by one electron. Different types of hybridization (sp^3, sp^2 or sp), based on the number of 2p-orbitals involved, can occur, as specified in the superscript.
In case of sp^3-hybridization, all 2p-orbitals and the 2s-orbital form a hybrid orbital. This leads

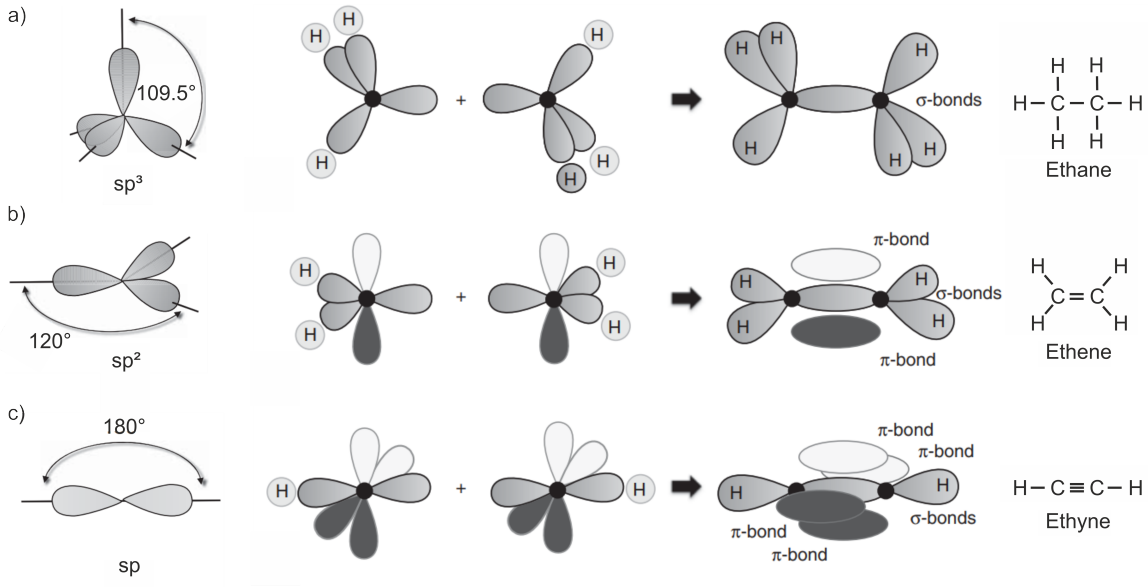

Figure 2.1: Hybridization of two carbon and several hydrogen atoms. The combination of a) six b) four and c) two hydrogen atoms with two carbon atoms yield ethane (sp^3), ethene (sp^2), and ethyne (sp), respectively. Figure from [18]

to a tetrahedral arrangement at an angle of 109.5 ° around the atomic nucleus, which is shown in Figure 2.1 a. If two carbon atoms form a single bond, ethane (C_2H_6) is formed. Each hybrid orbital is occupied by one of the four electrons, and each electron has a covalent bond to either the second carbon or a hydrogen atom. Covalent single bonds are also known as σ-bonds, where the pair of electrons forms a combined molecular orbital, the σ-orbital.

In case of sp^2-hybridization, as shown in Figure 2.1 b, two 2p- and the 2s-orbitals form a hybrid orbital. The three sp^2-orbitals are co-planar and form a 120 ° angle. The remaining p-orbital is orthogonal to the molecular plane. For ethene (C_2H_4), also known as ethylene, two of the sp^2-orbitals bind to a hydrogen atom, while the third sp^2-orbital binds to carbon. The remaining orthogonal p-orbital forms a weak π-bond between the p-orbitals of the two carbon atoms, leading to the formation of a π-orbital, with the two electrons of the π-bond having a shared maximum probability density both above and below the plane.

In case of sp-hybridization, only one 2p-orbital forms a hybrid orbital with the 2s-orbital, which results in two sp-orbitals that are arranged at an angle of 180 °, as illustrated in Figure 2.1 c. The two remaining p-orbitals are again orthogonal to the molecular plane. For ethyne (C_2H_2), also known as acetylene, each sp-orbital forms a σ-bonds to a hydrogen atom and to the other carbon atom, while the two remaining p-orbitals form two π-bonds with the p-orbitals of the other carbon atom.

The resulting molecular orbitals (MO) can be approximated as a linear combination of atomic orbitals (LCAO). For further discussion, it is assumed that both MOs are known solutions of the Schrödinger equation for the molecule.
The orbital energies can be assigned to the electrons in the orbitals. Each MO can be occupied by up to two electrons with opposite spins, so sorting them in ascending order according to Hund's rule yields a diagram of the sp^2-hybridization, as illustrated in Figure 2.2. At a given temperature T, these orbitals can be occupied or unoccupied. The electron distribution on the molecular orbitals is referred to as electron configuration.[19] Occupied orbitals contribute to the stabilization of the bond through their negative orbital energies. Therefore, the occupied orbitals with the highest energies are most relevant because they are most likely available for chemical reactions.

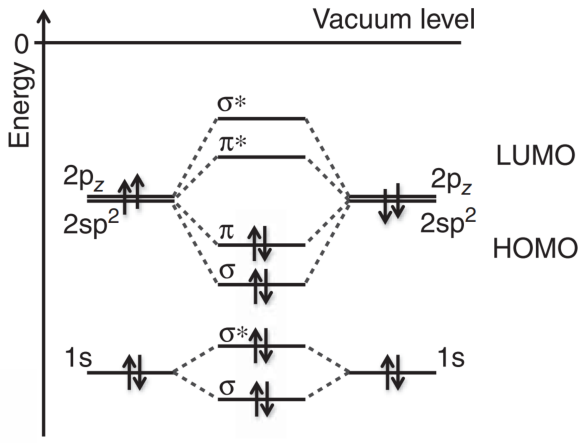

Figure 2.2: Energy diagram of ethylene with σ- and π-orbitals in sp^2-hybridization. The electrons occupy the binding σ- and π-orbitals, while the anti-binding σ*- and π*-orbitals are empty. Figure from [18].

2.1.2 From a carbon molecule to a polymer

The sp^2-hybridization allows for a variety of complex but stable conjugated molecules.[20] Through the spatial overlap of the p-orbitals, weakly bound π-π-electrons are quasi delocalized, which enables the movement of charge carriers within the polymer.
In organic molecules with a conjugated π-electron system, the electrons within the π-orbitals have the highest energies. The σ-bonds are represented by other occupied MOs at lower energies, which are less relevant for the electronic properties than the π-orbitals. Increasing the π-system, as depicted in Figure 2.3, results in a more pronounced delocalization of electrons, resulting in a decrease of the energy difference of the π-orbitals, which leads to an increase in the energy of the highest occupied molecular orbital (HOMO) and a decrease in the energy

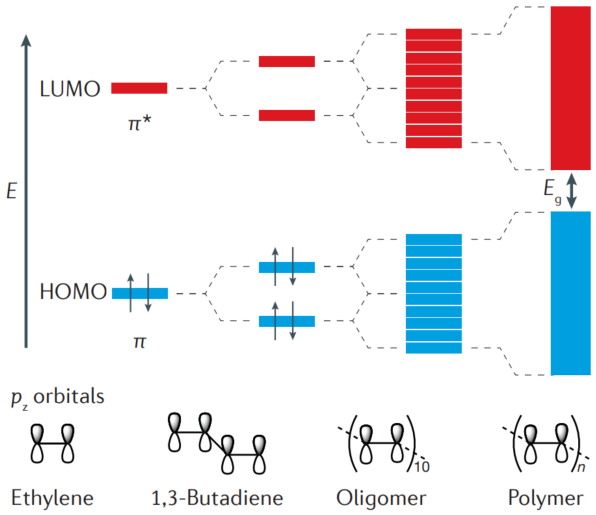

Figure 2.3: Schematic of the splitting of π-orbitals from a small molecule like ethylene to a highly complex polymer. By increasing the number of carbon atoms, the energy gap between HOMO and LUMO decreases. Figure from [21].

of the lowest unoccupied molecular orbital (LUMO). In organic semiconductors, the energy gap E_g between HOMO and LUMO usually ranges between 1.5 eV and 3 eV, with the HOMO corresponding to the valence band and the LUMO corresponding to the conduction band of inorganic semiconductors.[22] This energy gap determines the photon absorption and emission of the organic semiconductor. To excite an electron from an occupied to an unoccupied orbital, a photon needs sufficient energy. For large molecules and long polymer chains, as well as for small organic molecules, the π-bond is important. In the ideal case, due to the overlap of the π-orbitals, the electrons are delocalized over the entire polymer.[23] Because of the extension of the π-orbitals over the whole molecule, the approach of the MO is more accurate than the structural formula.

For the description of charge carrier reactions, the ionization potential (IP) and the electron affinity (EA) are used. While the IP is the energy that is needed to remove an electron, the EA is the energy that is gained by adding an electron to the molecule. As opposed to HOMO and LUMO, which are theoretical, quantum mechanical concepts, both IP and EA can be measured. HOMO and LUMO can be approximated by using Koopmans' theorem, assuming that ionization does not change the energy levels. Thus, the IP of a molecule is equal to the negative of the orbital energy of the HOMO, which is equivalent to removing an electron from the HOMO. The EA is equal to the negative LUMO-energy and corresponds to the addition of an electron to the LUMO. Molecules with low IP can donate an electron, which implies that they are good electron donor molecules, while molecules with a high EA can easily accept an electron, which makes them good electron acceptors. In reality, both the electron distribution and the MOs change

through ionization. This leads to a lower energy of the ionized molecule and both an overestimation of HOMO and an underestimation of LUMO through this approximation.[24, 25]
Several electron transfer reactions, which are illustrated in Figure 2.4 by the MO model of two molecules, with one being electron donating (D, donor) and one being electron accepting (A, acceptor), occur in the ground state. Through the higher HOMO-energy of the electron-donating molecule compared to the LUMO of the accepting molecule, an electron can transfer from HOMO to LUMO, as depicted in Figure 2.4 a. The photoinduced electron transfer is also relevant for organic semiconductors. In Figure 2.4 b, a photon with adequate energy (*hv*) can excite an electron from the HOMO to the LUMO, leading to a half-occupied HOMO. By exciting the donor, the electron in the LUMO of the donor can be transferred to the LUMO of the acceptor. By exciting the acceptor, a hole from the HOMO of the acceptor can be transferred to the HOMO of the donor. Furthermore, an electron transfer between an ionized and a neutral

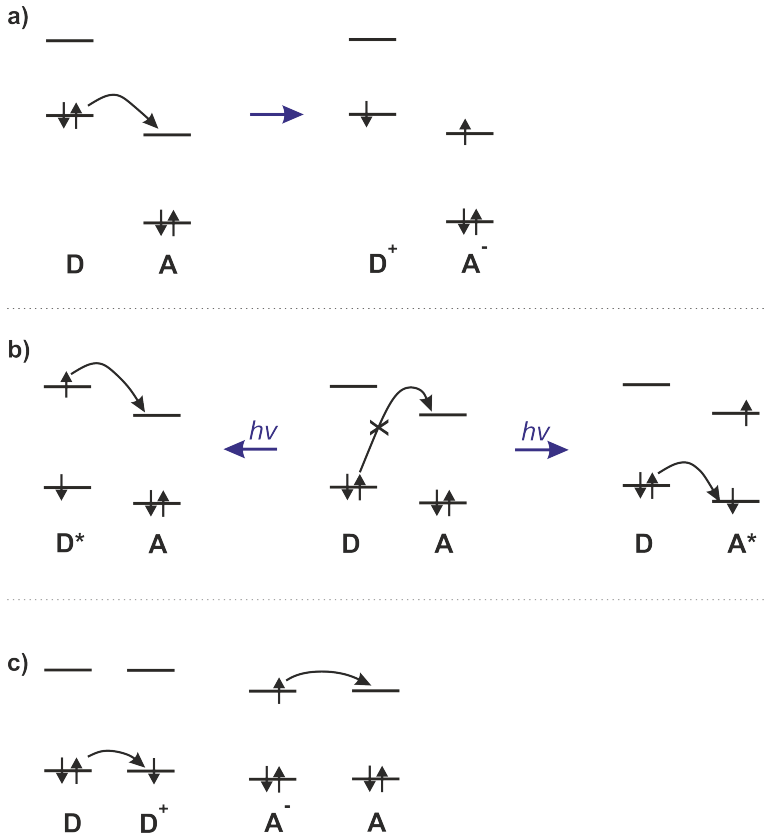

Figure 2.4: Electron transfer reaction of an electron donating (D) and an electron accepting (A) molecule. a) Through the offset between the HOMO of the donor and the LUMO of the acceptor, an electron can transfer. b) A photon with an energy *hv* can excite an electron from the HOMO of the donor or acceptor to the LUMO of the donor or acceptor, respectively, which leads to a half occupied HOMO and a further transfer. c) An electron can be transferred between an ionized and a neutral molecule. Figure from [26]. Published by Philipp Marlow under the Licence CC BY-SA 4.0.

molecule is possible, as illustrated in Figure 2.4 c.

While the MO theory assumes that the atomic nuclei are static, in reality they oscillate and rotate around their equilibrium position relative to each other. Therefore, an approximation that considers the transition between two energetic states of a molecule, as well as the wavefunctions of the electrons, the spins, and the vibrations of the atoms, is needed. Each orbital can be occupied by two electrons with opposite spin. During the transition of an electron from the ground state to the excited state, the spin persists. For light-harvesting devices, the spin does not have to be taken into account, therefore, only the electronic and vibrational wavefunction have to be considered. The Franck-Condon principle states that due to the much faster movement of the electrons compared to the movement of the atomic nuclei, the electronic and the vibrational wavefunctions can be considered independent of each other.[27] A graphical depiction of the Frank-Condon principle is included in Figure 2.5 a for the ground state S_0 and the first excited state S_1. Each electronic state S splits into different vibrational states v_M, i.e. different vibrational wavefunctions, with very small energy differences. The minima of the electronic states are slightly shifted due to the different equilibrium positions of the nuclei.[28]

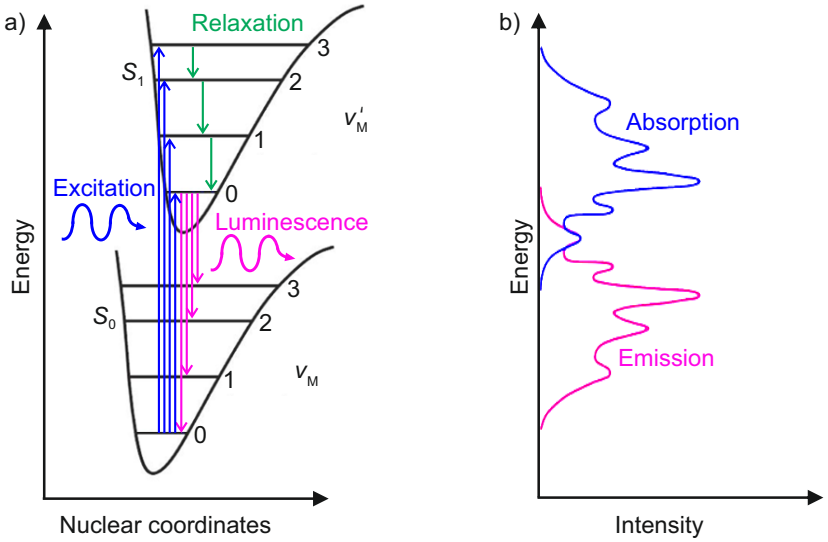

Figure 2.5: Graphical illustration of the Frank-Condon principle. a) Upon excitation, an electron is lifted from S_0 to the higher state S_1 with a vibrational state v'_M. The electron relaxes nonradiatively back to the lowest excited state v'_0 of S_1. Under the emission of a photon, it relaxes to the ground state S_0. Through vibrational relaxation, the electron reverts to v_0. b) Emission (luminescence) and absorption (excitation) spectra of to the energy diagram in a. The difference between the energy of emission and absorption corresponds to the Stokes shift.

Through the excitation of an electron by a photon with energy above the energy gap, the electron is lifted from S_0 to an energetically higher state S_1, with a vibration state v'_M. The change in both the electronic and vibrational states are referred to as a vibronic transition. The transition

has different probability rates, which depend on the vibrational wavefunction and are proportional to their overlap. As a result, some transitions occur more frequently than others.[29] After excitation, the electron relaxes nonradiatively back to the lowest excited S_1 state v'_0. By emitting a photon, it relaxes back to the v_M state of the ground state S_0. Through vibrational relaxation, the electron returns to v_0. As a result of recombination at impurities and relaxation losses, the rate of the nonradiative recombination is higher than the radiative recombination. Comparing both the absorption and emission energy in Figure 2.5 b shows, that the energy of the emitted photons is lower than the energy of the absorbed photons. In only one case, at the transition from S_0 v_0 to S_1 v'_0, an overlap occurs. This effect is referred to as "Stokes shift", which renders the material mostly transparent to its own radiation.

The transition from a molecule to a molecular solid often changes the energy landscape. In organic solids, molecules interact by weak van-der-Waals forces. Through fluctuating charges, temporary dipoles are induced, which lead to an attractive force.[30] The weak van-der-Waals forces lead to low melting points and low rigidities of most organic solids, which is why they are also referred to as soft matter. Several spectroscopic characteristics of single molecules are also recognizable in solids. However, terms such as HOMO and LUMO, which are defined for an individual molecule, are often wrongly used for the solid. In terms of molecular properties in the solid state, the big difference stems from the surrounding of each molecule by other molecules, which enables shielding of charges due to polarization. Therefore, an electron can be easily removed into vacuum through the partial shielding of the remaining positive charges from the environment, which reduces the IP in the solid state, compared to the single molecule. This rationale is also applicable to the EA and leads to a reduction of the energy difference between the IP and the EA. Since energy transport occurs through charged molecules, the energy difference between IP and EA is the transport energy $E_{\text{transport}}$. The change from a single molecule to a solid also influences the optical energy gap E_{opt}. The shift of IP and EA through polarization reduces the binding energy of an exciton (bound electron-hole pair) in the range of a few 100 meV.[31] The binding energy can be calculated by measuring IP, EA and E_{opt}. In inorganic semiconductors, Mott-Wannier excitons overcome the binding energy of $k_B T \approx 26$ meV at room temperature. Therefore, they can be approximated as pairs of free charge carriers. In organic semiconductors, instead of forming free electrons and holes, photoexcitation creates Frenkel excitons which cannot dissociate at room temperature. For the dissociation of Frenkel excitons, a minimum energy difference of 300 meV is required.[32]

2.1.3 Charge carrier transfer

Free charge carriers can be generated in different ways. A redox reaction, in which a strong oxidizing agent accepts electrons from the organic semiconductor, or a strong reducing agent donates electrons to the organic semiconductor, is one way of generating charge carriers.[33] Thus, the insulating organic semiconductor becomes conductive. This is actually a chemical redox reaction, but according to the creation of majority charge carriers in inorganic semiconductors, it is called doping. While n-doping corresponds to the reduction of a semiconductor, p-doping corresponds to its oxidation. Anions and cations are often more stable than the neutral molecule.[34]
Another way of generating charge carriers is the photoinduced electron transfer between donor-acceptor pairs, as shown in Figure 2.4 b. Especially in organic solar cells, photoinduced electron transfer is crucial. After absorbing a photon, the molecule relaxes to the lowest excited state S_1. This is known as Kasha's rule. The excitation energy is localized on a single molecule. Energy transport to a nearby molecule can occur by Förster or Dexter energy transfer, but the molecules remain electrically neutral (without charge separation).[19, 35]
The molecular arrangement in the solid state can also influence optoelectronic properties. In highly ordered crystals, because of the superposition of the wavefunction, the orbitals split energetically and form state bands that are similar to the valence and conduction bands of classical semiconductors. However, most polymers do not form crystals, because they are neither ideal nor free of defects and have no planar π-system over the whole molecule. Also, the electronic states of the polymers are not uniform. Along the polymer chain, the coupling of the electronic states is rather strong, resulting in a delocalization. This leads to a high charge carrier mobility μ along the chain. Between the chains, because of the dynamic disorder caused by molecular vibration, the coupling is rather weak, leading to states localized on individual segments. The charge carriers can move between localized states only by independent, thermally activated leaps. This transport mechanism is referred to as hopping transport.[36] While molecular crystals have a typical mobility on the order of μ = 40 cm^2/Vs, the mobility in blend layers of organic solar cells is in the range of 10^{-6} cm^2/Vs to 10^{-2} cm^2/Vs, mainly because of a lower molecular order. The low mobility leads to a low electrical conductivity σ of organic semiconductors, with $\sigma = e \cdot (\mu_n \cdot n + \mu_p \cdot p)$ and the elementary charge e, the charge carrier density of electrons n and holes p. Therefore, organic semiconductor layers need to be rather thin (a few 100 nm) in order to keep ohmic losses low. However, because of the high absorption coefficient of organic semiconductors, these thin layers already absorb a significant portion of incident light.

2.2 Organic solar cells

Organic solar cells convert sunlight into electricity by using the photovoltaic effect. They can exhibit many advantages over existing photovoltaic technologies. In addition to their excellent low light performance, they can be lightweight, flexible, and even semi-transparent.[5] Since the thickness of the light-harvesting layer is typically on the order of a few hundred nanometers, only small amounts of light-harvesting material are needed per area. Organic solar cells have the potential of low-cost fabrication by printing and coating processes, requiring special inks that determine the printing process and lead to optimal film quality and an energy payback time of only a few months.[6, 7]

2.2.1 Organic solar cell architectures

In organic semiconductors, both the generation and the transport of free charge carriers are challenging. Given that organic semiconductors are typically either good electron conductors (acceptors) or good hole conductors (donors), a blend of donors and acceptors is needed to split the excitons. Through excitation by a photon, a strongly bound exciton is generated, which can be separated at the interface of donor and acceptor domains. The diffusion length of an exciton is typically several tens of a nanometer.[37] If an exciton reaches the interface before recombining, it can be dissociated into an electron and a hole, which leads to the formation of an intermolecular charge transfer (CT) state. Therefore, an interface with large area is required. In theory, two layers on top of each other (homojunction) could achieve this. In reality, it is better to use a blend layer that enables efficient exciton dissociation at its large interface. This morphology can be achieved through the use of a bulk-heterojunction, in which a donor and an acceptor form an interpenetrating network. After dissociation of an exciton, both the donor and the acceptor are ionized. While the donor releases an electron or receives a positive charge, the acceptor takes the electron or donates a positive charge. The generation of the exciton is typically described by the absorption of the donor, but excitons can also be generated by the absorption of the acceptor. The charge carriers are collected at the electrodes. This concept is illustrated in Figure 2.6 a. In order to obtain high exciton dissociation rates, short transport paths to the electrodes are crucial. The simplest layout consists of a layer sandwiched between two electrodes with different work functions. One of the two electrodes has to be transparent, so that light can reach the light-harvesting layer. If the anode is chosen as a transparent electrode, the architecture is commonly referred to as being regular, whereas by choosing the cathode, it is referred to as inverted. Typically, the cathode consists of a material with a low work function and accepts electrons, while the anode consists of a material with a high work function and collects holes. Through thin transport layers between the light-harvesting layer and the

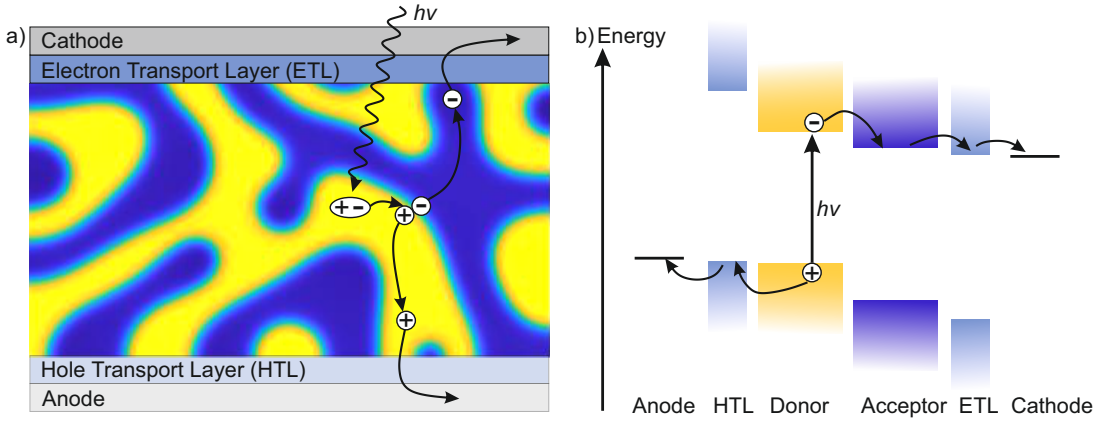

Figure 2.6: Organic solar cell in inverted architecture, with an illustration of the heterojunction and the energy diagram. a) After passing the cathode, a photon generates an exciton, which dissociates at the interface of donor and acceptor. The resulting charge carriers are transported to the respective electrodes. b) The generation and transport of charge carriers in the organic solar cell are shown in an energy diagram. The charge carrier transport between the different materials takes place through the transfer of electrons into unoccupied or partially occupied molecular orbitals at lower energy. Figure from [26]. Published by Philipp Marlow under the Licence CC BY-SA 4.0.

respective electrode, the selectivity for certain charge carriers and the alignment of the energy levels can be improved. The electron is transported to the cathode through the electron transport layer (ETL), and the hole is transported to the anode through the hole transport layer (HTL). If the contacts were not selective enough, free charge carriers could recombine at the wrong electrode, eventually causing losses. Also, the extraction of free charge carriers at the respective electrodes needs to proceed quickly, otherwise space charges build up, which influences the charge carrier collection. The energy diagram of the solar cell is illustrated in Figure 2.6 b.
The absorption of photons inside the light-harvesting layer depends on the absorption coefficient of the organic semiconductor, with a rather narrow band for the spectral absorption. The absorption profile, which describes how many of the incident photons are absorbed by each layer, is related to the optical constants and the thicknesses of the layers. Through typical layer thicknesses in the range of the wavelength of light, interference can occur. Reflection on the back electrode, incomplete absorption by too-small light-harvesting layer thicknesses, and parasitic absorption in other layers can result in losses.

2.2.2 Solar cell characteristics

The excitation of charge carriers inside the light-harvesting layer of organic solar cells depends on their electrical operating point. In a simplified model, only the two electrodes and the light-harvesting layer in between are considered. Since the mobility of the organic semiconductor is much lower than the mobility of the metal electrodes, it can be approximated as an insulator,

which leads to a metal-insulator-metal junction. The anode has a high work function Φ_{anode} and an ohmic contact to the donor's HOMO, while the cathode has a low work function Φ_{cathode} and an ohmic contact to the acceptor's LUMO. When the electrodes and the organic semiconductor are brought into contact, the Fermi levels align, which leads to a tilting of both the vacuum energy E_{Vac} and the HOMO-LUMO states and consequently to an internal electric build-in field in the light-harvesting layer.[18, 38] By adding an externally applied voltage V to the built-in field, as illustrated in Figure 2.7, an electric field is created that determines the transport of the generated free charge carriers, and a current I can be measured.

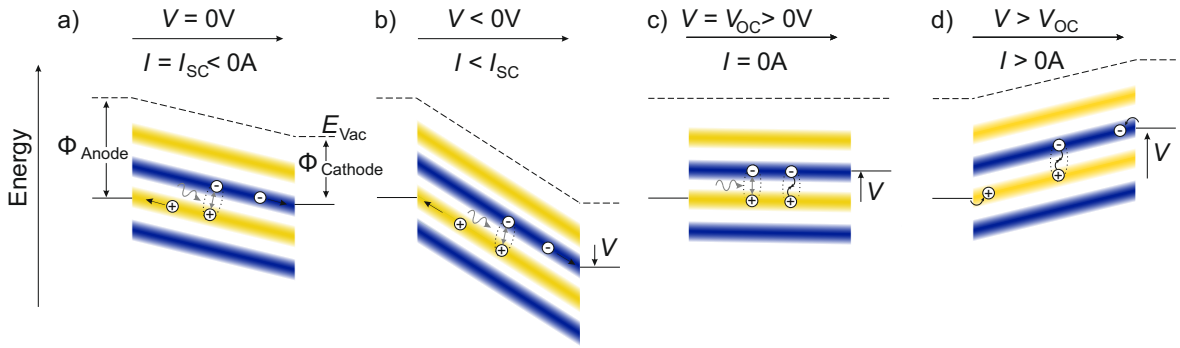

Figure 2.7: Working principle of an organic solar cell in a metal-insulator-metal junction model. By bringing two electrodes and the organic semiconductor in contact, an internal electric field is generated through the alignment of the Fermi levels, showing the donor in yellow and the acceptor in blue. The HOMO of the donor and the LUMO of the acceptor are relevant for the transport of the generated charge carriers. a) In short circuit, generated free charge carriers drift by the internal electric field and the short-circuit current I_{SC}, which can be measured externally, flows. b) By applying a negative voltage (reverse direction), the internal field increases, which leads to a faster drift of the charge carriers to the respective electrodes. c) By applying a positive voltage, the internal field decreases, until all generated charge carriers recombine at the open-circuit voltage V_{OC} and no current flows. d) At a voltage higher than V_{OC}, charge carriers are injected via the contacts and recombine at the light-harvesting layer. This leads to a rise of the device current even in the dark. Adapted from [18, 38].

Instead of the current, which depends on the area of the solar cell, the current density (J) is typically used. The voltage-to-current-density characteristic (J-V curve), as depicted in Figure 2.8, illustrates their dependence. In total darkness, the J-V curve corresponds to a diode. In reverse direction, no current flows and the diode is blocking. In forward direction, after an onset voltage, the current increases exponentially.

Through illumination, the J-V curve shifts by a photocurrent density. For $V = 0$ V, the electrodes are short-circuited, leading to drift of the free charge carriers to the respective electrodes. The generated photo current is referred to as short-circuit current density J_{SC} (Figure 2.7 a). For $V < 0$ V, the electric field increases, leading to a faster drift of the charge carriers and a reduction of the recombination losses (Figure 2.7 b). For $V > 0$ V, the electric field decreases, reducing the drift speed of the charge carriers and leading to recombination. When all generated charge

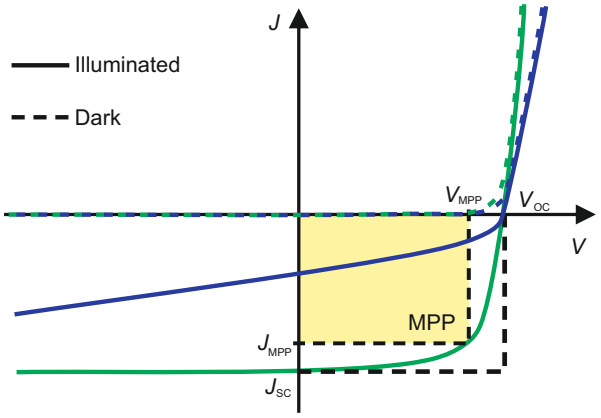

Figure 2.8: *J*-*V* curves of a good solar cell in green and a poor solar cell in blue, in the dark (dashed line) and under illumination (solid line). The maximum power point (MPP) describes the point where the product of voltage V_{MPP} and current density J_{MPP} is maximal. The corresponding output power is illustrated with a yellow rectangle. The highest output power that could be achieved is the product of the short-circuit density J_{SC} and the open-circuit voltage V_{OC}.

carriers recombine, no current flows, which leads to the open-circuit case at V_{OC} (Figure 2.7 c). If V increases further, the electrodes inject charge carriers into the light-harvesting layer, which leads to the recombination of both the injected and the generated charge carriers (Figure 2.7 d).

A solar cell converts electromagnetic radiation energy into electrical energy. The power density P results from the product of J and V. In the fourth quadrant of the *J*-*V* curve, this product is negative and power can be extracted from the solar cell. The point where most of the energy can be extracted is called the maximum power point MPP, with $P_{\mathrm{MPP}} = J_{\mathrm{MPP}} \cdot V_{\mathrm{MPP}}$. The highest photocurrent density that could be generated is J_{SC}. The highest voltage the solar cell operates under illumination is V_{OC}, where the generation and the recombination of charge carriers is equal. This leads to the theoretical maximum power $P_{\mathrm{max}} = J_{\mathrm{SC}} \cdot V_{\mathrm{OC}}$. The ratio of P_{MPP} to P_{max} is referred to as the fill factor FF.

$$\mathrm{FF} = \frac{P_{\mathrm{MPP}}}{P_{\mathrm{max}}} = \frac{J_{\mathrm{MPP}} \cdot V_{\mathrm{MPP}}}{J_{\mathrm{SC}} \cdot V_{\mathrm{OC}}}$$

To achieve a high fill factor, losses through recombination need to be minimized. Therefore, a microstructure with high molecular regularity and pure domain phases is essential to minimize the recombination losses due to an improvement of the morphology through the phase purity and good charge carrier transport. This allows the fabrication of solar cells with thicker light-harvesting layers, resulting in an increased absorbance, while still achieving efficient solar cells. To compare two solar cells, the power conversion efficiency η, also known under the acronym PCE, which describes how much solar power can be converted to electric power, is the most

crucial metric. While the input energy from the sun P_{in} is defined as 1000 W/m^2 by the AM 1.5G norm spectrum, the output of the solar cell P_{out} corresponds to P_{MPP}, which leads to:

$$\eta = \frac{P_{MPP}}{P_{in}} = \frac{FF \cdot J_{SC} \cdot V_{OC}}{P_{in}}$$

2.2.3 Equivalent circuit of a solar cell

The ideal J-V curves of solar cells can also be described by the One-diode equivalent circuit, as shown in Figure 2.9 a. The solar cell behavior in the dark is represented by a diode. Parallel to the diode is a current source, which represents the photocurrent density that is generated by illumination. In contrast to an ideal diode, a real solar cell has no perfect blocking. The leakage currents through the solar cell are symbolized by a parallel resistance R_P, while the serial resistance R_S summarizes the losses due to the conductance of the organic semiconductor, the transport between the different layers and the resistance of the leads.

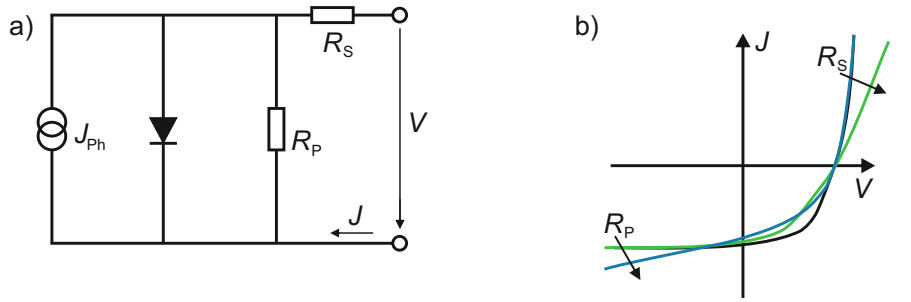

Figure 2.9: a) One-diode equivalent circuit of a solar cell. A diode describes the solar cell in the dark and a current source describes the photocurrent J_{Ph} that is generated under illumination. The parallel resistance R_P symbolizes the leakage currents through shorts, while ohmic losses are represented by the serial resistance R_S. b) Influence of parallel and serial resistance on the J-V curve. Through an increase of R_S, which is ideally zero, the slope of the J-V curve (blue) in operative direction is reduced, which leads to a decreased FF, while a decrease of R_P (green), which is ideally infinite, leads to a tilt at $V = 0$ V and also reduces the FF.

This results in the current density J of the solar cell dependent on the voltage V:

$$J(V) = J_0 \left(\exp\left(\frac{e(V - J \cdot R_S)}{n \cdot k_B T} \right) - 1 \right) - J_{Ph} + \frac{V - J \cdot R_S}{R_P}$$

The first term describes the behavior of the diode, with the reverse saturation current density J_0, the elementary charge e, the ideality factor of the diode n, the Boltzmann constant k_B and the temperature T. The second term contains the photoinduced current density J_{Ph} that is independent of the voltage. The third term accounts for the resistances. Their influence on the J-V curve is shown in Figure 2.9 b. Ideally, the parallel resistance is infinite, while the serial

resistance is zero. A decrease in parallel resistance leads to a tilt of the curve at $V < V_{MPP}$ (blue line compared to black line), for example, through local shorting within the layer. An increase in serial resistance leads to a reduced slope for $J > J_{MPP}$ (green line compared to black line). Both described resistance changes lead to a reduced J_{MPP} and V_{MPP}, directly decreasing the FF and the efficiency.

The ratio of extracted charge carriers to incident photons is called the external quantum efficiency (EQE). The EQE is dependent on light absorption and the collection of the charge carriers, while recombination reduces it. To determine the EQE, the spectral response *SR* of the solar cell is measured. The *SR* is the ratio of the photocurrent and the irradiated light power for each wavelength λ. From the spectral response, the EQE can be calculated to:

$$\mathrm{EQE}(\lambda) = SR(\lambda) \cdot \frac{h \cdot c_0}{\lambda \cdot e}$$

with Planck's constant h, the vacuum light velocity c_0 and the elementary charge e.[39, 40] By combining the EQE with transmission and reflection measurements, the internal quantum efficiency IQE can be calculated. The IQE indicates how many of the photons that were absorbed in the light-harvesting layer, generate a charge carrier that reaches the electrodes.

The total J_{SC} can also be calculated by integrating the solar spectral irradiance $E_{solar}(\lambda)$ and the EQE over the wavelength.

$$J_{SC} = \int \mathrm{EQE}(\lambda) \cdot E_{solar}(\lambda) \mathrm{d}\lambda$$

The V_{OC} is determined by the charge-transfer state and thus is linked to the offset between the HOMO of the donor and the LUMO of the acceptor.[41, 42] With increasing offset, a higher V_{OC} is possible. The V_{OC} also depends on parameters such as temperature, exciton generation rate, charge carrier mobility, charge carrier lifetime, and recombination rate.[41, 42]

The D-A morphology is crucial for an efficient solar cell. The choice of solvent or thermal annealing can change the morphology, which can influence all processes and loss mechanisms.[42] In theory, the idea of a perfectly blended bulk-heterojunction with two interpenetrating phases is possible. In reality, at least three phases exist, two pure material phases and a mixed phase. The pure material phases should be large enough to enable a sufficient charge carrier transport, while being small enough to prevent recombination. The relevance of mixed phases, where dissociation at the interface and extraction towards the electrodes via transportation routes are possible, has been demonstrated in the last years.[43, 44, 45, 46] Ideally, the mixed phase is directly adjacent to the pure phases, which leads to efficient charge carrier separation.

2.3 Organic nanoparticles

Most organic semiconductors are soluble in halogenated solvents such as chloroform or chlorobenzene, which are harmful to the environment and often toxic to humans. When using these solutions as inks for large-scale printing, the required safety measures would drive up the fabrication costs. Organic semiconductors are insoluble in environmentally friendly solvents such as water or alcohol. However, they can be dispersed in eco-friendly liquid agents as nanoparticles, hence omitting the use of toxic solvents in the printing process. The solar cells in this work are fabricated by using a light-harvesting layer deposited from nanoparticle dispersions. Therefore, in the following section, the basics of nanoparticle formation are described.

2.3.1 Nanoprecipitation

Two routes can be used to obtain nanoparticle dispersions. The most often used method features a miniemulsion, in which a solution of the organic material is emulsified in an immiscible nonsolvent.[47] Small droplets of the solution within the nonsolvent are produced by ultrasonication. A surfactant stabilizes the emulsion, and the solvent is subsequently removed by thermal evaporation, yielding a dispersion of solid nanoparticles. Because most surfactants worsen the performance of the solar cell, excess surfactant has to be subsequently removed by dialysis.[48] While the dialysis is rather complex, this process has been successfully employed for several organic semiconductors.[10, 12, 13]
The simplest route is the nanoprecipitation method. This method does not require any surfactants, thus allowing for a pure dispersion of the organic material. In batch nanoprecipitation, for example, inside a beaker, the solution of the organic material is injected into a beaker with a miscible nonsolvent whilst stirring. The solubility of the organic semiconductor in this mixture is rapidly reduced, leading to the collapse of polymer chains or aggregation of molecules and the formation of particles.
So far, two pathways are possible for nanoparticle formation: One way is to perform separate nanoprecipitations for donors and acceptors. For the semiconducting donor polymer poly(3-hexylthiophene-2,5-diyl) (P3HT), the formation of stable nanoparticle dispersions in an eco-friendly nonsolvent such as water or ethanol is readily possible, while other polymers are unstable and flocculate.[49] Mixing both the donor and acceptor nanoparticle dispersions would produce a blend dispersion. The drawback of this approach is, that only a few materials form stable nanoparticles, most of them being donors. The other possibility is to blend the two organic materials to a solution and form blend-particles from one nanoprecipitation. Created from a blend solution of P3HT and the fullerene indene-C_{60} bisadduct (ICBA), these dispersions have

previously been used for the fabrication of organic solar cells with an efficiency close to the efficiency of organic solar cells from halogenated solvents.[8]
In theory, three different forms of nanoparticles are possible: janus particles, core-shell particles and blend particles, as illustrated in Figure 2.10.

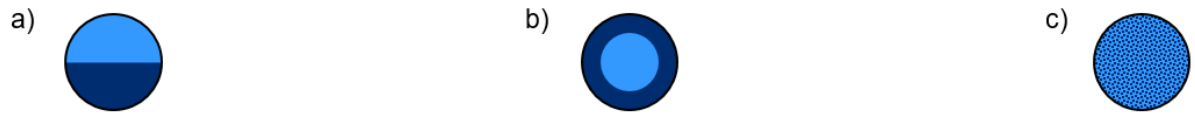

Figure 2.10: Architectures of nanoparticles. a) A janus particle has two different surfaces, while b) a core-shell particle is separated into a core and a shell with richer and depleted material concentration, which occurs mostly in miniemulsions. c) A blend particle consists of a rather uniform material mix, which occurs in nanoprecipitation.

Janus particles have two different surfaces of two different materials. The formation of these particles is rather complex and requires special nanoprecipitation techniques. Neither the nanoprecipitation nor the miniemulsion method form janus particles.[50, 51, 52] The core-shell particles comprise two domains: the core inside the particle and the shell around the core. They form from a blend solution through the effect of the different surface energies of the materials.[53] In drug delivery systems, the core-shell structure is used to protect the core through a robust shell.[51] Nanoparticles from miniemulsion can form a particular type of core-shell particles, with one material being richer in the core (fullerene), while the other is richer in the shell (P3HT).[53, 54] In blend particles, the materials are mixed uniformly. Gärtner et al. proved with small-angle neutron scattering and transient absorption spectroscopy that nanoparticles from nanoprecipitation in beakers are blend particles.[55]
Nanoprecipitation is enabled by either batch nanoprecipitation or continuous-flow nanoprecipitation. For batch nanoprecipitation, only a specific amount of material is usable, which is used all at once. One example of batch nanoprecipitation is the nanoprecipitation in a beaker, in which a specific amount of solution is injected rapidly into the nonsolvent in a beaker. In contrast, the continuous-flow nanoprecipitation uses a continuous feed of solution and nonsolvent, which enables a continuous process of nanoprecipitation instead of a batch nanoprecipitation.

Batch nanoprecipitation

The most facile nanoprecipitation process is the nanoprecipitation in a beaker, as schematically illustrated in Figure 2.11. An organic material that is soluble in a fluid agent (hereafter called solvent) dissolves and forms a solution. A nonsolvent that is miscible with the solvent but does not dissolve the organic material is filled into a beaker and placed on a hotplate, where a

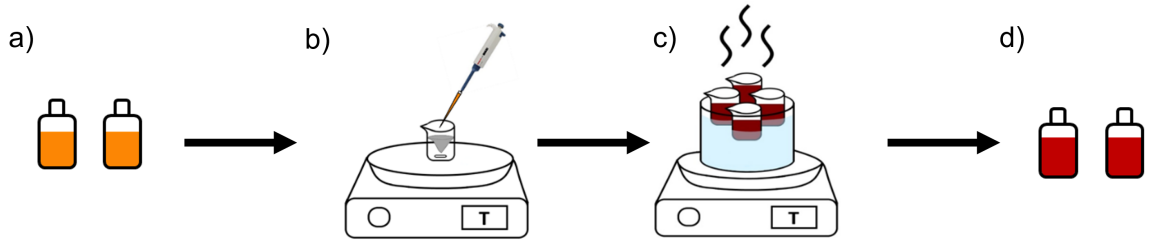

Figure 2.11: Schematic of the beaker nanoprecipitation. a) The organic material is dissolved in the solvent. b) In a beaker on a hotplate, the nonsolvent is heated and stirred by a magnetic stirrer. The solution is injected inside the stirred nonsolvent with a pipette. Because the solubility of the organic material is strongly reduced in the solvent/ nonsolvent mixture, the material precipitates and forms nanoparticles. c) To remove the solvent, the dispersion is heated on a hotplate inside a water bath above the boiling temperature of the solvent and below the boiling temperature of the nonsolvent. This step is referred to as reduction. d) In the end, a stable nanoparticle dispersion is achieved.

magnetic stirrer mixes the nonsolvent and creates a vortex. The solution is rapidly injected into the stirred nonsolvent, as shown in Figure 2.12.

Through the mixing of solvent and nonsolvent, the solubility of the organic material is rapidly reduced, and nanoparticles form. These particles first nucleate and then grow until they reach colloidal stability and form a stable dispersion.[15, 26] To remove the toxic solvent and increase the nanoparticle concentration, the dispersion is heated on a hotplate inside a water bath. Henceforth, this step is referred to as reduction. Ideally, the temperature is chosen above the boiling temperature of the solvent and below the boiling temperature of the nonsolvent. In the end, a stable nanoparticle dispersion with the concentration of the initial solution remains. Subsequently, the concentration can be further increased.

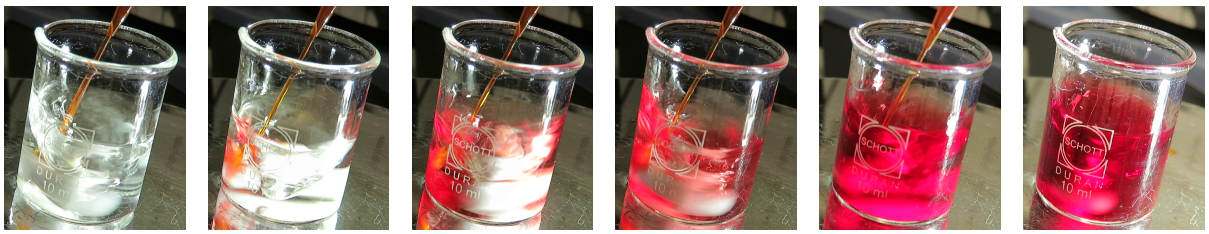

Figure 2.12: Real time pictures of the nanoprecipitation of P3HT. The solution is injected into the beaker with the stirred nonsolvent. The solubility is rapidly reduced, which leads to nanoparticle formation and the color-shift of P3HT from orange to red.

In this work, analytical grade chloroform and analytical grade ethanol (emsure), purchased from Merck, were used as solvent and nonsolvent, respectively, without further purification.

Although the batch nanoprecipitation process is fast and simple, it has many disadvantages, mostly because controlling the nanoprecipitation process is rather difficult. Both the mixing time and the position where the solution is injected into the nonsolvent inside the vortex can

vary. This leads to a high batch-to-batch variation of the particle size distribution. Preliminary tests showed that for higher concentrations, for example, 10 g/L, a nonoptimal nanoprecipitation can influence the average nanoparticle size by up to 50 nm. For particles with an average of 80 nm, this deviation is problematic and each batch can produce a dispersion of different qualitiy. This process is not readily transferable to larger beakers, because the mixing times in larger volumes deviate substantially from the small-scale process.

Continuous Flow Nanoprecipitation

In principle, the nanoprecipitation processes of continuous flow nanoprecipitation and batch nanoprecipitation do not differ. However, while a single nanoprecipitation inside the beaker is performed, a steady feed of solution and nonsolvent during the continuous flow nanoprecipitation leads to a continuous nanoprecipitation process. Therefore, the production of nanoparticles is directly dependent on the control of the nanoprecipitation process.
For the continuous flow nanoprecipitation, a microfluidic setup is perfectly suited. In the past, microfluidic systems were used for controlled continuous-flow syntheses in drug manufacturing, for live cell microscopic imaging in biomedical science, as well as for chemical analysis and lab-on-a-chip applications in molecular and biological analysis, just to name a few.[16, 37, 50, 56, 57] They offer rapid mixing of small amounts of liquids within channels with diameters of less than 500 µm and excellent scalability via parallelization. Through the mixing chip, the mixing of several fluids is highly controllable.[56, 57] In addition to the principal scalability of microfluidic systems, this nanoprecipitation process is well controllable and the reproducibility of the nanoparticle size is improved compared to the common batch nanoprecipitation approach. It is easy to achieve high throughput by simply using multiple mixing chips and syringe pumps. With the use of these pumps, continuous production of dispersion without interruption is feasible. The setup of the microfluidic system is further described in Chapter 5.1.

2.3.2 Nanoparticle formation

As phase separation does not occur spontaneously, the formation of a new phase requires an energy expenditure. Therefore, a homogeneous nucleation process occurs, as described in classical nucleation theory (CNT).[58, 59, 60, 61] For the nanoprecipitation, the nucleation process that determines the morphology of the new phase is an important step, because it allows an initial classification of the particle separation from solution. At the beginning of the separation, small droplets or particles, referred to as nuclei, form from the homogeneous mixture. The nuclei are prone to dissolution, which results from their high surface areas compared to their

volume, leading to a high number of molecules at the surface. The nuclei form and grow until they are stable.[60] Not all nanoparticles are stable in size; Figure 2.13 shows the four different growth processes: Ostwald ripening, aggregation, sedimentation, and coalescence.

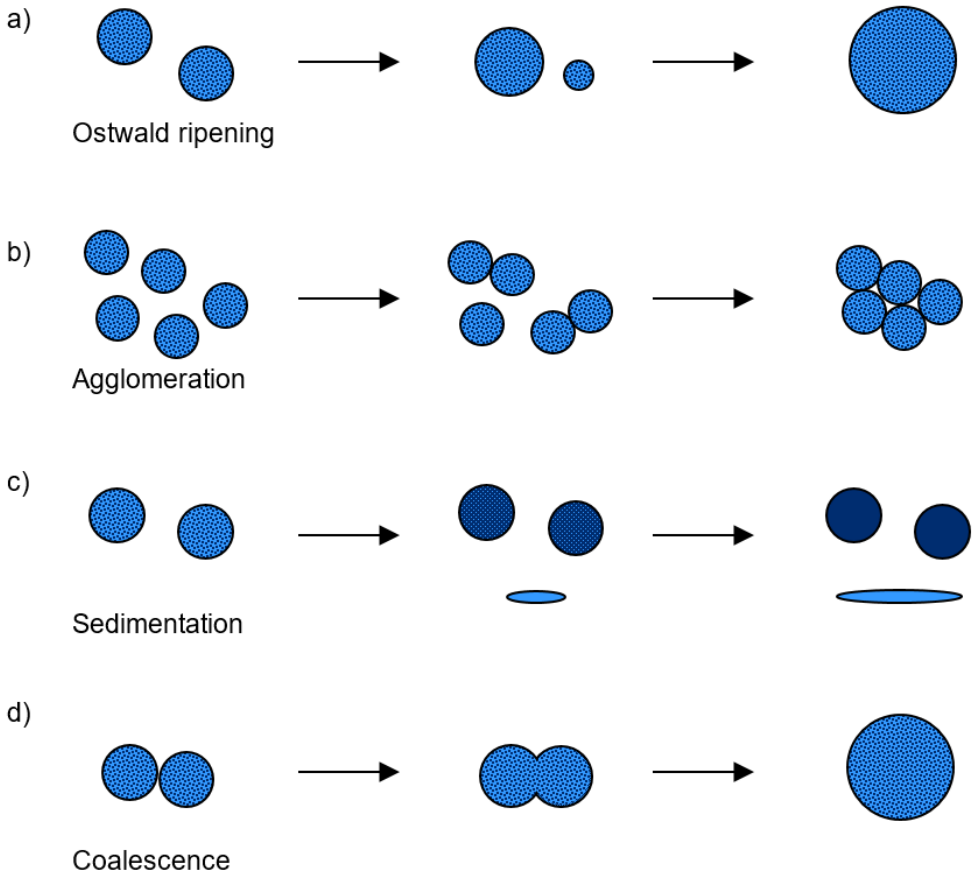

Figure 2.13: Four different growth procedures of nanoparticles. a) During Ostwald ripening, some particles inside a dispersion grow because of the high solubility and surface energy from smaller particles through the diffusion of material. b) During aggregation, particles stay together after they meet through Brownian motion and form a network of particles. c) During sedimentation, a separation between particle phase and liquid phase can appear through gravitational forces or a change in potential energy. d) During coalescence, two particles with the same composition meet and merge into one larger particle.

Particles inside the dispersion can grow through material diffusion, as shown in Figure 2.13 a. This process is referred to as Ostwald ripening. Through the high surface area of smaller particles, the atoms or molecules of smaller particles diffuse into larger particles until they reach equilibrium.[62] Particles that stick together after they meet through Brownian motion are referred to as agglomerates (Figure 2.13 b). These particles form a network of single particles. One way to counteract the agglomeration is by colloidal repulsion. Separation between the particle phase and the liquid phase that occurs through gravitational forces or a change in potential energy is referred to as sedimentation (Figure 2.13 c). This leads to settling or creaming of a

material. Coalescence, as shown in Figure 2.13 d, is the process by which two particles with the same composition meet and merge into one larger particle. This results in a separation into two phases, the organic material phase and the nonsolvent phase.[63] All these instabilities can occur during a nanoprecipitation process. It is difficult to distinguish these effects in a dispersion because of mutual influence and similar macroscopic results.

For polymer nanoparticles, growth and aggregation are difficult to distinguish due to the high intermolecular forces between macromolecules.[62, 64] Polymers also tend to build amorphous structures, leading to similar material properties of the primary and agglomerated particles. In addition, aggregation of organic nanoparticles is irreversible.[65] Without stabilization, the dispersion would always separate. Therefore, while the nucleation of primary particles might mark a lower limit for the particle size, the colloidal stability determines the particle size of a stable dispersion. For the nanoparticle synthesis process, this is the most important part.[64, 66] By improving the stabilization of the dispersion, for example, by adding an additive, the agglomeration stops earlier and the average nanoparticle size is reduced.

A nanoparticle dispersion is only stable as long as particle-particle forces (particle interaction) prevent agglomeration.[67] Therefore, three stability mechanisms can occur. These mechanisms are steric stabilization, depletion stabilization and electrostatic stabilization. Steric stabilization occurs if the macromolecules are attached to the nanoparticles surface through adsorption or covalent bonding. The macromolecules separate the nanoparticles from each other. If the interaction between the macromolecules and the dispersion medium is sufficient, the nanoparticle shells cannot collide or merge.[67]

The depletion stabilization occurs in a system with fully dissolved, but non-adsorbed macromolecules. By adding more of the non-adsorbed macromolecule, the system collapses, and the dispersion starts to flocculate until a limiting concentration is reached and the system restabilizes. Free macromolecules can also impart stability in otherwise unstable dispersions, for example, by forming a depletion layer near the surface of the nanoparticle.[68, 69]

The electrostatic stabilization needs charges at the surface of the particle. Counter ions compensate the surface charges and form a diffuse ion layer around the particle.[66] The repulsion between the ion layers stabilizes the dispersion. Through van-der-Waals forces, which act between the particles, dispersions can still become unstable, which is described by the DLVO-theory (named after Boris Derjaguin, Lew Dawidowitsch Landau, Evert Verwey and Theodoor Overbeek).[67] But through the electrostatic stabilization, which counteracts the van-der-Waals forces, particles need to overcome an energy barrier for aggregation. A sufficient high energy barrier leads to a stable dispersion. A low energy barrier increases the probability of an aggregation and the average particle size increases over time.[66, 70]

3 Materials

In this chapter, the selection of organic semiconductors is motivated. In organic solar cells, a blend of a donor and an acceptor is needed to split the excitons. First, the donor polymer poly(3-hexylthiophene-2,5-diyl) (P3HT), the only known material for organic solar cells that forms nanoparticles on its own, is described. In the second part, organic electron acceptors are discussed. When acceptor materials such as well-known fullerenes are added, the blend nanoparticle dispersions become sufficiently stable for solar cell fabrication. By replacing the fullerenes with small-molecule acceptors (NFA), solar cells with high efficiencies are possible.

3.1 Donor materials

To date, several known polymers can be used as donor. Some of the first materials that were used for organic solar cells were polymers based on polyphenylene vinylene (PPV). However, the performance of PPV-based polymers is limited by their low hole mobility and the relatively large energy gap of 2.5 eV.[71] Due to their good charge carrier transport properties, thiophene-based polymers have always been promising candidates for donors.[72, 73] By adding flexible alkyl side chains to the thiophene ring, the thiophene becomes soluble.[74, 75] By increasing the chain length, the solubility increases.[75] In combination with a fullerene acceptor and by using thermal annealing, solar cells with an efficiency of 3.5 % were achieved.[76]

3.1.1 P3HT

The best-known polythiophene polymer is poly(3-hexylthiophene-2,5-diyl) (P3HT). The chemical structure is illustrated in Figure 3.1 a, with the different positions on the thiophene ring marked. P3HT consists of a series of thiophene rings that are linked through the 2- and 5-positions. The hexyl group can be added at positions 3 or 4.
Depending on the hexyl group position of the thiophene repeat units, different arrangements are possible, as shown in Figure 3.1 b. Two neighboring thiophene rings with the same position of the hexyl group have a head-to-tail (H-T) configuration. If the repeating units are arranged toward each other, the configuration is called head-to-head (H-H), whereas a configuration in which the two hexyl groups are opposite to each other is called tail-to-tail (T-T). These polymer configurations show the regioregularity, which is the geometric symmetry of the monomers

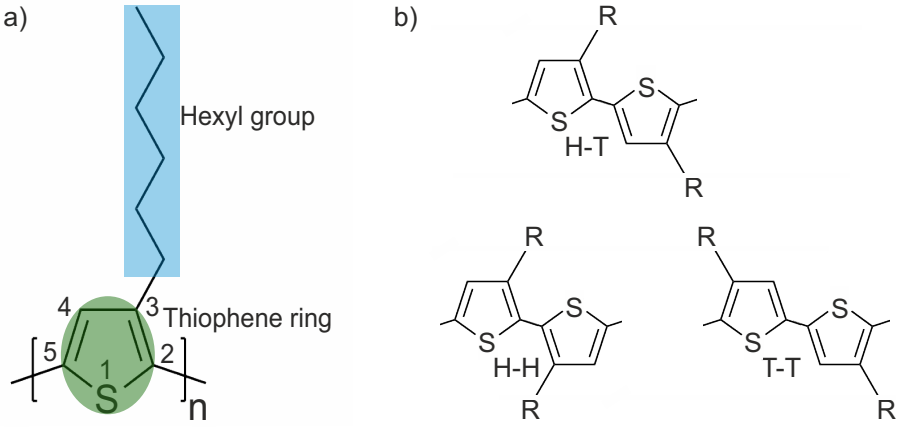

Figure 3.1: Structure of P3HT. a) P3HT consists of several thiophene rings (in green) that are linked at position 2 and 5. At position 3, a hexyl group (in blue) is attached. b) Depending on the position of the hexyl groups attached to the thiophene ring, different polymer configurations are possible.

along the polymer chains.[77] If primarily the H-T configuration occurs, P3HT is referred to as regioregular (RR). By mixing all polymer configurations randomly, P3HT exhibits a regiorandom (rra) configuration, with the lowest possible regioregularity of 50 %. Figure 3.2 illustrates the structural difference between regioregular and regiorandom P3HT. The regioregularity of the polymers affects the mobility of the charge carriers, the morphology of the mixture with the acceptor and the crystallinity, leading to amorphous structures for rra-P3HT.[78, 79] The regioregularity can be determined by ^{1}H NMR.[80]

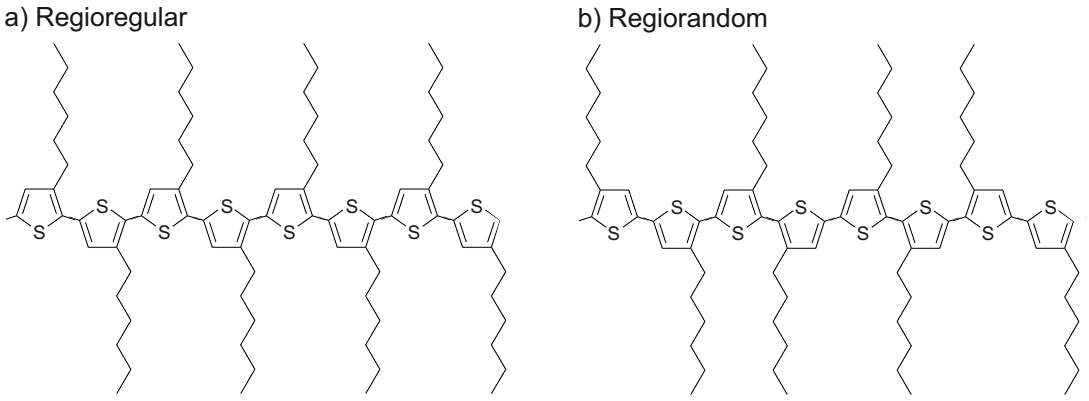

Figure 3.2: Structure of P3HT. a) RR-P3HT exhibits a regular order of the monomers, with all hexyl groups attached to the 3-position of the thiophene and only a H-T configuration. b) For rra-P3HT, monomers and the position of the hexyl groups change randomly, leading to a reduced symmetry.

The regularity of P3HT also influences its absorbance. The solution of both RR-P3HT and rra-P3HT have similar appearance, as shown in Figure 3.3 a-b. After nanoprecipitation, while

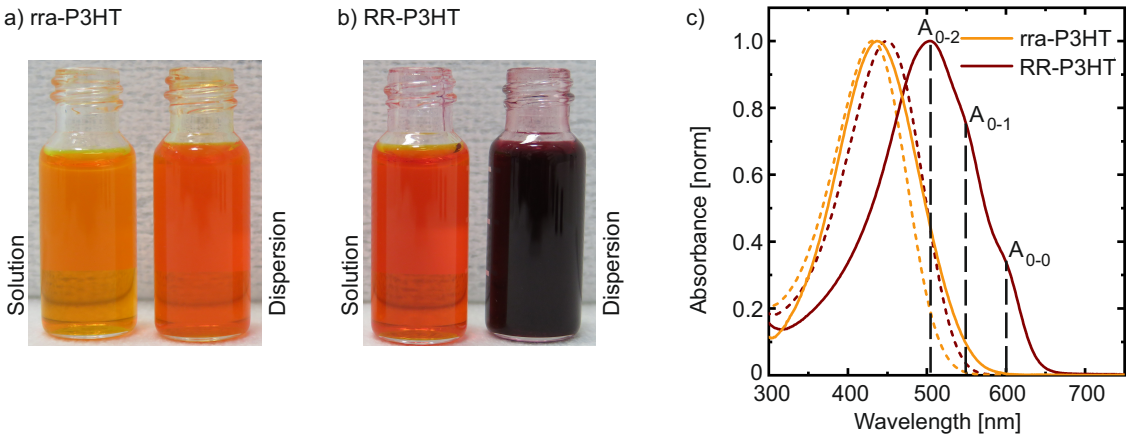

Figure 3.3: Spectral change of rra-P3HT and RR-P3HT upon transition from chloroform solution to ethanol dispersion. a) For rra-P3HT, a slightly visible color change between the solution and the dispersion occurs. b) For RR-P3HT, the typical red-shift between solution and dispersion is clearly visible. c) The absorbance spectra of rra-and RR-P3HT, both in solution and in dispersion show these changes. While the change from solution to solid nanoparticles of rra-P3HT in orange only leads to a maximum shift of 5 nm, for RR-P3HT in dark red, it shifts by 50 nm.

the absorbance of rra-P3HT changes only slightly, RR-P3HT shows the typical red shift (bathochromic shift) of the absorbance peak and the formation of two new absorbance shoulders as shown in Figure 3.3 c.

In the literature, this spectral change is well known for P3HT.[81, 82] Since chloroform is a good solvent for P3HT, the interaction of the solvent molecules with P3HT is strong. Thus, the polymer chains cannot align, and the angle between the repeating units changes constantly. Yet, temporarily, individual repeating units can align, and delocalization can occur along the chain. This leads to an absorbance that consists of the superposition of regions with random conjugation length.[83] During nanoprecipitation, chloroform is displaced by ethanol, which is a poor solvent for P3HT. This results in a P3HT alignment and a π-π- stacking of the polymer segments.[84] The excitonic coupling of the aggregated chains both intrachain (along the chain) and interchain (along the π-π- stacking) leads to the red shift of the absorbance and the emergence of three absorbance peaks $A_{0\text{-}0}$, $A_{0\text{-}1}$ and $A_{0\text{-}2}$. Those three peaks represent the excitation from the electronic ground state of P3HT into different vibronic states. The ratio of $A_{0\text{-}0}$ to $A_{0\text{-}1}$ provides information about the crystallinity of the aggregated polymer and thus about the molecular order.[85] The semi-crystalline domains of P3HT have a high intrachain order, while interchain coupling dominates in the amorphous domains.[85] In P3HT nanofibers with highly ordered semi-crystalline domains, the ratio of $A_{0\text{-}0}$ to $A_{0\text{-}1}$ is equal to one.[84] In nanoparticles, $A_{0\text{-}0}$ is much weaker than $A_{0\text{-}1}$, indicating a moderate semi-crystalline order.[86] Through the

rapid solvent exchange during nanoprecipitation, the P3HT chains collapse very quickly and only form ordered domains in small areas.

For P3HT, also the chain lengths can differ. Instead of the chain length, commonly, the molecular weight (MW) of the polymer chain is specified, which is the relative molecular mass of a monomer and the amount of monomers in one chain. A P3HT monomer consists of 10 carbon atoms, 14 hydrogen atoms and 1 sulfur atom, which leads to a molar mass of one monomer of 166.28 g/mol. Commercial P3HT is typically classified at average MW of 20k-45k, 50k-70k, and 85k-100k, with k = 1000. By synthesizing P3HT, a special MW can be achieved. The P3HT used in this work has a MW of 50k-70k g/mol, which leads to 300 to 421 monomers per P3HT chain.

The MW influences the optical properties. For layers of P3HT with a low MW, the absorbance maximum shifts towards lower wavelengths, which indicates a reduced ordering of P3HT. The shoulder at 605 nm, which correlates with the interchain stacking that is related to the packing of P3HT chains, is weaker than for P3HT with higher MW. Also, the IP of P3HT changes by varying the MW. Liu et al. showed that, by increasing the MW of P3HT, the IP measured by photoelectron spectroscopy in air (PESA) decreases. By blending P3HT with a fullerene (here: $PC_{61}BM$), a light-harvesting layer can be fabricated. Through thermal annealing, a change in morphology could be observed through the aggregation of fullerene agglomerates, leading to an enhanced separation of P3HT and fullerenes for increasing MW. For higher MW, the size of the agglomerates decreases, which could be due to the decreased chain mobility of P3HT that slows down the assembly of fullerenes. In organic solar cells, increasing MW led to a decrease in J_{SC} in the low MW regime, which could result from weaker absorption and non-optimal morphology.[80] For higher MW, this results in a reduced chain mobility and an increase in the entanglements per chain, eventually leading to a reduced FF.

Polydispersity refers to the difference in molecular weight. If all polymer chains have the same length and thus weight, the polymers are called monodisperse. Commonly, the synthesized polymers for organic solar cells are not monodisperse but polydisperse. The polydispersity index PDI = $\frac{M_w}{M_n}$ describes the ratio of the weight average molar mass M_w and the number average molar mass M_n.[87] The two chosen P3HTs from Rieke Metals, RR-P3HT and rra-P3HT, have a PDI of 2 and 2.5, respectively.

Synthesis

P3HT can be obtained by several synthesis routes. The best known routes are the synthesis by McCullough, Rieke, and Grignard, which is also known as the GRIM method. The schematics of the three synthesis routes are shown in Figure 3.4.

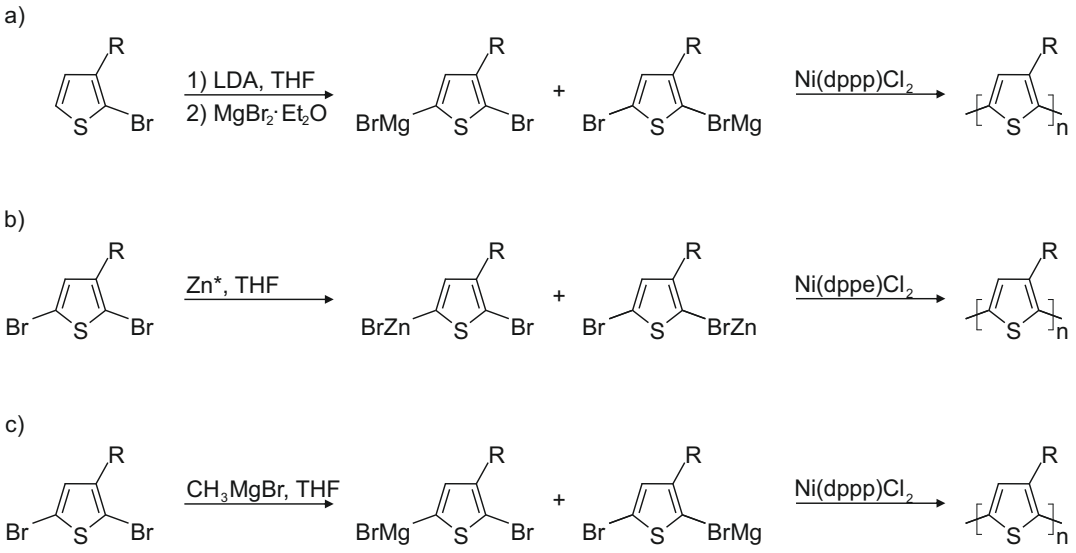

Figure 3.4: Syntheses of regioregular P3HT (R = C_6H_{13}). a) The McCullough method was one of the first syntheses of P3HT.[88]. b) The synthesis by Rieke with Rieke zinc yields the P3HT that was used in the following work.[89] c) The GRIM method is the most common synthesis route.[90]

McCullough and Lowe were among the first groups of scientists to find a synthesis route for polythiophenes that enabled a regiospecification of the polymer. Instead of a random specificity, almost exclusively head-to-tail coupling was possible. In the "McCullough synthesis", which is shown in Figure 3.4 a), 2-bromo 3-alkylthiophenes reacts to two regioisomers under specific conditions by first adding lithium diisopropylamide (LDA) and then magnesium bromide diethyl etherate ($MgBr_2 \cdot Et_2O$).[88, 91] While in theory both regioisomers can occur, in reality, mostly one of them occurs, while only 1 %-2 % of the monomers have the other regioisomerisation. Using a nickel-catalyzed cross-coupling reaction, by polymerization, poly-3-alkylthiophenes with a regioregularity of 91 % were achieved.[32]

Rieke et al. started with 2,5-dibromothiophene and used reactive Rieke zinc (Zn*), a special, highly reactive metal powder, suspended in tetrahydrofuran (THF).[89, 92] During the reaction, which is illustrated in Figure 3.4 b, again, two regioisomers can occur, while one has only a probability of 3 % of occurring.[93] By cross-coupling with a nickel-based catalyst ($Ni_2(dppe)Cl_2$), poly(3-alkylthiophene) with an increased regioregularity of 99 % can be achieved.[94]

Given that both McCullough and Rieke used highly reactive metals and required cryogenic temperatures, the GRIM method was developed. Starting from a dibromo 3-alkylthiophene monomer, the addition of an alkyl / vinyl Grignard reagent results in a magnesium-bromine exchange reaction.[90] Two regioisomers form, with a distribution of 85 %:15 %. By using a

nickel-based catalyst ($Ni_2(dppp)Cl_2$), the polymerization achieves poly(3-alkylthiophenes) with a regioregularity of 99 %.[94]
After the syntheses have been performed, all polymers require purification. Depending on the different purification steps, different amounts of catalysts can persist in the polymer powder. For the Rieke P3HT used in this work, the polymers contain less than 0.01 % of metal remnants.

Nanoparticles

P3HT was one of the first organic solar cell materials that showed stable nanoparticle formation. In 2010, Millstone et al. published their results on stable surfactant-free P3HT nanoparticles. By adding the organic solution dropwise into stirred ethanol, P3HT nanoparticle dispersions with an average size of 30 nm were achieved.[49] While the initial concentration of P3HT was rather low with a maximum concentration of 0.5 g/L and a solution-to-nonsolvent ratio of 1:10, the work of Millstone et al. demonstrated the proof-of-concept for the use of P3HT nanoparticles in field effect transistors.

3.2 Acceptor materials

In solar cells, in addition to a donor, an electron acceptor is needed. Two categories of electron-accepting materials exist. The first category are the well-known fullerenes, which have a carbon core, mostly C_{60} or C_{70}, and functional side groups. The second category are the non-fullerene acceptors (NFA). They are more complex and led to higher efficiencies in recent years.

3.2.1 Fullerenes

Carbon molecules that form conjugated hollow spheres of fused rings with five or six atoms are called fullerenes. The number of carbon atoms in a fullerene determines the structure. In theory, the smallest possible fullerene is C_{20}, consisting of 12 five rings, with 20 carbon atoms. In reality, because of the high curvature of C_{20} and the strain coming from two five rings next to each other, this structure is energetically unfavorable.[95] Therefore, two five-rings cannot be adjusted to each other, which is also known as the isolated pentagon rule (IPR). Instead, the smallest fullerene that forms is C_{60}, as illustrated in Figure 3.5 a, with 12 five rings (pentagon) and 20 six rings (hexagon).
Each carbon atom is bonded to three other carbon atoms, by two single bonds with a bond length of 1.46 Å and a double bond with a bond length of 1.40 Å, as determined by NMR.[95] This structure results in a highly symmetrical molecule that is also known as Buckminster fullerene. This alternating bond structure is called the Kekulé structure and stabilizes the C_{60}-sphere.

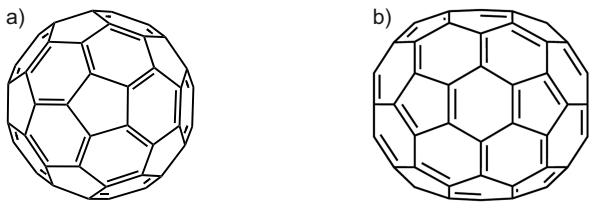

Figure 3.5: Structure of a) the "soccer-ball-shaped" C_{60}-fullerene and b) the "ellipsoid-shaped" C_{70}-fullerene. These two hollow carbon spheres are the basis for all fullerenes. By adding functional side chains, the optical and electrical properties can be changed and the solubility increases.

The next larger and stable fullerene C_{70} is illustrated in Figure 3.5 b, with 12 pentagons and 25 hexagons. While C_{60} has the form of a "soccer ball", C_{70} has an ellipsoidal form with eight different bonding lengths. The different core structure reduces the symmetry, which directly influences the absorbance in the visible spectral range.[95, 96, 97, 98]
The synthesis of fullerenes can be performed in different ways via the generation of a carbon-rich vapor or plasma. The common method is the arc technique, in which an electric discharge between two graphite electrodes emits a carbon soot that comprises fullerenes, from which the fullerenes are extracted by purification. In this synthesis, mainly C_{60} and C_{70} are produced, while fullerenes with higher molecular weight through more carbon atoms occur rarely, making them more expensive.[95]
Different isomers of fullerenes with the same number of carbon atoms, but with different geometrical structures, exist. Depending on the distribution of the pentagons to the hexagons, they can be characterized. For C_{60}, this results in 1812 isomers, while C_{70} has 8149 isomers.[99, 100] Due to IPR, the probability of all isomers to occur is low.

Given that both C_{60} and C_{70} have a poor solubility in most organic solvents, functional side groups are often added.[101, 102] Through a variation of the side chains, chemical characteristics such as solubility, miscibility, and morphology of the fullerenes can be changed.[103] The functional groups can also influence the electrical properties such as charge carrier mobility, HOMO and LUMO. Increasing the LUMO of the fullerenes allows a higher V_{OC} and commonly improves the solar cell performance.[104] In 1995, the first paper of an organic solar cell with a fullerene as the electron-accepting n-type semiconductor was published.[105] Since then, several fullerene derivatives, differing in the selection of the side chains, were investigated as electron acceptors in organic solar cells. The chemical structures of a selection of commonly used fullerenes are shown in Figure 3.6.

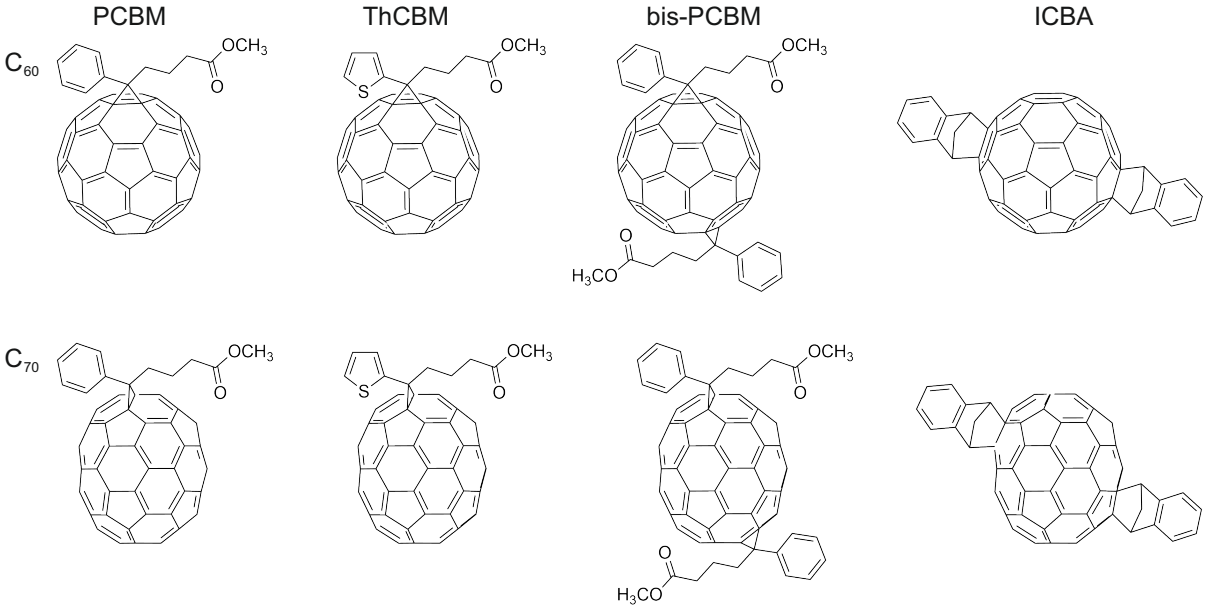

Figure 3.6: Structure of fullerenes commonly used in organic solar cells. PCBM has a phenyl group with a methyl butanoate attached to the core. Instead of the phenyl group, ThCBM has a thienyl group. The bisadducts bis-PCBM and ICBA have two functional groups attached at two different positions of the fullerene. By attaching two phenyl groups with a methyl butanoate, bis-PCBM occurs, by attaching two indenes, ICBA occurs.

PCBM

The methanofullerene derivate $PC_{61}BM$ is the best-known fullerene derivative. It was the first fullerene acceptor to be used in solution processed organic solar cells and it is still the most used fullerene to date.[105, 106] By adding a diazoalkane compound to C_{60}, a phenyl ring and a methyl butanoate attach to the C_{60}-core.[105, 106] While the phenyl group was originally used only for synthetic convenience, the methyl butanoate group allowed better solubility in organic solvents.[105] Further experiments showed that modifications of the phenyl group again led to a poor solubility in organic solvents.[107] Many electronic and optical properties of $PC_{61}BM$ are comparable to C_{60}.

ThCBM

Another idea was the use of similar chemical groups in the donor and acceptor, which should promote miscibility and lead to smaller domain sizes. For better blending with P3HT, the phenyl group was changed to a thienyl group. Compared to PCBM, this did not change the electronic characteristics, such as the electron mobility of the fullerene.[103, 108] Instead, it reduces the solubility in organic solvents such as chlorobenzene.[103] Although the miscibility of ThCBM with P3HT is improved, the solar cell performance did not improve.[109]

bis-PCBM

Instead of changing the side group to achieve better miscibility, bis-PCBM carries a second phenyl ring with a methyl butanoate, leading to a bisadduct of PCBM and changing the energy levels. As a consequence, the LUMO increases by 0.1 eV, leading to a higher V_{OC}.[110, 111] The change in structure leads to an increase of the number of isomers, which could influence the electron transport.[106] Simulations by Lenes et al. showed that by enhanced disorder, the mobility of the bisadduct is smaller than PCBM.[112] This leads to a decreased photocurrent and a reduced fill factor of the solar cells.[111] Therefore, a lot of optimization work was necessary to achieve efficient solar cells using bis-PCBM.

ICBA

Another way to further increase the LUMO is the implementation of ICBA, an indene-C_{60} bisadduct.[113] This synthesis is rather facile compared to the synthesis of PCBM. Through the functional groups, ICBA has both a higher absorption in the visible range than PCBM and a better solubility in common organic solvents.[114, 115] With ICBA, the LUMO is increased by 0.07 eV compared to bis-PCBM, resulting in an increased V_{OC} and therefore an increased PCE.[114, 116] One reason for this could be the weaker tendency of segregation of ICBA in combination with P3HT, compared to PCBM, which can prevent material separation during annealing.[115] In organic nanoparticles, this effect could hinder flocculation during the reduction step.

C_{70}-fullerenes

The most frequently used alternative to $PC_{61}BM$ is $PC_{71}BM$. Because of the stronger absorbance of the C_{70}- fullerenes in the visible range, the photocurrent increases due to enhanced light harvesting of the fullerenes, leading to an improved solar cell performance.[108, 110, 117, 118] Typically, the C_{70} derivates show a higher solubility. While the C_{60} derivatives typically do not have isomers, the reactions of C_{70} lead to a mixture of isomers.[106, 117] In the case of $PC_{71}BM$, three isomers form. Fortunately, a separation of the isomers is not necessary and the mix still leads to good results.
Changes in previously described C_{60} derivatives also occur for C_{70}-fullerenes, which show similar behavior.[118, 119, 120, 121, 122] Changing the phenyl group to a thienyl group did not make a significant difference between the solar cell performance of $PC_{71}BM$ and $ThC_{71}BM$. For bisadducts, the change from C_{60} to C_{70} did not impact the solar cell performance. Although bis-$PC_{72}BM$ exhibits a stronger absorbance than $PC_{62}BM$, the mixture of isomers again results in a decrease of the electron mobility and hinders the improvement of the solar cell performance.

3.2.2 Nonfullerene acceptors

All organic electron accepting materials that do not have a fullerene core, are summarized as non-fullerene acceptors (NFA). These materials are typically small molecules or polymers. NFAs have the advantage of wide tunability of their optical and electronic properties. Through their chemical structure, they can absorb visible light and therefore complement the absorbance spectra of the donor. Their energy levels, energy gap, planarity, and crystallinity can be tuned by molecular design, leading to high solar cell performance.[123] One way to enable this is by using the structure of A2-A1-D-A1-A2. For example, an s-indaceno[1,2-b:5,6-b']dithiophene (IDT) is used as donor D, a 1,2,3-benzothiadiazole (BT) as acceptor A1 and a rhodanine as acceptor A2 to form IDTBR.

IDFBR

The small molecule acceptor IDFBR (chemical name: (5Z,5'Z)-5,5'-((7,7'-(6,6,12,12-tetraoctyl-6,12-dihydroindeno[1,2-b]fluorene-2,8-diyl)bis(benzo[c][1,2,5]thiadiazole-7,4-diyl))bis(methanylylidene))bis(3-ethyl-2-thioxothiazolidin-4-one)) was developed by McCullough et al. as an acceptor with a high LUMO of 3.7 eV.[124, 125] The high LUMO helps to improve the V_{OC}. With a HOMO of 5.75 eV and an optical energy gap of 2.05 eV, it absorbs between 400 nm and 600 nm and therefore contributes to the current.[126] The chemical structure of IDFBR is shown in Figure 3.7 a, with the molecular formula 76C, 92H, 6N, 2O, 6S.

IDTBR

Another small molecule with a structure similar to IDFBR is IDTBR (chemical name: (5Z,5'Z)-5,5'-((7,7'-(4,4,9,9-tetraoctyl-4,9-dihydro-s-indaceno[1,2-b:5,6-b']dithiophene-2,7- diyl) bis (benzo[c][1,2,5]thiadiazole-7,4-diyl))bis(methanylylidene))bis(3-ethyl-2-thioxothiazolidin-4-one)). One of the benzene rings at the fluorene molecule is replaced by a thiophene ring. Two IDTBRs, which only differ in their side chains, exist, as shown in Figure 3.7 b-c. While O-IDTBR contains linear n-octyl side chains, EH-IDTBR contains branched ethylhexyl side chains. This leads to a minimal red shift in the absorbance of the solid of O-IDTBR, compared to EH-IDTBR. Both O-IDTBR and EH-IDTBR have a low energy gap, with a HOMO of 5.51 eV or 5.58 eV and a LUMO of 3.88 eV or 3.9 eV, respectively.[127] This results in an absorbance between 500 nm and 800 nm. The chemical structure of IDTBR is shown in Figure 3.7 d, with the molecular formula 72C, 88H, 6N, 2O, 8S.

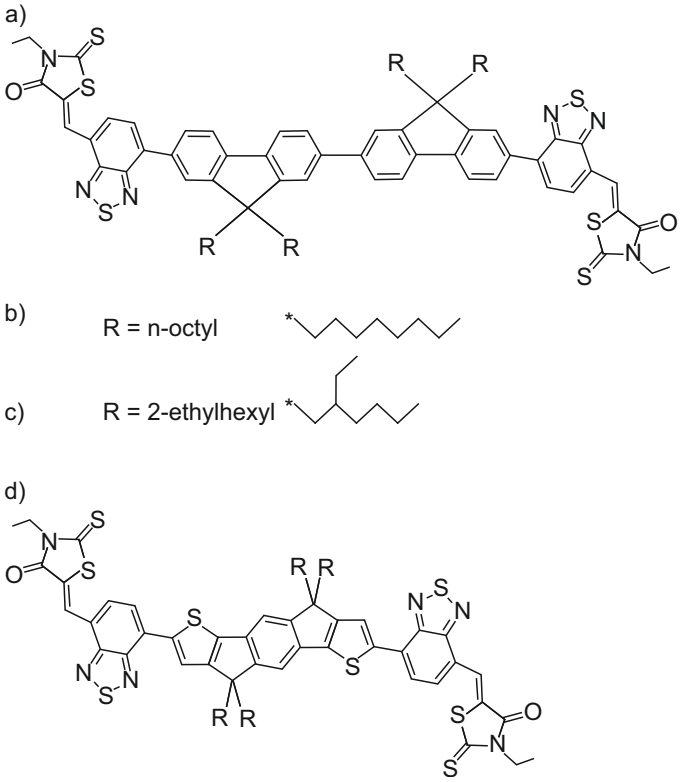

Figure 3.7: a) Chemical structure of IDFBR, b) with an n-octly group attached, O-IDFBR is formed. b) Adding the n-octly group forms the linear O-IDTBR, c) adding the ethylhexyl group forms the branched EH-IDTBR d) from the chemical structure of IDTBR.

CO_i8DFIC

The small molecule CO_i8DFIC (chemical name: 2,2-[[4,4,11,11-tetrakis(4-hexylphenyl)-4,11-dihydrothieno[2, 3:4,5]thieno[2,3-d]thieno[2,3:4,5]thienov[2,3:4,5]pyrano[2,3:4,5]thieno[2,3:-4,5]thieno[3,2-b]pyran-2,9-diyl]bis[methylidyne(5,6-difluoro)]]), also known as NFA 146, is illustrated in Figure 3.8 a, with the molecular formula 94C, 76H, 4F, 4N, 4O, 6S.[128, 129] It can be used as strong near infrared absorber, with a narrow optical energy gap of 1.62 eV, a HOMO of 5.5 eV and a LUMO of 3.88 eV.[130] CO_i8DFIC is mostly used in ternary systems and tandem organic solar cells due to the complementary absorbance.[130, 131]

ITIC

ITIC enables very high solar cell efficiencies (chemical name: 3,9-bis(2-methylene-((3-(1,1-dicyanomethylene)-6,7-dichloro)-indanone))-5,5,11,11-tetrakis(4-hexylphenyl)-dithieno[2,3-d:2',3'-d']-s-indaceno [1,2-b:5,6-b']dithiophene), with a HOMO of 5.48 eV and a LUMO of 3.83 eV.[132] The chemical structure is illustrated in Figure 3.8 b, with the molecular formula

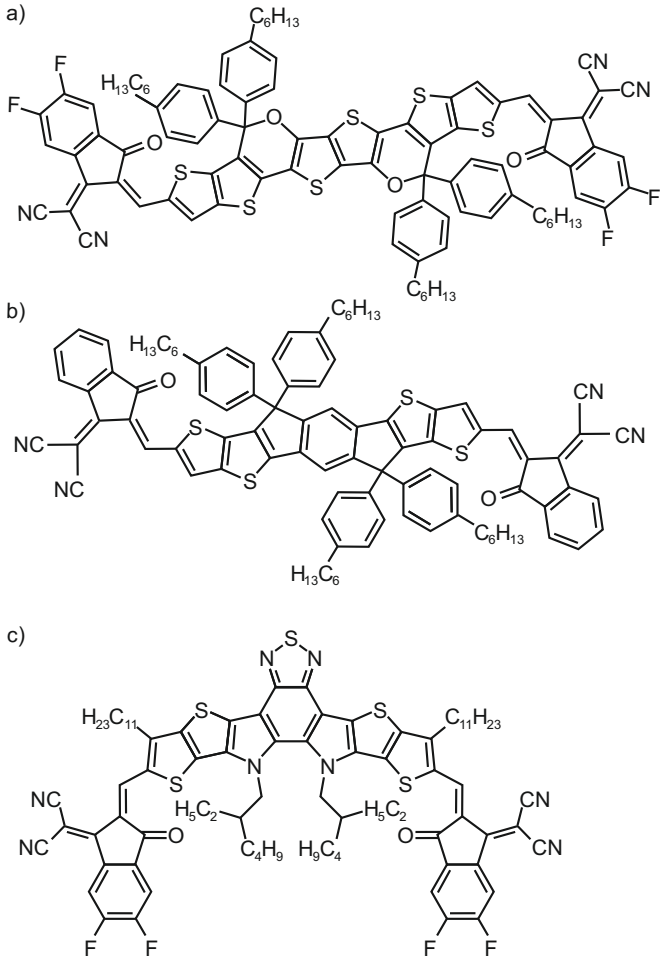

Figure 3.8: Chemical structure of the NFAs a) CO_i8DFIC, b) ITIC and c) Y6. Because of the complementary absorbance of CO_i8DFIC, it is mostly used in ternary systems and tandem organic solar cells. ITIC and Y6 are efficient organic electron acceptors.

94C, 78H, 4Cl, 4N, 4O, 6S. In 2016, Zhao et al. achieved solar cells with an efficiency of over 11 % by using ITIC as an electron acceptor.[133]

Y6

Another NFA that allows for very high organic solar cell efficiencies is Y6 (chemical name: 2,2'-((2Z,2'Z)-((12,13-bis(2-ethylhexyl)-3,9-diundecyl-12,13-dihydro-[1,2,5]thiadiazolo [3,4-e] thieno[2",3":4',5']thieno[2', 3':4,5]pyrrolo[3,2-g]thieno[2',3':4,5]thieno[3,2-b]indole-2,10-diyl)bis(methanylylidene))bis(5,6-difluoro-3-oxo-2,3-dihydro-1H-indene-2,1-diylidene))dimalononitrile), also known as BTP-4F. Y6 has a HOMO of 5.63 eV and a LUMO of 4.04 eV. Its structure is shown in Figure 3.8 c, with the molecular formula 90C, 102H, 4Cl, 8N, 2O, 5S.[128, 129]

4 Experimentals

The following chapter describes the different measurement techniques that are used for the characterization of nanoparticle dispersions (4.1), nanoparticular layers (4.2), or solar cells (4.3).

4.1 Analysis of dispersions

The characterization of size and shape of nanoparticle and the stability of the dispersion thereof is crucial. This often encompasses multiple measurements at different times after nanoprecipitation.

4.1.1 Dynamic light scattering

One of the most important parameters is the size of the nanoparticles, because it can be an indicator of the stability of the dispersion. Due to the small particle size, identifying a successfully nanoprecipitated dispersion with the naked eye is rather difficult, while the recognition of an unsuccessful nanoprecipitation is straightforward. The flocculation of the nanoparticles leads to sedimentation of the material on the bottom of the container, which is shown in 4.1 a. The aggregation of the nanoparticles during the process leads to a visible movement of the larger particles through Brownian motion, which is shown in Figure 4.1 b. For stable dispersions with particles smaller than 10 µm, as shown in Figure 4.1 c, it is not possible to see particles with the naked eye. Therefore, the dynamic light scattering machine (DLS) Zetasizer Nano ZS by Malvern Panalytical is used. In order to measure the particle size, the dispersions are diluted

Figure 4.1: Different dispersions diluted in a cuvette. a) In a highly unstable dispersion with large particles, the particles flocculate and sediment at the bottom of the cuvette. b) In a dispersion that aggregates, the large particles move visibly inside the nonsolvent by Brownian motion. c) In a stable dispersion with nanoparticles, no particle movement is visible.

inside a quartz cuvette and inserted into the cuvette shaft of the DLS. The DLS setup is illustrated in Figure 4.2. A laser beam at a wavelength of 633 nm passes through the cuvette and is scattered by the nanoparticles inside the dispersion that move by Brownian motion. A detector measures the time-resolved intensity of the scattered light under a specific angle (backscatter mode: 173 °, frontscatter mode: 13 °), which results from the interference of the scattered photons. The particles move continuously, which leads to a fluctuation in the intensity of the scattered light. A smaller particle size increases the motion speed and, therefore, the intensity fluctuation. The fluctuations are detected by a digital autocorrelation system in a time range from nanoseconds to microseconds. Therefore, fast fluctuations lead to a short decay time. This links the fluctuations to the movement of the particles and can be fitted by exponential functions with specific parameters, which correlate to a particle size distribution.[134]

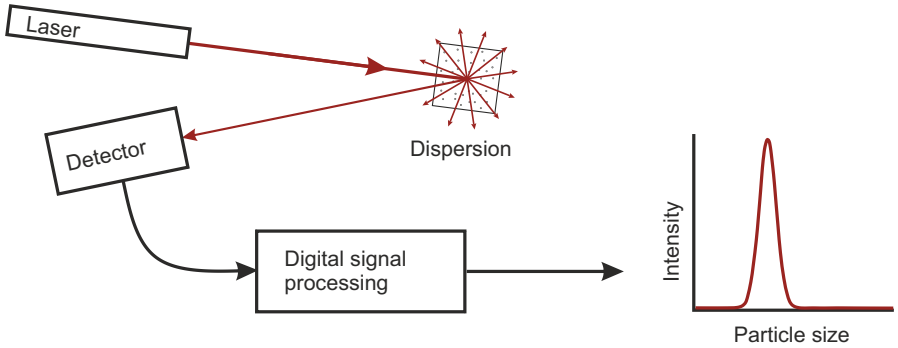

Figure 4.2: Schematic of the dynamic light scattering setup. A laser beam of coherent light (633 nm) irradiates the cuvette. The nanoparticles inside the dispersion scatter the light in all directions. A detector records the time-resolved intensity of the scattered light under a specific angle and through digital signal processing, the particle size distribution is calculated.

In Figure 4.3, the measurement signal (a, d, g), the correlation (b, e, h), and the size distribution (c, f, i) of the DLS measurements are shown for different particle sizes. The system determines the diffusion coefficient of the particles, which is inverse to the particle size. In dispersion, all particles move through Brownian motion by collision with solvent molecules. Smaller particles diffuse faster than larger particles; therefore, a fast fluctuation of the backscattered light correlates with smaller particles. An algorithm fits the autocorrelation of the backscattered light with either the distribution or the average particle size.[135] The system models the diffusion of monodisperse spherical particles inside a medium with known refractive index and viscosity. In reality, the particles are not monodisperse, but polydisperse. This generates an error in the particle size, which increases with increasing polydispersity of the dispersions. Because the size distribution is weighted by the intensity of scattered light and because the scatter intensity depends on the nanoparticle size, the measurement results of dispersions require careful interpretation. For particles with a diameter smaller than 1/10 of the wavelength, the light scattering

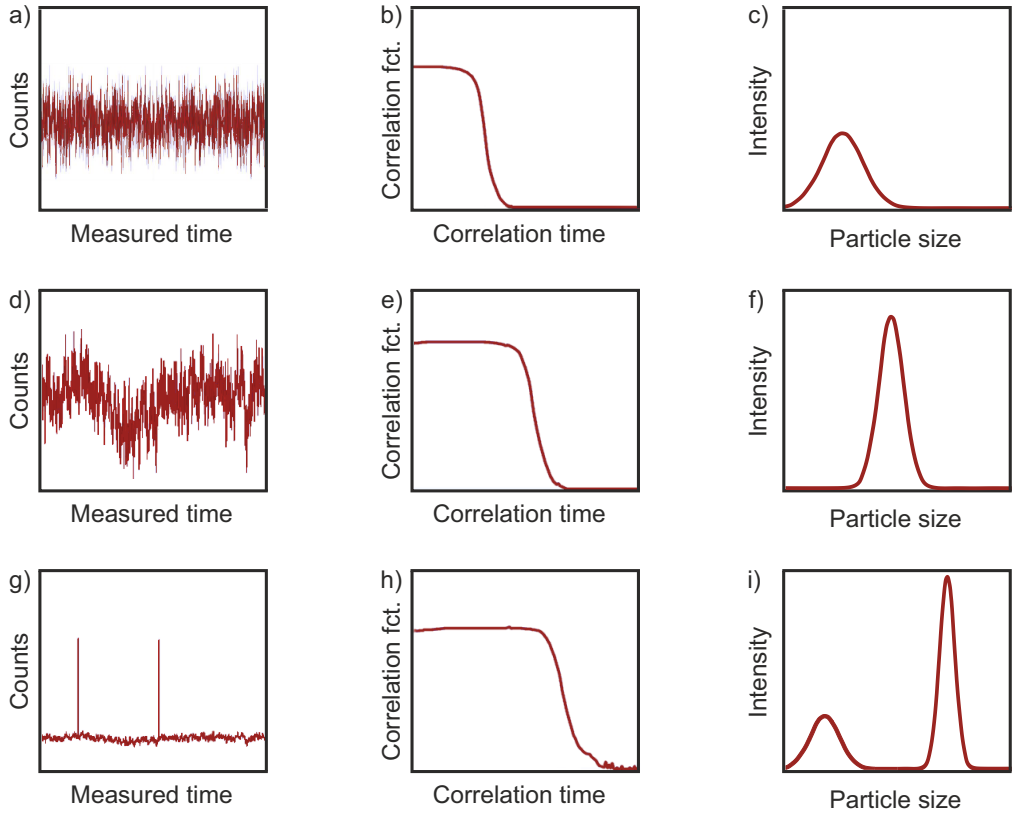

Figure 4.3: DLS: (a,d,g) Measurement signal (counts over time) of the DLS sample, (b,e,h) Correlation function over time and (c,f,i) size distribution over intensity. a) For small particles, the measurement signal is rather uniform, b) the correlation function vanishes sharply at a low correlation time. c) The size distribution over the intensity shows smaller particles with a wide distribution. d) For large particles, the measurement signal shows less fluctuation due to less Brownian motion, e) the correlation function decreases at a medium correlation time and the decay is broader. f) The size distribution shows larger particles with a narrow distribution. g) For mixed particles or particles that are too large, peaks in the count rate occur. h) In the correlation function, the decay happens at a high correlation time and is noisy. i) The size distribution contains both small and large particles.

is dominated by Rayleigh scattering, and the intensity I is angle independent and depends on the particle size by the sixth power of the radii.[136] The DLS can provide the particle distribution over number, volume, or intensity. Figure 4.4 illustrates the influence of the different distributions.

In a dispersion with high density of nanoparticles with small nanoparticle size and some larger particles, this information is provided by the number distribution, as shown in Figure 4.4 a. The volume distribution in Figure 4.4 b describes an almost equal amount of the two sizes of the nanoparticles due to the influence of the particle size on the third power of the radii. In the intensity distribution, larger particles can conceal the presence of smaller nanoparticles. For particles that are significantly larger than 1/10 of the wavelength, light scattering becomes increasingly angle dependent. While DLS detects scattered light in the backward direction,

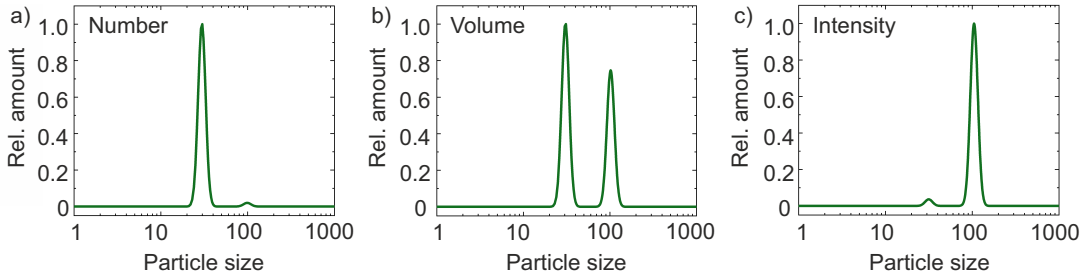

Figure 4.4: Important distributions resulting from the DLS measurement. a) For the number distribution, the amount of nanoparticles is calculated. b) The volume distribution describes the amounts of nanoparticles by volume. c) The intensity distribution describes the light scattering of the nanoparticles. Figure from [26]. Published by Philipp Marlow under the Licence CC BY-SA 4.0.

large particles scatter light in the forward direction, reducing the influence of large particles. Therefore, sizes between 0.3 nm and 10 µm are measurable.[134]
The autocorrelation function g_2 mathematically describes the similarity of the signal at a time $t+\tau$ with the signal at an earlier time t, which leads to: [137]

$$g_2(\tau) = \frac{\langle I(t) \cdot I(t+\tau) \rangle}{\langle I(t) \rangle^2}$$

Angle brackets represent the average over the duration of the experiment. For monodisperse dispersions, the autocorrelation function decays monoexponentially to:

$$g_2(\tau) = B + \beta \cdot e^{-2Dq^2\tau}$$

with the baseline B, an instrument constant β, the diffusion coefficient D, and the dispersion vector q.[137] The dispersion vector can also be stated as:

$$|q| = \frac{4\pi n}{\lambda_0} \cdot \sin\left(\frac{\theta}{2}\right)$$

with the wavelength λ_0 of the used laser, the scatter angle θ, and the refractive index n at λ_0.[138] The desired nanoparticle diameter d_H can be determined by the Stokes-Einstein law through the diffusion coefficient D:

$$d_\mathrm{H} = \frac{k_\mathrm{B} T}{3\pi\eta D}$$

with the Bolzmann constant k_B, the temperature T and the viscosity η. With these formulas, the only parameters that are left to be determined are the temperature T, which is typically 20 °C, and both the refractive index n_0 and the viscosity η of the nonsolvent. Thus, the calculated nanoparticle diameter corresponds to the hydrodynamic diameter d_H, assuming that the measured particles are solid monodisperse spheres. Typically, the cumulant method is used, with

the model of a Gaussian size distribution: The logarithm of the autocorrelation function is fitted by a polynom, which leads to an average particle size. Therefore, the resultant data of DLS are the average particle size, referred to as z-average, and the polydispersity index (PDI), which are both approximations and not direct measurements. In reality, the particles are covered by a small solvent shell inside the nonsolvent that moves through the nonsolvent and can slightly affect the measurement. Therefore, the size of the nanoparticles can differ slightly. Also, the geometric form of the particles cannot be determined, whereby the assumption of spheres can distort the calculated particle size. Nevertheless, the results are comparable to those of other measurement techniques such as small-angle x-ray scattering, atomic force microscopy, or electron microscopy. To compare the average particle size of different dispersions, this method is both fast and sufficiently precise. For an absolute size distribution of the particles within the dispersion, other techniques such as nanoparticle tracking would provide more reliable data.

4.1.2 Centrifugation

In some experiments, the reduction of the dispersion can lead to inconclusive results. This happens mostly for low concentrations and small particles. The first measurements typically show larger particles, but after one minute, the average particle size decreases and reaches the expected value. The explanation for this phenomenon is that some larger agglomerations inside the dispersion disturb the initial measurement, but sediment over time. When the dispersion is centrifuged, the agglomerations settle quickly, and hence the DLS measurements become more reliable. For this reason, all dispersions were centrifuged for 2 minutes at 14.500 rpm inside the centrifuge MiniSpin Plus by Eppendorf, as shown in Figure 4.5 a. This treatment also

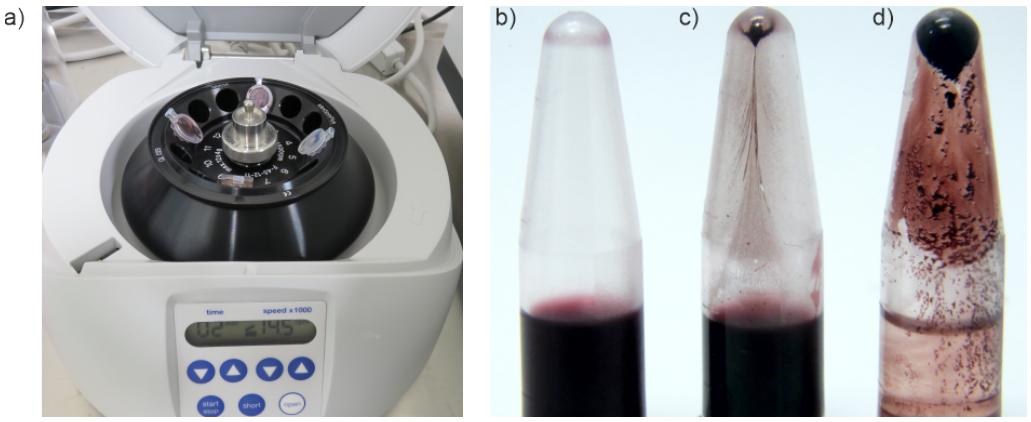

Figure 4.5: a) Centrifugation setup. b) In a highly stable dispersion, no materials sediment during centrifugation. Sometimes, individual agglomerates sediment, but their amount is negligible. c) In an unstable dispersion, some material separates, resulting in a sedimentation. d) In the extreme case, the flocculation of particles results in a collapse of the dispersion, with the total separation of the semiconductor and the nonsolvent.

empirically increases the long-term stability of organic dispersions. For a stable dispersion, as shown in Figure 4.5 b, no sediment at the bottom of the centrifuge tube was observed. In an unstable semiconductor blend dispersion, two different behaviours could be observed. Either one of the two materials starts to separate, leading to a sedimentation of some material, as shown in Figure 4.5 c, or the dispersion collapses, as shown in Figure 4.5 d. This demixing can also take place in dispersions with only one semiconductor, mostly resulting in the collapse of the dispersion. In inorganic nanoparticle dispersions, centrifugation of the dispersion is necessary to inhibit the growth of nanoparticles and to separate larger particles and impurities from smaller particles.

4.1.3 Long-term stability

To verify the stabilization of dispersions, long-term measurements are required. Therefore, the dispersions are stored in the dark inside a cabinet under controlled temperature and air condition. Once a week, an aliquot of the dispersion is diluted, measured by DLS, and the change in particle size over time is documented. While the average nanoparticle size in a stable dispersion typically changes only by a few nanometers over time, the particle size of an unstable dispersion increases significantly within weeks.

4.1.4 UV-Vis-NIR absorbance spectroscopy

After the reduction step, the actual concentration of particulate matter within a dispersion often differs from the initial concentration. By centrifugation, some parts of the dispersed material may be removed, which can also change the blend ratio of materials. Absorbance measurements (UV-vis-NIR spectrometer from Agilent, two-beam operation mode) were used to validate changes in the dispersion concentration. A broad-band light source generates light from 175 nm to 3300 nm. A monochromator selects the wavelength of the probing beam. A beam splitter divides the beam into reference and probe beam. A photodetector measures the intensities of the transmitted light and the difference in absorption between the two beams is calculated.
For measuring thin films, a reference glass substrate is used to subtract the absorption of the glass and the reflection at the glass-air transition from the measured signal. However, thin-film reflections and interference inside the thin films can impact the measured signal. Liquids such as solutions or dispersions can be measured in quartz cuvettes. While quartz allows measurements in the UV range, most solvents absorb in this range, affecting the measurement and preventing measurements below a wavelength of 240 nm. By using a cuvette with the same solvent as a reference, both the absorption of the solvent and the reflection at the quartz can be subtracted.

Typically, the absorption A is calculated from the measured transmission T by $A = 1 - T$. Therefore, reflection, which mostly occurs in thin films, and scattering at the nanoparticles are neglected. The transmission describes the ratio of the light intensity I_S after passing the sample to the light intensity I_0 before passing the sample. The logarithmic absorption A_λ, also known as absorbance, can be calculated by the transmission T_λ and by the Beer–Lambert law to:

$$A_\lambda = -\log_{10}(T_\lambda) = \log_{10}\left(\frac{I_0}{I_S}\right) = \varepsilon_\lambda \cdot c \cdot l$$

with the molar absorption coefficient ε_λ, the concentration c and the optical path length l. Through the linear dependence of the absorbance on the concentration, an unknown concentration can be determined by the comparison with a known concentration. In a semiconductor blend, the influences of the materials on each other have to be excluded. In addition, the materials must have a distinct absorbance characteristic to enable the deconvolution into individual spectra. By comparison of the measured spectra with the known absorbance of the initial dispersion in ethanol or the initial solution in chloroform, the concentration can be determined. From the absorbance spectrum, both the concentration and the acceptor:donor ratio can be estimated. To compare the dispersion with the initial solution, the dispersion is redissolved in a cuvette with chloroform. The absorbance spectrum of the redissolved dispersion can be fitted linearly with two individual spectra of the known references, as shown in Figure 4.6, which allows an

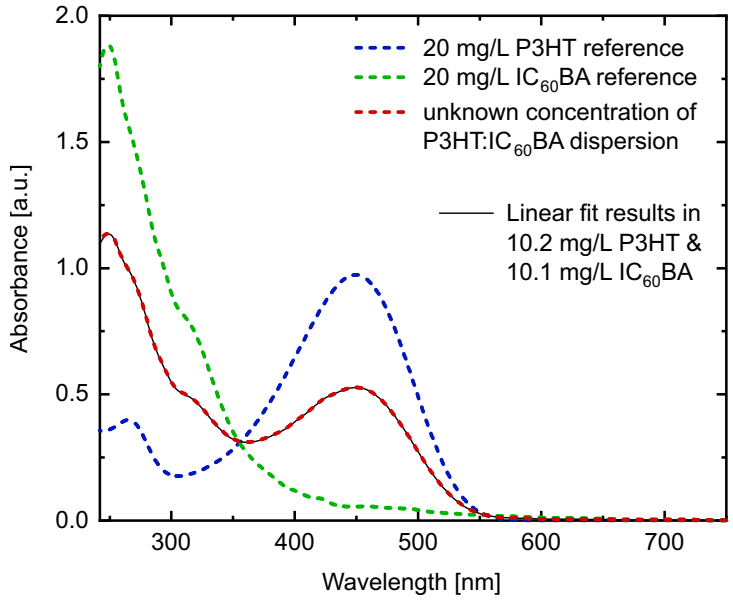

Figure 4.6: Absorbance spectra of P3HT:$IC_{60}BA$. The red line represents the absorbance of the blend, dissolved in chloroform, with an unknown concentration. To estimate the unknown concentration, the two reference spectra pure P3HT solution in blue and pure $IC_{60}BA$ in green were fitted linear, results in the solid black line that perfectly matches the unknown concentration.

estimation of the total concentration and the ICBA-to-P3HT ratio. To compare the concentration and the ratio, the typical measurement range is 230 nm to 800 nm. Below a wavelength of 230 nm, both chloroform and ethanol absorb and disturb the measurement. Above 800 nm, the absorbance of the semiconductors is rather low and impurities of the quartz cuvettes can result in an underestimation of the absorbance. Therefore, higher concentrations are needed to ensure proper measurements.
While the absorbance of P3HT can be measured in ethanol, the acceptors like the fullerene ICBA do not form stable nanoparticle dispersions in ethanol. Therefore, the estimation of the concentration of the dispersion in ethanol is hindered. Instead, different crystallization peaks of P3HT can be observed. Another important peak in the absorbance of nanoparticle dispersions in ethanol is located at 970 nm. This peak is associated with the polaron of P3HT.[14, 26, 139, 140]

4.1.5 PLQY

To determine the molecular interactions between P3HT and the fullerenes, such as their miscibility, the photoluminescence quantum yield (PLQY) is measured, using a FS5 spectrofluorometer from Edinburgh Instruments with the cuvette holder attached to the integrating sphere module SC-30. The PLQY describes the ratio of emitted to absorbed photons of the sample under test. In Figure 4.7, the PLQY setup is illustrated. A broad-band xenon lamp is used as a light source and is spectrally split by a monochromator. The monochromatic beam of the incident light is focused onto the sample inside the integrating sphere. The integrating sphere is a hollow sphere coated with polytetrafluoroethylene (PTFE), which makes it highly reflective.

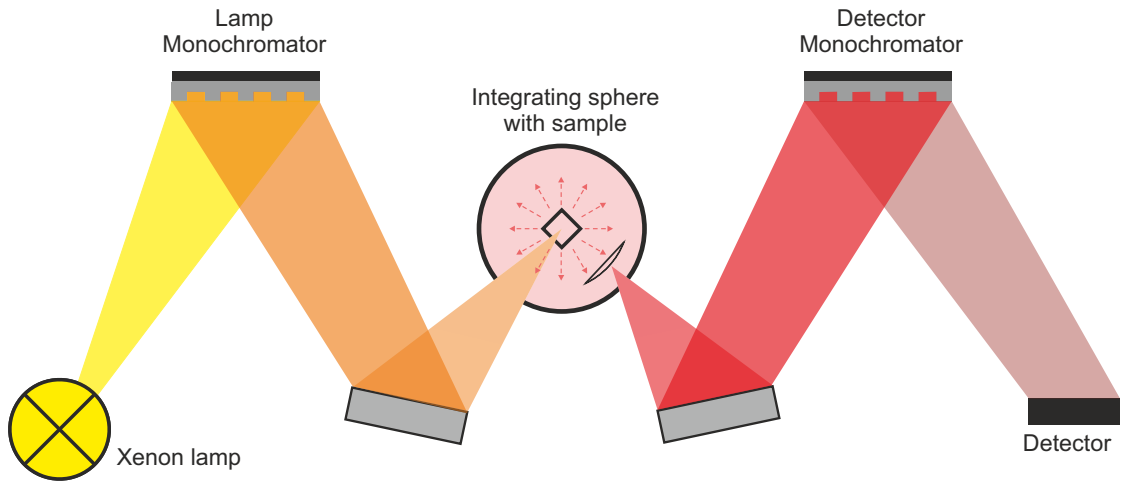

Figure 4.7: Schematic setup of the PLQY spectrofluorometer. The radiation of a broad-band xenon lamp is spectrally split by a monochromator and focused on the measured sample. To measure the photoluminescence, the emitted radiation is again split by another scanning monochromator and focused onto a detector (photomultiplier tube).

It has two slits, one for the incident excitation beam to irradiate the sample and one for the reflected emission beam towards the detector. Photoluminescence occurs in all directions. The light is then reflected at the surface of the integrating sphere. An aperture shields the entrance to the detector, so that only photons that have been previously reflected in the sphere reach the detector monochromator, where the beam is spectrally dispersed before it is detected at a photomultiplier tube (detector). To correct spectral fluctuations of the lamp, a monitor photodiode is used, while filters are used to suppress higher orders of light. Through the respective monochromators, both the emission spectra and the excitation spectra can be varied separately. By adding fullerenes to the nanoparticles, the PLQY-signal is reduced through quenching of the excited states of the polymer. More quenching of the PLQY corresponds to more efficient interaction between the materials.[141, 142]

Therefore, an aliquot of the stock dispersion was separately diluted with ethanol (precipitation: 200 µL dispersion with initial c_D = 2 g/L, diluted in 3.8 mL ethanol, $c_{diluted}$ = 25 mg/L; reduction: 50 µL dispersion with c_D = 2 g/L, diluted in 3.95 mL ethanol, $c_{diluted}$ = 25 mg/L). The scatter spectrum S is the spectrum around the excited wavelength. While 500 nm was chosen for excitation, the spectrum was measured from 470 nm to 530 nm, resulting in the measurement of only scatter light that is reflected in the integrating sphere. The emission spectrum E was recorded from 530 nm to 900 nm, resulting in the measurement of exclusively light that is emitted from the sample under test. For reference, a cuvette with ethanol was used. The intensity of the scatter plots was too high, eventually saturating the detector. Therefore, a ND2 filter was used and the spectra were later scaled by factor a 100. The quantum yield PLQY can be calculated by:

$$\mathrm{PLQY} = \frac{E_S - E_{Ref}}{S_{Ref} - S_S}$$

with the emission spectra of the sample E_S and of the reference E_{Ref} and the scatter spectra of the sample S_S and of the reference S_{Ref}. The calculation of the PLQY was performed using the software Fluoracle from Edinburgh Instruments.

4.2 Layer characterization

In order to determine the properties of nanoparticular thin films, the dispersions are deposited on a glass substrate.

4.2.1 Atomic Force Microscopy

Atomic force microscopy (AFM) can be used to characterize nanoparticles, which does also reveal the shape and topography of nanoparticle samples. Here, a Dimension Icon by Bruker is used. An AFM is based on the interaction between a tip and the surface of the sample. By scanning over the sample surface, a three-dimensional profile can be created. To prevent the degradation of the sensitive layers by oxygen or water, the AFM is placed inside a nitrogen glovebox. Figure 4.8 illustrates the measurement principle. On a cantilever with a specific spring constant, a probing tip is attached with a radius of 10-40 nm. The distance between the surface of the sample and the tip is controlled by a piezo actuator. If the tip is in direct contact with the sample, it can experience attractive or repulsive forces through van-der-Waals forces or coulomb repulsion, resulting in a deflection or torsion of the cantilever. A laser beam is focused onto the back of the cantilever, where it is reflected and detected by a four-quadrant photodiode. Through the up, down, and sideways displacements of the tip during scanning, the cantilever deflects the laser beam which is then detected by the four-quadrant photodiode. Due to the height information from the piezo actuator, a height profile can be generated. Tilting and bending of the cantilever can be deduced by the software of the system.[143]

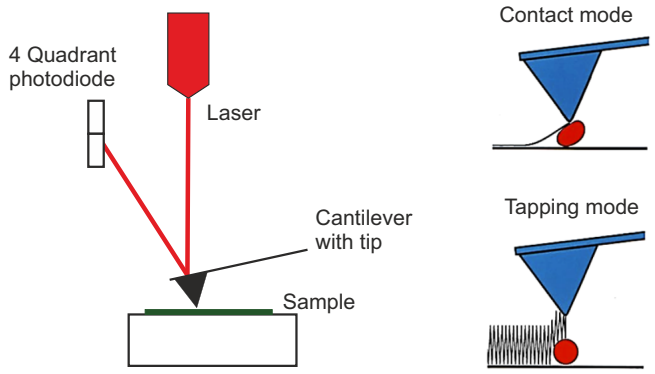

Figure 4.8: Working principle of an AFM. A laser beam is focused onto the cantilever, and reflected onto the four-quadrant photodiode, which monitors the changes of the laser beam. The x-, y- and z-position of the AFM probe hence yields a topographic map of the sample. Typically, either contact mode or tapping mode are chosen.

Typically, either the contact mode or tapping mode are chosen. In contact mode, the sample and the tip are in continuous contact. The force between tip and sample, which is indicated by

the deflection of the cantilever, is kept constant, i.e. the deflection setpoint. In tapping mode, the sample and the tip are only in contact for a short time. This reduces both the damage to the surface and the contamination of the tip. For this work, only the tapping mode was used on nanoparticular layers deposited from dispersion on glass substrates. The cantilever is mechanically excited near its resonant frequency. As the tip approaches the surface, the interaction between the tip and the sample surface changes the frequency of the oscillation, resulting in a decrease of the oscillation amplitude.[144] The piezo actuator adjusts the deflection amplitude to the initial value. This adjustment results in the height profile of the measured sample surface.[145]

4.2.2 Tactile profiler

To measure the thicknesses of the layers, the tactile profiler Dektak XT (Bruker) is used. Most samples are either glass substrates with a light-harvesting layer or solar cells with a layer stack. Since profilers can only measure the total layer thickness rather than individual layers, the bottom layers are measured separately and subtracted from the total layer thickness to determine the individual layer thickness. For the sample preparation, the layers need to be scratched without damaging the glass substrate. Therefore, plastic tweezers or metal canulas are used, depending on the rigidity of the material. The samples are placed on the work plate, as shown in Figure 4.9 a.

Varying the scanning distance, the measurement duration, the speed and the force of the stylus on the sample allows the adjustment of the measurements. In Figure 4.9 b, the measurement settings for a common P3HT layer on glass are depicted. Attached to a scanning unit is a diamond stylus with a radius of 2 µm. The stylus comes into contact with the sample and scans the surface of the sample. Through contact, the surface of the sample can be damaged. For soft

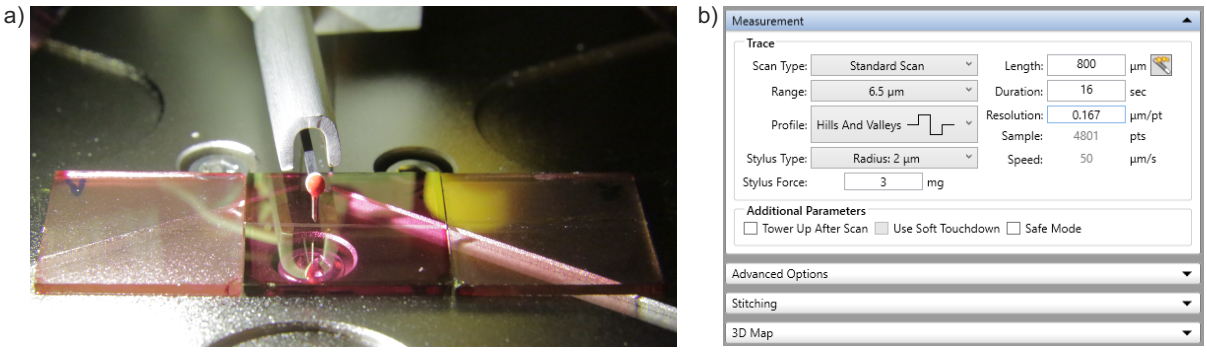

Figure 4.9: a) Sample under the stylus during a measurement. From the non-scratched surface, the stylus scans vertically through the scratch and back on the non-scratched surface. b) Typical settings for a measurement of a P3HT sample. The length and the duration of the measurement are adjusted for best measurement resolution.

materials, the stylus can scratch the layer, which falsifies the measured layer thickness. The deflection of the stylus is used by the software to create a profile line and results in a height profile.

4.2.3 Digital optical microscope

The surfaces of the layers were investigated with the digital microscope Smartzoom 5 from Carl Zeiss AG. Like in a normal optical microscope, the incident light beam is focused onto the sample. The reflected light enters the objective and creates an image which is captured by the camera. For the Smartzoom 5, two different illumination modes can be chosen: the ring light and the coaxial brightfield illumination mode.
In the ring light mode, eight LEDs are arranged in a ring around the lens, as shown in Figure 4.10 a. The light evenly irradiates the sample, which results in excellent illumination without casting shadows. In this mode, only reflecting structures can be detected, because only scattered light reaches the detector. The individual segments of the LEDs can also be controlled separately, which allows selective illumination under specific angles. The ringlight mode is primarily used for edges and particles. It is exemplified in Figure 4.10 b, showing a P3HT layer with $PC_{61}BM$-rich clusters. In contrast to the smooth layer, the clusters are highly reflective. In coaxial brightfield measurements, the light source is located behind the lens. The light beam is guided through the optics and reflected at the surface of the sample. Therefore, mostly non-scattered light that is reflected back vertically is detected. The coaxial brightfield is mostly used to visualize thin, transparent, or non-reflective layers, which are otherwise invisible. Likewise, the contrast between two materials of similar color can be investigated, leading to an image as depicted in Figure 4.10 c. While the clusters are rather dark, the material contrast in the smooth

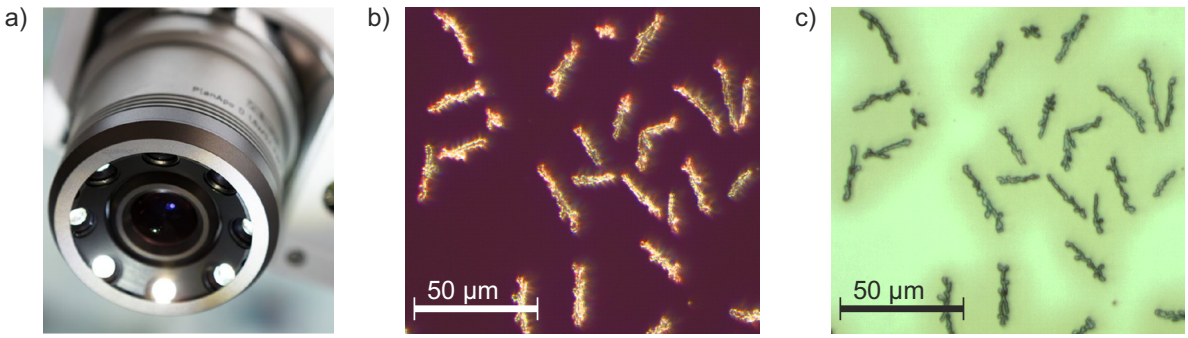

Figure 4.10: a) Objective of the Smartzoom 5 microscope, with a ring of eight LEDs arranged around the lens. b) Image of a representative P3HT:$PC_{61}BM$ layer, showing $PC_{61}BM$-rich clusters, at a magnification of 2200× in the ring light illumination mode, mostly highlighting the highly reflective $PC_{61}BM$ clusters. c) In coaxial brightfield illumination mode, the material contrast in the smooth layers becomes visible.

layer is visible. The objective with the lowest magnification in our setup enables a magnification of 34×, which can be used for stitching images, while the objective with the highest magnification enables a magnification of 2200×, which is more suitable for small structures. The software of the digital microscope and the calibration enable image processing, where, for example, the distance between two structures can be measured and scales can be added.

4.3 Solar cell fabrication and characterization

To assess the quality of the nanoparticle dispersions for optoelectronical applications, solar cells containing light-harvesting layers made from nanoparticle dispersions were fabricated and characterized. Therefore, a glass substrate with a layer of indium-tin-oxide (ITO) was used as the cathode. The substrates were cleaned first with glass cleaner and a Q-tip and afterwards in an ultrasonic bath inside a beaker with acetone and 2-propanol. The substrates were then exposed to oxygen plasma for 2 minutes to remove any organic residues. On top of the ITO, a 10 nm thin electron transport layer (ETL) of zinc oxide nanoparticles (ZnO-NP) was deposited from 1-butanol by spincoating. The layers were thermally annealed for 10 minutes on a hot plate at 120 °C. On top of the ETL, the light-harvesting layer containing the polymer-fullerene nanoparticle blend was applied multiple times. Since the nanoparticles inside the dispersion are not soluble in ethanol, multiple spincoating steps on top of each other enable the deposition of thick and closed layers. On top of the light-harvesting layer, a hole transport layer (HTL) of poly(3,4-ethylenedioxythiophene):polystyrene sulfonate (PEDOT:PSS, HTL Solar, Heraeus) with a thickness of 25 nm was deposited and annealed at 120 °C for 10 minutes. A 100 nm silver anode was thermally evaporated. A schematic of the fabrication process is depicted in Figure 4.11. Apart from the electrodes, all layers were spincoated.

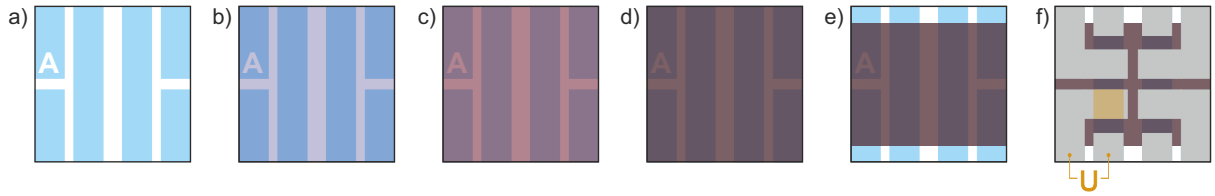

Figure 4.11: Schematic of the solar cell fabrication process. a) On a cleaned glass substrate with the structured ITO anode, b) a thin electron transport layer (ZnO-NP) is deposited. c) The light-harvesting layer is applied by multiple spincoating steps from nanoparticle dispersion. d) On top of the light-harvesting layer, PEDOT:PSS is deposited as hole transport layer. e) The border area is scratched to enable the contact between ITO and f) the silver anode that is thermally evaporated and structured by mask. Each substrate carries four identical solar cells. The light-harvesting area of one solar cell is highlighted in orange.

4.3.1 Solar Simulator

To determine their power conversion efficiencies, the solar cells are electrically characterized by recording their *J*-*V* curve under illumination and in the dark. With a power supply unit, a specific voltage is applied, while the device current is measured. In our setup, the source meter unit (SMU) Keithley 2420 was used for both applying the voltage and measuring the current. The resistance of the test leads was compensated by using a four-wire measurement setup. Thus, the typical characteristics of solar cells that were described in chapter 2.2, including the open-circuit voltage (V_{OC}), the short-circuit current density (J_{SC}), the maximum power point (MPP), the fill factor (FF) and the power conversion efficiency (PCE), can be determined. A solar simulator that mimics the spectrum of the sun is used as a light source. More precisely, the spectra are adjusted to the AM 1.5g solar spectrum according to the ASTM G173-03 standard.[146] The ASTM AM 1.5g is an idealized solar spectrum, which represents the irradiation at a solar zenith angle of 48.2 ° at sea level. Compared to the vertical irradiation of the sun, the sun light travels 1.5 times the air mass (AM) and therefore has a 1.5 times higher transit distance through the atmosphere at the zenith angle of 48.2 °. The irradiance is specified as 1000 W/m^2.
For this work, two different solar simulators with AAA classification were used, one of which utilizes a xenon lamp, while the other operates with LEDs. The xenon solar simulator (Sciencetech Lightline AX-LA 200) produces irradiation that resembles sunlight. With optical filters, the spectrum is adjusted to AM 1.5g. The LED solar simulator (Newport Oriel Verasol-2) consists of several narrow-band LEDs that are combined to produce AM 1.5g. The spectra of AM 1.5g and both solar simulators are shown in Figure 4.12.
Since the spectral fit of the xenon solar simulator for wavelength below 800 nm is more accurate, it was the first choice for most measurements. Only for sensitive samples that would already degrade in UV-light, the LED solar simulator was used due to the lack of UV-light. The AAA classification implies that the spectrum matches the solar spectrum AM 1.5g between 400 nm and 1100 nm, while the area is irradiated with high uniformity at a non-fluctuating irradiation. Nevertheless, to adjust the irradiance strength of the solar simulators to AM 1.5g, a reference is needed. For reference, a calibrated silicon solar cell (Newport 91150-KG5) with a KG5 glass filter was used. The silicon solar cell is positioned inside the holder under the solar simulator, and the irradiance is adjusted until the reference produces the short-circuit current expected under AM 1.5g irradiation. For best results, the device under test (DUT) must perfectly match the spectral sensitivities of the reference.

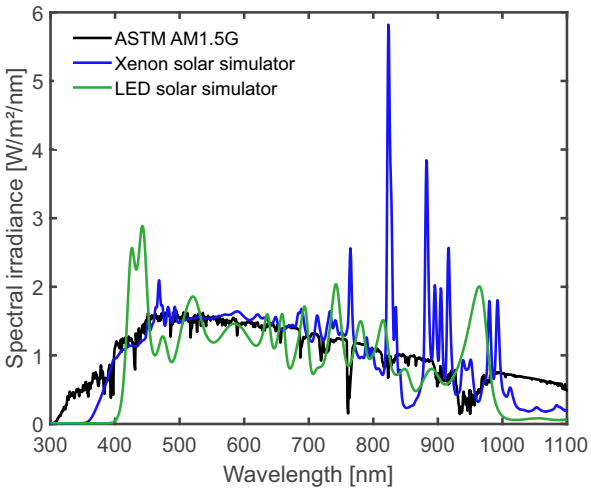

Figure 4.12: Spectral irradiation of the solar simulators compared to the ASTM AM1.5g sun spectra in black. The LED solar simulator (green) consists of several LEDs, which can be tuned individually. The xenon solar simulator (blue) works with different optical filters to reconstruct the solar spectrum. Figure from [139] with color changes. Published by Felix Manger under the Licence CC BY-SA 4.0.

In reality, a spectral mismatch calculation is required for high accuracy, that is, the current density needs to be corrected, which also leads to a correction of the efficiency. The spectral mismatch calculation factor SMCF is determined by:

$$\mathrm{SMCF} = \frac{\frac{I_{\mathrm{DUT,SolSim}}}{I_{\mathrm{DUT,AM1.5g}}}}{\frac{I_{\mathrm{Ref,SolSim}}}{I_{\mathrm{Ref,AM1.5g}}}} = \frac{\int \lambda \cdot \mathrm{EQE}_{\mathrm{DUT}}(\lambda) \cdot E_{\mathrm{SolSim}}(\lambda)\,\mathrm{d}\lambda}{\int \lambda \cdot \mathrm{EQE}_{\mathrm{DUT}}(\lambda) \cdot E_{\mathrm{AM1.5g}}(\lambda)\,\mathrm{d}\lambda} \cdot \frac{\int \lambda \cdot \mathrm{EQE}_{\mathrm{Ref}}(\lambda) \cdot E_{\mathrm{AM1.5g}}(\lambda)\,\mathrm{d}\lambda}{\int \lambda \cdot \mathrm{EQE}_{\mathrm{Ref}}(\lambda) \cdot E_{\mathrm{SolSim}}(\lambda)\,\mathrm{d}\lambda}$$

with the spectral irradiance of the solar simulator E_{SolSim} and AM 1.5g $E_{\mathrm{AM1.5g}}$, the EQE of the DUT $\mathrm{EQE}_{\mathrm{DUT}}$ and the reference $\mathrm{EQE}_{\mathrm{Ref}}$. Typically, the EQE of the reference and both spectral irradiances are known; therefore, only the EQE of the DUT needs to be measured. The SMCF of all solar cells was calculated, with a slight underestimation of the current density. Typically, due to a deviation of less than 1 %, no solar cell adjustment was necessary. For light-harvesting layer thicknesses above 120 nm, the current of the solar cell is slightly underestimated by up to 3 % .

4.3.2 EQE

External quantum efficiency (EQE) measurements are used to determine the spectral contributions to the photocurrent of organic solar cells. As described in chapter 2.2, the EQE is the ratio of the number of extracted charge carriers to the number of the incident photons. A xenon lamp (LOT Oriel 450W LSH601) is chosen as light source (with the monochromator LOT Oriel

Omni-λ300 and the color filter wheel MSZ3122). The monochromatic light is directed to the DUT through a fiber, where it irradiates the DUT, creates a current that is amplified by a transfer impedance amplifier (Femto Metrology OE-200S) and is converted to a voltage signal. By increasing the wavelength stepwise, for example, in 5 nm steps, a spectral determination of the photocurrent distribution is possible. To compensate fluctuations of the light source during measurement, the beam is split into two after passing the monochromator to direct a small amount of light onto a monitor diode (Hamamatsu K1713-09). The signal of the monitor diode is amplified by another transfer impedance amplifier. The measurement was first performed with a calibrated reference photo diode (Newport 818-UV-20925) with a known spectral response, leading to a known illumination intensity of the measurement. By the repetition of the measurement with the DUT using the same settings, the SR_{DUT} can be calculated by the reference SR_{Ref}, and the measured current I for both the reference and the DUT at each individual wavelength. This leads to:

$$SR_{\mathrm{DUT}} = \frac{I_{\mathrm{DUT}}}{I_{\mathrm{Ref}}} \cdot SR_{\mathrm{Ref}} \cdot \frac{I_{\mathrm{M,Ref}}}{I_{\mathrm{M,DUT}}}$$

with the correction of the monitor diode I_{M} for both the reference and the DUT.

5 Ink fabrication via microfluidics for organic solar cells

While the process of the beaker nanoprecipitation (see 2.3.1) enables a fast and facile screening, the transition from lab-scale to large-area coating of nanoparticular inks on roll-to-roll machines is challenging. To ensure a large-scale supply of nanoparticular ink, a scalable and reproducible synthesis is needed. This can be achieved in a continuous-flow system, such as a microfluidic setup, which is introduced in this chapter. Preliminary work has been conducted in the bachelor thesis of *A. Ardelt*, who investigated different synthesis parameters of the microfluidic setup, and in the bachelor thesis of *F. Mintel*, who examined the influence of the nanoparticle size on the behavior of solar cells for the blend of P3HT and ICBA.
In the first section, the setup of the microfluidic system is described, followed by an investigation of the process parameters: through the adjustment of the different speeds of the syringe pumps, the initial concentration of the solution, and the irradiation of the microfluidic setup, nanoprecipitation is highly controllable, resulting in reproducible nanoparticle sizes and highly stable dispersions. Afterwards, solar cells incorporating a nanoparticular light-harvesting layer are examined and compared to solar cells with a light-harvesting nanoparticular layer from inks that were nanoprecipitated inside a beaker. The results of this chapter were published in K. Fischer et al., *Microfluidics: continuous-flow synthesis of nanoparticle dispersions for the fabrication of organic solar cells* Advanced Materials Technologies 2022, *7*(11), 2200297.[147]

5.1 Microfluidic setup

The microfluidic setup consists of two syringe pumps (LA-110 high pressure from Landgraf Laborsysteme HLL), two glass syringes, tubing, a microfluidic mixing chip (Micromixer chip from dolomite microfluidics), and a vial or beaker to collect the dispersion. The syringes are placed inside the syringe pumps and connected to the microchip via tubing. Through the tubes, both the solution and the nonsolvent are guided separately into the quartz glass microchip. A schematic of the setup is depicted in Figure 5.1 a. In Figure 5.1 b, a photo of the setup is shown. In the microchip, mixing takes place. Therefore, the microchip is the most important part of the microfluidic setup and has to be chosen carefully. Several microchips for mixing fluids exist.

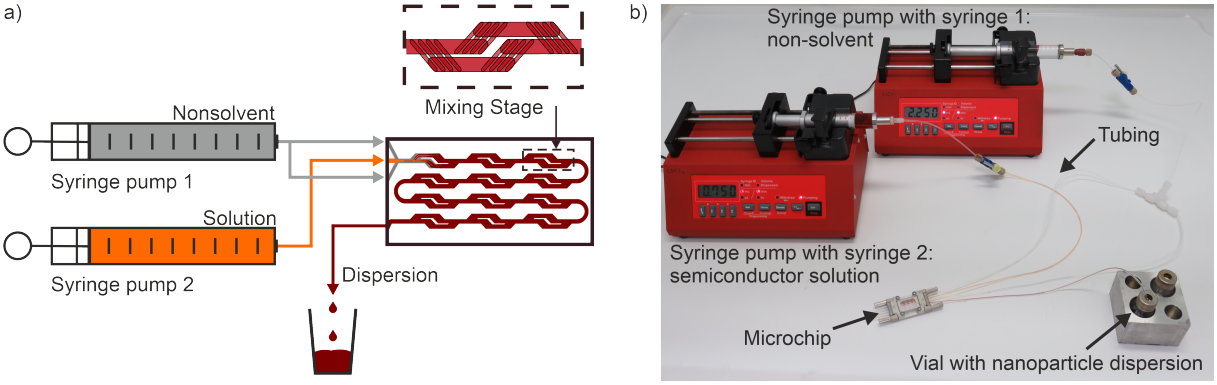

Figure 5.1: Setup of the microfluidic system. a) Scheme and b) photo of the microfluidic system and its components. The semiconductor/chloroform solution (orange) and the nonsolvent ethanol (gray) are loaded into the syringe pumps. The syringe pumps feed both the solution and the nonsolvent through tubes into the micromixer chip, where the nanoparticle dispersions are formed by nanoprecipitation under rapid mixing through the split and recombine principle. The dispersion (red) is then collected in a vial or a beaker. From semiconductor solution to dispersion, a distinct change of color becomes visible in both the microfluidic chip and the tubes.

They differ in channel width and geometry, which are important parameters for mixing.[148] In macrofluidics, mostly gravitational and inertial forces determine the process results. In microfluidics, mostly frictional forces and surface tensions are dominant. Therefore, the Reynolds number *Re* as the ratio of inertial forces to frictional forces plays an important role: [16, 56, 57]

$$Re = \frac{\rho \cdot \mu \cdot L}{\eta} = \frac{\mu \cdot L}{\nu}$$

Re depends on the density of the liquid ρ, the flow speed μ, a characteristic linear dimension L, which here is the channel width, the dynamic viscosity η and the kinematic viscosity ν.[16, 149, 150] Two different flow characteristics, laminar flow and turbulent flow, are classified by *Re*.

At small *Re* ($Re < 2{,}000$), the friction of force is dominant. The flow is mostly laminar, and the liquids mix by diffusion. This leads to a rather slow mixing process. At large Reynolds numbers ($Re > 3{,}500$), the inertial force is much stronger than the frictional force. The flow is mostly turbulent, and the liquids mix rather quickly. At intermediate Reynolds numbers, the flow pattern is difficult to predict. Several intermediate states with both laminar and turbulent elements exist.[16, 149, 150] Due to the small dimensions of the microfluidic chip, the Reynolds number is rather small. In straight channels, a laminar flow prevails, with a rather slow mixing.[57] Therefore, we chose a quartz glass micromixer chip with twelve mixing stages. The micromixer chip is depicted in Figure 5.2 a. The mixing stages create vortices by splitting and recombining the flow, resulting in rapid mixing of the solution and the nonsolvent. Photos captured through

an optical microscope at different stages of the mixing process are assembled in Figure 5.2 b - g, with P3HT dissolved in chloroform and ethanol as nonsolvent. The time stamps are calculated from the total flow rate Q = 3 mL/min and the chip dimensions, with the starting time 0 ms at the inlet of the chip.

With the injection of the semiconductor solution (orange, center tube) and the nonsolvent (clear, top and bottom tubes) in Figure 5.2 b, a laminar flow forms. This flow splits and recombines multiple times in the following mixing stages (Figure 5.2 c-e), which creates vortices and en-

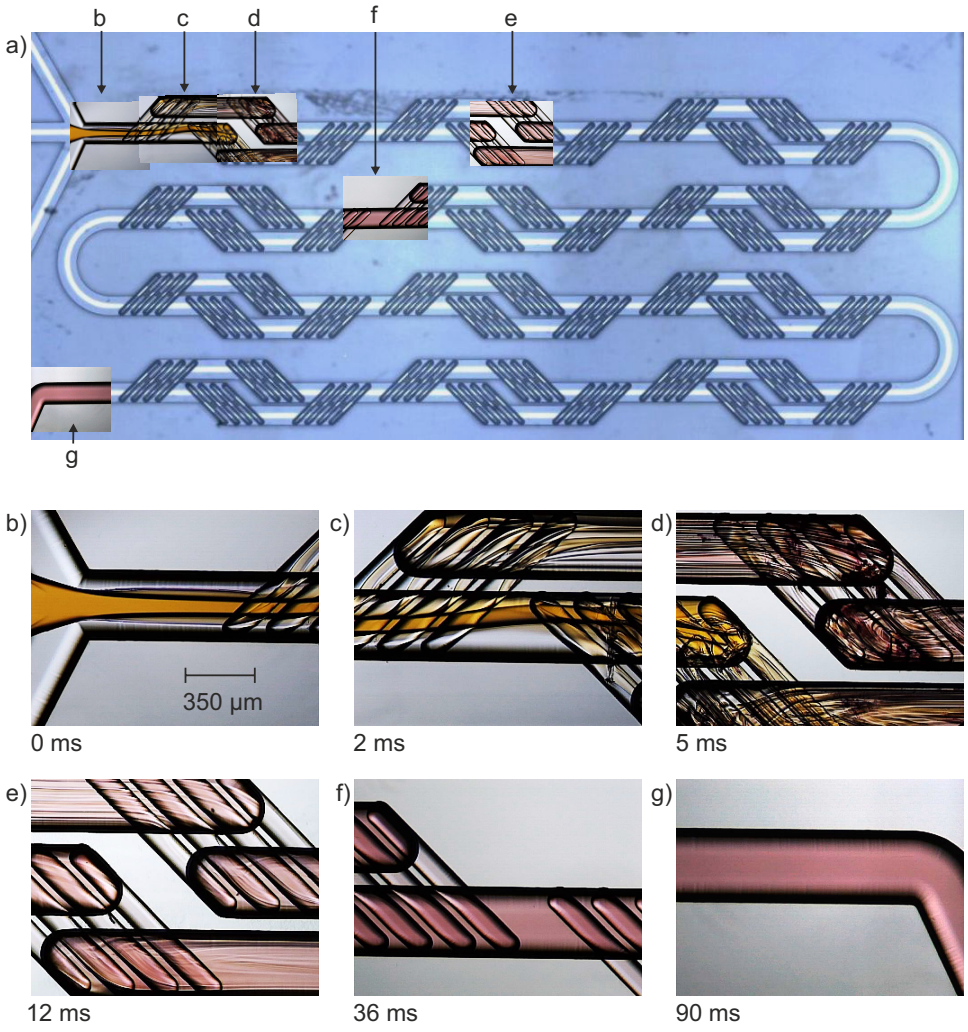

Figure 5.2: Tracking the solvent/nonsolvent mixture through the micromixer chip, with the calculated time stamps at a flow rate Q = 3 mL/min. a) In the microscope picture of the chosen micromixer chip, the sections that are shown in the following pictures are highlighted. b) The semiconductor solution (solvent, orange) and the nonsolvent (clear) are injected right before the first mixing stage at 0 ms. c-e) Through splitting and recombining, vortices are created in the flow, which leads to mixing of solution and nonsolvent. The color shift from orange to red indicates the aggregation of P3HT and hence the formation of nanoparticles. f) After 36 ms, the dispersion looks homogeneously colored, which indicates the end of the nanoparticle formation process. g) After 90 ms, the dispersion leaves the micromixer chip.

ables rapid mixing of solution and nonsolvent. At each mixing stage, the mixture becomes more homogeneous, which leads to a lowering of the semiconductor solubility within the mixture. The bathochromic shift from orange to red indicates the transition of soluble material to aggregated material and is well known for P3HT.[55, 56] After 36 ms, the color does not change further and the dispersion appears homogeneously red, indicating the end of the nanoparticle formation process (Figure 5.2 f). After 90 ms, the dispersion leaves the chip and is collected in a vial or a beaker (Figure 5.2 g). The beaker is placed inside a water bath at a fixed temperature to reduce the volume of the dispersion to the initial volume of the solution and to remove the chloroform.

5.2 Parameters influencing the microfluidic nanoprecipitation

Besides a functional setup, which is important for the microfluidic nanoprecipitation, several other parameters control the nanoparticle formation process and influence the nanoparticle size. Some of these parameters, such as the flow rate of the semiconductor solution Q_S and the flow rate of the nonsolvent Q_{NS}, can be controlled by the syringe pumps. Other variables such as the semiconductor concentration in the solvent c_S or the illumination conditions can be changed manually. Changing the microchip would change the nanoprecipitation. The choice of nonsolvent also directly influences the nanoparticle formation process. Previous experiments have proven that ethanol is a suitable nonsolvent for P3HT.[26, 55, 151, 152] As described in the following section, the temperature of the solution is crucial, otherwise P3HT starts to crystallize, leading to less reproducible nanoparticle formation. Surprisingly, varying the temperature of either the nonsolvent or the mixing chip or both between 16 °C and 50 °C does not influence the nanoprecipitation process and thus the average size of the nanoparticle. All potential synthesis parameters are discussed in more detail below.

5.2.1 Changing the Microchip

The appropriate choice of the microchip is crucial for the nanoprecipitation process. The microfluidic chip is the heart of the setup and therefore has to be chosen with care. Several microchips can be used for microfluidic setups. In most microfluidic systems in drug delivery, a droplet junction chip is the first choice. By using two non-miscible solvents, organic material droplets form inside a carrier phase. Those droplets have a large surface area. The contact of the semiconductor solution with the nonsolvent could support the controlled mixing and the formation of nanoparticles. The droplet junction chip is for laminar use and mixes only by diffusion. If ethanol and chloroform are used, the formation of droplets is not possible through the miscibility of the two solvents. By using a "droplet X-junction chip" (microfluidic chip

from dolomite microfluidics), the input and output flows can be varied, which leads to different mixing patterns of the "droplet X-junction chip". Using the confluence setup of the micromixer chip, a laminar flow is achieved, as shown in Figure 5.3 a. Changing the input and output to a flow where the solution and the nonsolvent meet head-on leads to a side-by-side flow as shown in Figure 5.3 b. In both cases, a laminar flow with a tiny mixing zone occurs and the solution and the nonsolvent are not homogeneously mixed when leaving the chip. Therefore, the precipitated particles are very large (>150 nm). By increasing the flow rates, the flow pattern changes into a mixed laminar-turbulent flow and some vortices occur. Through these vortices, the two fluids change their mixing behavior. Still, the solution and the nonsolvent do not mix completely inside the chip and the particles are rather large. To produce smaller nanoparticles, a more turbulent mixing is needed. In the setup discussed here, it is not possible to increase the flow rates any further to achieve a more turbulent flow. By changing the inputs and the output of the chip, different flow patterns can be achieved. However, mixing in this microchip is not sufficient, which can be seen in Figure 5.3, where the typical color shift of P3HT from orange

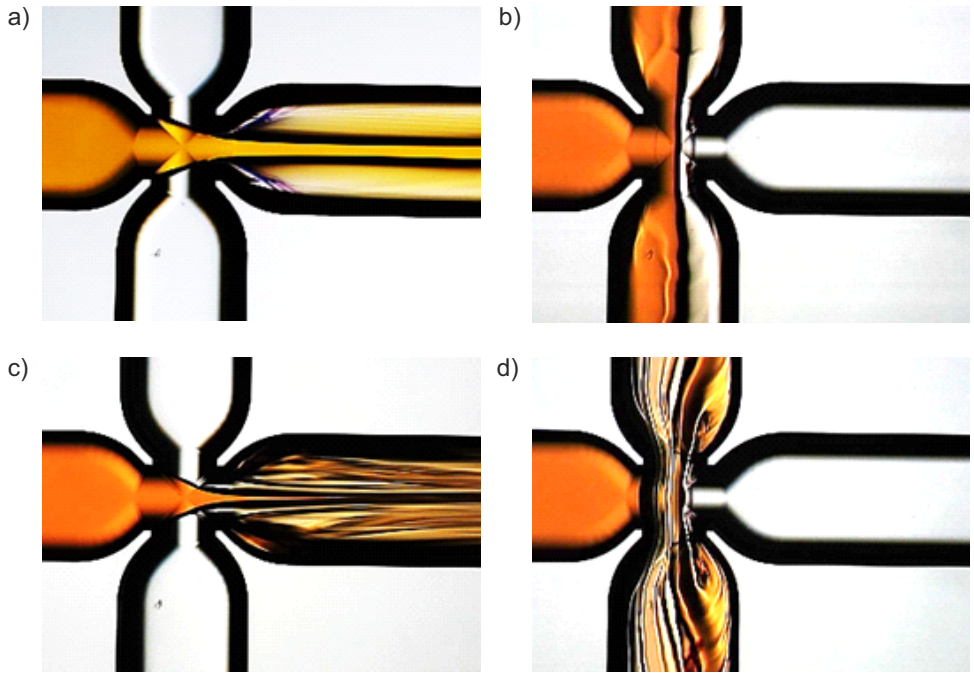

Figure 5.3: Microscope photos of the "droplet X-junction chip". a,c) The semiconductor solution (orange, left tube) and the nonsolvent (clear, top and bottom tubes) form a new flow into the right tube. b,d) The semiconductor solution (orange, left tube) and the nonsolvent (clear, right tube) meet head-on and form a new flow into the top and bottom tube. While in a-b the low flow rates lead to a laminar flow and mixing by diffusion, the higher flow rates in c-d lead to a laminar-turbulent mixed flow with some vortices. In all cases, the mixing is not sufficient for the nanoparticle formation process, as indicated by the missing color shift of P3HT from orange to red.

to red is missing, which implies that nanoparticles do not form. This shows that the geometry of the mixing chip is crucial for nanoprecipitation.

5.2.2 Semiconductor solution

The semiconductor solution also influences the nanoparticle formation process. Typically, the semiconductor is dissolved in the solvent of choice. Heat is applied for several hours to ensure complete dissolution. For materials with a poor solubility, the dissolution can even take several days. Since P3HT is highly soluble in chloroform, 10 g/L of P3HT are fully dissolved in less than 20 minutes, when stirred. Therefore, the solution is stirred at 47 °C on a hot plate. For the nanoprecipitation process, the dissolution time is crucial because it influences the stability of the nanoparticle dispersion. Preliminary experiments showed that during batch nanoprecipitation of aged solution, the overall nanoparticle size increases. After less than a day, the size already doubles. In microfluidics, this change is more pronounced and even visible, as depicted in Figure 5.4. While a freshly prepared solution leads to a homogeneous nanoparticle dispersion as pictured in Figure 5.4 a, an aged solution (here: two days) leads to the formation of agglomerates that flow through the channels of the microfluidic chip. At the bottleneck between the channel and the branches, the agglomerates settle on the glass walls and grow, as shown in Figure 5.4 b. While some agglomerates travel through the chip and cause the dispersion to collapse, others clog the channels and damage the microfluidic setup.

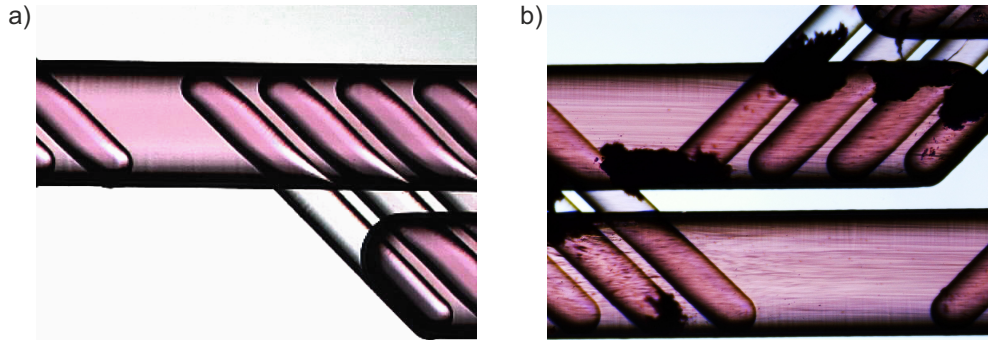

Figure 5.4: Microfluidic mixing stage during nanoprecipitation for two different P3HT solutions. a) In a freshly prepared solution (c_S = 2 g/L)), no agglomeration occurs, which leads to a homogeneous dispersion. b) During the nanoprecipitation, the old solution (2 days old, c_S = 2 g/L) starts to form agglomerates, which settle on the glass walls, where they grow and clog the microfluidic branches. After nanoprecipitation, the dispersion flocculates and the P3HT sediments, leading to phase separation.

In literature, the aging of P3HT is described in several reports. This aging occurs slowly due to the weak interaction between the P3HT chains, typically in the range of weeks.[72, 153] Bielecka et al. showed that the absorbance spectra of P3HT dissolved in chloroform does not change after several days, while an aging time of 6 months led to additional red-shifted

peaks.[154] These red-shifted peaks are the result of aggregation within the solution, which is associated with a crystallization effect of P3HT and the formation of ordered nanowires. The storage conditions also influence the solution. Typically, reheating the solution can lead to the dissolution of these aggregates. While the aged solution during this work remained on the hot plate all the time, this effect could be neglected. However, the agglomerations shown in Figure 5.4 b prove that this effect of aged solutions is not negligible. Therefore, all solutions are freshly prepared to prevent agglomeration of nanoparticles during the process.

5.2.3 Pumping Parameters

Through the syringe pumps, the flow rates Q and the dispensed volume can be adjusted. Instead of the flow rate of the semiconductor solution Q_S and the nonsolvent Q_{NS}, the total flow rate through the microfluidic chip $Q = Q_S + Q_{NS}$ and the volume fraction of the nonsolvent $\varphi_{NS} = \frac{Q_{NS}}{Q_S+Q_{NS}}$ turned out to be more descriptive.
To find a process window for these parameters, initial tests with pure chloroform and ethanol are performed. While both ethanol and chloroform are colorless liquids, the difference in their refractive index leads to a visible mixing inside the micromixer stages, as pictured in Figure 5.5 a. In reality, a wide range of Q and φ_{NS} is feasible. Only the chosen syringe pumps limit the range of parameters and lead to a process window of 1 mL/min $< Q <$ 4 mL/min and 65 % $< \varphi_{NS} <$ 80 %.

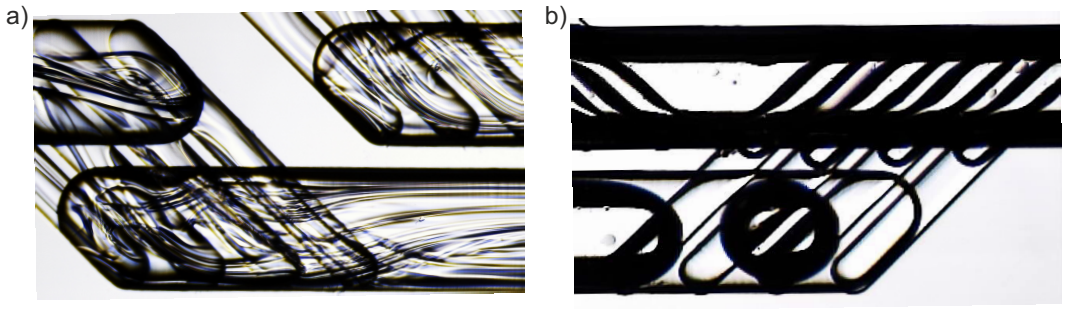

Figure 5.5: Mixing stages of the micromixer chip, a) containing the mixture of ethanol and chloroform. Due to the different refractive indexes of ethanol and chloroform, the mixing of the two colorless liquids is visible. b) Preconditioning of the setup is important to remove air bubbles, which would otherwise disturb the mixing process.

For $Q <$ 1 mL/min, a backflow of the nonsolvent into the solvent tube is detected, which is caused by the technical limitations of the syringe pumps. This backflow leads to nanoprecipitation inside the tubing or the solution syringe that renders the results useless and therefore has to be avoided. It can also cause clogging of the system. For $Q >$ 4 mL/min, the resistance to the flow inside the branches of the microfluidic channel is too high and leads to strong working

loads on the syringe pumps, which results in a backflow into the solution syringe and causes the system to stop. While both limits of Q come from the syringe pumps, the lower limit of φ_{NS} comes from the solution to nonsolvent ratio. At $\varphi_{NS} < 50\,\%$, P3HT is still soluble inside the ethanol-chloroform mixture and no nanoparticles are formed. At $50\,\% < \varphi_{NS} < 65\,\%$, the remaining chloroform fraction inside the dispersion is too high for an immediate nanoprecipitation of P3HT, which leads to ripening of the nanoparticles after leaving the chip and sometimes even results in flocculation of the dispersion. For the upper limit, the syringe pumps are again the limiting factor. At an intermediate $Q = 2$ mL/min, a $\varphi_{NS} > 80\,\%$ leads to a backflow. Since both Q and φ_{NS} depend on the same variables, changing one parameter can affect the other. Nevertheless, both process windows appeared very reliable. In particular, the implementation of stronger pumps will change the process windows.

To achieve reproducible results, the microfluidic chip is preconditioned right before every nanoprecipitation process. Through this preconditioning, air bubbles inside the micromixer stages are removed, as shown in Figure 5.5 b. In order to achieve this, neat chloroform and ethanol are injected with the process flow rates. This leads to a cleaning of the whole setup and avoids any backflow of either nonsolvent or solution into the respective feed tubes. Also slightly different tubing path lengths can be neglected. A 2-way inline valve is used to switch from neat chloroform to the semiconductor solution directly before the process is started. This prevents a backflow into the tubing during the change of the syringes. After nanoprecipitation, the dispersion is collected at the end of the microchip inside a beaker or a vial and is directly characterized in a dynamic light scattering setup (DLS, see 4.1.1) for the determination of the nanoparticle size. P3HT solution in chloroform was used at a concentration of 0.5 g/L to test if nanoprecipitation is possible or if the chip is immediately clogged. This test also elucidated the problem of the air bubbles inside the mixing stages, leading to aggregation of the material, as illustrated in Figure 5.6. Through preconditioning and the use of a 2-way inline valve, this can be prevented.

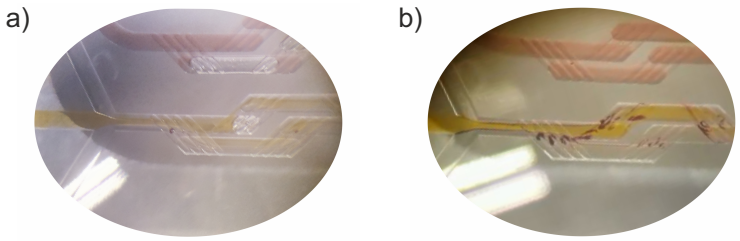

Figure 5.6: Mixing stages of the micromixer chip. a) Through air bubbles inside the mixing stages, mixing is hindered. b) This leads to aggregation inside the channels and branches and disturbs the nanoprecipitation.

To estimate the dependence of the nanoprecipitation on Q and φ_{NS}, a blend of P3HT and the fullerene acceptor ICBA, dissolved in chloroform with an initial concentration of 2 g/L, is chosen. This blend is used to enable the fabrication of solar cells from the nanoparticle dispersion. Varying Q between 1 mL/min and 4 mL/min as well as varying φ_{NS} between 60 % and 83 % produces nanoparticles with sizes between 30 and 46 nm, as summarized in Table 5.1.

Table 5.1: Average nanoparticle size (in nm) of dispersions synthesized inside the micromixer chip, after injecting a P3HT:ICBA/chloroform solution (c_S = 2 g/L) into the nonsolvent ethanol *versus* the nonsolvent volume fraction φ_{NS} and the total flow rate Q. The average of at least three different samples that were measured 10 times each was chosen.

φ_{NS} [vol%]	Q [mL/min]				
	1	1.5	2	3	4
60	46 ± 7.0 [a)]	40 ± 2.4 [a)]	37 ± 2.1 [a)]	31 ± 1.0 [a)]	30 ± 0.5 [a)]
66	38 ± 0.3	35 ± 0.5	33 ± 0.8	32 ± 0.3	30 ± 0.5
75	42 ± 0.3	35 ± 0.8	35 ± 0.8	33 ± 0.4	32 ± 0.6
80	40 ± 0.4	38 ± 0.5	34 ± 0.4	34 ± 0.3	-[c)]
83	-[b)]	40 ± 0.5	35 ± 0.6	35 ± 0.2	-[c)]

[a)] ripening of the nanoparticles over time, due to a too small nonsolvent volume fraction φ_{NS}; [b)] backflow and uncontrolled nanoprecipitation through the low flow rate of the semiconductor solution Q_S; [c)] preconditioning is not possible.

Towards higher Q, a decrease in nanoparticle size can be observed, which is in accordance with an earlier report of Nikoubashman et al., where faster mixing produced smaller nanoparticles for the simulation of polystyrene nanoparticle formation.[155] In contrast, the influence of φ_{NS} on the nanoparticle size is rather small. At either end of the process windows, uncertainties occur.

Typically, for the fabrication of solar cells, higher concentrations of the organic semiconductors are used to form a light-harvesting layer with the target thickness of 180 nm-200 nm.[152, 156, 157] From solution, only a single spincoating step is necessary to deposit the light-harvesting layer. A second deposition on top of the first layer would partially dissolve the layer. For nanoparticles, this is not an issue. As a result of the non-solubility of the polymer in ethanol, no dissolution of the light-harvesting layer occurs, which enables multiple sequential depositions to form a smooth, thick layer. Depending on the concentration of the dispersion, different numbers of deposition steps are needed to form a layer with a target thicknesses. Hence, dispersions with a higher semiconductor concentration are favored because they reduce the number of thin-film deposition steps. This can be achieved by increasing the concentration of P3HT:ICBA in the chloroform solution. Therefore, the nanoprecipitation experiments are repeated with an

increased initial semiconductor concentration of c_S = 5 g/L in chloroform. As a result, the process modification did not only increase the concentration of semiconductors in the dispersion, but also yielded larger nanoparticles, as illustrated in Table 5.2. Also, a higher probability for the clogging of the microfluidic chip was observed. However, with the total flow rate Q of 3 mL/min and a nonsolvent volume fraction φ_{NS} of 75 %, parameters for a stable nanoprecipitation process could be identified.

Table 5.2: Average nanoparticle size (in nm) of dispersions synthesized inside the micromixer chip, after injecting a P3HT:ICBA/chloroform solution (c_S = 5 g/L) into the nonsolvent ethanol *versus* the nonsolvent volume fraction φ_{NS} and the total flow rate Q. The average of at least three different samples that were measured 10 times each was chosen.

φ_{NS} [vol%]	Q [mL/min]		
	2	3	4
66	-[a)]	49 ± 0.5	-[a)]
71	52 ± 1.0	50 ± 0.8	48 ± 0.4
75	54 ± 0.6	51 ± 0.5	50 ± 0.6
78	54 ± 0.5	51 ± 0.5	50 ± 0.5
80	-[a)]	55 ± 0.5	-[b)]

[a)] not investigated; [b)] preconditioning is not possible.

5.2.4 Influence of Illumination

Another parameter towards tailored nanoparticle sizes is the intensity of ambient or artificial light. Through irradiation of the light-harvesting material, the nanoparticle size can be varied, which enhances the colloidal stability for less clogging of the microfluidic channels. Our recent experimental observations suggest that photoexcitation of organic semiconductors during nanoprecipitation increases the electrostatic stability of nanoparticle dispersions on P3HT nanoparticles.[151] By adding a fullerene acceptor such as ICBA, which has a residual solubility in ethanol (chapter 6.1.1), the dissociation of negative photogenerated charges on ICBA and positively charged P3HT inside the nanoparticles is promoted, which enhances the electrostatic stabilization of the dispersion and leads to a smaller average nanoparticle size. For the experiments above, a spotlight LED was used.

In a beaker, the path length of the irradiation throughout the semiconductor/solvent/nonsolvent mixture is several centimeters. Through gradually attenuating, a strong variation of the process parameters within the same process, and hence a strong variation of the nanoparticle size within one batch can occur. In contrast, a precise control of irradiation during nanoprecipitation in

the microfluidic setup is enabled: due to the small channel width of 125 µm, the absorbance is effectively homogeneous throughout the channel and the incoming irradiation prevails through the volume in which the nanoparticles form.

To investigate the effect of irradiance, first, a commercially available RGB-LED strip is used to examine the influence of the three different narrow-band LEDs. The LED strip was wrapped around the microchip to enable homogeneous irradiation. The average nanoparticle size after nanoprecipitation under irradiation with blue, green, red, and white light is shown in Table 5.3, with white light as a combination of blue, green, and red.

Table 5.3: Effect of irradiation of the micromixer chip on the P3HT:ICBA nanoparticle size (Q = 3 mL/min, φ_{NS} = 75 %, c_S = 2 g/L) by a RGB-LED strip.

Light source	white	blue	green	red	dark
Nanoparticle size [nm]	72 ± 0.9	73 ± 0.7	82 ± 0.5	137 ± 6 [a)]	- [b)]

[a)] flocculation over time; [b)] immediate flocculation.

While the dispersion which was irradiated by red light flocculated, the other illuminated dispersions remained stable, as shown in Figure 5.7. In combination with the results from Table 5.3, this suggests that blue light is best suited for irradiation of the microchip and that the intensity of illumination is crucial. Previous experiments (see 5.2.3) have shown that strong irradiation during nanoprecipitation in the microfluidic chip can produce nanoparticles with sizes down to 30 nm.

This effect was further investigated for other light sources. In total darkness, that is, upon wrapping the microchip in aluminum foil, the formation of large aggregates caused the clogging of the chip. After turning off the room light and the fumehood light (0.18 W/m^2, fluorescent lamp), the residual light is already sufficient to achieve nanoparticles with sizes below 100 nm.

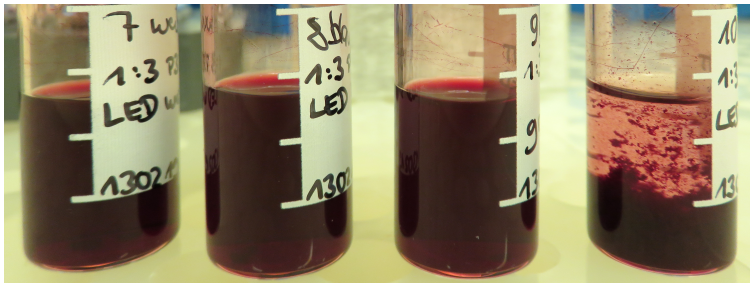

Figure 5.7: Nanoparticle dispersions of P3HT:ICBA (c_S = 2 g/L), with irradiation from a RGB-LED strip during nanoprecipitation. For irradiation with a white (blue plus green plus red), blue, and green LED, the dispersions remained stable, while the irradiation with the red LED led to flocculation of the nanoparticles and separation.

The ambient light of the fumehood and the room light (1.17 W/m^2, fluorescent lamp) resulted in a decrease of the nanoparticle size to 71 nm. The nanoparticle size decreased further to 34 nm by using a very bright spotlight LED.
The effect of stronger irradiation was systematically investigated by mounting a tunable surface-emitting chip-on-board LED (COB-LED, 2.1 cm × 2.1 cm) beneath the micromixer chip. The nanoparticle sizes *versus* concentration of the P3HT:ICBA solution and *versus* irradiance are summarized in Table 5.4.

Table 5.4: Effect of irradiation of the micromixer chip on the P3HT:ICBA nanoparticle size (Q = 3 mL/min, φ_{NS} = 75 %). The emission spectra of the light sources are shown in Figure 5.8. The reported nanoparticle size and the standard deviation are the average of at least three different samples, each of which was measured 10 times individually.

Light source	Irradiance [W/m^2]	d [nm] at c_S = 2 g/L	d [nm] at c_S = 5 g/L	d [nm] at c_S = 10 g/L
Residual light	0.18	96 ± 0.5	102 ± 0.6	127 ± 0.9
Ambient light	1.17	71 ± 0.6	84 ± 0.4	113 ± 1.9
COB-LED at 0.5 A	1,440	31 ± 0.3	53 ± 2.0	95 ± 5.5
COB-LED at 1 A	2,800	29 ± 0.2	47 ± 0.5	70 ± 0.9
COB-LED at 2 A	5,270	30 ± 0.6	45 ± 0.2	69 ± 0.7
COB-LED at 3 A	7,400	33 ± 0.4	46 ± 0.4	64 ± 0.4
Spotlight LED	7,600	34 ± 0.4	52 ± 0.2	84 ± 0.8

The electrical power of the COB-LED at the maximum operation current (3 A) is 100 W. The nanoparticle size converges in the range of 29nm to 33 nm towards stronger irradiance. Higher P3HT:ICBA concentrations in chloroform (c_S = 5 g/L, c_S = 10 g/L) result in larger nanoparticles, but again a reduction and convergence of the nanoparticle size towards stronger irradiation was observed. The reduction of the nanoparticle size under stronger irradiation results from an increase in the number of photogenerated charges, terminating the growth of the nanoparticles at an earlier stage.[86] A saturation of the number of photogenerated charges at the surface of the nanoparticle can be the reason for the convergence of the nanoparticle size towards stronger irradiation. The increase of nanoparticle size towards higher P3HT:ICBA concentrations at constant irradiation is in agreement with previous reports by Millstone et al. on batch-nanoprecipitated neat P3HT nanoparticles and Nikoubashman et al. on simulation of flash nanoprecipitation of polystyrene.[64, 155]

Only for the spotlight, the relation between total irradiance and effect on the nanoparticle size does not fit. While the spotlight shows the highest total irradiance, the use of the COB-LED enables a smaller average nanoparticle size. The reason for this is the irradiated area. While the COB-LED is an area emitter, which irradiated the entire chip homogeneously over an area of 2.1 cm $\times$ 2.1 cm, the spotlight is a point light source and the irradiation differs depending on the position. This leads to a high irradiance for the measurement of the emission spectra, because the area of the detector is smaller than the area of the chip. However, for low concentrations, the spotlight is a sufficient light source.

The emission spectra of the light sources are provided in Figure 5.8. For the COB-LED and the spotlight, they were measured at a distance of 0 cm, which is equivalent to the position of the irradiation in contact with the microchip during nanoprecipitation.

By changing the operation current of the COB-LED, i.e. the brightness, the nanoparticle size can be tailored, as described below (see section 5.4).

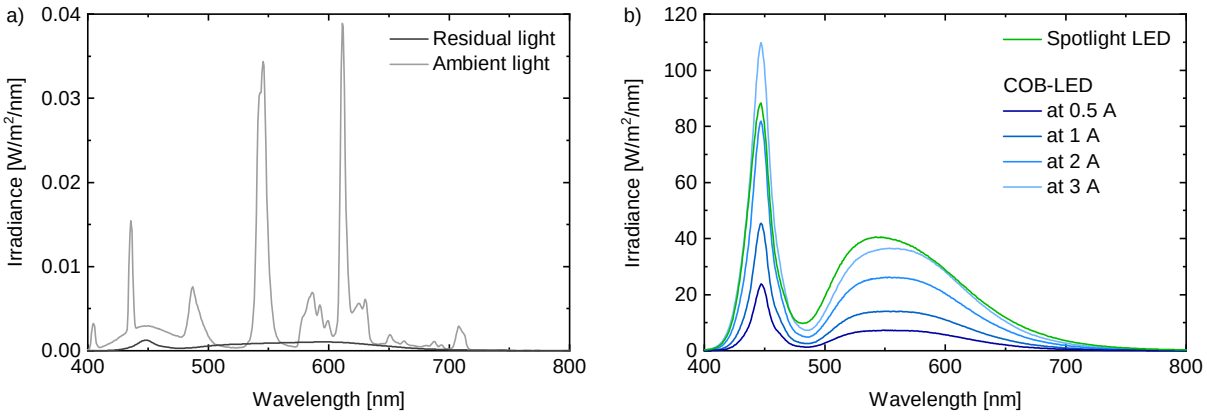

Figure 5.8: Emission spectra of the light sources specified in Table 5.4. a) Residual light: Light after all obvious light sources (fume hood irradiation and the room light) were switched off. Ambient light: Room light and fume hood lighting, but no other notable light sources were switched on. b) Spectra of the spotlight LED and the COB-LED in dependence on the operation current. The microfluidic chip was placed either directly on top of the COB-LED or under the Spotlight LED. Except for the fume hood irradiation, all light sources are based on yellow phosphors integrated into blue LEDs.

5.2.5 Temperature

The temperature can influence the nanoprecipitation in different ways. First of all, the temperature of the solution, as discussed earlier, can influence the nanoprecipitation, mainly through polymer crystallization in the solution. The temperature of the nonsolvent was examined, but did not influence the size of the nanoparticles at all. Presumably, both solution and nonsolvent could cool down while flowing through the thin pipes. The influence of the temperature during nanoprecipitation can be investigated by positioning the chip inside a water bath. The tem-

perature chosen during the reduction of the dispersion determines the speed of the chloroform removal.

The strong effect of illumination on the nanoprecipitation requires steady light sources. Therefore, the white light of the LED strip was used to exclude the influence of illumination from the investigation of heat on the nanoprecipitation. To adjust and maintain the temperature, a water bath in a beaker is used. The LED strip is wound around the beaker to achieve a homogeneous irradiation of the chip from all sides. The chip is placed in the middle of the water bath. After achieving the respective temperature, a hold time of 5 minutes ensures a constant temperature. The position of the chip must be fixed, as slight repositioning of the chip leads to different results. The results of a temperature variation from room temperature (20 °C) to 50 °C in 5 °C steps are summarized in Table 5.5.

Table 5.5: Effect of the temperature on the P3HT:ICBA nanoprecipitation (Q = 3 mL/min, φ_{NS} = 75 %, c_S = 2 g/L). A water bath and a defined irradiation by a LED strip (white light from RGB-LEDs) were used to investigate the effect a change in illumination. To enable comparable results, the chip was fixed in the middle of the water bath through this measurement series.

Temperature	20 °C	22 °C	25 °C	30 °C	35 °C	40 °C	45 °C	50 °C
Nanoparticle	48 nm	48 nm	50 nm	50 nm	51 nm	52 nm	54 nm	54 nm
size	± 0.3	± 0.2	± 0.2	± 0.5	± 0.2	± 0.5	± 0.2	± 0.5

Starting from room temperature, an increase in the water bath temperature leads to a gradual increase in nanoparticle size. Overall, the change in the nanoparticle size of 6 nm is moderate. To further investigate the influence of temperature, in addition to the LED strip, a spotlight LED is used. The spotlight is positioned next to LED-band to enable stronger illumination. To determine whether the water bath is relevant for the nanoprecipitation, as a reference experiment, the setup without water is investigated. By comparing the reference at two different illumination conditions with two nanoprecipitations inside the water bath, the temperature effect is investigated. The results are summarized in Table 5.6 and show that the light influence indeed outshines the temperature influence. When omitting water, the nanoparticle size is smaller, compared to the experiments with water. One reason for this could be the refractive index of water, which changes the light distribution and reduces the amount of incident light on the chip. Because of the influence of the positioning of the chip inside the water bath on the nanoprecipitation, which impedes the reproducibility of the nanoprecipitation, in the following process, the influence of temperature is neglected, while the influence of irradiation is highlighted.

Table 5.6: Effect of the water bath for two temperatures (20 °C and 47 °C) combined with two different light sources on the P3HT:ICBA nanoparticle size (Q = 3 mL/min, φ_{NS} = 75 %, c_S = 2 g/L), compared to results without a water bath. The LED strip provides white light from RGB-LEDs, and the spotlight is used to increase the amount of irradiation on the chip, leading to a smaller average nanoparticle size. To enable comparison of results, the chip was fixed in the middle of the water bath through all nanoprecipitations.

Light source	no water bath	20 °C water bath	47 °C water bath
LED strip	47 nm ± 0.3	49 nm ± 0.5	57 nm ± 0.4
LED strip and spotlight	35 nm ± 0.2	44 nm ± 0.3	48 nm ± 0.5

While the temperature during mixing is of minor importance, during the reduction of the dispersion, it is critical. In batch nanoprecipitation, a water bath temperature of 80 °C is typically used (see 2.3.1). For P3HT dispersion from microfluidics, this is also possible. However, for blends, this leads to material segregation in the dispersions. At first, some fullerenes float on the surface and form floes, as pictured in Figure 5.9 a, and a phase separation starts to occur. By evaporating all of the nonsolvent, a solid layer of nanoparticles, covered by fullerene rich floes, forms, as pictured in Figure 5.9 b.

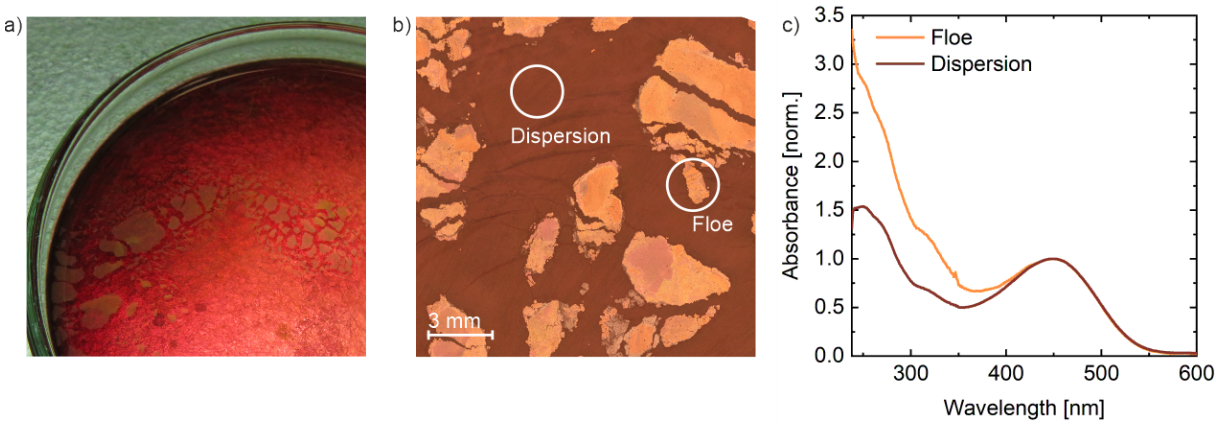

Figure 5.9: Separation of P3HT and ICBA during the reduction step. a) First, material separates from the dispersion and forms floes. b) After evaporating the nonsolvent, the solid layer of floes forms above the dried dispersion. c) Comparison of the absorbance of the dispersion and the dissolved material show that the floes are fullerene-rich.

To determine the material composition, floes and nanoparticles are redissolved in chloroform. Yet, only measuring a floe is not possible, due to the adherence of some dried dispersion underneath the floe. The absorbance measurements of the two solutes in Figure 5.9 c show that the floes are rich in fullerene, while the dried dispersion areas are blended equally. The P3HT to

fullerene ratio of the dried dispersion shows that small amounts of fullerene are missing.
This phase separation of P3HT and ICBA always occurs, due to the residual solubility of ICBA (see 6.1.1). Although it cannot be prevented, the percentage loss can be reduced by increasing the semiconductor concentration. A high temperature during the reduction of the dispersion leads to a fast evaporation of ethanol, but it also increases the speed of the chloroform removal. If the chloroform is removed too fast, the fullerene floats and forms floes. A large surface during reduction, such as the evaporation in a petri dish, can also lead to a fast evaporation of chloroform and again to floating. Therefore, preliminary experiments showed that is best to perform the reduction at moderate temperatures (e.g. 47 °C) inside a beaker and not a petri dish. While this results in a prolonged duration of the reduction, it enables a safe reduction to the initial concentration with only minor material loss.

5.2.6 Semiconductor concentration

The semiconductor concentration can also influence the average nanoparticle size. Therefore, the three concentrations already examined c_S = 2 g/L, 5 g/L and 10 g/L and the concentration of 7 g/L are investigated. For each concentration, two nanoprecipitations were performed. The average nanoparticle sizes are summarized in Table 5.7. By increasing the concentration of

Table 5.7: Influence of the variation of the semiconductor concentration on the nanoparticle size. Four different concentrations were chosen to produce P3HT:ICBA nanoparticles (Q = 3 mL/min, φ_{NS} = 75 %). An increase of the concentration leads to an increase in the nanoparticle size. The spotlight was chosen as the light source.

Concentration (g/L)	2	5	7	10
Nanoparticle size	34 nm ± 0.3	55 nm ± 0.7	68 nm ± 0.5	89 nm ± 0.5

the semiconductor solution, the nanoparticle size increases. An increase of the concentrations is equivalent to an increase in the amount of material for nanoprecipitation. In the theory of nucleation and growth, more material leads to an increased number of nuclei, which grow until they reach colloidal stability. If more material can aggregate, larger particles form, and the growth process of the nanoparticles ends later.
For concentrations above 10 g/L, achieving stable nanoparticle dispersions is challenging and could not be achieved via microfluidics. High semiconductor concentrations such as 10 g/L also lead to clogging of the chip over time, due to the formation of large particles.
Another influencing parameter is the ratio of donor to acceptor. This effect does not differ for beaker nanoprecipitation and microfluidics and it will be discussed in chapter 6. In this chapter, only a ratio of 1:1 by volume is examined.

Résumé

From the investigated parameters above, a flow rate of Q = 3 mL/min at a nonsolvent fraction of φ_{NS} = 75 % appears to be a good compromise for all further experiments. Henceforth, a common spotlight LED with a power of 7,610 W/m^2 provides strong irradiation and was used, if not specified otherwise. For the nanoprecipitation, the microfluidic micromixer chip is chosen, with a preconditioning before synthesis. The solution is freshly prepared for every experiment, with a concentration of 5 g/L for the fabrication of solar cells, and reduced inside a water bath at 47 °C.

5.3 Reproducibility and stability of dispersions

After exploring all principle process parameters (5.2) on the nanoprecipitation and defining a process window for the microfluidic process, two questions remained: "How reproducible is this process?" and "What is the long-term stability of the dispersions?"

5.3.1 Reproducibility

For using the microfluidic setup, the chosen material has to form nanoparticles and the quality of the dispersion must not differ during each run and for all syntheses. To investigate whether the quality during one continuous flow nanoprecipitation process (here: run) is stable, the maximum amount of solution and nonsolvent that can be used for the nanoprecipitation is chosen. The chosen syringes (maximum load: 10 mL) limit the amount of nonsolvent that can be used. To achieve a dispersion with more than 3 mL solution (for φ_{NS} of 75%, 9 mL ethanol and 3 mL solution can be used), φ_{NS} is changed to 66 % (with 6 mL solution and 9 mL ethanol). To collect sufficient amounts of dispersion, after each milliliter of solution, a fresh beaker is used. This results in a maximum of six dispersions per run. Each dispersion is measured three times in eight measurements runs. The data of two different solutions of P3HT:ICBA (blended 1:1 by weight, with c_S = 2 g/L) are summarized in Table 5.8 for two different illumination conditions. With the overall variation in the average particle size differing less than 2 nm, the six collected dispersions per run can be considered equal. Therefore, the stability of the nanoparticle size is excellent when using the continuous-flow nanoprecipitation. The production of larger quantities of dispersion is particularly relevant for the fabrication of solar cells. However, while the difference between run 1 and run 2 seems negligible, notably, run 1 and run 2 slightly differ in the choice of light source, leading to the difference in nanoparticle size.
To examine the reproducibility across different nanoprecipitations, several nanoprecipitations are performed under similar conditions using four different concentrations. The results are

Table 5.8: Nanoparticle size after continuous flow nanoprecipitation (Q = 3 mL/min, φ_{NS} = 66 %, c_S = 2 g/L), for two different runs. After each mL of solution, a fresh beaker was chosen to collect the dispersion. The six dispersions were measured by DLS and the average nanoparticle size was calculated. With a deviation of less than 2 nm, the dispersion can be considered equal across the run. For run 1 and 2, two different light sources were chosen.

Run	1	2	3	4	5	6	average
Run 1	56 nm	54 nm	57 nm	57 nm	56 nm	55 nm	56 nm
	± 0.2	± 0.3	± 0.1	± 0.2	± 0.4	± 0.6	± 1.2
Run 2	61 nm	59 nm	58 nm	58 nm	60 nm	59 nm	59 nm
	± 0.5	± 0.2	± 0.6	± 0.8	± 0.2	± 0.2	± 1.2

summarized in Figure 5.10 a. By using c_S of 2 g/L, 7 g/L and 10 g/L, 14 different dispersions are examined, while 22 different dispersions are examined at c_S with 5 g/L. The data points of the measured nanoparticle sizes at different concentrations show a narrow distribution, which indicates a reproducible process.

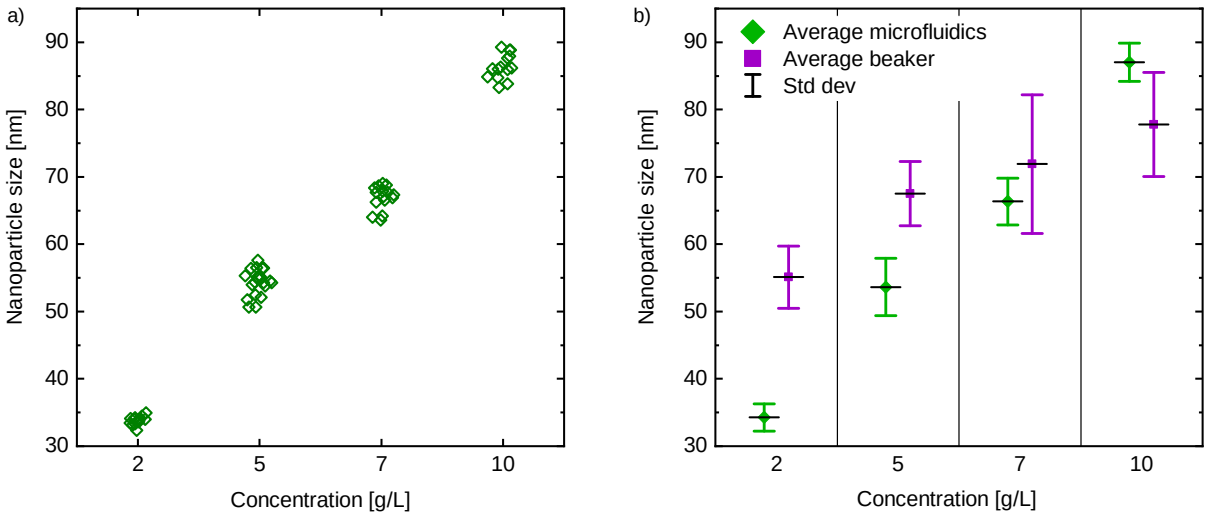

Figure 5.10: Nanoparticle sizes of dispersions at two different semiconductor concentrations for several individual nanoprecipitations. a) Fabricated via microfluidics (Q = 3 mL/min, φ_{NS} = 75 %), the measured nanoparticle sizes of the different dispersions and concentrations show a narrow distribution. By using c_S of 2 g/L, 7 g/L and 10 g/L, the results of 14 different dispersions are shown, while 22 different dispersions are examined for c_S with 5 g/L. b) To compare the nanoprecipitaion via microfluidics to the batch nanoprecipitation, on six different days, dispersions with all respective concentrations were fabricated. From the measured nanoparticle sizes, an average size with a standard deviation was calculated, with the results from microfluidics marked in green and from beaker nanoprecipitation in violet. The comparison shows that dispersions from microfluidics are more reproducible, as seen by the smaller standard deviation.

To evaluate whether the reproducibility is significant, on six different days, six dispersions are synthesized via microfluidics and beaker nanoprecipitations at four different concentrations. Each solution of P3HT and ICBA is freshly prepared. Each concentration contains the same semiconducting solution, diluted in different bottles to achieve the respective concentration. This ensures that concentration fluctuations occur in both nanoprecipitation processes. The average nanoparticle size at each parameter is calculated, as depicted in Figure 5.10 b. The size distribution for the nanoparticle dispersion from microfluidics shows a narrower standard deviation than the size distribution from the beaker nanoprecipitation, which is equivalent to a smaller nanoparticle size variation and therefore a higher reproducibility. In contrast, mostly at higher concentrations, the beaker nanoprecipitations lead to a nanoparticle size variance of almost 20 nm. The largest difference in nanoparticle size per concentration occurs for 2 g/L, with more than 10 nm difference between the largest nanoparticle size from microfluidics and the smallest nanoparticle size from beaker nanoprecipitation. Except for the highest concentration, the nanoparticle dispersions from microfluidics show smaller average nanoparticle sizes compared to the results from the beaker nanoprecipitation.
As a result of the high volume during nanoprecipitation inside a beaker, the overall influence of the light is reduced. However, increasing the concentration has a negligible effect on the transparency of the dispersion inside the beaker. For microfluidics, a higher concentration results in a distinct opacity of the channels through the dispersion. Therefore, the light influence is crucial and is reduced at higher concentrations.

5.3.2 Stability

After the reproducible synthesis of nanoparticle dispersions, the dispersions have to be stored, requiring temporal stability. The storage can influence this stability and lead to flocculation. In our lab, three different bottles can be chosen for storage, one HDPE plastic bottle and two glass bottles (transparent and brown glass). To compare the storage in all three bottles, large volumes of dispersion were fabricated by microfluidic nanoprecipitation, reduced and measured by DLS. To exclude influences from the nanoparticle size, two different concentrations are chosen. The lower concentration of c_D = 2 g/L produces an average nanoparticle size of 37 nm, while the higher concentration of c_D = 7 g/L produces an average nanoparticle size of 60 nm. Both nanoparticle sizes are measured after the reduction step and are in accordance with the size directly after nanoprecipitation. An equal amount of dispersion is stored in each bottle, and an aliquot is measured weekly for the next five weeks. A flocculated dispersion was not measured; a dispersion with an average nanoparticle size larger than 150 nm was considered flocculated. The results are summarized in Figure 5.11. Depending on the chosen storage bot-

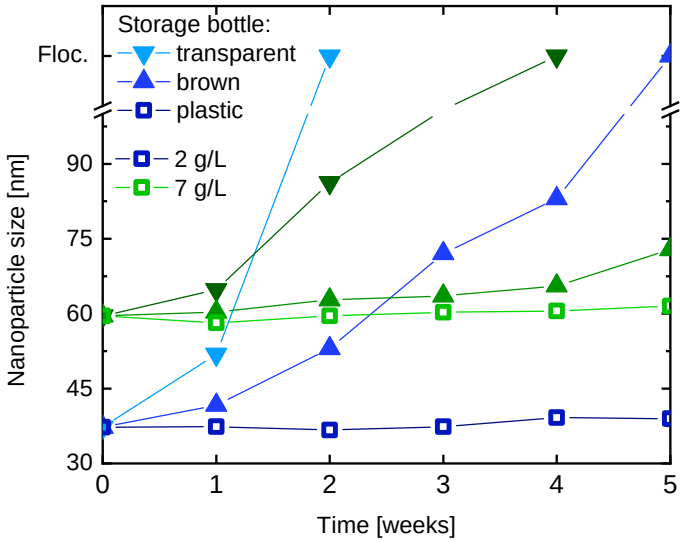

Figure 5.11: Nanoparticle size over weeks of two dispersions with different concentrations, stored in different bottles. In blue, a dispersion of c_D = 2 g/L with an initial particle size of 37 nm after reduction and in green, a dispersion of c_D = 7 g/L with an initial particle size of 60 nm after reduction are shown. While the dispersions stored in transparent glass bottles flocculated after a few days, the nanoparticle size of dispersions stored in brown glass bottles grew slower, but also flocculated eventually. Only the dispersions stored in plastic bottles, illustrated by hollow rectangles, remained stable. The individual measurement points were connected with a line to guide the eye.

tle, the stability of the dispersion over several weeks varies. While the dispersions stored in plastic bottles remain stable at both concentrations for more than five weeks, the dispersions stored in transparent glass bottles flocculate at both concentrations. The storage in brown glass bottles leads to flocculation of the lower concentrated dispersion, whereas the nanoparticles of the higher concentrated dispersion only grew a few nanometers. Eventually, also the dispersions with high concentrations that are stored in the brown glass bottle flocculate. Brown glass bottles are typically used to protect the solution from light, while transparent glass bottles enable illumination of the content. Plastic bottles are opaque and reduce illumination, but do not prevent all light from reaching into the dispersion. However, the samples are stored in the dark, which should exclude any effects arising from illumination. To ensure that illumination does not lead to aggregation, the transparent glass bottle is further wrapped up in aluminum foil. This, however, promoted the flocculation of the dispersion. The influencing parameters could be production residues that remain inside the bottle or an ion exchange between the glass and the dispersion. Both could enable aggregation and thus flocculation. Precleaning of the glass bottles with ethanol or 2-propanol increases the lifetime of the dispersion. Hence, in the following, dispersions are only stored in plastic bottles and glass bottles are excluded.

After showing that dispersions stored inside plastic bottles remain stable and do not agglomerate for at least a few weeks, long-term stability measurements are conducted, as summarized in

Figure 5.12. For more than half a year, the average size of seven dispersions synthesized by microfluidics with a concentration of 5 g/L are measured weekly, using DLS. For the measurement of the nanoparticle size of diluted dispersions, an aliquot is taken from the stock solution, while the dispersion is stored in a cabinet in the dark. The resulting nanoparticle dispersions are remarkably stable. Over weeks, only minor variations between the different dispersions and measurements occurred. These nanoparticle dispersions synthesized by microfluidics maintained their nanoparticle size even after one year and demonstrated excellent long-term stability.

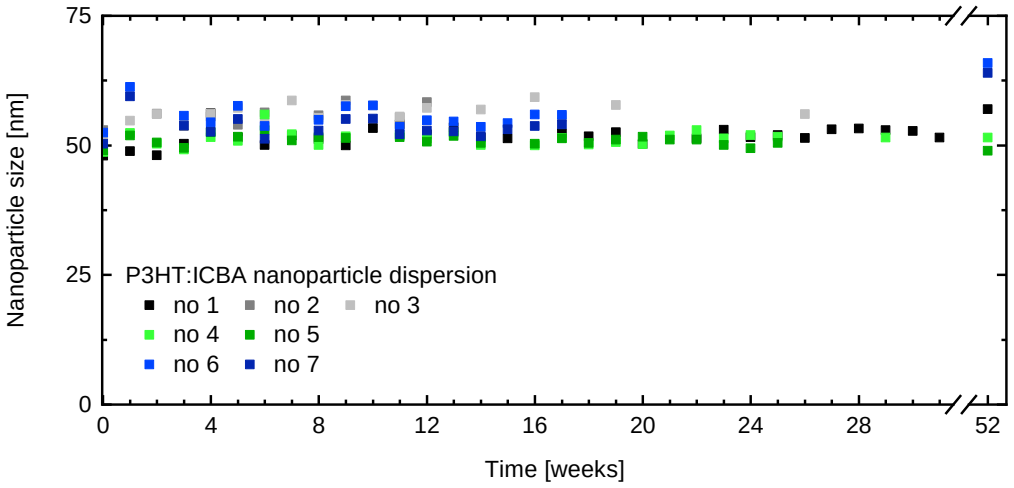

Figure 5.12: Shelf-stability of nanoparticle dispersions. The nanoparticle sizes of 7 dispersions (c_D = 5 g/L) fabricated by microfluidics are monitored over one year. By taking aliquots from stock solutions, the size measurements are conducted. In the second half of the experiment, only selected dispersions are measured due to small residual amounts of stock solution. None of the dispersions showed any signs of sedimentation or nanoparticle aggregation. Only two dispersions exhibit slightly increased nanoparticle sizes after one year. This figure was published in [147].

Résumé

Using the parameters from section 5.2, nanoparticle dispersions with very reproducible results could be synthesized. The nanoparticle size distributions in dispersions, synthesized inside the micromixer chip under continuous-flow conditions, exhibit smaller sizes with a narrower standard deviation, compared to beaker nanoprecipitation under otherwise identical conditions. The resulting nanoparticle dispersions are remarkably stable, with a nanoparticle size that persists at least one year, demonstrating the excellent long-term stability of the nanoparticle dispersions from microfluidics.

5.4 Solar cell performance

By adjusting all the parameters that influence the nanoprecipitation in microfluidic processes, nanoparticle dispersions with a high shelf-stability were synthesized. This process enables high reproducibility and excellent scalability. In this chapter, the influence of the distinct properties of nanoparticle dispersions on the processing and the performance of solar cells is investigated.

5.4.1 Layer Formation

To investigate the suitability of the dispersions for the formation of light-harvesting layers, nanoparticulate P3HT:ICBA layers are fabricated by spin casting the dispersion onto glass substrates. Using AFM, the topography of the layers and the nanoparticle distribution can be analyzed (AFM, see 4.2.1). In Figure 5.13, the topography of the as-cast layers of dispersions

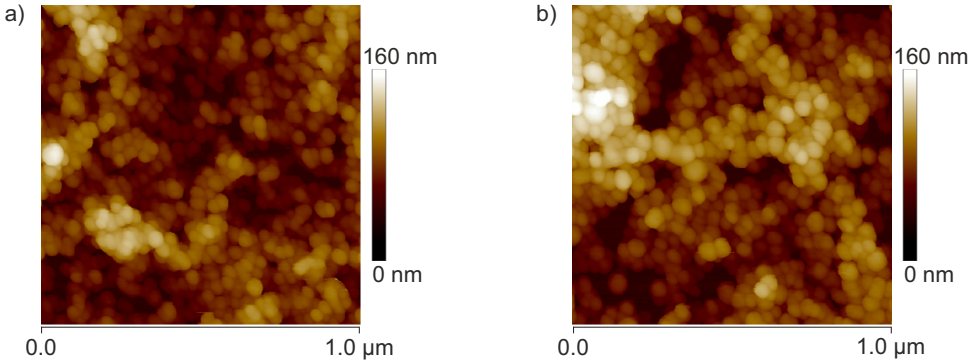

Figure 5.13: AFM topography of nanoparticulate layers, deposited from a dispersion with a concentration of a) c_D = 2 g/L and b) c_D = 5 g/L. The layers were spin cast (one spincoating step, no multiple depositions), afterwards, the layers were not annealed. Both layers show a homogeneous distribution of nanoparticles on the glass substrate. The nanoparticles appear uniform in size and shape. The average nanoparticle size is in accordance with the DLS measurements. In both images, voids are visible, which indicates that further deposition steps and thermal annealing are required to form closed layers.

with c_D = 2 g/L or c_D = 5 g/L (synthesized from semiconductor solutions with c_S = 2 g/L or c_S = 5 g/L, respectively) are shown. The two dispersions had an average nanoparticle size of 35 nm and 55 nm (measured by DLS), respectively. The results of the AFM measurement are in accordance with those of the DLS measurement. Notably, the nanoparticles within either layer appear uniform in size and shape. Spin casting the dispersion one time on the glass substrate results in a layer with voids and does not enable closed layers. Therefore, repeated deposition by spin coating and thermal annealing are vital, requiring further considerations.[55] First, the number of spincoating steps that are necessary to achieve a closed layer needs to be determined. Second, the influence of the nanoparticle size on the unity and thickness of the layer has to be examined.

The influence of the nanoparticle size on the formation of the layer can be determined by changing two process parameters. First, the change in the concentration of the semiconductor solution directly influences the nanoparticle size. Second, the chosen light source affects the nanoparticle size. Preliminary tests showed that solar cells from dispersions with low concentration lead to a reduced parallel resistance and deteriorate the solar cell performance. Dispersions with high concentrations lead to thick layers and hamper the investigation of the influence of the layer thickness due to the missing adjustability. Therefore, varying the concentration is not an option.
The influence of illumination, as outlined above, affects the nanoparticle size at a fixed concentration. For a medium concentration of c_D = 5 g/L, typically, the nanoparticle size ranges between 45 nm and 100 nm. The tunable COB-LED is chosen as light source to ensure that only the irradiance and not the spectrum influences the nanoprecipitation. By varying the current between 10 mA and 1 A, reproducible nanoparticle sizes between 80 nm and 50 nm can be achieved. Lower currents lead to flickering of the LED, whereas higher currents lead to a heating of the chip during nanoprecipitation, both of which cause irreproducible results. Therefore, the two limiting currents (10 mA and 1 A) are chosen for further investigation, resulting in two different dispersions with nanoparticle sizes of either 50 nm or 80 nm. In the following section, these dispersions are referred to as 50-nm-dispersion and 80-nm-dispersion.
With these dispersions, solar cells with inverted architecture are fabricated, as described in chapter 4.3, with ZnO as ETL and PEDOT:PSS as HTL. By applying the dispersion multiple times, different layer thicknesses can be achieved. Between 2 and 25 deposition steps are applied for both dispersions. The solar cell results of the 50-nm-dispersion and the 80-nm-dispersion are summarized in Table 5.9 and in Table 5.10, respectively.
Each layer thickness entry represents at least three substrates that are fabricated in different batches, i.e., 12 individual solar cells. The layer thickness is measured with a tactile profiler (see 4.2.2). Due to the uncertainty of measurement, the light-harvesting layer thickness is rounded to five nanometers. Depending on the concentration of the dispersion, which slightly varied between the different nanoprecipitations, a tailored light-harvesting layer thickness is achieved. The *J*-*V* curves of solar cells with three different layer thicknesses are illustrated in Figure 5.14.

While layers with a thickness above 130 nm lead to deterioration of the solar cell performance, all solar cells with light-harvesting layer thicknesses below 40 nm were shorted, which was likely caused by an insufficient coverage of the sample. Using four deposition steps and a light-harvesting layer thickness of 50 nm, a PCE of 4 % could be achieved. In general, FF and J_{SC} are governed by the absorption of photons, the generation of charge carriers, and the competition between extraction and recombination of free charge carriers.[158, 159] Due to the higher ab-

Table 5.9: Key parameters of the nanoparticulate solar cells fabricated from the 50-nm-dispersion (c_D = 5 g/L) *versus* the light-harvesting layer thickness *t*, at an annealing temperature of 150 °C.

t [nm]	V_{OC} [mV]	J_{SC} [mA/cm²]	FF [%]	PCE [%]
40	850 ± 1	6.4 ± 0.1	57 ± 1	3.1 ± 0.1
50	848 ± 1	7.5 ± 0.1	62 ± 1	4.0 ± 0.1
60	844 ± 1	7.3 ± 0.1	61 ± 1	3.8 ± 0.1
70	845 ± 1	7.2 ± 0.1	60 ± 1	3.7 ± 0.1
80	842 ± 1	7.2 ± 0.1	59 ± 1	3.6 ± 0.1
90	835 ± 1	7.4 ± 0.1	57 ± 1	3.5 ± 0.1
115	843 ± 1	7.8 ± 0.1	52 ± 1	3.4 ± 0.1
160	835 ± 2	7.3 ± 0.1	43 ± 1	2.6 ± 0.1
190	834 ± 1	5.9 ± 0.1	42 ± 1	2.2 ± 0.1
270	770 ± 1	4.1 ± 0.1	37 ± 1	1.2 ± 0.1

Table 5.10: Key parameters of the nanoparticulate solar cells fabricated from the 80-nm-dispersion (c_D = 5 g/L) *versus* the light-harvesting layer thickness *t*, at an annealing temperature of 150 °C.

t [nm]	V_{OC} [mV]	J_{SC} [mA/cm²]	FF [%]	PCE [%]
50	854 ± 3	7.4 ± 0.2	63 ± 1	4.0 ± 0.1
70	850 ± 2	7.2 ± 0.1	61 ± 1	3.7 ± 0.1
80	848 ± 4	7.0 ± 0.1	59 ± 1	3.5 ± 0.1
90	846 ± 2	7.2 ± 0.1	56 ± 1	3.4 ± 0.1
110	845 ± 3	7.7 ± 0.1	52 ± 1	3.3 ± 0.1
130	852 ± 1	8.3 ± 0.1	48 ± 1	3.4 ± 0.1
150	846 ± 3	8.0 ± 0.1	44 ± 1	3.0 ± 0.1
180	840 ± 1	6.8 ± 0.1	43 ± 1	2.4 ± 0.1

sorbance in a thicker layer, more charge carriers are generated and can be extracted. This results in an increase in J_{SC}. However, as a consequence of a nonideal morphology, charge carriers can recombine before reaching the electrodes. This reduces the FF and can also decrease J_{SC}, as summarized in Figure 5.14.

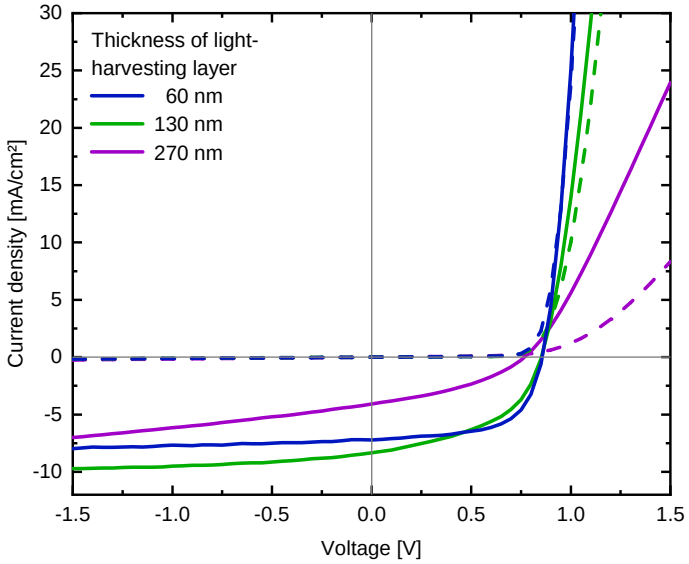

Figure 5.14: *J-V* curve of three solar cells with different light-harvesting layer thicknesses. The *J-V* curve of the solar cell with a light-harvesting layer thickness of 60 nm in blue resembles the curve of an ideal diode. At a layer thickness of 130 nm, as shown in green, the MPP shifts, due to the increased J_{SC} and the FF decreases through losses. The layer with a thickness of 270 nm in violet shows the decrease of J_{SC} through further losses and the typical tilting of the *J-V* curve through a decrease of R_P and an increase of R_S.

5.4.2 Annealing temperature

Earlier literature reported that the annealing temperature can also influence the performance of solar cells. Gärtner et al. suggested annealing temperatures between 150 °C and 180 °C in order to join the nanoparticles for best charge carrier transport.[8, 152] To check whether the optimum of the annealing temperature depends on the nanoparticle size, temperatures between 100 °C and 180 °C were investigated at a constant annealing time of 10 minutes. In Table 5.11,

Table 5.11: Key parameters of the nanoparticulate solar cells fabricated from the 50-nm-dispersion (c_D = 5 g/L) *versus* annealing temperature T_{Ann}, with a light-harvesting layer thickness of 60 nm.

T_{Ann} [°C]	V_{OC} [mV]	J_{SC} [mA/cm^2]	FF [%]	PCE [%]
100 [a)]	-	-	-	-
120 [a)]	-	-	-	-
150	851 ± 1	7.2 ± 0.1	60 ± 1	3.8 ± 0.1
160	854 ± 1	6.8 ± 0.1	60 ± 1	3.5 ± 0.1
170	861 ± 1	6.6 ± 0.1	60 ± 1	3.4 ± 0.1
180	869 ± 2	6.3 ± 0.1	60 ± 1	3.3 ± 0.1

[a)] Not measurable

the solar cell parameters for the 50-nm-dispersion are summarized for a light-harvesting layer thickness of 60 nm.

At low annealing temperatures of 100 °C and 120 °C, the solar cells are shorted. Under the microscope, as pictured in Figure 5.15 a-b, cracks and some delamination are visible. A sample with an optimal annealing temperature of 150 °C shows a smooth layer without cracks, as depicted in Figure 5.15 c.

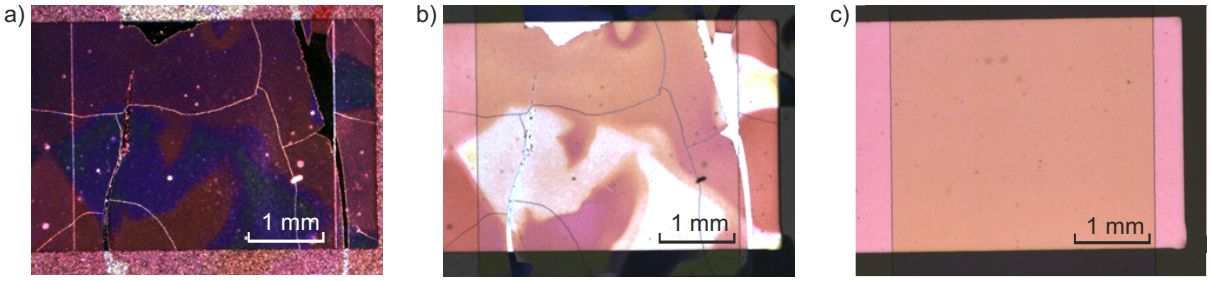

Figure 5.15: Microscope images of solar cells with a light-harvesting layer thickness of 60 nm, fabricated by multiple deposition of a nanoparticle dispersion, at different annealing temperatures. a) In the ringlight mode, at T_{Ann} = 100 °C, the layers show cracks and delamination. b) In coaxial brightlight mode, the same layer as shown in a) shows a high color contrast, implying that the layer is uneven and that some parts are delaminated. c) A smooth, homogeneous layer in coaxial brightlight mode does not show any cracks.

These cracks may be the result of a partially closed light-harvesting layer. Usually, the light-harvesting layer acts as a barrier between the acidic HTL PEDOT:PSS and the acid-sensitive ETL ZnO. For the as-cast layers of nanoparticle dispersion, the distribution of the nanoparticles on the glass substrate is visible, as shown in Figure 5.16 a. By thermal annealing of the layers at moderate temperatures of 100 °C or 120 °C, the nanoparticles start to coalesce, which leads to a smoothing of the layer. The voids start to fill, but the nanoparticle structure is still noticeable, as shown in Figure 5.16 b-c. By increasing T_{Ann} further, larger domains form and further smoothing of the layers leads to a decrease in the roughness of the layer, as illustrated in Figure 5.16 d-f. Very smooth layers are achieved at T_{Ann} of 180 °C, as shown in Figure 5.17 b. For solar cells, coalescence of the nanoparticles and smoothing of the layer are crucial. As the voids between the nanoparticles are closed, which reduces shorts, the nanoparticles are no longer separated. Thus, generated excitons cannot be trapped within particles, which reduces recombination losses and leads to an increase of J_{SC}, as shown in Table 5.11 for T_{Ann} = 150 °C. Preliminary tests showed that annealing temperatures below 150 °C result in solar cells with a decreased J_{SC} in the best case and shorted solar cells in the worst case. When the temperature is increased further, J_{SC} is reduced, indicating that the transport of the charge carriers is compromised, which may be attributed to a domain separation of ICBA and P3HT, which disrupts

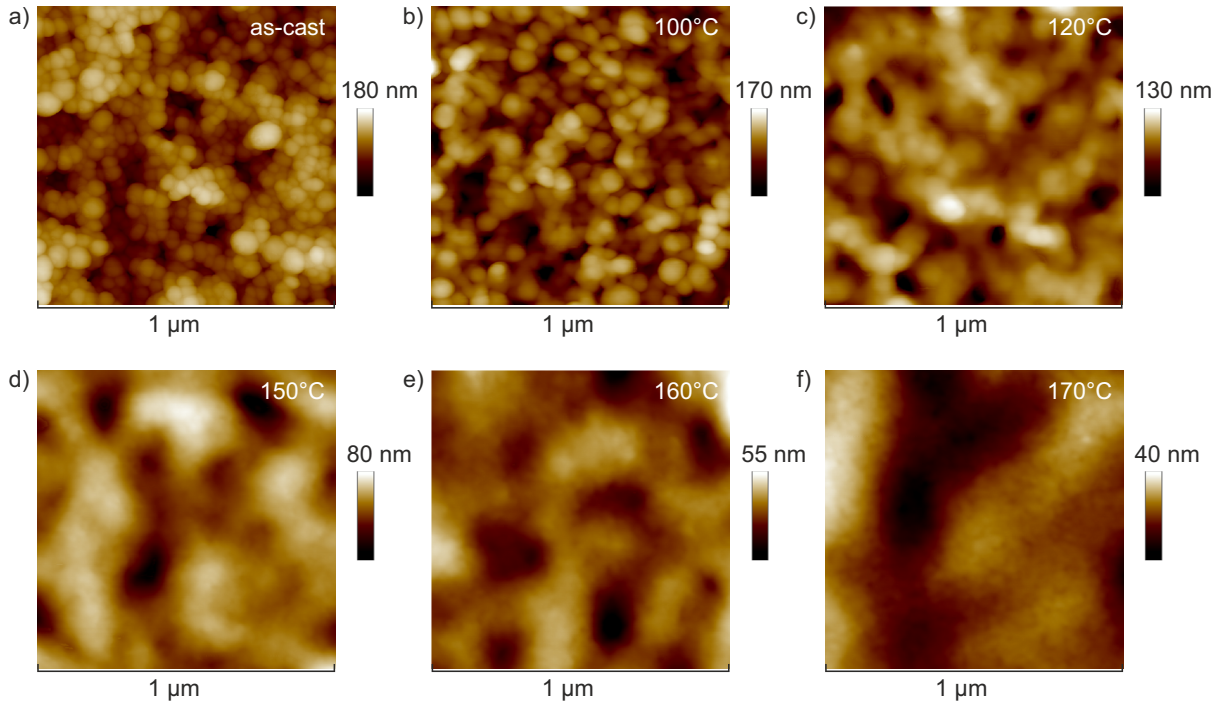

Figure 5.16: AFM measurements of the topography of P3HT:ICBA nanoparticulate layers on glass substrate at different annealing temperatures. Multiple deposition steps are used for the layer formation. a) For the as-cast sample, the nanoparticles are clearly visible and evenly distributed on the glass sample. The topography of the nanoparticles shows that there are still some voids. b) At T_{Ann} = 100 °C, the nanoparticles start to coalescent and the shape starts to blur. c) Increasing the temperature from 120 °C to d) 150 °C leads to a smoothing of the layer, while voids are not visible anymore. e) At 160 °C, the layer flattens further, until d) a roughness of the layer of 40 nm is reached at 170 °C.

the continuous paths of the charge carriers.[160, 161] This separation cannot be determined by AFM, because the material contrast between P3HT and ICBA is too low.

By increasing the annealing temperature to 180 °C, very smooth layers with a roughness of 15 nm, as illustrated in Figure 5.17 b, are achieved. However, with increasing annealing temperatures, solar cell efficiencies decreased, following significant decreases in J_{SC}, while the V_{OC} increased slightly.

The same effect is observed on solar cells with a light-harvesting layer deposited from the 80-nm-dispersion: By increasing the annealing temperature from 150 °C to 180 °C, the V_{OC} slightly increases by 20 mV, while the J_{SC} decreases by 0.5 mA/cm^2, reducing the efficiency. The annealed layers in Figure 5.17 c-d show the same smoothing as described above. By increasing the annealing time from the commonly chosen 10 minutes to 30 minutes, the solar cell performance does not change, as summarized in Table 5.12. This is an important result, because it indicates that minor annealing time changes, for example, by temperature fluctuations of the hot plate, do not influence the solar cell performance.

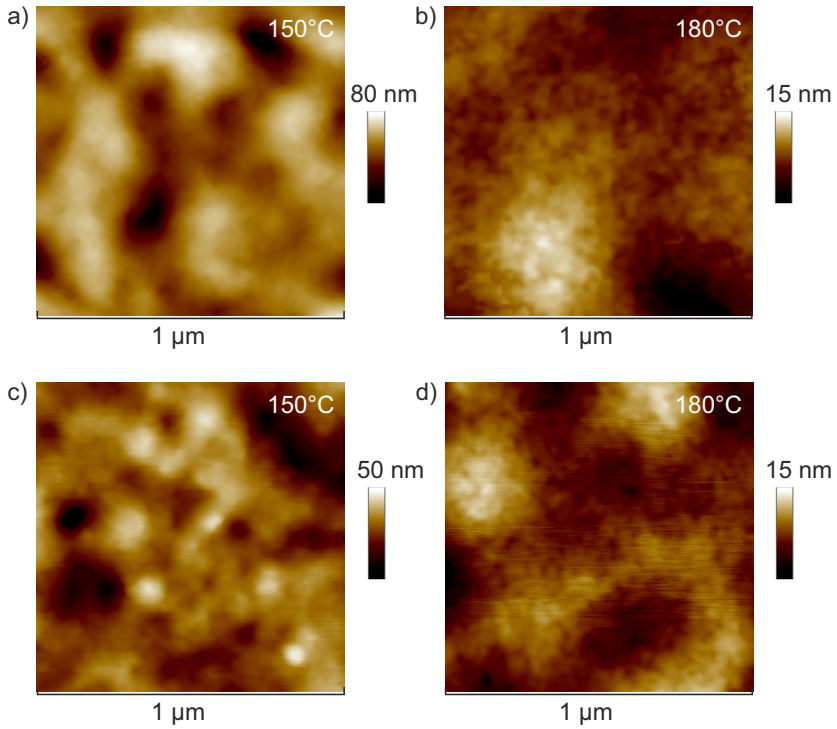

Figure 5.17: AFM topography of nanoparticulate layers deposited from a P3HT:ICBA dispersion with an average nanoparticle size of a-b) 50 nm or c-d) 80 nm (Q = 3 mL/min, φ_{NS} = 75 %, c_D = 5 g/L) on glass substrates. By increasing the annealing temperature from 150 °C (a,c) to 180 °C (b,d), the roughness decreases and smooth layers form.

Table 5.12: Key parameters of the nanoparticulate solar cells fabricated from dispersion (c_D = 5 g/L) with an average nanoparticle size of 80 nm *versus* the annealing temperature T_{Ann} and the annealing time τ_{Ann}, with a light-harvesting layer thickness of 60 nm.

T_{Ann} [°C]	τ_{Ann} [min]	V_{OC} [mV]	J_{SC} [mA/cm^2]	FF [%]	PCE [%]
150	10	848 ± 3	7.3 ± 0.1	61 ± 1	3.8 ± 0.1
150	30	847 ± 1	7.3 ± 0.1	61 ± 1	3.8 ± 0.1
180	10	867 ± 3	6.7 ± 0.1	62 ± 1	3.6 ± 0.1
180	30	862 ± 3	6.8 ± 0.1	62 ± 1	3.6 ± 0.1

5.4.3 Solar cells: Microfluidics vs. Beaker nanoprecipitation

With the optimal light-harvesting layer thickness determined, the results of the solar cells are compared to solar cells with a light-harvesting layer deposited from dispersions, synthesized by beaker nanoprecipitation, also referred to as batch processing. Therefore, both nanoprecipitation processes are tailored to yield nanoparticles of similar size (microfluidics: 52 nm, batch nanoprecipitation: 58 nm) at a total concentration of 5 g/L. By varying the number of

deposition steps, the thickness of the light-harvesting layer is again adjusted for optimal device performance. To form smooth, closed layers, the samples are thermally annealed after layer deposition at 150 °C for 10 minutes. The *J*-*V* curves of the respective 'hero devices' are depicted in Figure 5.18, with light-harvesting layers deposited from dispersions that are synthesized by either batch processing or in the microfluidic system at a concentration of (5 g/L) and with light-harvesting layer thicknesses of 50 nm, both showing a PCE of about 4 %.

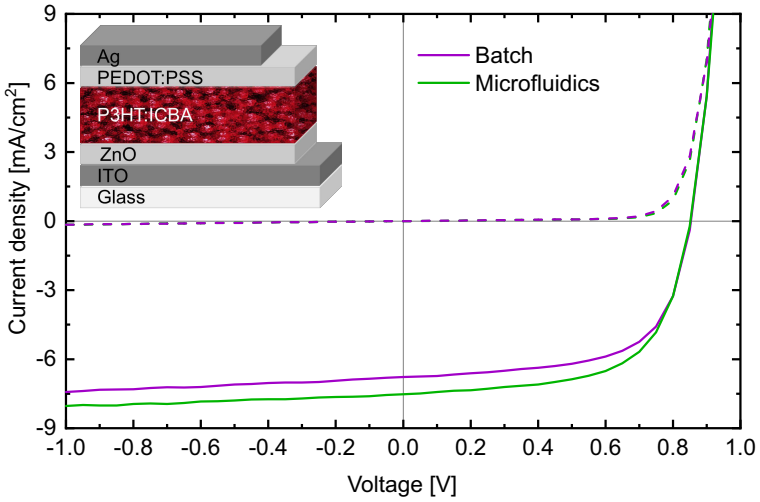

Figure 5.18: *J*-*V* curve of the two 'hero' nanoparticulate solar cells, with light-harvesting layers deposited from dispersions that were fabricated either by batch processing (violet) or in the microfluidic system (green) at a concentration of c_D = 5 g/L and with a light-harvesting layer thicknesses of 50 nm, both showing PCEs of about 4 %.

The key parameters of solar cells with nanoparticulate light-harvesting layers from nanoparticle dispersions from microfluidics or beaker nanoprecipitation are summarized in Table 5.13 and Table 5.14, respectively.

Both Tables 5.13 and 5.14 show the same trend of the changing solar cell key parameters, as already discussed in Table 5.9. By increasing the light-harvesting layer thickness, the absorbance and thus J_{SC} increases, while both V_{OC} and FF decrease, resulting in an overall decrease of PCE. Above a layer thickness of 130 nm, J_{SC} decreases.

To optically compare the two different nanoparticle fabrication routes, the four solar cell characteristics are plotted in separate graphs, as shown in Figure 5.19 *versus* the light-harvesting layer thickness.

As shown above, the solar cells with thin light-harvesting layers exhibit the highest efficiencies, due to their high FF. By increasing the thickness of the light-harvesting layer, both V_{OC} and FF are reduced, while J_{SC} increases in the lower thickness regime and then decreases towards higher thicknesses, indicating higher losses due to recombination. In particular, because of

Table 5.13: Key parameters of the nanoparticulate solar cells fabricated from dispersion (c_D = 5 g/L) *versus* the number of deposition steps (#depositions) and the corresponding thickness of the light-harvesting layer *t*. The dispersion was synthesized via continuous-flow nanoprecipitation.

#depositions	*t* [nm]	V_{OC} [mV]	J_{SC} [mA/cm]	FF [%]	PCE [%]
4	50	849 ± 1	7.6 ± 0.1	62 ± 1	4.0 ± 0.1
5	65	856 ± 1	7.2 ± 0.1	61 ± 1	3.8 ± 0.1
6	80	843 ± 9	7.1 ± 0.1	59 ± 1	3.6 ± 0.1
7	90	836 ± 8	7.3 ± 0.1	57 ± 1	3.5 ± 0.1
8	110	844 ± 3	7.7 ± 0.1	52 ± 1	3.4 ± 0.1
10	130	852 ± 1	8.2 ± 0.1	47 ± 1	3.3 ± 0.1
12	155	848 ± 1	7.9 ± 0.1	45 ± 1	3.0 ± 0.1
15	185	836 ± 4	6.9 ± 0.1	43 ± 1	2.5 ± 0.1
17	200	827 ± 1	5.8 ± 0.1	42 ± 1	2.0 ± 0.1

Table 5.14: Key parameters of the nanoparticulate solar cells fabricated from dispersion (c_D = 5 g/L) *versus* the number of deposition steps (#depositions) and the corresponding thickness of the light-harvesting layer *t*. The dispersion was synthesized by batch nanoprecipitation.

#depositions	*t* [nm]	V_{OC} [mV]	J_{SC} [mA/cm]	FF [%]	PCE [%]
3	50	854 ± 2	6.8 ± 0.1	63 ± 1	3.6 ± 0.1
4	70	852 ± 1	7.0 ± 0.1	62 ± 1	3.7 ± 0.1
5	85	848 ± 1	7.1 ± 0.1	59 ± 1	3.5 ± 0.1
6	105	844 ± 1	7.4 ± 0.1	55 ± 1	3.4 ± 0.1
7	120	842 ± 1	7.8 ± 0.1	50 ± 1	3.3 ± 0.1
8	135	839 ± 1	7.8 ± 0.1	46 ± 1	3.0 ± 0.1
10	170	832 ± 1	7.0 ± 0.1	44 ± 1	2.6 ± 0.1
12	200	825 ± 1	6.1 ± 0.2	43 ± 1	2.2 ± 0.1

the higher J_{SC}, solar cells from microfluidic nanoparticle dispersions exhibit slightly better performance than solar cells from batch-processed nanoparticle dispersions.

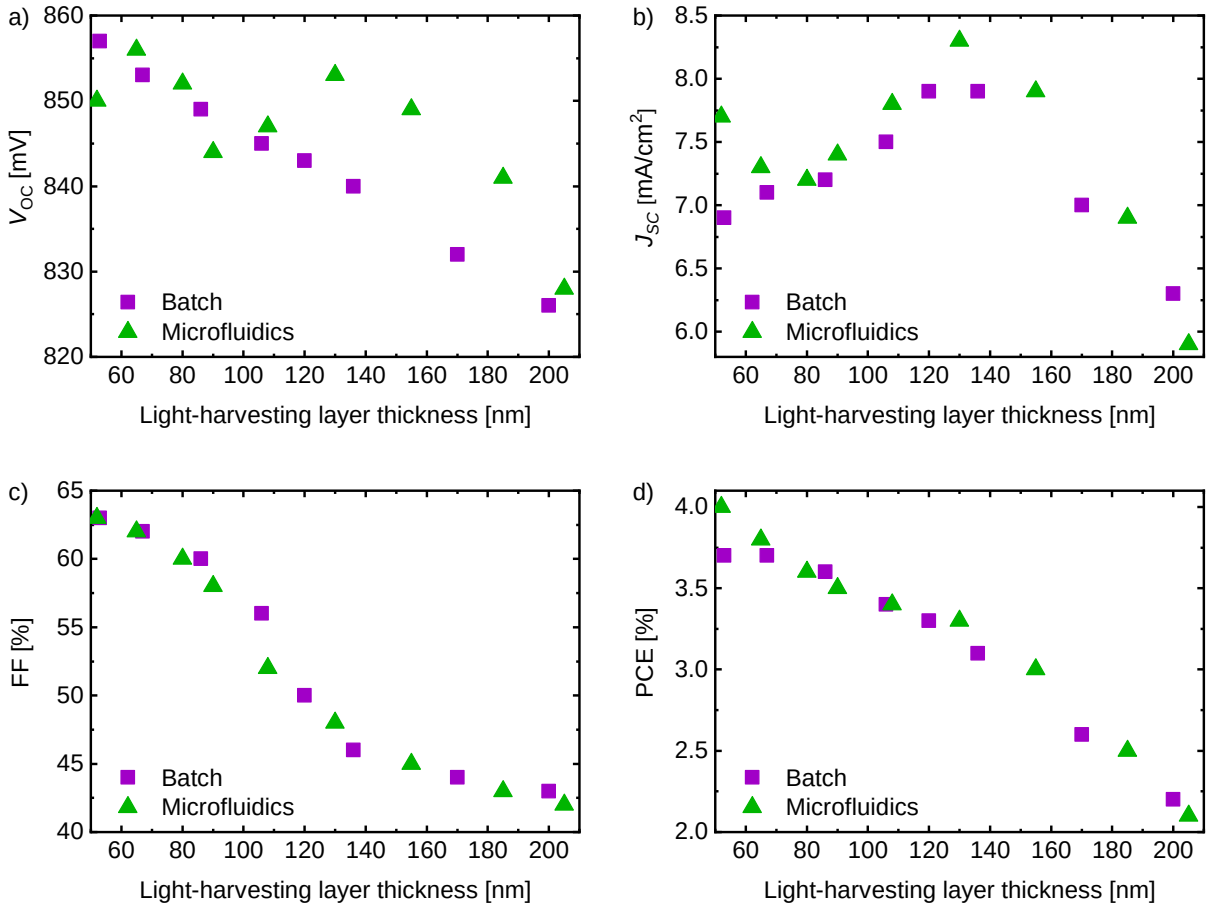

Figure 5.19: Influence of the light-harvesting layer thickness on the key parameters of the solar cells fabricated from either batch nanoprecipitated (violet) or microfluidic nanoprecipitated (green) dispersions. By increasing the layer thickness, a) V_{OC} decreases slightly and b) J_{SC} first increases and later decreases for thicker layers, while both c) the FF and d) the PCE decrease.

5.5 Résumé

In this chapter, a nanoprecipitation process by microfluidics was introduced. This process is highly controllable and enables a reproducible synthesis of nanoparticle dispersions. With the irradiation as the most important processing parameter, dispersions with a tunable nanoparticle size can be achieved, exhibiting shelf-stabilities of over one year.

These dispersions were used to fabricate solar cells with tailored light-harvesting layer thicknesses. While the nanoparticle sizes in the range between 50 nm and 80 nm do not directly influence the solar cell performance, the light-harvesting layer thickness does, as illustrated in Figure 5.20. In this figure, the PCE of all fabricated solar cells with a light-harvesting layer deposited from nanoparticle dispersions, fabricated by microfluidics, are summarized. One of the most crucial results is achieving a smooth, closed light-harvesting layer, which is only pos-

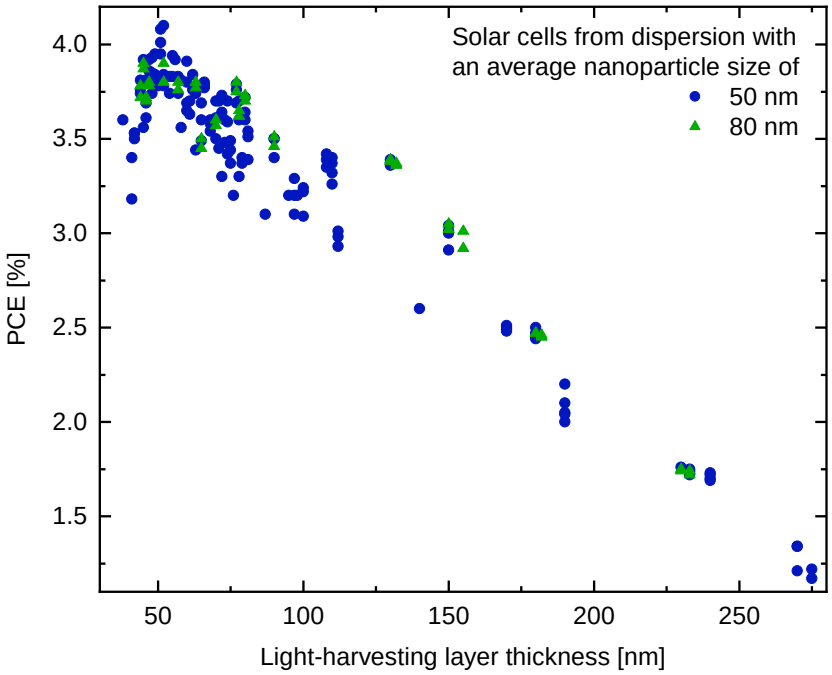

Figure 5.20: Graphical summary of the PCE of all fabricated solar cells from a dispersion synthesized by microfluidics *versus* the light-harvesting layer thickness. Dispersions with an average nanoparticle size of 50 nm and 80 nm are represented by blue circles and green rectangles, respectively.

sible with more than three spincoating steps and T_{Ann} above 120 °C. A PCE of over 4 % was achieved at light-harvesting layer thicknesses of 50 nm.

In the last section, solar cells with a light-harvesting layer deposited from dispersions, that were synthesized by microfluidics or by batch nanoprecipitation, were compared. Solar cells fabricated from microfluidic nanoparticle dispersions exhibit slightly better performance than solar cells fabricated from batch-processed nanoparticle dispersions because of the higher J_{SC}.

6 Binary P3HT:fullerene blends: Role of the fullerene solubility and miscibility

While microfluidics is a scalable nanoprecipitation method, it is not suitable for the screening of new, unknown organic semiconductors. If agglomeration occurs during the nanoprecipitation, the microfluidic chip will be clogged. The screening of metastable dispersions that flocculate over time is the main advantage of the batch nanoprecipitation, as introduced in 2.3.1.
As shown in 3.2.1, several fullerenes with different functional groups exist. While it is already known that P3HT and the blend of P3HT:$IC_{60}BA$ form stable nanoparticle dispersions, initial tests with the most commonly used fullerene acceptor $PC_{61}BM$ did not result in stable dispersions.[8, 11, 147, 151] Previous to this work, there were no publications of other stable P3HT:fullerene dispersions without a surfactant. In the first section of the following chapter, the impact of different fullerenes on the nanoparticle formation in combination with P3HT is investigated. In the second section, the changes in nanoparticle size *versus* the concentration of fullerene, as it was investigated in the bachelor thesis of *P. Große Hokamp*, are summarized. In the third section, solar cells are fabricated with a nanoparticulate light-harvesting layer comprising the blend of P3HT and either of the fullerene. The solar cells from stable blends were investigated in the bachelor thesis of *K. Bitsch*, with a PCE of the hero device of 4.5 %. The results of this chapter are summarized in the manuscript by K. Fischer et al. *On the formation of polymer:fullerene nanoparticle dispersions: The role of miscibility*, in preparation.[162]

6.1 Parameters affecting the nanoparticle formation

To investigate the formation of nanoparticles and the differences between the respective fullerenes, the two most commonly used fullerenes, PCBM and ICBA, and two rarely used fullerenes, the thienyl-substituted derivative (ThCBM) and the bisadduct of PCBM (bis-PCBM), are chosen, with either a C_{60}- or a C_{70}-core. For the nanoprecipitation, P3HT and the respective fullerene derivative are separately dissolved in chloroform and mixed to prepare the blend solution. By adding chloroform, the desired concentration is achieved. Ethanol was chosen as a non-solvent due to its high miscibility with chloroform. To compare the influence of the different fullerenes on the nanoparticle size, nanoparticles from a pure P3HT solution are fabricated, too.

The results are summarized in Table 6.1. Initially, the blends of P3HT with all chosen fullerenes result in nanoparticle dispersions, with nanoparticle sizes that do not differ during the measurement. However, after nanoprecipitation, the nanoparticle dispersions can be classified by their average size below 40 nm and above 45 nm into two categories. Dispersions with an average nanoparticle size below 40 nm, such as P3HT:PC_{61}BM, P3HT:ThC_{61}BM, P3HT:bis-PC_{62}BM, and P3HT:bis-PC_{72}BM, started to flocculate over time. Sedimentation of fullerene-rich agglomerates could be observed within the first hour, while a stable nanoparticle dispersion of mainly P3HT remained in the chloroform-ethanol mixture. In contrast, dispersions with an average nanoparticle size above 45 nm, such as P3HT:PC_{71}BM, P3HT:ThC_{71}BM, P3HT:IC_{60}BA, and P3HT:IC_{70}BA, remained stable.

Table 6.1: Average nanoparticle size d of P3HT and P3HT:fullerene dispersions (c_{P3HT} = 1 g/L) immediately after nanoprecipitation and reduction of the dispersion to the initial concentration (nonsolvent volume fraction φ_{NS} = 75 %).

Fullerenes	d [nm] after nanoprecipitation	d [nm] after reduction	Remaining amount[a)] [wt %]
PC_{61}BM	39 ± 1[b)]	40 ± 1[c)]	35
PC_{71}BM	49 ± 1	50 ± 1	100
ThC_{61}BM	40 ± 1[b)]	40 ± 1[c)]	30
ThC_{71}BM	49 ± 1	51 ± 1	95
IC_{60}BA	45 ± 1	44 ± 1	90
IC_{70}BA	46 ± 1	48 ± 1	100
bis-PC_{62}BM	36 ± 1[b)]	37 ± 1[c)]	15
bis-PC_{72}BM	38 ± 1[b)]	37 ± 1[c)]	10
P3HT	53 ± 2	46 ± 1	100

[a)] Remaining amount of fullerene in the dispersion after reduction, compared to initial amount immediately after nanoprecipitation.[b)] Sedimentation over time leads to a separation of P3HT and fullerene; [c)] Sedimentation during reduction leads to demixing.

If dispersions tend to flocculate over time, the reduction of the dispersions directly after nanoprecipitation leads to a more pronounced sedimentation. This results in a massive sedimentation of fullerene from within the dispersion, while again a stable P3HT-rich nanoparticle dispersion remains. To estimate the remaining amount of fullerene in the final concentration, an aliquot of dispersion is dissolved in chloroform and the absorbance spectra are measured, as depicted in Figure 6.1 a-b. Then, the absorbance spectra are fitted to the absorbance spectra of both P3HT and the fullerene, as depicted in Figure 6.1 c-d. From the absorbance measurements, the relative

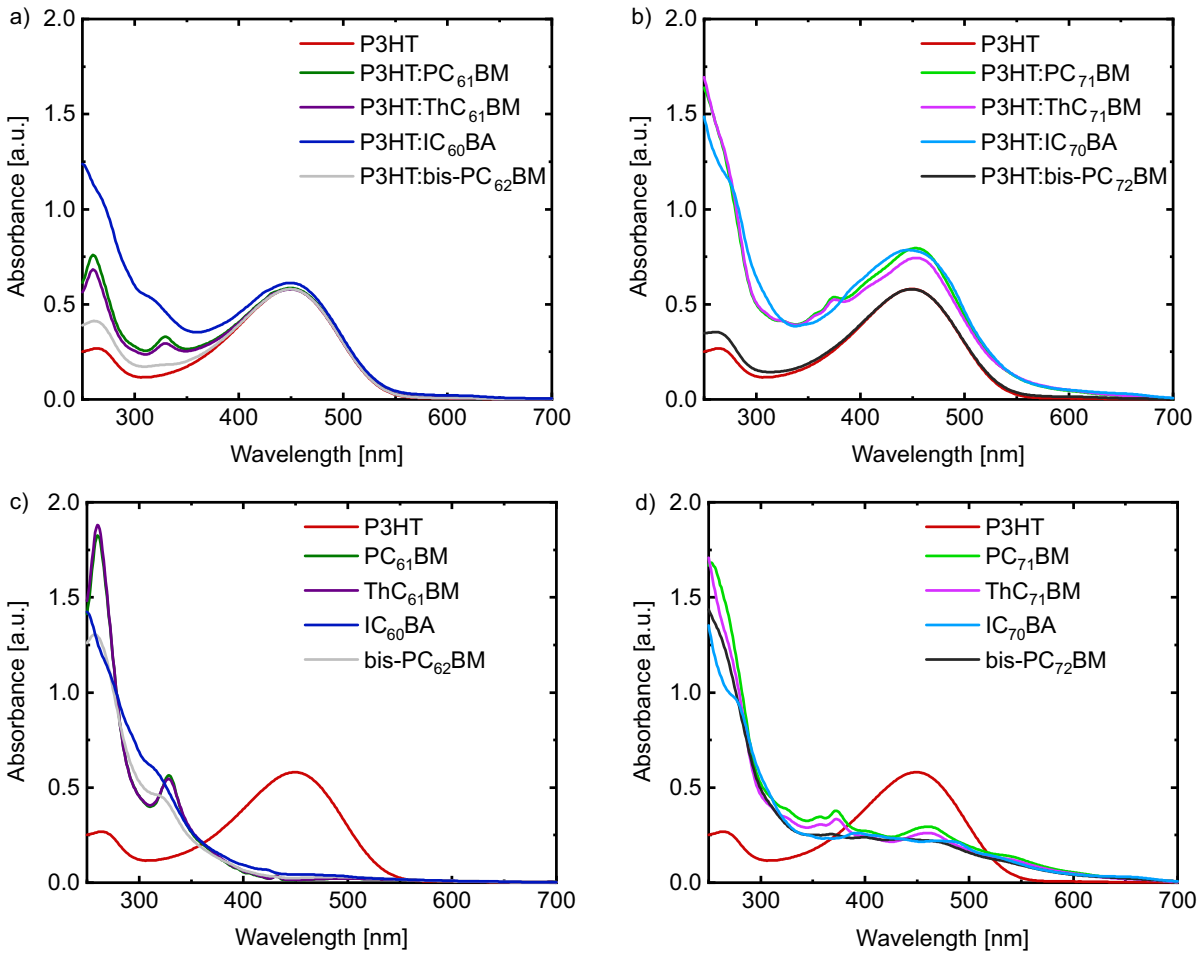

Figure 6.1: a-b) Absorbance spectra of the dispersions after reduction, redissolved in chloroform, with different C_{60}-fullerenes (a) and C_{70}-fullerenes (b). c-d) Absorbance spectra of P3HT and fullerene mixture in chloroform, with different C_{60}-fullerenes (c) and C_{70}-fullerenes (d).

amount of fullerene in the reduced dispersion can be calculated. The last column of Table 6.1 lists the fraction of fullerenes that remained in the dispersion *versus* the initial fullerene content. In previous experiments, the influence of $IC_{60}BA$ on the nanoparticle size was discussed. Polymer blends with fullerenes form smaller nanoparticles than neat polymers, both under illumination and in the dark.[26, 151] In this experiment, the presence of fullerenes during nanoprecipitation appears to be helpful and leads to a reduced nanoparticle size, even for otherwise unstable blends. This indicates that a share of the fullerenes is incorporated into the nanoparticles, while the residual material remains in the dispersion and leads to flocculation.

The separation of polymers and fullerenes is detrimental for the dispersions. In stable nanoparticle dispersions, no separation occurs. Ideally, stable dispersions also persist during reduction. In Figure 6.2, the normalized absorbance spectra of the dispersions diluted in ethanol after nanoprecipitation and after reduction are depicted. Changes in the absorption indicate

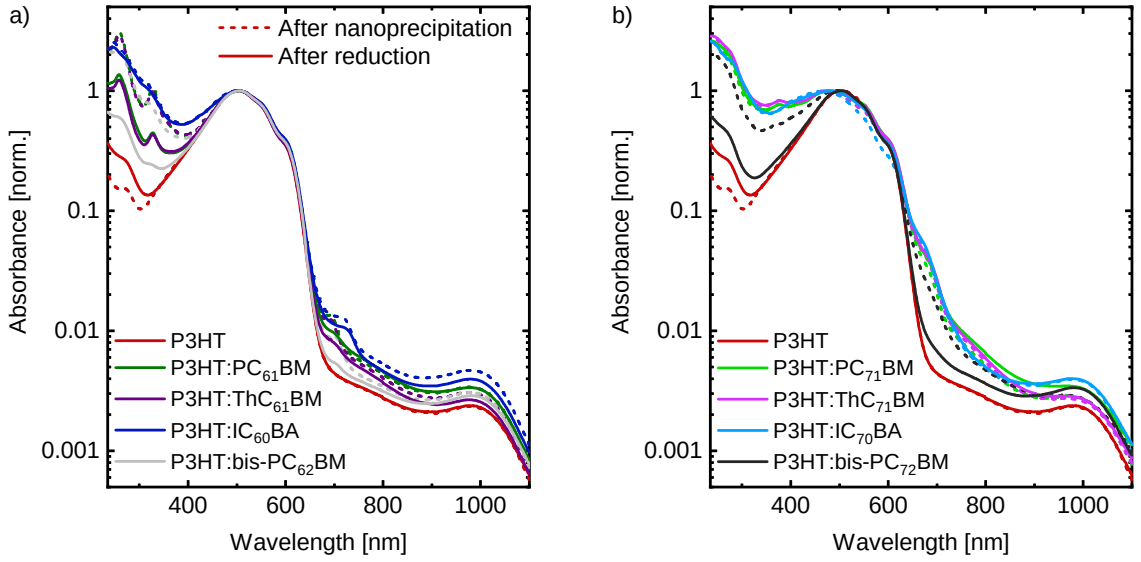

Figure 6.2: Normalized absorbance of P3HT and a) the C_{60}-fullerenes and b) the C_{70}-fullerenes after nanoprecipitation (dashed lines) and after reduction (solid lines). For the stable nanoparticle dispersions, both lines differ little. In the unstable dispersions, a huge difference between 250 nm and 500 nm occurs, which is caused by flocculation of the fullerene. While pure P3HT nanoparticles already have a polaron band at 970 nm, all blends show the polaron band, which is slightly more pronounced for the stable dispersions.

unstable dispersions, with respect to changes in their composition, molecular order, and size. Stable nanoparticle dispersion, such as P3HT:IC_{60}BA, show almost no change in absorbance. While all nanoparticle dispersions show almost the same maximum of P3HT at 500 nm, they differ between 700 and 1000 nm. The absorbance feature at 970 nm stems from positive self-charging and is known as the polaron band of P3HT.[26, 139, 140] We recently showed that nanoparticle dispersions can be stabilized against agglomeration by extrinsic charging of the nanoparticles.[151] Likewise, by adding fullerene to the nanoprecipitation process, the polaron band of P3HT becomes more pronounced, indicating additional charging of the polymer that supports stabilization.

6.1.1 Residual solubility

Previously, we observed that IC_{60}BA has a notable solubility of about 0.1 g/L in the ethanol:chloroform mixture (4:1 by volume).[26] This residual solubility can help carry the negative counter charge away from the nanoparticles to the solution, which is essential to produce some net-charging of the nanoparticles. Yet, the solubilities of the different fullerene derivatives in this work are different, which may explain the impact on the nanoparticle stability. Therefore, the residual solubilities of the different fullerenes were measured. Small amounts of all fullerenes were dissolved in either pure ethanol or the mixture of ethanol and chloroform (3:1 by volume,

corresponding to φ_{NS} = 75 %). The solutions were stirred for two days. After the stirring, the excess material was left to sediment for one day. The solution was separated from the sediment and afterwards centrifuged for 10 minutes to remove insoluble fullerenes. Again, the concentrations were determined by comparison of the absorbance spectra. The calculated solubilities are listed in Table 6.2. While pure ethanol represents the final dispersion after reduction, the mixture of ethanol and chloroform corresponds to the initial state during nanoprecipitation.

Table 6.2: Residual solubility of the different fullerenes and P3HT in both pure ethanol (corresponds to the reduced dispersion) and a mixture of ethanol and chloroform (corresponds to the mixture right after nanoprecipitation). While all fullerenes show residual solubilities, P3HT appears insoluble.

Material	Solubility in ethanol [mg/L]	Solubility in mixture[a)] [mg/L]
$PC_{61}BM$	2	30
$PC_{71}BM$	7	60
$ThC_{61}BM$	2	26
$ThC_{71}BM$	5	50
$IC_{60}BA$	60	185
$IC_{70}BA$	12	30
bis-$PC_{62}BM$	120	> 600
bis-$PC_{72}BM$	40	140
P3HT	< 1	< 1

[a)] Mixture of 75 % ethanol and 25 % chloroform.

In fact, the residual solubility of the examined fullerenes differs, with bis-$PC_{62}BM$ exhibiting the highest residual solubility. $IC_{60}BA$ has a moderate residual solubility. At low concentrations in the range of the residual solubility, a lot of material remains dissolved after nanoprecipitation, leading to flocculation during chloroform removal and significantly changing the donor to acceptor ratio. This was already discussed in previous publications and may explain the loss of $IC_{60}BA$, bis-$PC_{62}BM$ and bis-$PC_{72}BM$ in Table 6.1.[26, 162]

While these fullerene losses, due to higher solubility, appear disadvantageous towards achieving stable, mixed nanoparticle dispersions, the same property may also have a positive effect on the nanoparticle formation. The residual solubility of the fullerenes can support the displacement of the negative counter charges in solution.[151] Through increased colloidal stability, due to nanoparticle charging, the average nanoparticle size decreases. Interestingly, the smallest nanoparticles can be achieved, when the fullerene concentration is on the order of the residual solubility, which is further shown in section 6.2.

6.1.2 Miscibility

By changing the functional groups, the miscibility of the respective fullerenes with the polymer changes. According to the literature, blend layers of P3HT and fullerenes tend to form crystalline phases of P3HT, as well as pure fullerene-rich phases and mixed amorphous phases.[109, 163, 164, 165] Depending on the miscibility of the particular fullerene and P3HT, these amorphous phases are more or less distinct. Chen et al. investigated the limit of miscibility of the four fullerenes $IC_{60}BA$, bis-$PC_{62}BM$, $ThC_{61}BM$ and $PC_{71}BM$, blended with P3HT, by neutron reflectometry and compared them to the miscibility of P3HT:$PC_{61}BM$.[109, 165] To achieve blend-layers, they prepared bilayers of P3HT on top of the respective fullerenes and thermally annealed their samples at 140 °C for 30 minutes. Better miscibility of polymers and fullerenes promoted more intimate mixtures. The highest miscibility was found for $ThC_{61}BM$, followed by both $PC_{61}BM$ and $PC_{71}BM$ and then by $IC_{60}BA$. The lowest miscibility was gained for bis-$PC_{62}BM$.[109, 166] This trend is inversely proportional to the crystallinity of P3HT in the blend, where an annealed layer of P3HT:bis-$PC_{62}BM$ has the highest crystallinity, followed by P3HT:$IC_{60}BA$, with the lowest P3HT crystallinity for P3HT:$ThC_{61}BM$.[109] Earlier literature reported that a blend-layer of P3HT:$PC_{61}BM$ tends to separate and PCBM clusters form on top of the layer upon thermal annealing.[167, 168, 169] Experiments on layers comprising P3HT or blends of P3HT and C_{60}-fullerenes, deposited from chlorobenzene solution onto glass substrates, show the same results, as depicted in Figure 6.3 a-e for the as-cast and in Figure 6.3 f-j for the thermally annealed layers.

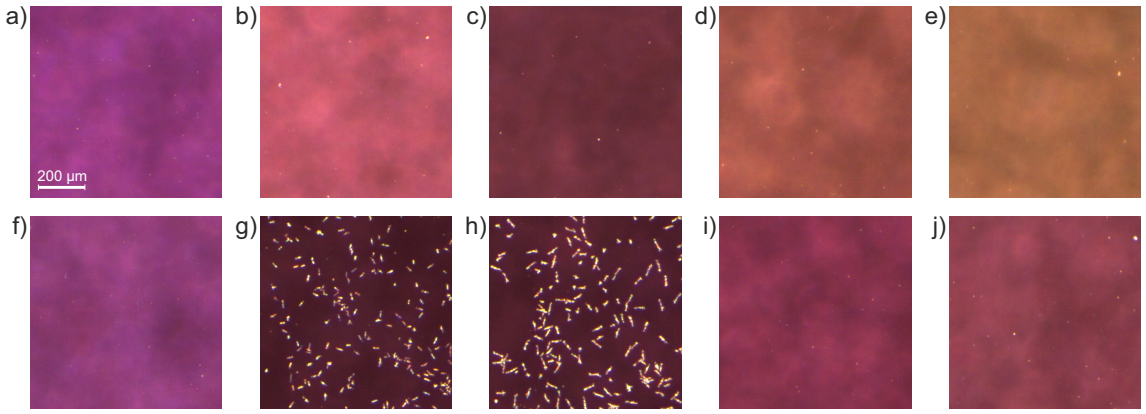

Figure 6.3: Microscope pictures of a-e) as-cast and f-j) annealed (150 °C, 30 min) layers of pure P3HT (a,f), P3HT:$PC_{61}BM$ (b,g), P3HT:$ThC_{61}BM$ (c,h), P3HT:bis-$PC_{62}BM$ (d,i), and P3HT:$IC_{60}BA$ (e,j) (P3HT concentration 20 g/L in CB, P3HT:fullerene ratio 1:1 by weight). While all the as-cast samples show a smooth surface, the annealed layers of P3HT with both $PC_{61}BM$ and $ThC_{61}BM$ show the characteristic separation of the fullerene into clusters. Neither pure P3HT nor the mixed layers with the bisadduct fullerenes show this behavior.

While layers of pure P3HT do not change during annealing, $PC_{61}BM$ phase-separates. Also the blend of P3HT:$ThC_{61}BM$, which has a better miscible with P3HT than $PC_{61}BM$, starts to phase-separate. The fullerenes of the bisadducts are highly miscible with P3HT and do not separate visually.[168, 170] The minor color change, that is consistent with the absorbance measurement in Figure 6.4, is a sign of a more crystalline structure of the layers of the P3HT:bisadduct after thermal annealing.

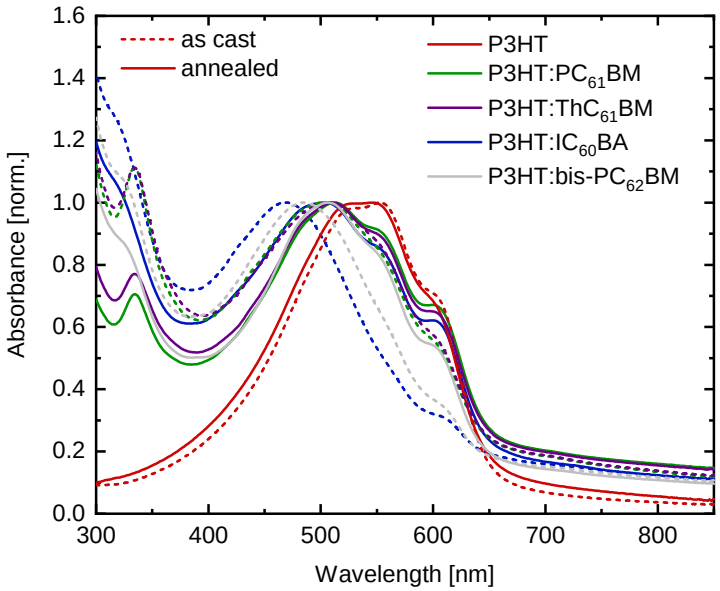

Figure 6.4: Absorbance spectra of the layers from Figure 6.3 for both the as-cast (dotted lines) and the thermally annealed samples (solid lines), normalized to the P3HT peak. Through thermal annealing, the crystallinity of the P3HT layer increased slightly. The blends with the bisadducts show an obvious peak shift, indicating more crystalline structures. The blends of P3HT with $PC_{61}BM$ and $ThC_{61}BM$ show a minor increased P3HT crystallinity after thermally annealing, while the fullerene peaks between 300 nm and 400 nm decrease. This can be explained by demixing and the formation of fullerene-rich clusters.

6.1.3 PLQY

The relative degree of the miscibility can also be concluded from the PLQY in Figure 6.5. A pure P3HT dispersion of both the nanoprecipitated and the reduced dispersion exhibits a PLQY of 1.7 %. With the addition of fullerenes into the nanoparticles, the PLQY decreases through quenching of the excited states of the polymer. This effect is known for layers deposited from a blend solution.[141] A stronger quenching of the PLQY corresponds to a more efficient interaction between the materials.[142] Through the miscibility of the fullerenes with P3HT, the PLQY changes. The dispersions containing the C_{60}-fullerenes exhibit a higher PLQY than the dispersions containing C_{70}-fullerenes. Notably, bis-PCBM exhibits the highest PLQY in each groups, which is in accordance with the results from a previous publication by Guilbert et al. and

Westacott et al. about the PL of blend layers of P3HT:$PC_{61}BM$ and P3HT:bis-$PC_{62}BM$ from solution.[170, 171] While stable systems with P3HT and the fullerenes $PC_{71}BM$, $ThC_{71}BM$, $IC_{60}BA$, and $IC_{70}BA$ only show a minor increase in their PLQY after the reduction of the dispersion, the PLQY of unstable systems tends to increase toward the PLQY of pure P3HT nanoparticle dispersions, which indicates demixing. However, the PLQY is not as high as that of pure P3HT, indicating that small amounts of fullerenes remain within the nanoparticles. This assumption can be confirmed by the results of the absorbance measurement from Figure 6.1

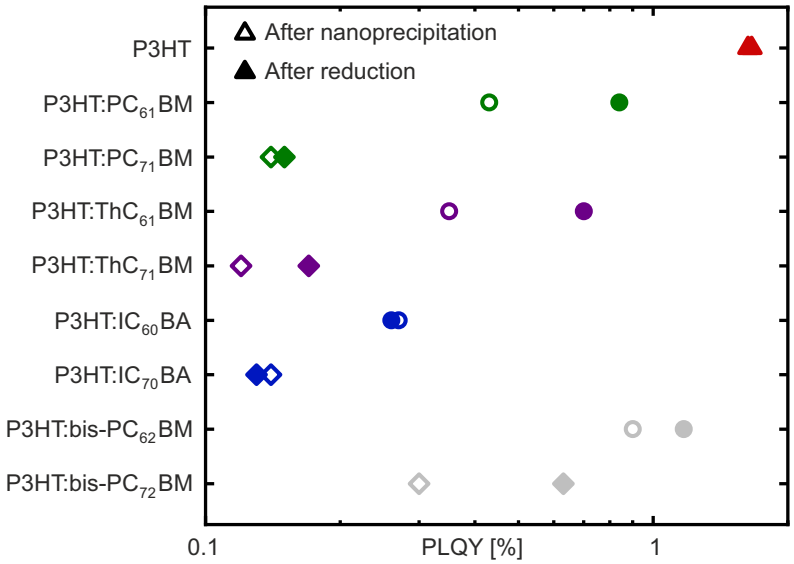

Figure 6.5: Comparison of the PLQY of P3HT and P3HT:fullerene nanoparticle dispersions, either after nanoprecipitation (empty symbols) or after reduction (filled symbols). Dispersions that contain C_{60}-fullerenes are represented by circles, dispersions that contain C_{70}-fullerenes are presented by squares, the pure P3HT dispersions are presented by triangles. While the blend of P3HT with fullerenes that form a stable dispersion exhibits a low PLQY, the unstable dispersions exhibit a higher PLQY, the latter of which is changing during the reduction step, indicating demixing.

In summary, a lot of parameters influence the nanoparticle formation. A small residual solubility of the fullerenes can support the displacement of the negative counter charge by dissolved fullerenes in solution, resulting in a decreased nanoparticle size in the range of the residual solubilities through an increase in colloidal stability. A high residual solubility, e.g of bis-$PC_{62}BM$, in combination with a low miscibility can hinder the nanoparticle formation. Employing $IC_{60}BA$, which has a higher miscibility and a lower residual solubility than bis-$PC_{62}BM$, a stable nanoparticle dispersion can be achieved. The miscibility of the polymer and the fullerenes is another important parameter for the nanoparticle formation, which is directly influenced by the interaction between the materials and the material separation. The low miscibility of bis-$PC_{72}BM$, together with the low quenching of the PLQY leads to flocculation. Both $PC_{61}BM$ and $ThC_{61}BM$ are known for their high miscibility with P3HT, but also a separa-

tion from the polymers during thermal annealing, resulting in a sedimentation of the fullerenes from the dispersion. The two corresponding C_{70}-fullerenes, $PC_{71}BM$ and $ThC_{71}BM$, as well as $IC_{70}BA$ show a low PLQY, which indicates an efficient interaction between the materials, resulting in stable nanoparticle dispersions.

6.2 Influence of the fullerene concentration

Through the miscibility of P3HT and the respective fullerenes, the concentration of fullerenes that remain within the nanoparticles differs, while the residual solubility influences the nanoparticle formation and the concentration of fullerenes within the dispersion. Thus, the concentration of fullerenes could also influence the nanoparticle formation process and, therefore, the average nanoparticle size. The dispersions above had an initial c_{P3HT} of 1 g/L and therefore a concentration that is too low to build solar cells. To consider influence of the concentration of fullerenes on the size of the nanoparticles and therefore the influence on solar cells, a higher concentration c_{P3HT} of 2.5 g/L is chosen, while the concentrations of fullerene is varied. Starting with a blend of P3HT and $IC_{60}BA$, the concentration of $IC_{60}BA$ is varied between 0.002 g/L and 10 g/L. In Figure 6.6, the sizes of the resulting nanoparticles *versus* the fullerene concentration are summarized directly after nanoprecipitation. The two gray lines represent the residual solubilities of $IC_{60}BA$ in ethanol (EtOH) and in the mixture of ethanol and chloroform (EtOH:$CHCl_3$, 3:1 by volume). For each concentration, at least three nanoprecipitations are conducted. The results are also compared with a pure P3HT dispersion (ICBA concentration 0 g/L). By further increasing the concentration of $IC_{60}BA$ during nanoprecipitation, first, the average size of the nanoparticles decreases slightly until the residual solubility in ethanol is reached. In this range, the fullerenes are still soluble in ethanol, which indicates that increasing the fullerene concentration leads to more fullerenes that carry the negative counter charge away from the nanoparticle and therefore to a reduction in nanoparticle size. At concentrations inside the range of the residual solubility of ethanol and the mixture, the results are inconsistent and the reproducibility of different nanoprecipitations is low, indicating that the nanoprecipitation is sensitive, e.g. to tiny concentration fluctuations that can directly influence the nanoparticle size. By further increasing the fullerene concentrations, more fullerenes are incorporated into the nanoparticles, until a saturation is reached. By increasing the concentration above 2 g/L, the nanoparticle size increases, too. It should be noted that dispersions of P3HT:$IC_{60}BA$ with a ratio greater than 1:1.5 lead to a growth of the nanoparticles over time. Excess fullerenes sediment, until a P3HT:$IC_{60}BA$ ratio of 1:1.5 is reached in the remaining dispersion.
By reducing the dispersion, the size of the nanoparticles differs slightly, as summarized in Figure 6.7. After centrifugation, the standard deviation of the measured nanoparticle size is

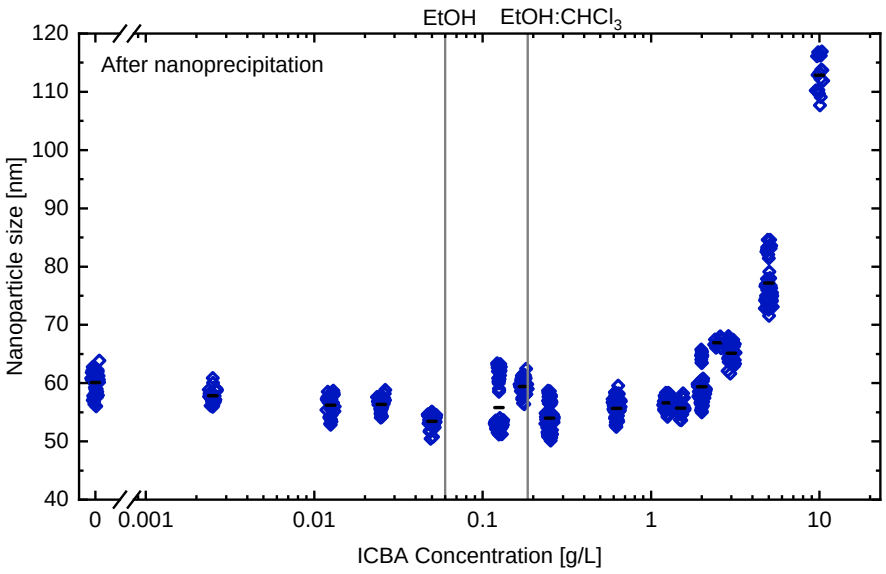

Figure 6.6: Average nanoparticle size of a P3HT:$IC_{60}BA$ blend, measured immediately after nanoprecipitation, *versus* the ICBA concentration at a constant c_{P3HT} = 2.5 g/L. The two gray lines represent the residual solubilities of $IC_{60}BA$ in ethanol (EtOH) and in the mixture of ethanol and chloroform (EtOH:$CHCl_3$, 3:1 by volume). An increase of the fullerene concentration first results in a minor decrease of the nanoparticle size below the residual solubility in ethanol. Between the residual solubility of ethanol and the mixture, the results are inconsistent, leading to a low reproducibility in the different nanoprecipitations. Above the residual solubility of the mixture, increasing the fullerene concentration results in more fullerenes being incorporated into the nanoparticles, until a maximum is reached at a P3HT:ICBA ratio of 1:1.5 (by weight) and the excess sediments. Each data point represents one measurement. At least three different dispersions were measured per concentration, with each dispersion measured 10 times.

reduced, not changing the trend from Figure 6.6. Even though the stability in this range is low, it seems to be the most important range for blends of P3HT:$IC_{60}BA$. Therefore, three different fullerene derivatives are investigated to elucidate this trend. $PC_{71}BM$ is another fullerene that forms stable nanoparticles by blending with P3HT, while $PC_{61}BM$ does not form stable nanoparticles. Both fullerenes show a comparable residual solubility that is rather low compared to $IC_{60}BA$. Due to the high residual solubility, bis-$PC_{62}BM$ is also chosen. Since neither $PC_{61}BM$ nor bis-$PC_{62}BM$ remained within the dispersion when blended 1:1 with P3HT, the remaining concentrations of fullerene from Table 6.1 are chosen as the maximum concentration that is investigated.

Starting with P3HT:$PC_{71}BM$, with a residual solubility in ethanol and the mixture of 7 mg/L and 60 mg/L, respectively, a concentration below the residual solubility in ethanol, a concentration between the two residual solubilites and four different concentrations above the residual solubility of the mixture are investigated towards the synthesis of nanoparticle dispersions. The resulting nanoparticle sizes are summarized in Figure 6.8 a-b immediately after nanoprecipitation and after the reduction of the dispersion.

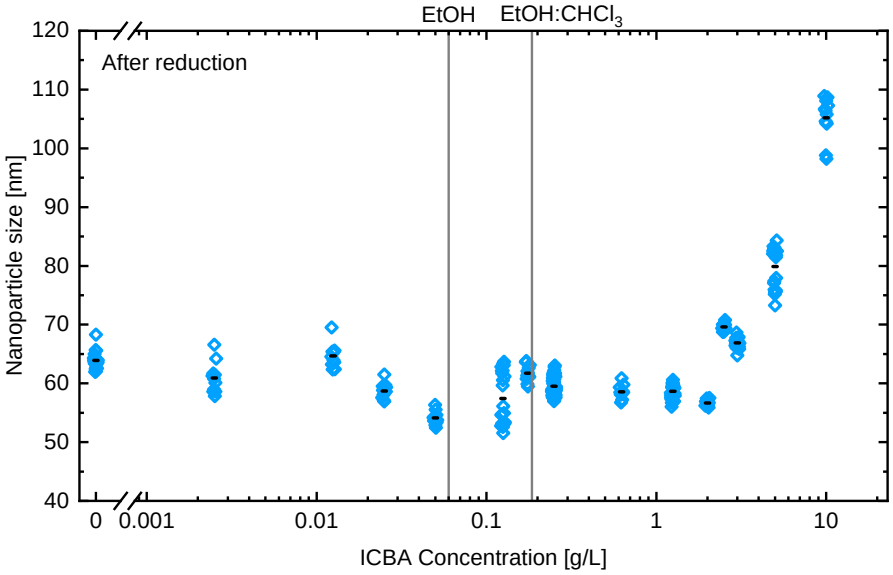

Figure 6.7: Average nanoparticle sizes of P3HT:$IC_{60}BA$ blends, immediately after reduction of the dispersion, *versus* ICBA concentration at a constant c_{P3HT} = 2.5 g/L. An increase of the fullerene first results in a slightly decreased nanoparticle size below the residual solubility in ethanol. Between the residual solubility of ethanol and the mixture, the results are irreproducible. Above the residual solubility of the fullerene inside the ethanol:chloroform mixture, increasing the fullerene concentration results in more fullerene that is incorporated into the nanoparticles, until a maximum is reached at a P3HT:ICBA ratio of 1:1.5 (by weight) and the excess sediments. Each data point represents one measurement. At least three different dispersions are synthesized per concentration, with each dispersion measured 10 times.

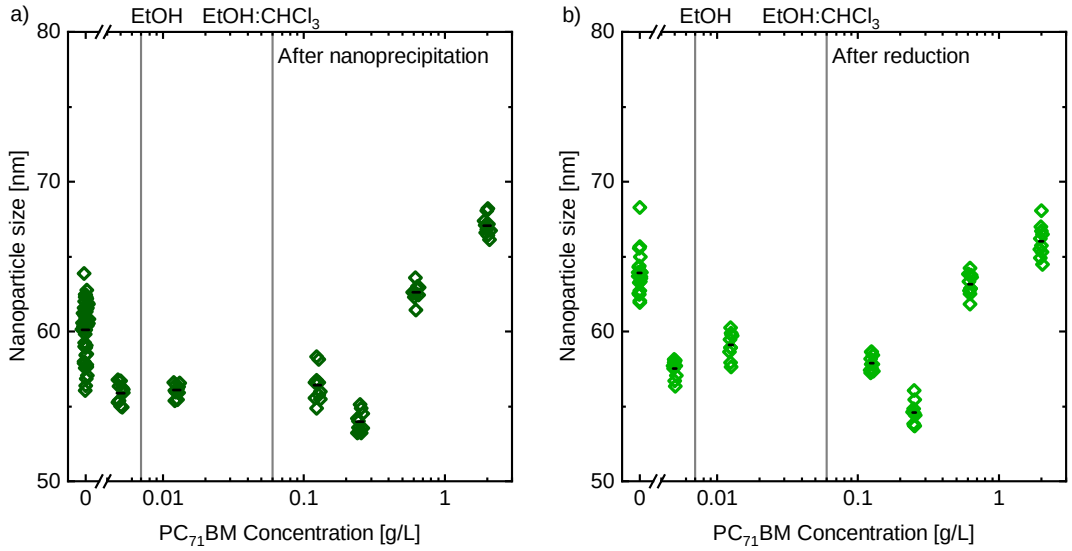

Figure 6.8: Average nanoparticle size of a P3HT:$PC_{71}BM$ blend *versus* $PC_{71}BM$ concentration at a constant c_{P3HT} = 2.5 g/L, a) immediately after nanoprecipitation and b) after reduction of the dispersion. Each data point represents one measurement. At least two different dispersions are measured per concentration, with each dispersion measured 10 times.

Although all concentrations formed stable dispersions, even after the reduction of the dispersions, the trend of the growth of the nanoparticle size above the residual solubilites was visible for higher concentrations. For low concentrations, the difference is in the range of the uncertainty of the DLS measurement and therefore negligible. By increasing the concentration of fullerenes, more fullerenes are incorporated into the nanoparticles, resulting in an increase of the average nanoparticle size, as previously shown in Figures 6.6 - 6.8.
While $PC_{61}BM$ has almost the same residual solubility as $PC_{71}BM$, the formation of nanoparticles differs a lot. Again, one concentration is chosen below the residual solubility concentration of ethanol, one concentration in between the two residual solubility concentrations, and two concentrations above the residual solubility of the mixture, as summarized in Figure 6.9.

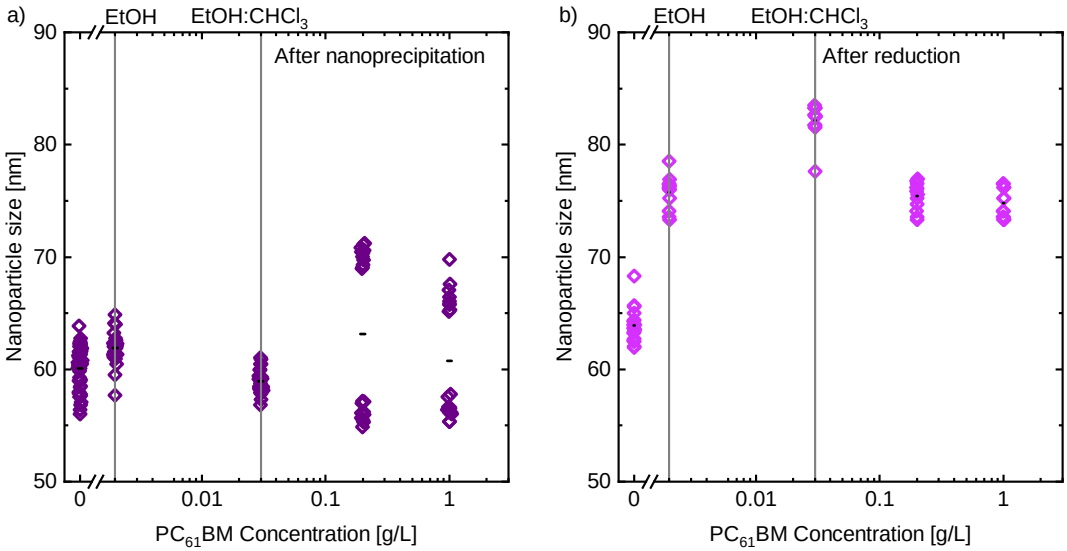

Figure 6.9: Average nanoparticle size of a P3HT:$PC_{61}BM$ blend *versus* $PC_{61}BM$ concentration at a constant c_{P3HT} = 2.5 g/L, a) immediately after nanoprecipitation and b) after reduction of the dispersion. Each data point represents one measurement. At least two different dispersions are measured per concentration, with each dispersion measured 10 times.

While low fullerene concentrations produce nanoparticles with about the same size, at a concentration above the residual solubility concentration of the mixture, the results allude to the same ambiguity that was previously shown for the blend of P3HT:$IC_{60}BA$ above the residual solubility. This leads to high batch-to-batch variations of the nanoparticle sizes. After the reduction of the dispersion, the average nanoparticle size is further increased, resulting in unstable dispersions that tend to flocculate over time. The attempt of preparing layers from the unstable dispersion results in many agglomerates and, upon application on glass substrates by spin coating, the formation of "comets", as depicted in Figure 6.10, compared to a homogeneous layer from the blend with lower concentration of $PC_{61}BM$, occurs.

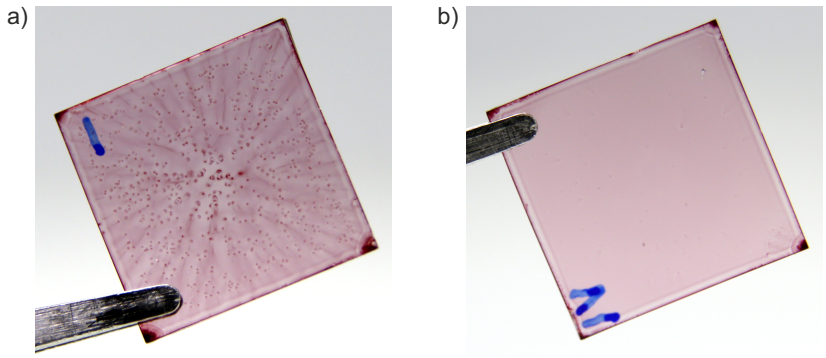

Figure 6.10: P3HT:$PC_{61}BM$ layers from two nanoparticle dispersions with c_{P3HT} = 2.5 g/L, but different $PC_{61}BM$ concentrations. a) The blend with c_{PCBM} = 1 g/L forms a rough layer with a lot of agglomerates and comets, resulting in shorted solar cells. b) At c_{PCBM} = 0.03 g/L, a smooth layer is formed without any agglomerates. While this layer could be implemented in solar cells, the low concentration of fullerenes would not result in an efficient solar cell performance due to the low dissociation efficiency of charge carriers.

In contrast to all other fullerenes, bis-$PC_{62}BM$ has a rather high residual solubility. It was previously shown that dispersions with concentrations above the residual solubility of the mixture were not stable; therefore, only concentrations below are considered. The resulting nanoparticle sizes are summarized in Figure 6.11. Due to the high residual solubilities, a broader process window opens up, resulting in a confirmation of the trend of Figure 6.6.

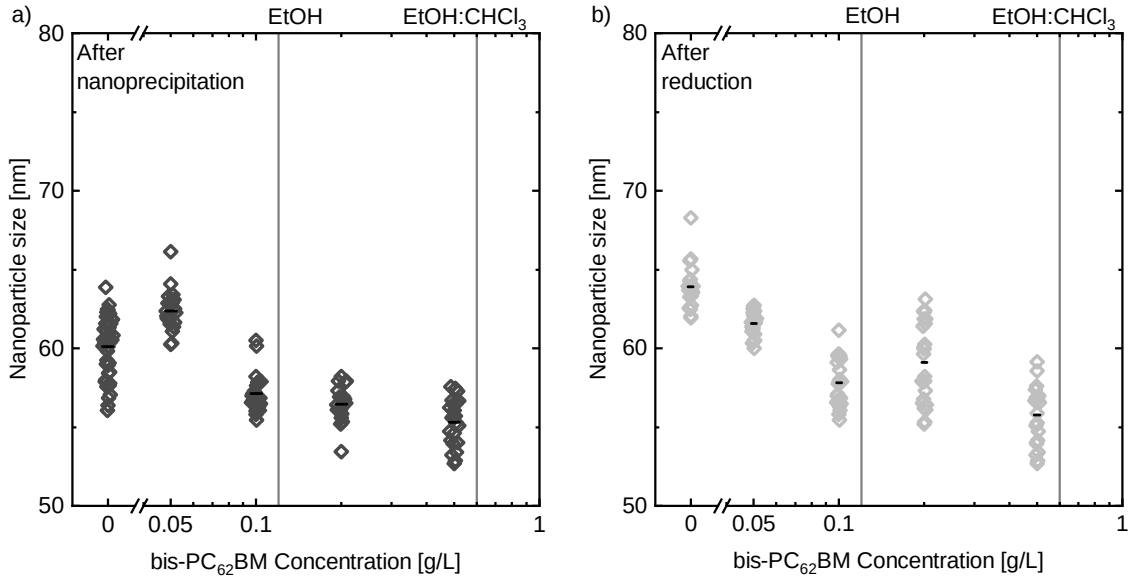

Figure 6.11: Average nanoparticle size of a P3HT:bis-$PC_{62}BM$ blend, over varying bis-$PC_{62}BM$ concentration at a constant c_{P3HT} of 2.5 g/L, a) directly after nanoprecipitation and b) after reduction of the dispersion. Each data point represents one measurement, while at least two different dispersions are measured per concentration, with each dispersion measured 10 times.

Again, by increasing the concentration of fullerenes, the nanoparticle size decreases slightly, but the nanoparticle sizes show a stronger deviation from the average. This effect is more pronounced in reduced dispersions and can be explained by the chloroform evaporation during the reduction step, during which the fullerenes become less soluble.

The conclusion of the experiments so far would be that the concentration of fullerene directly influences the average nanoparticle size. At a fullerene concentration below the residual solubility in ethanol, all fullerene derivatives form stable dispersions with a decrease in the average nanoparticle size. By increasing the concentration of the fullerenes to the residual solubility of the mixture, the nanoparticle size decreases further, but in this regime, an enhanced variance was observed during the nanoprecipitation process which can lead to inconsistent results. Depending on the chosen fullerene, the stability of the dispersion changes. For the fullerenes that did not remain in sufficient quantity inside the dispersion, like $PC_{61}BM$ and bis-$PC_{62}BM$, small concentrations of fullerene below the residual solubility of the mixture initially remain inside the dispersion and lead to a decrease of the nanoparticle size. After the reduction step, this effect is gone and stable P3HT dispersions with sedimented fullerenes remain. Fullerenes that formed stable blend dispersions at a P3HT:Fullerene ratio of 1:1, such as $PC_{71}BM$ and $IC_{60}BA$, formed stable dispersions at all concentrations, except for fullerenes in excess of 1:1.5. In addition, the average nanoparticle size only differs slightly between nanoprecipitation and reduction.

6.3 Solar cells from "stable" dispersions

The results of the chapter above indicate that, by using a blend of P3HT and various fullerenes, stable nanoparticle dispersions can be achieved. By reducing the fullerene concentration, also unstable blends that did not form solar cells before can be investigated.

6.3.1 Stable dispersions

According to the literature, blends of P3HT:ICBA with a mixing ratio of 1:0.8 produce most efficient solar cells from solution with a light-harvesting layer thickness of 200 nm.[152, 156, 157] In section 5.4, it was shown that solar cells with a light-harvesting layer thickness of 50 nm perform best, while light-harvesting layer thicknesses above 130 nm deteriorate the J_{SC} and hence the PCE. To compare solar cells with light-harvesting layers deposited from blend dispersions of P3HT and the different fullerenes, two different light-harvesting layer thicknesses are chosen. A thin layer of 60 nm is achieved by spin casting the dispersion 4 times onto the ETL, while a thick layer of 120 nm is achieved with 8 deposition steps. Many of the dispersions from Figure 6.7 formed smooth layers. However, dispersions with a ratio above 1:1 led to rough

layers through agglomeration during the deposition and thus are unsuitable for deployment in organic solar cells. Therefore, only one concentration above the ratio 1:1 is investigated further. The key parameters of the solar cells are listed in Table 6.3. While the dispersions with a reduced concentration of ICBA of less than 0.125 g/L show excellent layer formation, most solar cells are either shorted or allow a current flow in reverse direction, resulting in only one working solar cell for each variation, with a PCE of less than 0.5 %. Therefore, they are not listed in Table 6.3.

Table 6.3: Key parameters of the nanoparticulate solar cells fabricated from dispersion (c_{P3HT} = 2.5 g/L) at different $IC_{60}BA$ concentrations.

$c_{IC_{60}BA}$ [g/L]	Ratio[a)]	t [nm]	V_{OC} [mV]	J_{SC} [mA/cm^2]	FF [%]	PCE [%]
0.125	1:0.05	50	645 ± 10	3.2 ± 0.1	44 ± 1	0.9 ± 0.1
0.175	1:0.07	50	721 ± 20	3.7 ± 0.1	45 ± 1	1.2 ± 0.1
1.5	1:0.6	60	868 ± 3	7.4 ± 0.1	60 ± 1	3.8 ± 0.1
2	1:0.8	60	854 ± 1	7.5 ± 0.1	64 ± 1	4.1 ± 0.1
2.5	1:1	50	853 ± 2	6.8 ± 0.1	63 ± 1	3.6 ± 0.1
3	1:1.2	80	853 ± 1	5.3 ± 0.1	53 ± 1	2.4 ± 0.1
0.125	1:0.05	100	715 ± 7	1.4 ± 0.1	47 ± 3	0.5 ± 0.1
0.175	1:0.07	105	660 ± 2	1.7 ± 0.1	45 ± 1	0.5 ± 0.1
1.5	1:0.6	120	859 ± 2	7.8 ± 0.1	48 ± 1	3.2 ± 0.1
2	1:0.8	140	841 ± 1	9.2 ± 0.2	53 ± 1	4.1 ± 0.1
2.5	1:1	120	842 ± 1	7.8 ± 0.1	50 ± 1	3.3 ± 0.1
3	1:1.2	150	838 ± 2	4.2 ± 0.1	46 ± 1	1.6 ± 0.1

[a)] Ratio of P3HT:$IC_{60}BA$ by weight.

The best results are obtained with a ratio of 1:0.8, independent of the light-harvesting layer thickness. For the chosen P3HT concentration of 2.5 g/L, this ratio is achieved at a ICBA concentration of 2 g/L. The most significant impact on the solar cell performance at different ICBA concentrations is J_{SC}. This suggests that the materials are highly intermixed and form an excellent interpenetrating network, leading to a high dissociation rate, while a sufficient quantity of paths for the charge carrier transport exists. Therefore, only blends of P3HT:$PC_{71}BM$ with a slightly varying $PC_{71}BM$ concentration around the optimal ratio of 1:0.8 are investigated. The results are summarized in Table 6.4. In accordance with the results from solution processing, the combination of P3HT and $PC_{71}BM$ produces efficient solar cells, again with an optimum at a ratio of 1:0.8.

Table 6.4: Key parameters of the nanoparticulate solar cells fabricated from dispersion (c_{P3HT} = 2.5 g/L) at different $PC_{71}BM$ concentrations.

$c_{PC_{71}BM}$ [g/L]	Layer thickness [nm]	V_{OC} [mV]	J_{SC} [mA/cm^2]	FF [%]	PCE [%]
1.75	50	614 ± 4	8.0 ± 0.1	61 ± 3	3.0 ± 0.2
2	55	625 ± 2	8.4 ± 0.1	61 ± 1	3.2 ± 0.1
2.5	50	614 ± 2	8.4 ± 0.1	62 ± 1	3.2 ± 0.1
1.75	140	612 ± 2	9.6 ± 0.31	51 ± 1	3.0 ± 0.1
2	135	602 ± 2	10.2 ± 0.3	53 ± 1	3.2 ± 0.1
2.5	135	599 ± 3	9.2 ± 0.3	49 ± 1	2.8 ± 0.1

With the two other fullerenes that formed stable nanoparticle dispersions, $IC_{70}BA$ and $ThC_{71}BM$, solar cells with a light-harvesting layer from nanoparticle dispersions have never been built before. In light of the known similarities of $ThC_{71}BM$ and $PC_{71}BM$, the same P3HT:fullerene ratio is used for the fabrication of solar cells. Their key parameters are summarized in Table 6.5.

Table 6.5: Key parameters of the nanoparticulate solar cells fabricated from dispersion, incorporating a P3HT:$ThC_{71}BM$ blend layer with a ratio of 1:0.8 (c_D = 4.5 g/L).

Layer thickness [nm]	V_{OC} [mV]	J_{SC} [mA/cm^2]	FF [%]	PCE [%]
60	557 ± 2	8.3 ± 0.1	58 ± 1	2.7 ± 0.1
85	560 ± 4	8.2 ± 0.1	56 ± 1	2.6 ± 0.1
105	565 ± 2	8.8 ± 0.2	54 ± 1	2.7 ± 0.1
125	571 ± 2	9.9 ± 0.2	47 ± 1	2.7 ± 0.1

Compared to the blend with $PC_{71}BM$, the solar cells from P3HT:$ThC_{71}BM$ lack primarily in V_{OC}, resulting in a slight, but significant decrease of the PCE. Interestingly, the FF decrease and the increase of J_{SC} towards thicker layers compensate each other, leading to almost no change in PCE.

The last fullerene that is investigated is $IC_{70}BA$. Given that the blend of P3HT:$IC_{70}BA$ forms stable nanoparticles and that nanoparticles from P3HT:$IC_{60}BA$ perform well in solar cells, solar cells with $IC_{70}BA$ are promising candidates. In solution, the blend of P3HT:$IC_{70}BA$ achieves the highest PCE, compared to the other fullerene acceptors.[114, 172] Due to the similarity to $IC_{60}BA$, the optimal ratio of 1:0.8 is used, resulting in the solar cell performance in Table 6.6.

Table 6.6: Key parameters of the nanoparticulate solar cells fabricated from dispersion, incorporating a P3HT:$IC_{70}BA$ blend layer with a ratio of 1:0.8 (c_D = 4.5 g/L).

Layer thickness [nm]	V_{OC} [mV]	J_{SC} [mA/cm^2]	FF [%]	PCE [%]
55	866 ± 2	7.9 ± 0.1	64 ± 3	4.4 ± 0.1
75	860 ± 2	7.8 ± 0.2	63 ± 1	4.3 ± 0.1
105	855 ± 2	8.0 ± 0.2	60 ± 1	4.1 ± 0.1
140	847 ± 5	9.4 ± 0.2	46 ± 1	3.6 ± 0.1

Due to the higher absorbance of $IC_{70}BA$, J_{SC} is increased, compared to P3HT:$IC_{60}BA$, which results in a solar cell 'hero device' with a PCE of 4.5 % for the thin layer. By increasing the thickness of the layer, again J_{SC} increases, while both V_{OC} and FF decrease, resulting in a reduced PCE.

6.3.2 Unstable dispersions

Above, four fullerenes could be identified, that formed a stable blend and therefore enabled the fabrication of solar cells. However, for the four fullerenes $PC_{61}BM$, $ThC_{61}BM$, bis-$PC_{62}BM$, and bis-$PC_{72}BM$, a separation from the dispersion occurs. According to the literature, $PC_{61}BM$ and $ThC_{61}BM$ have similar electronic characteristics.[103] Above, it was shown that the blend with $PC_{71}BM$ performed better than $ThC_{71}BM$. Since $PC_{61}BM$ is also more frequently used, it will be investigated in the following paragraph. Since bis-$PC_{62}BM$ has a higher residual solubility, it will be investigated instead of bis-$PC_{72}BM$.

Starting with the blend of P3HT:$PC_{61}BM$, the four reduced fullerene concentrations 1 g/L, 0.2 g/L, 0.03 g/L, and 0.002 g/L are chosen, with a constant c_{P3HT} = 2.5 g/L. With these dispersions, solar cells are built. Because thin layers tend to exhibit shorts, thicker layers are also considered. The results are listed in Table 6.7.

Although J_{SC} and FF are reduced, compared to solar cells with P3HT:$PC_{71}BM$, at least PCEs of almost 2 % are achieved. Theoretically, the solar cell performance would probably increase if more fullerene was incorporated, but this is not an option here. Notably, a rather quick use of the dispersion after reduction is crucial. Otherwise, the dispersions flocculate, resulting in layers as shown in Figure 6.10 a and shorted solar cells. Although lower $PC_{61}BM$ concentrations do not produce properly working solar cells, the formed layers appear rather smooth, without comets or agglomerates. Furthermore, the cracks shown in section 5.4.2 are not visible.

To investigate if closed layers can be fabricated with dispersions that had a low concentration of $PC_{61}BM$, layers on glass substrates are fabricated and the topography is scanned by AFM.

Table 6.7: Key parameters of the nanoparticulate solar cells fabricated from dispersion, incorporating a P3HT:$PC_{61}BM$ blend layer at different blend ratios (c_{P3HT} = 2.5 g/L).

c_{PCBM} [g/L]	Layer thickness [nm]	V_{OC} [mV]	J_{SC} [mA/cm^2]	FF [%]	PCE [%]
0.002	-[a)]	17 ± 6	0.2 ± 0.1	19 ± 11	0
0.002	-[b)]	290 ± 193	0.2 ± 0.1	30 ± 9	0
0.03	-[a)]	75 ± 34	0.5 ± 0.1	26 ± 6	0
0.03	-[b)]	473 ± 100	0.7 ± 0.1	35 ± 4	0.1
0.2	45	298 ± 68	1.2 ± 0.1	37 ± 6	0.1 ± 0.1
0.2	95	446 ± 17	0.8 ± 0.1	44 ± 5	0.2 ± 0.1
1	55	603 ± 25	6.7 ± 0.1	46 ± 5	1.9 ± 0.3
1	100	624 ± 6	7.0 ± 0.1	42 ± 1	1.8 ± 0.1

[a)] approximate layer thickness of 50 nm; [b)] approximate layer thickness of 100 nm.

The as-cast samples are illustrated in Figure 6.12 a-c. In Figure 6.12 d-f, the thermally annealed samples are depicted.

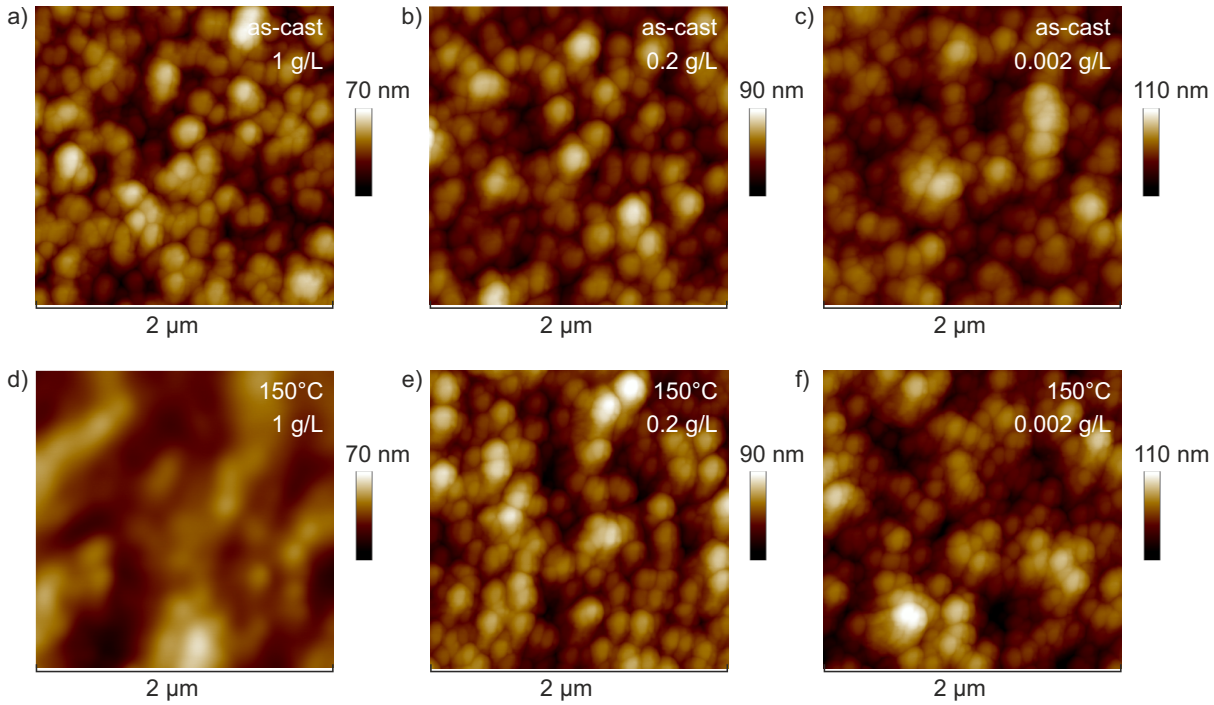

Figure 6.12: AFM measurement of a P3HT:$PC_{61}BM$ blend, at different $PC_{61}BM$ concentrations, a-c) as-cast and d-f) thermally annealed at 150 °C. a) For the layer with a fullerene concentration of 1 g/L, the difference between the as-cast sample, where the single particles are visible, and d) the annealed layer, which shows a coalescence layer, is distinct. For lower concentrations of (b,e) 0.2 g/L and (c,f) 0.002 g/L, no difference is noticeable between the as-cast and the annealed layer, implying that no coalescence of the particles occurred, due to the low fullerene concentration.

By heating a layer that is processed from a solution of P3HT and $PC_{61}BM$, the separation of $PC_{61}BM$ is known and leads to a formation of fullerene clusters. For the nanoparticulate layers, it is assumed that this separation could lead to a filling of the voids, resulting in a closed layer, as shown in Figure 6.12 a compared to d. By reducing the fullerene concentration, less fullerene can fill the voids, leading to shorted solar cells, as shown in Table 6.7. A pure layer of P3HT nanoparticles, as shown in Figure 6.13, confirms this.

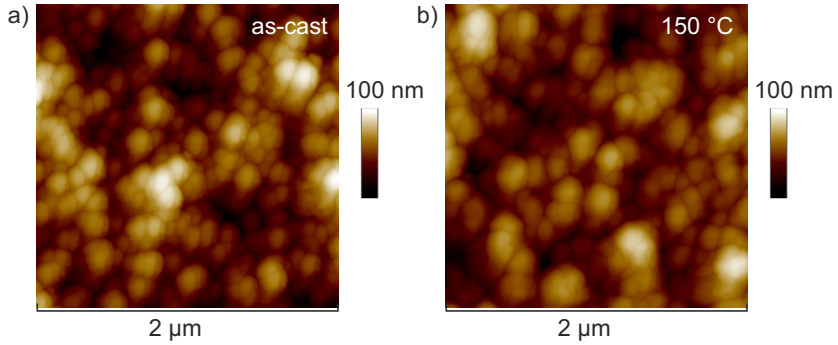

Figure 6.13: AFM measurement of P3HT layers a) as-cast and b) annealed at 150 °C. Both layers show the topography of nanoparticles on a glass substrate, without any coalescence of the nanoparticles.

No difference is observed between the as-cast layer in Figure 6.13 a and the annealed layer in Figure 6.13 b. Both layers show the topography of a nanoparticulate layer, equally distributed on a glass substrate. During thermal annealing, no coalescence occurs and the particles remain separated. Yet, a layer of pure P3HT nanoparticles cannot be used as light-harvesting layer because the voids will short the solar cells. In comparison, solar cells with a light-harvesting layer from a P3HT solution perform because of the smooth layer.

The situation differs slightly for solar cells from layers incorporating bis-$PC_{62}BM$. While bis-$PC_{62}BM$ has a remarkably high residual solubility in ethanol, the remaining concentration of fullerene inside the blend dispersion is drastically lower than for $PC_{61}BM$ (see 6.1, Table 6.1), with the maximum concentration of fullerene of 0.5 g/L. Dispersions with higher concentrations of bis-$PC_{62}BM$ flocculated rapidly and thus could not be evaluated. In Table 6.8, the resulting solar cell parameters are listed for two different light-harvesting layer thicknesses.

Due to the reduced concentration of bis-$PC_{62}BM$, a maximum PCE of 0.5 % is possible, with very low J_{SC} and a slightly reduced FF. Due to the higher HOMO of bis-$PC_{62}BM$ compared to $PC_{61}BM$, in theory, a higher V_{OC} could be achieved. However, because of the low concentration of bis-$PC_{62}BM$ inside the blend, the increased V_{OC} from literature is not reached. Nevertheless, it is also possible to fabricate solar cells with this fullerene derivative. Interestingly, the characteristics of solar cells from low concentrations is better than that of solar cells with $PC_{61}BM$, resulting in a measurable PCE. This could be a result of the remaining soluble

Table 6.8: Key parameters of the nanoparticulate solar cells fabricated from dispersion, incorporating a P3HT:bis-$PC_{61}BM$ blend layers with different blend ratios (c_{P3HT} = 2.5 g/L) at two different layer thicknesses. The light-harvesting layer thicknesses from 4 and 8 deposition steps are 50 nm and 100 nm, respectively.

$c_{bis\text{-}PCBM}$ [g/L]	#deposition	V_{OC} [mV]	J_{SC} [mA/cm^2]	FF [%]	PCE [%]
0.05	4	176 ± 22	0.9 ± 0.1	35 ± 3	0.1 ± 0.1
0.05	8	643 ± 22	0.8 ± 0.1	49 ± 5	0.2 ± 0.1
0.1	4	203 ± 41	1.2 ± 0.1	34 ± 5	0.1 ± 0.1
0.1	8	613 ± 2	0.8 ± 0.1	55 ±2	0.3 ± 0.1
0.2	4	350 ± 35	1.4 ± 0.1	39 ± 4	0.2 ± 0.1
0.2	8	602 ± 8	1.1 ± 0.1	50 ± 2	0.3 ± 0.1
0.5	4	582 ± 12	2.0 ± 0.1	46 ± 5	0.5 ± 0.1
0.5	8	606 ± 3	1.2 ± 0.1	47 ± 1	0.3 ± 0.1
0.5	- [a)]	364 ± 72	1.4 ± 0.2	41 ± 3	0.2 ± 0.1

[a)] thin layer from bis-$PC_{62}BM$, dissolved in ethanol (0.5 g/L), on top of a 50 nm thick nanoparticulate P3HT layer.

fullerene within the dispersion. The topography examination of the dispersion deposited on a glass substrate, as summarized in Figure 6.14, once again show no difference between the as-cast layers (Figure 6.14 a-d) and the annealed layers Figure 6.14 e-h).
This indicates that in fact the slightly soluble fullerene fills the voids, but does not assist in the coalescence of the nanoparticles, resulting in nanoparticular layers that are not shorted. To prove this, solar cells with a thin layer of bis-$PC_{62}BM$ solved in ethanol, spin cast on top

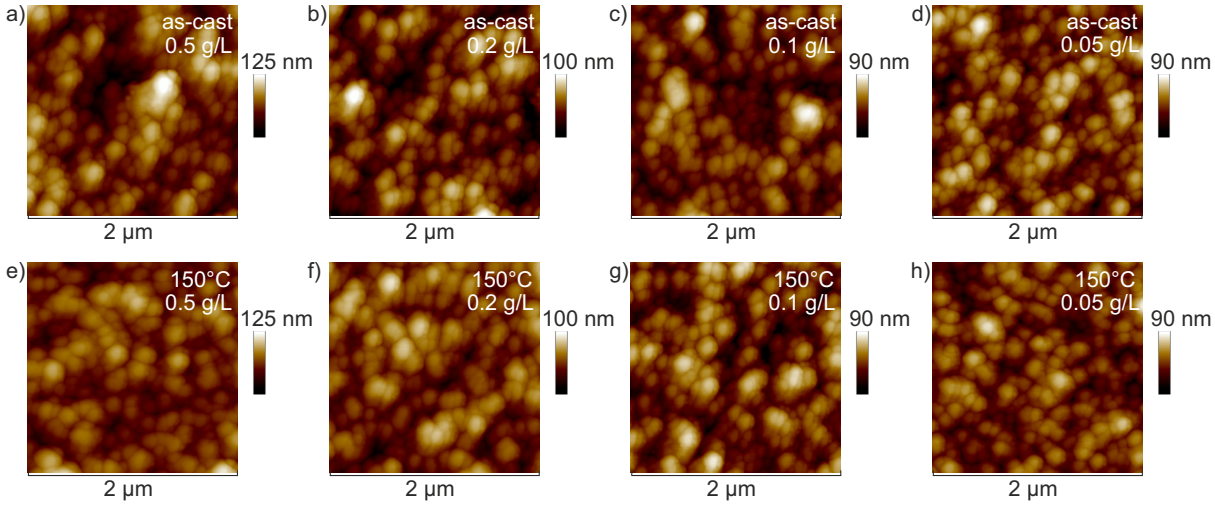

Figure 6.14: AFM measurement of P3HT:bis-$PC_{61}BM$ blend layers on glass, for different bis-$PC_{61}BM$ concentrations, for a-d) as-cast and e-h) thermally annealed layers.

of a light-harvesting layer of pure P3HT nanoparticles, are fabricated. While solar cells with nanoparticulate light-harvesting layers from P3HT dispersions are shorted, the solar cells with the thin layer show weak solar cell behavior, with all solar cell key parameters measurable. The results of a thin layer of bis-$PC_{62}BM$, dissolved in ethanol (0.5 g/L), on top of a 50 nm nanoparticulate P3HT layer, are shown in the last row of Table 6.8.

6.4 Résumé

In this chapter, eight different fullerene derivatives were investigated. First, the residual solubility was determined, followed by an examination of the miscibility of the respective fullerenes and P3HT. While the blend of the four fullerene derivatives $PC_{71}BM$, $ThC_{71}BM$, $IC_{60}BA$, and $IC_{70}BA$ with P3HT led to stable nanoparticle dispersions, the four fullerene derivatives $PC_{61}BM$, $ThC_{61}BM$, bis-$PC_{62}BM$, and bis-$PC_{72}BM$ did not form stable dispersions at a ratio of 1:1 (P3HT:fullerene). The main reasons are the different miscibilities, residual solubilities, preference of separations and interactions between the materials. Second, the influence of the fullerene concentrations on the nanoparticle sizes were investigated. Initially, an increase of the concentration up to the residual solubility of the fullerene results in a decreased nanoparticle size through an increased colloidal stability. A small residual solubility can support the displacement of the negative counter charge to the fullerene in solution. Above the residual solubilities, more fullerene is incorporated into the nanoparticles, resulting in an increased nanoparticle size, until an excess of fullerene results in sedimentation. For the stable dispersions from P3HT:$PC_{71}BM$ and P3HT:$IC_{60}BA$, the average nanoparticle size after reduction did only differ slightly compared to the nanoparticle size after nanoprecipitation. For the investigated unstable blends, such as P3HT:$PC_{61}BM$ and P3HT:bis-$PC_{62}BM$, the average nanoparticle size increased after reduction, while some fullerene sedimented. However, for the combination of P3HT and the different fullerene derivatives, a stable nanoparticle dispersion with a difference in the concentration of fullerene could be achieved, enabling the fabrication of solar cells. The *J*-*V* curves of the best solar cells of each blend are illustrated in Figure 6.15. While solar cells with ICBA show a higher V_{OC}, the solar cells from $PC_{71}BM$ and $ThC_{71}BM$ have a higher J_{SC}.
For the blend of P3HT:bis-$PC_{62}BM$, only small concentrations of bis-$PC_{62}BM$ remained inside the dispersion. Because of this, solar cells with a PCE of only 0.5 % could be achieved. With the blend of P3HT:$PC_{61}BM$, slightly more fullerene remained inside the dispersion, leading to a PCE of 2 %. This result is remarkable, considering that the ratio of P3HT to $PC_{61}BM$ is only 1:0.4. The V_{OC} is similar to the V_{OC} of the blend of P3HT and $PC_{71}BM$, but the J_{SC} is decreased, due to the low fullerene concentration, resulting in a reduced charge carrier transport.

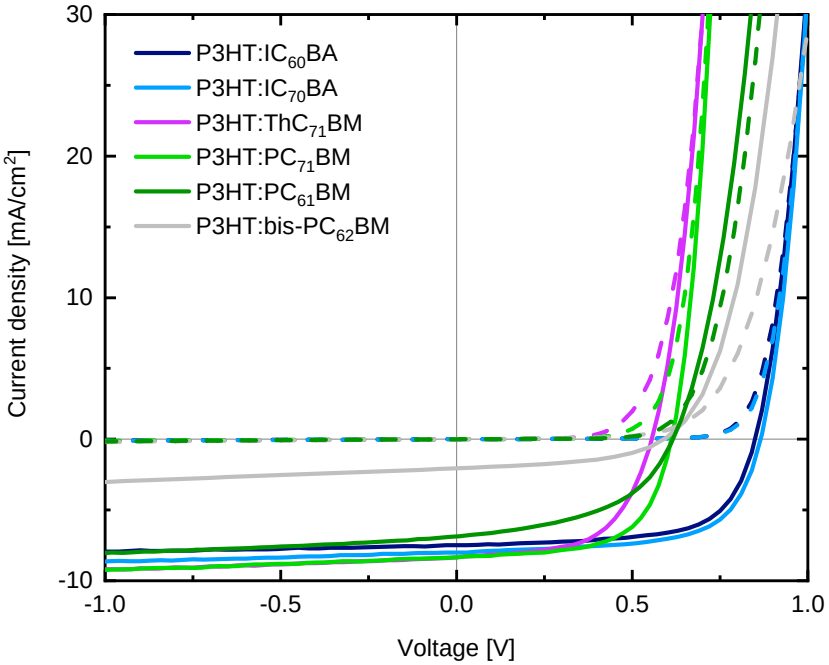

Figure 6.15: Summary of the *J*-*V*-curves of the above mentioned solar cell 'hero devices' with a light-harvesting layer fabricated from a nanoparticle dispersion. All solar cells are fabricated in inverted architecture, with a comparable light-harvesting layer thickness of around 50 nm. However, the concentration of fullerene inside the dispersion differs.

With a PCE of 4.5 %, the best solar cells could be achieved with a light-harvesting layer from the blend of P3HT:$IC_{70}BA$.

7 Stabilization of P3HT:Acceptor blends with a ternary approach

In the previous chapter (6), it was shown that some fullerenes such as $PC_{71}BM$ and $IC_{60}BA$ form stable nanoparticle dispersions in a blend with P3HT, while others, such as $PC_{61}BM$, tend to separate and lead to flocculation of the dispersion. While both the residual solubility and miscibility were investigated, the miscibility with the polymer is the most significant part (see 6.1). One way of changing the miscibility is by using a ternary system. Into the solution of blend, that does not form a stable dispersion, amounts of fullerenes that form stable dispersions in combination wit P3HT are added, resulting in a stable ternary blend, until at a specific amount, the dispersions starts to separate, as described in the first section. Using, for example, P3HT:$PC_{61}BM$ with $PC_{71}BM$, less fullerene separates compared to P3HT:$PC_{61}BM$, because of the incorporation of the fullerene into the nanoparticles. The investigation of the ternary blend dispersions was done in the bachelor thesis of *K. Bitsch*.
By changing the second acceptor from a fullerene derivative to an NFA (for NFA, see: 3.2.2), another acceptor material group is examined.
In the last section, instead of using a second acceptor, another donor material, the regiorandom P3HT, is used. Due to the amorphous phases of the rra-P3HT, the incorporation of the acceptor can be increased. These results are further examined in the bachelor thesis of *H. Bletzinger*.

7.1 Third component: fullerene

Using a blend of fullerenes has a lot of advantages in solution processed solar cells. For example, by using tiny amounts of bis-$PC_{62}BM$ in combination with $PC_{61}BM$, the formation of fullerene-rich clusters after thermal annealing is suppressed.[169] For other combinations, such as $PC_{61}BM$ and $PC_{71}BM$, the addition of $PC_{71}BM$ changes the crystallinity, resulting in less crystals with smaller sizes.[173, 174] These changes of the semi-crystallinity could also influence the nanoparticle formation process, thus increase the incorporation of fullerene into the nanoparticles. For the nanoparticles, the miscibility of P3HT and fullerene is a critical factor, as discussed in section 6.1.
In order to examine the influence of the suppressed separation, the previously mentioned blends of $PC_{61}BM$ and $PC_{71}BM$ in combination with P3HT are investigated at different fullerene ratios

at a constant ratio of P3HT to fullerene (1:1, by weight, total concentration of 2 g/L). Although it is known that the best solar cells are fabricated at a ratio of 1:0.8 (see 6.3), the ratio of 1:1 is chosen, assuming that some amount of fullerene might be lost during the reduction step.
In Figure 7.1 a, the measured nanoparticle size *versus* the amount of $PC_{61}BM$ is summarized immediately after nanoprecipitation. Initially, with all blend combinations, nanoparticle dispersions with measurable sizes are achieved. The nanoparticle size can be subdivided into two groups, depending on the excess of the respective fullerene. In blends with an excess of $PC_{61}BM$, the average nanoparticle size is slightly smaller, compared to blends with an excess of $PC_{71}BM$. While the residual solubility of $PC_{61}BM$ is rather low in the mixture and the fullerenes do not form stable nanoparticles on their own, the only explanation is an incorporation of $PC_{61}BM$ into the nanoparticles. At an excess of $PC_{61}BM$, less fullerene can be incorporated into the nanoparticles. By increasing the amount of $PC_{71}BM$, more fullerene gets incorporated into the nanoparticles, resulting in an increase in the average nanoparticle size.
After reduction, the results change due to a partly flocculation of fullerenes. To examine the fullerene loss during reduction, the absorbance spectra of the blends, redissolved in chloroform, are measured and the results of six chosen blends are summarized in Figure 7.2. Nevertheless, it should be mentioned that all dispersions were synthesized immediately after each other, resulting in a short holding time for the first reduced dispersions before centrifugation, enabling sedimentation. While blends with less than 10 % $PC_{71}BM$ flocculate during the reduction, in blends with $PC_{71}BM$ amounts in the range of 15 % and 40 %, some fullerene visually sediments.

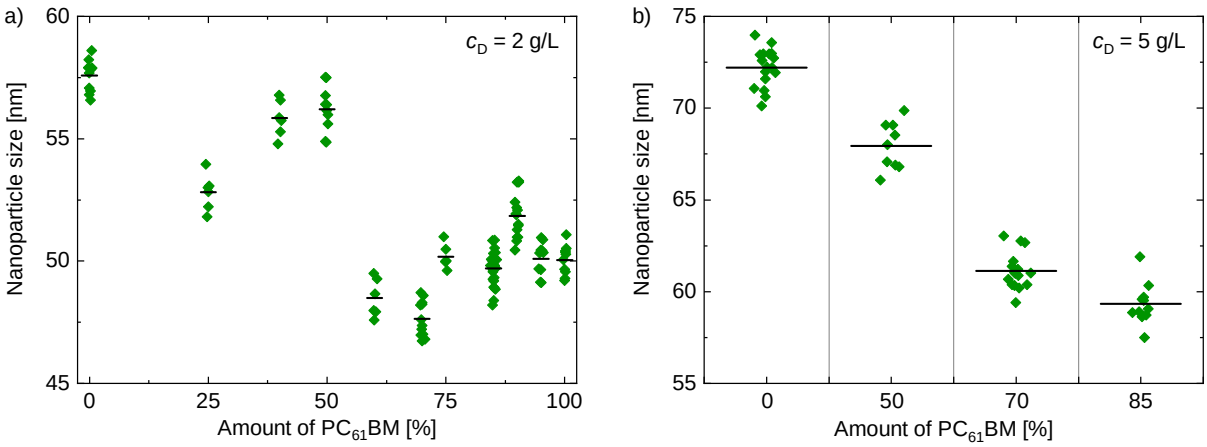

Figure 7.1: Nanoparticle size after nanoprecipitation, measured by DLS, *versus* the amount of $PC_{61}BM$. 0 % $PC_{61}BM$ corresponds to 100 % $PC_{71}BM$, while 50 % correspond to a $PC_{61}BM$:$PC_{71}BM$ ratio of 1:1 by weight. a) At a total concentration of 2 g/L, by slightly increasing the amount of $PC_{61}BM$, the average nanoparticle size does not differ. At 50 % $PC_{71}BM$, the nanoparticle size decreases. b) For four different fullerene ratios, dispersions with a higher concentration (c_D = 5 g/L) are synthesized for the fabrication of solar cells. At both concentrations, an increase of the amount of $PC_{61}BM$ results in a decreasing nanoparticle size.

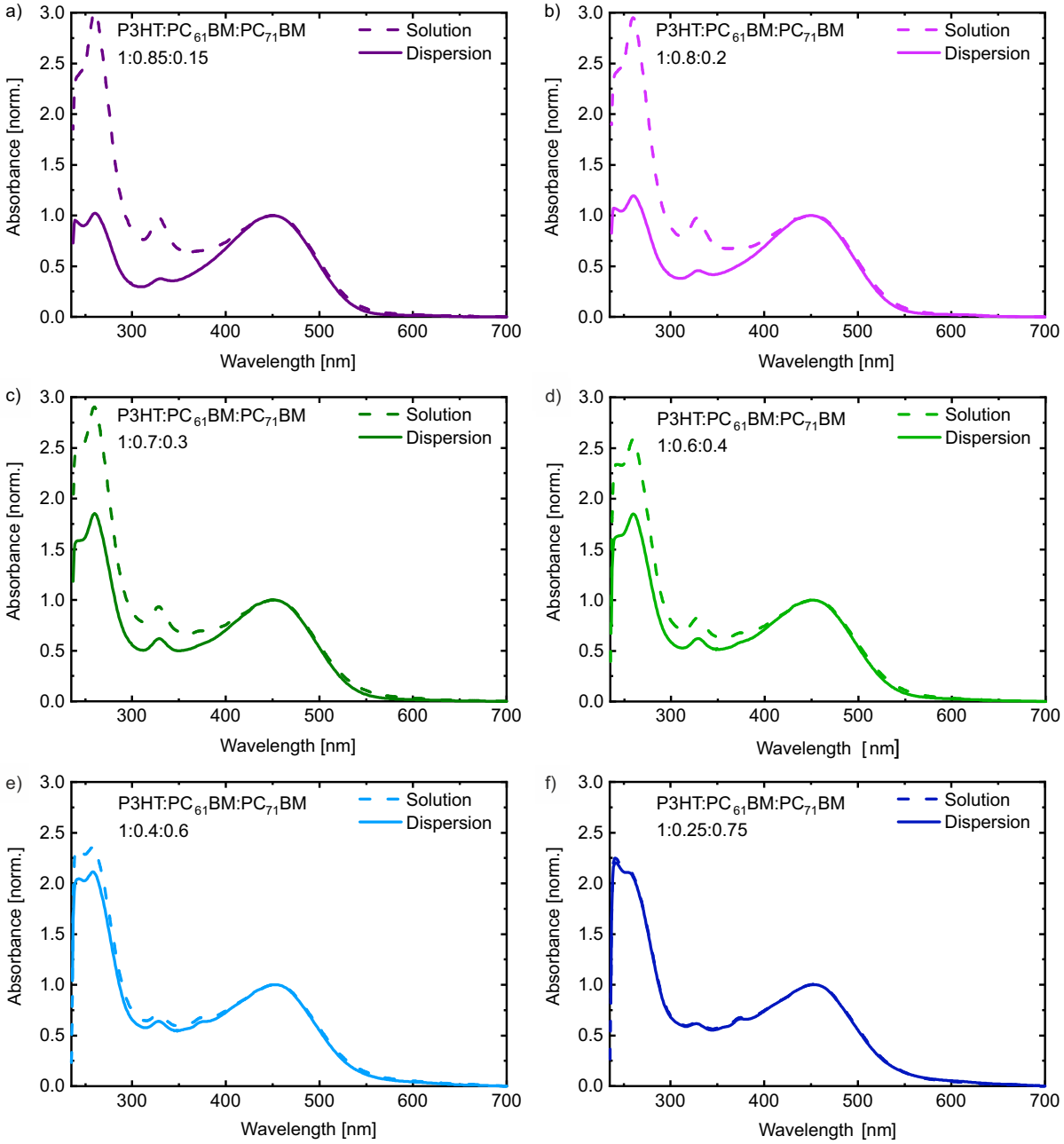

Figure 7.2: Absorbance measurements of different blends of P3HT:PC_{61}BM:PC_{71}BM at a total concentration of 2 g/L, normalized on the P3HT-Peak at 450 nm. The dashed line represents the reference solution in chloroform, the solid line corresponds to the dissolved dispersion after reduction. By increasing the amount of PC_{71}BM, where a) to f) correspond to 85 %, 80 %, 70 %, 60 %, 50 % and 25 % PC_{61}BM, respectively, an increase in PC_{71}BM results in reduced fullerene losses, with no noticeable loss for 75 % PC_{71}BM.

For the blend with more than 50 % PC_{71}BM, almost no fullerene is lost and the nanoparticle dispersion can be classified as stable.

The solid line corresponds to the reduced dispersion, while the dashed line represents the initial solution of the blend, both normalized on the P3HT peak at 450 nm. From the absorbance measurements, the spectra of the pure materials dissolved in chloroform are fitted to the blend spectra to calculate the ratio of the remaining materials. The calculated ratio is then compared to the initial ratio, with the results summarized in Table 7.1. For the ratio of, for example, 1:0.5:0.5, a maximum of 50 % $PC_{61}BM$ and 50 % $PC_{71}BM$ is possible. In reality, there are only 40 % $PC_{61}BM$ and 47 % $PC_{71}BM$ inside the dispersion, resulting in a reduced amount of 87 % fullerene, compared to P3HT. In all measured dispersions, it is always assumed that no P3HT is lost in the process. However, by reducing the volume from 4 mL (3 mL ethanol with 1 mL chloroform) to 1 mL (nanoparticle dispersion with only ethanol), small uncertainties of the total concentration due to slightly volume variances are possible, which can result in small concentration deviations. In addition, the increase of $PC_{71}BM$ results in an increase in the signal at 450 nm and hinders an optical comparison. In order to compensate this, variations are neglected by normalizing the absorbance to the local maximum of P3HT at 450 nm.

Table 7.1: Calculation of the ratio of the remaining material of P3HT, $PC_{61}BM$ and $PC_{71}BM$ from the absorbance spectra in Figure 7.2, compared to the initial ratio of the blend at c_D = 2 g/L. While no P3HT is lost during the reduction step, a lot of fullerene sediments for high amounts of $PC_{61}BM$. By decreasing the amount of $PC_{61}BM$, less fullerene sediments, and more $PC_{61}BM$ remains inside the dispersion.

Initial ratio [a)]	P3HT	$PC_{61}BM$	$PC_{71}BM$
1:0.85:0.15	1	0.15	0.08
1:0.80:0.20	1	0.2	0.1
1:0.75:0.25	1	0.3	0.15
1:0.70:0.30	1	0.33	0.2
1:0.65:0.35	1	0.34	0.25
1:0.60:0.40	1	0.38	0.32
1:0.50:0.50	1	0.4	0.47
1:0.40:0.60	1	0.38	0.58
1:0.25:0.75	1	0.25	0.75

[a)] Initial ratio of P3HT:$PC_{61}BM$:$PC_{71}BM$

The results of the calculation of the fullerene that remains inside the dispersion support the idea of an increased $PC_{61}BM$ incorporation into the nanoparticles, assisted by $PC_{71}BM$. According to the literature, for solution processed solar cells, the formation of an acceptor-alloy of the fullerene blend is known.[175, 176] Notably, in dispersion, all blends with less than 75 % $PC_{71}BM$ show a sedimentation of both $PC_{71}BM$ and $PC_{61}BM$. Due to the miscibility

of $PC_{61}BM$ and $PC_{71}BM$, the loss of $PC_{71}BM$ can be explained. While small amounts of $PC_{71}BM$ sediment, an increased fraction of $PC_{61}BM$, compared to the binary blend, remains inside the dispersion, suggesting an exchange of $PC_{71}BM$ through $PC_{61}BM$. For a blend of P3HT:$PC_{71}BM$, the fullerene does not sediment.

The best known fullerene blend is PCBM with technical grade (tech-PCBM). Typically, most of the material is $PC_{61}BM$, followed by $PC_{71}BM$ and other derivatives.[173, 177] Although the fullerenes are incompletely separated, they nominally have the same high purity. The separation of the fullerene is both expensive and requires a lot of energy. Therefore, the renunciation of the separation is an advantage.
Since blends of 90 % $PC_{61}BM$ and 10 % $PC_{71}BM$ initially result in a measurable dispersion, tech-PCBM with the same ratio is investigated. While initially nanoparticles were formed, after a few minutes, the dispersions flocculated, resulting in separation of the dispersion. Presumably, higher derivatives or some impurities lead to flocculation, ruling out tech-PCBM for further studies.
To examine the influence of the $PC_{61}BM$ amount on the solar cell performance, four of the fullerene ratios are additionally evaluated at a total concentration c_D = 5 g/L. While dispersions with more than 85 % $PC_{61}BM$ flocculated, a rather quick processing of the light-harvesting layers after the synthesis of the dispersion is necessary. The distribution of the nanoparticle size *versus* the amount of $PC_{61}BM$ is illustrated in Figure 7.1 b. For the chosen ratios, the trend of an increase in average nanoparticle size by decreasing the amount of $PC_{61}BM$ is also applicable.
To prevent additional sedimentation due to holding times, each dispersion is used immediately after reduction. Due to this, almost all fullerene remains inside the dispersion, as analyzed by the results of the calculations, as shown in Table 7.2.
This is especially important for dispersions with less than 50 % $PC_{71}BM$. The absorbance spectra of the different blends are summarized in Figure 7.3 a, again normalized to the P3HT peak

Table 7.2: Calculation of the ratio of the remaining material of P3HT, $PC_{61}BM$ and $PC_{71}BM$ from the absorbance spectra in Figure 7.3 a, compared to the initial ratio of the blend at a concentration of c_D 5 g/L.

Initial ratio [a)]	P3HT	$PC_{61}BM$	$PC_{71}BM$
1:0.85:0.15	1	0.60	0.10
1:0.7:0.3	1	0.55	0.25
1:0.5:0.5	1	0.47	0.46
1:0:1	1	0	0.98

[a)] Initial ratio of P3HT:$PC_{61}BM$:$PC_{71}BM$

at 450 nm. The solid line corresponds to the reduced dispersion, whereas the dashed line is the reference from the initial solution.

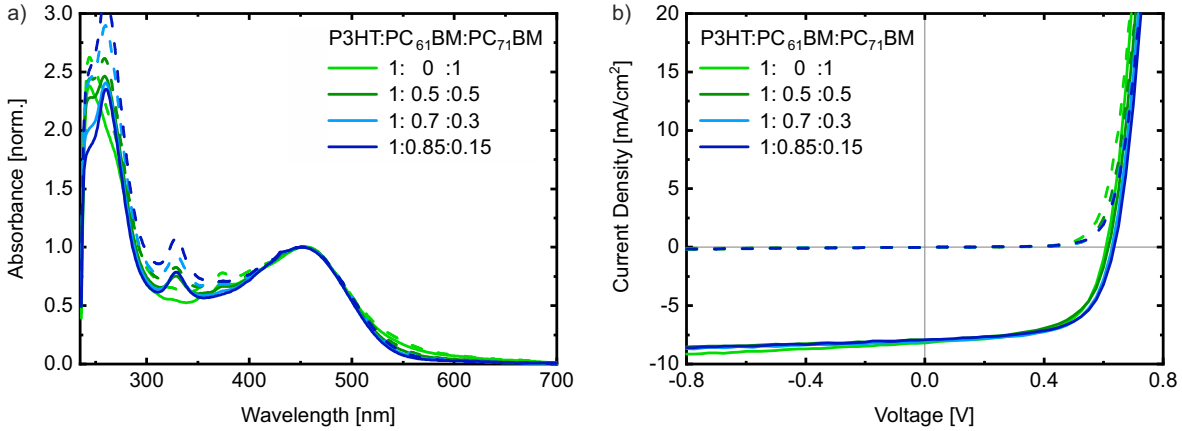

Figure 7.3: a) Absorbance measurements of the dispersions with different blend ratios. The dashed line corresponds to initial solution, while the solid line represents the reduced dispersion. b) *J*-*V* curve of solar cells with a light-harvesting layer fabricated from the dispersions in a, with a light-harvesting layer thickness of 55 nm and a total concentration of 5 g/L. For all four dispersions, similar results can be achieved.

The results in Table 7.2 also support the idea that $PC_{71}BM$ helps to incorporate $PC_{61}BM$ into the blend nanoparticle. By reducing the $PC_{71}BM$ amount, less $PC_{61}BM$ can be incorporated into the nanoparticles, which leads to an excess of $PC_{61}BM$ and therefore a sedimentation, resulting in a smaller average nanoparticle size. However, by comparing the total concentrations from Table 7.1 and Table 7.2, a temporal influence on the stabilization of the dispersion can be suggested, due to a reduced material loss for reduced holding times. For dispersions with less than 50 % $PC_{71}BM$, over time, $PC_{61}BM$ sediments. However, for the total concentration of 5 g/L, within two hours after centrifugation, a much lower material sedimentation occurred.
From these four dispersions with a total concentration of 5 g/L, solar cells in inverted architecture are fabricated. The *J*-*V* curves of the four 'hero devices' are shown in Figure 7.3 b, with the key parameters listed in Table 7.3.
For all dispersions, smooth layers without comets could be fabricated. With a light-harvesting layer thickness of approximately 55 nm at four deposition steps, the layer thickness is comparable, indicating that the loss of fullerene is negligible. While FF and PCE differ slightly among the variations, the solar cells with more $PC_{61}BM$ show a slightly higher V_{OC}, while the solar cells with more $PC_{71}BM$ have a slightly increased J_{SC}. In chapter 6.3, the optimal blend ratio of P3HT:$PC_{71}BM$ of 1:0.8 was identified, resulting in solar cells with a PCE of 3.2 %. The data for this blend combination are added to Table 7.3, last row. Due to the slightly reduced V_{OC} and FF at an increased J_{SC}, the PCE is similar to the ternary solar cells. The advantage of using

Table 7.3: Key parameters of the nanoparticulate solar cells fabricated from dispersion, incorporating P3HT:$PC_{61}BM$:$PC_{71}BM$ blend layers at four different blend ratio (c_{P3HT} = 2.5 g/L, P3HT:fullerene 1:1 by weight) and light-harvesting layer thicknesses of 55 nm.

Inital ratio[a)]	V_{OC} [mV]	J_{SC} [mA/cm^2]	FF [%]	PCE [%]
1:0.85:0.15	631 ± 3	8.0 ± 0.1	62 ± 1	3.2 ± 0.1
1:0.7:0.3	624 ± 5	8.0 ± 0.1	62 ± 1	3.1 ± 0.1
1:0.5:0.5	616 ± 1	7.9 ± 0.1	61 ± 1	2.9 ± 0.1
1:0:1	607 ± 3	8.1 ± 0.1	62 ± 1	3.0 ± 0.1
1:0:0.8[b)]	625 ± 2	8.4 ± 0.1	61 ± 1	3.2 ± 0.1

[a)] Initial ratio of P3HT:$PC_{61}BM$:$PC_{71}BM$; [b)] Result from Table 6.4, with a P3HT:$PC_{71}BM$ ratio of 1:0.8 by weight;

the ternary system with the fullerene blend instead of using only $PC_{71}BM$ is the price. Given that $PC_{71}BM$ is more rare than $PC_{61}BM$, $PC_{71}BM$ is more expensive. However, the stability of the ternary material dispersion is reduced for ratios with less than 50 % $PC_{71}BM$, resulting in sedimentation and therefore material loss over time.

To prove that this concept also works for other fullerenes, further combinations are investigated. While combinations of two C_{60}- or two C_{70}-fullerenes could also work, because of their similar absorbance, an investigation is difficult. In the resulting calculation, it cannot be determined which material sediments. Therefore, only absolute fullerene contents can be specified. Only in the case of a successful incorporation of all the material into the nanoparticles, a statement could be made. However, neither blending bis-$PC_{72}BM$ to the other C_{70}-fullerenes nor the blend of C_{60}-fullerenes with $IC_{60}BA$ resulted in a successful incorporation without loss of material. Instead, huge amounts of fullerenes sedimented. Due to the high similarity of the absorbance spectra, it cannot be determined whether the formation of an acceptor alloy resulted in an even sedimentation of both fullerenes or whether only one of the fullerenes flocculated. Therefore, no further predictions can be made.

Both the use of bis-$PC_{72}BM$ with $IC_{60}BA$ and bis-$PC_{62}BM$ with the stable C_{70}-fullerenes resulted in an immediate sedimentation of the material and no remaining bis-PCBM in any dispersion. While both $IC_{60}BA$ and $IC_{70}BA$ form stable nanoparticles with P3HT, also the ternary blend does, without losing any fullerene for higher concentrations, as depicted in Table 7.4

With the dispersions from the ternary blend, solar cells are fabricated in inverted architecture, with different light-harvesting layer thicknesses. Because $IC_{70}BA$ absorbs more visible light, a slightly higher J_{SC} is expected for the ternary blend, compared to solar cells with P3HT:$IC_{60}BA$ from chapter 6.3. Instead, the solar cell performance is similar to solar cells from P3HT:$IC_{60}BA$, as summarized in Table 7.5, achieving a PCE of 4 %.

Table 7.4: Calculation of the ratio of the remaining material of P3HT, $IC_{60}BA$ and $IC_{70}BA$ from the measured absorbance spectra, compared to the initial ratio of the blend at a P3HT concentration of c_{P3HT} 2.5 g/L.

Initial ratio [a)]	P3HT	$IC_{60}BA$	$IC_{70}BA$
1:1:0	1	1	0
1:0.4:0.4	1	0.4	0.4
1:0:1	1	0	1

[a)] Initial ratio of P3HT:$IC_{60}BA$:$IC_{70}BA$

Table 7.5: Key parameters of the nanoparticulate solar cells with light-harvesting layers fabricated from dispersions with a P3HT:$IC_{60}BA$:$IC_{70}BA$ ratio of 1:0.4:0.4 (c_{P3HT} = 2.5 g/L) at four different thicknesses of the light-harvesting layer.

Layer thickness	V_{OC} [mV]	J_{SC} [mA/cm^2]	FF [%]	PCE [%]
60	853 ± 1	7.3 ± 0.1	63 ± 1	4.0 ± 0.1
85	850 ± 2	7.4 ± 0.1	61 ± 1	3.8 ± 0.1
100	847 ± 2	8.0 ± 0.1	59 ± 2	3.9 ± 0.2
145	845 ± 2	9.2 ± 0.1	51 ± 1	4.0 ± 0.1

The last combination that is investigated is the blend with ThCBM. Given that PCBM and ThCBM are rather similar, as known from the literature, the difference is expected to be negligible.[103] Due to these similarities, in addition to the combination of $ThC_{61}BM$ and $ThC_{71}BM$ with P3HT, also blends of $ThC_{61}BM$ with $PC_{71}BM$ and $PC_{61}BM$ with $ThC_{71}BM$ are examined. Because it was already shown that an excess of $PC_{61}BM$ leads to increased sedimentation, the lowest chosen amounts of C_{70}-fullerene in the blend are 15 %. The results of all combinations are listed in Table 7.6.

The blends with a ratio of 0.85:0.15 show a drastically reduced ratio, while the best final ratio can be achieved with P3HT, $PC_{61}BM$ and $ThC_{71}BM$. Dispersions with less than 50 % C_{70}-fullerene show a rather quick sedimentation and high losses of fullerenes. Only the combination of P3HT with $PC_{61}BM$ and $ThC_{71}BM$ results in a stable dispersion with almost no sedimentation. Therefore, the dispersions from this ternary blend are chosen for the fabrication of solar cells, with the key parameters listed in Table 7.7. Solar cells from the ternary blend have a V_{OC} of 586 mV. Interestingly, the V_{OC} lies directly between the V_{OC} of solar cells with a light-harvesting layer from P3HT:$ThC_{71}BM$ (557 mV) and P3HT:$PC_{71}BM$ (608 mV). However, due to the reduced J_{SC}, the PCE of 2.7 % is lower than for solar cells from P3HT:$PC_{61}BM$:$PC_{71}BM$ with a PCE of 3.2 %, resulting in solar cells that are comparable to P3HT:$ThC_{71}BM$.

Table 7.6: Calculation of the ratio of the remaining material of P3HT, C_{60}-fullerene and C_{70}-fullerene from the measured absorbance spectra, compared to the initial ratio of the blend at a concentration of c_D 5 g/L, with either ThCBM or PCBM.

Initial ratio [a)]	P3HT	$ThC_{61}BM$	$ThC_{71}BM$
1:1:0	1	0.3	0
1:0.85:0.15	1	0.37	0.02
1:0.5:0.5	1	0.4	0.3
1:0:1	1	0	0.95

Initial ratio [a)]	P3HT	$ThC_{61}BM$	$PC_{71}BM$
1:1:0	1	0.3	0
1:0.85:0.15	1	0.35	0
1:0.7:0.3	1	0.4	0.15
1:0.5:0.5	1	0.3	0.3
1:0:1	1	0	1

Initial ratio [a)]	P3HT	$PC_{61}BM$	$ThC_{71}BM$
1:1:0	1	0.35	0
1:0.85:0.15	1	0.5	0.1
1:0.7:0.3	1	0.48	0.12
1:0.5:0.5	1	0.45	0.5
1:0:1	1	0	0.95

[a)] Initial ratio of P3HT:C_{60}-fullerene:C_{70}-fullerene

Table 7.7: Key parameters of nanoparticulate solar cells with light-harvesting layers fabricated from dispersions with a P3HT:$PC_{61}BM$:$ThC_{71}BM$ ratio of 1:0.5:0.5 (c_{P3HT} = 2.5 g/L) at four different light-harvesting layer thicknesses.

Layer thickness	V_{OC} [mV]	J_{SC} [mA/cm^2]	FF [%]	PCE [%]
60	586 ± 3	7.8 ± 0.1	60 ± 1	2.7 ± 0.1
85	586 ± 4	8.0 ± 0.1	56 ± 1	2.6 ± 0.1
110	590 ± 1	8.6 ± 0.1	52 ± 2	2.6 ± 0.2
150	585 ± 2	9.0 ± 0.2	44 ± 1	2.3 ± 0.1

In summary, fullerene blends with P3HT show the stabilization of an otherwise unstable dispersion by the addition of fullerenes that form a stable dispersion in combination with P3HT, resulting in a ternary dispersion blend. Depending on the ratio and the chosen fullerene derivatives, stable dispersions can be achieved due to an incorporation into the nanoparticles. The ratios indicate that up to this amount of C_{60}-fullerenes, stable dispersions with less than 30 % fullerene loss can be achieved, as summarized in Table 7.8 for all combinations. By adding $PC_{71}BM$ to P3HT and the respective fullerenes, a ternary dispersion with up to 85 % of $PC_{61}BM$ and slightly less than 50 % of $ThC_{61}BM$ could be synthesized, respectively. With $ThC_{71}BM$, less than 70 % of $PC_{61}BM$ and approximately 50 % of $ThC_{61}BM$ could be stabilized inside the dispersion. For the combination of P3HT:$PC_{61}BM$:$IC_{70}BA$, less than 50 % of $PC_{61}BM$ can be stabilized inside the ternary blend. All further combinations of $IC_{60}BA$, which forms a stable dispersion in the binary blend, result in stable dispersions. Both bis-$PC_{62}BM$ and bis-$PC_{72}BM$ result in dispersions with no remaining amount of bis-PCBM. Combinations of fullerenes with the same core, such as $IC_{60}BA$ and $PC_{61}BM$ or bis-$PC_{72}BM$ and $PC_{71}BM$, resulted in sedimentation of fullerenes. Due to the similar absorbance, the calculation of the remaining fractions is not possible.

Table 7.8: Combinations of two fullerenes in a blend with P3HT (starting ratio: P3HT:fullerene 1:1 by weight). After nanoprecipitation and reduction of the dispersions, some ratios remained stable, while others tend to separate in all blends. The ratios indicate that up to this amount of C_{60}-fullerene, a dispersion is formed, with separation of less than 30 % of the respective fullerenes after reduction.

Fullerenes	$PC_{71}BM$	$ThC_{71}BM$	bis-$PC_{72}BM$	$IC_{70}BA$	$IC_{60}BA$
$PC_{61}BM$	85 %	< 70 %	X	50 %	X*
$ThC_{61}BM$	< 50 %	50 %	X	-	X*
$IC_{60}BA$	✓	-	X	✓	-
bis-$PC_{62}BM$	X	X	X	X	X*
bis-$PC_{72}BM$	X*	X*	-	X*	X

-: not tested; <: less than; ✓: always stable dispersions obtained; X: no stable dispersions obtained; X*: rather not stable, inconclusive results due to similar absorbance, no calculation possible.

7.2 Third component: NFA

While the addition of a fullerene that forms stable dispersions to an otherwise unstable blend of P3HT and fullerene resulted in a stabilization effect of the ternary blend dispersion, this concept is applied to NFAs. Preliminary experiments showed that NFAs do not form stable dispersions in combination with P3HT. They also have no measurable residual solubility in ethanol or the

mixture. While some combinations lead to an immediate flocculation of the acceptor, such as ITIC and IDTBR, the use of Y6 results in a collapse of the dispersion, with a sediment of both Y6 and P3HT in ethanol. This collapse indicates a high miscibility of the materials, but the dispersions could not be stabilized. Solely the combination of IDFBR and P3HT resulted in stable dispersions. Due to the similar absorbance, no efficient solar cells could be fabricated (see 7.3).

According to the literature, the use of small amounts of fullerenes, mostly $PC_{71}BM$, in a blend with polymers and the NFAs improved the morphology.[178, 179, 180, 181] Chen et al. showed that the domain size of the polymer increased because of the fullerene, resulting in a more distinct interface between donor and acceptor that facilitates the charge carrier transport and leads to less charge recombination. Therefore, the ternary solar cells are more efficient than the respective binary solar cells.[178, 182]

Starting with ITIC, 5 different ratios of P3HT and $PC_{71}BM$ are investigated, with a ratio of P3HT:$PC_{71}BM$:ITIC between 1:0.5:0.5 and 1:0.85:0.15. For all blends, an initial nanoparticle size between 45 nm and 55 nm could be achieved, but the measurement was always disturbed by larger particles, while the number of larger particles increased over time. Immediately after nanoprecipitation, the dispersion has a distinctive dark blue color impression that differs from the typical red of P3HT dispersions. During the reduction, a large amount of ITIC is lost, resulting in less than 5 % ITIC in the final dispersion, as illustrated in Figure 7.4 a, and again a red dispersion with a dark blue sediment.

The blends of P3HT:$PC_{71}BM$:Y6 differ from the blend containing ITIC. While initially a dispersion can by synthesized, during the size measurement, the nanoparticles grow and aggregates inside the dispersion form. During the reduction, a huge amount of material sediments, consisting of not only Y6, but also P3HT and PCBM, resulting in a collapse of the dispersion, with all material sedimented, as depicted in Figure 7.4 b.

With IDTBR and P3HT:$PC_{71}BM$, initially, nanoparticles form. This results in a blue dispersion, compared to the red P3HT:$PC_{71}BM$ dispersion. After reduction, a lot of IDTBR is sedimented and the materials are separated. By examining the dispersion and the sediment, this separation is visible, as illustrated in Figure 7.4 c for EH-IDTBR. While the color of the dispersion changes to the typical P3HT red, the sediment is blue, showing the same separation for both EH-IDTBR and O-IDTBR.

Therefore, the addition of an NFA to the dissolved blend solution with a nanoprecipitation afterwards does not achieve stable nanoparticle dispersions that contain any NFA. While some blends initially result in measurable nanoparticle dispersions, the NFAs flocculate during reduction, resulting in material separation. By comparing the results of the absorbance spectra, it seems that tiny amounts of NFA remain inside the redissolved dispersion, as shown in Fig-

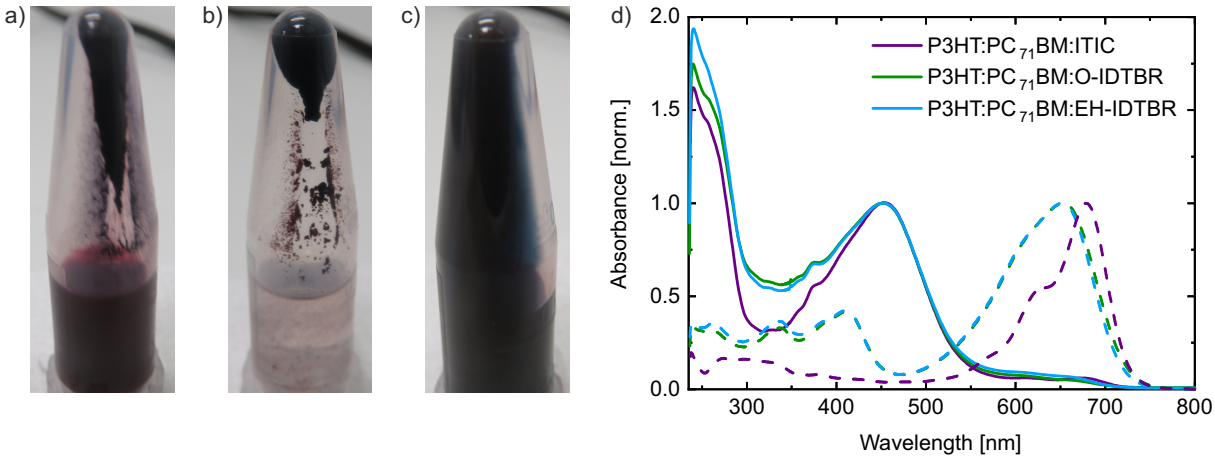

Figure 7.4: Material separation of a dispersion with P3HT:$PC_{71}BM$ and the different NFAs. a) By using ITIC, mostly ITIC sediments, while a stable dispersion without ITIC remains. b) Adding Y6 to a dispersion leads to a collapse of the dispersion and total material separation. c) With IDTBR (here: EH-IDTBR), the NFA sediments, while a stable dispersion remains. As the results of O-IDTBR and EH-IDTBR did not differ, only one is shown here. d) The absorbance spectra of the different dispersions, redissolved in chloroform, show that only tiny amounts of NFA remain inside the final dispersion. For the blend with Y6, the measurement of an absorbance spectrum was not possible due to total separation.

ure 7.4 d. However, in some cases, the remaining NFA worsens the layer formation and leads to rough layers that are mostly shorted, whereas in other cases, no remaining NFA could be found in the layer.

7.3 Third component: rra-P3HT

Instead of adding another electron acceptor, there is also the possibility of adding another donor. Due to the high similarity to RR-P3HT and the miscibility, rra-P3HT is further investigated. The main difference between the two P3HTs is the different arrangement of the monomers (see 3.1.1), resulting in semi-crystalline domains for RR-P3HT and amorphous domains for rra-P3HT. These amorphous domains can enable an incorporation of acceptor, while the two P3HTs are miscible and therefore allow the formation of ternary blend dispersions.

Similar to RR-P3HT, pure rra-P3HT, dissolved in chloroform, initially forms nanoparticles after nanoprecipitation into ethanol, as illustrated in Figure 7.5. Because of the missing semi-crystallinity of rra-P3HT, the typical red-shift of RR-P3HT does not occur, resulting in an orange dispersion, comparable to the initial solution.

The average nanoparticle size does not differ when varying the concentration or illumination conditions, always resulting in an initial average nanoparticle size of around 45 nm. However, during the reduction, this changes. By increasing the illumination during nanoprecipitation, the nanoparticles aggregate during the reduction, which results in flocculation. This effect increases

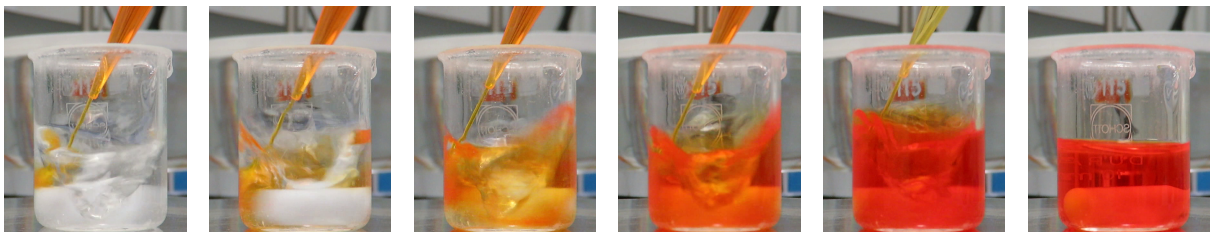

Figure 7.5: Real time pictures of the nanoprecipitation of rra-P3HT, dissolved in chloroform. The solution is injected into the beaker with the stirred nonsolvent. The solubility is rapidly reduced, which leads to nanoparticle formation. The red-shift known from RR-P3HT does not occur.

strongly by increasing the irradiation intensity and can even result in a total flocculation immediately after nanoprecipitation. This light-sensitivity is a problem for the characterization. Up to date, every measurement that contains a light source, such as absorbance measurements, PLQY measurements and even the DLS measurements, results in the collapse of the dispersion during the measurement. Therefore, a reduced number of five DLS measurements with a reduced measurement time of 6 s is chosen. Each dispersion is diluted in at least two cuvettes to compare the results. To evaluate whether rra-P3HT is suitable as a third component, the nanoparticle formation in a blend with RR-P3HT is first investigated, with the results listed in Table 7.9. As previously shown, rra-P3HT forms nanoparticles with an average size of 45 nm after nanoprecipitation, but during reduction, the nanoparticle size increases. By adding RR-P3HT to rra-P3HT, the nanoparticle size increases slightly, compared to dispersions with rra-P3HT after nanoprecipitation. However, after reduction, the nanoparticle sizes do not differ from the initial nanoparticle size. All combinations of rra-P3HT and RR-P3HT lead to nanoparticle dispersions without any material loss and are therefore considered as stable blends.

Table 7.9: Average nanoparticle sizes d of different blends of rra-P3HT and RR-P3HT, after nanoprecipitation and after reduction, with a concentration c_D = 2 g/L and no additional light source.

		d [nm]	d [nm]
rra-P3HT	RR-P3HT	after nanoprecipitation	after reduction
1	0	45 ± 1	61 ± 1
0.75	0.25	47 ± 1	47 ± 1
0.5	0.5	49 ± 1	50 ± 1
0.25	0.75	58 ± 1	58 ± 1
0	1	80 ± 1	78 ± 1

With this knowledge, binary blends of rra-P3HT and fullerenes or NFAs are investigated, resulting in nanoparticles with an initial average size between 40 nm and 80 nm, depending on the P3HT:acceptor ratio. The average nanoparticle sizes of the dispersions containing different acceptors after nanoprecipitation and reduction are summarized in Figure 7.6.
After the reduction step, the average size increases drastically, resulting in nanoparticles in the range of 60 nm and 90 nm for $PC_{61}BM$ and $PC_{71}BM$ and above 100 nm for $IC_{60}BA$. Notably, the blend dispersions of ICBA and rra-P3HT do not remain stable for more than a few hours, while the blends with the two different PCBMs both remain stable for at least a few days.
The combination of rra-P3HT with NFAs is comparable to RR-P3HT with NFAs, with most blends not remaining stable. While the blends of rra-P3HT with Y6 and CO_i8DFIC result in dispersions that grow during the measurements, ITIC seems to form a measurable dispersion. However, after reduction, most of the NFA and some rra-P3HT is sedimented, resulting in a smaller nanoparticle size. The attempt of fabricating layers from the blends of ITIC:rra-P3HT and CO_i8DFIC:rra-P3HT resulted in very rough layers that looked like sandpaper, rendering them not useful. For EH-IDTBR:rra-P3HT, the NFA flocculated again. Only in combination with O-IDTBR or IDFBR, stable dispersions could be achieved, with a huge amount of material remaining inside the dispersion.
To further investigate rra-P3HT, a blend dispersion with either O-IDTBR, $IC_{60}BA$ or IDFBR is synthesized at a total concentration of 5 g/L and a donor:acceptor ratio of 1:1, with the goal of

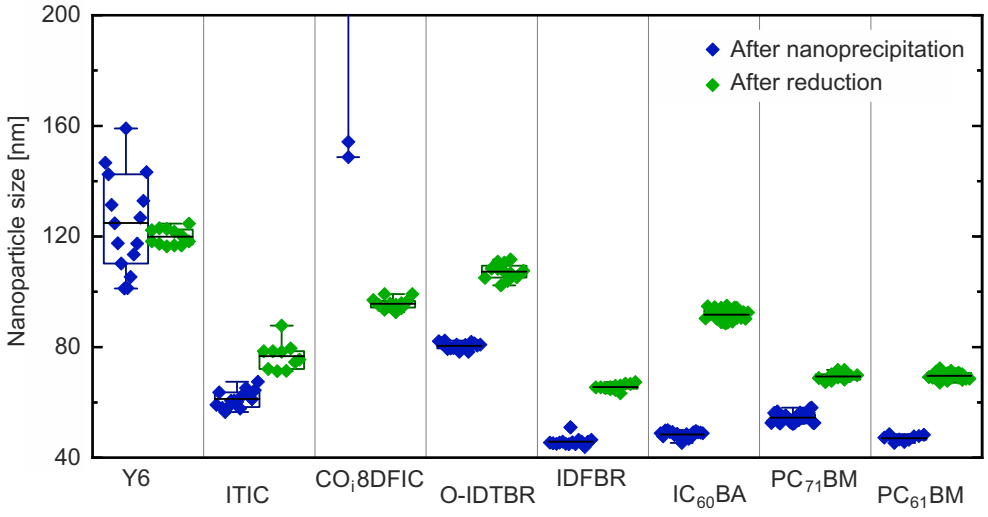

Figure 7.6: Average nanoparticle sizes of the s of rra-P3HT and different acceptors (ratio 1:1 by weight), at a total concentration of 2 g/L, measured immediately after nanoprecipitation (blue squares) and after reduction (green squares). For each dispersion, at least 2 different samples are measured, due to the degradation of the dispersions during the DLS measurement.

fabricating solar cells. To compare these results, blend dispersions with the same acceptors and RR-P3HT are fabricated, with the average nanoparticle sizes listed in Table 7.10.

Table 7.10: Average nanoparticle sizes d of different blends, after nanoprecipitation and after reduction, with a concentration c_D of 5 g/L.

Donor	Acceptor	d [nm] after nanoprecipitation	d [nm] after reduction
rra-P3HT	IDFBR	52 ± 1	83 ± 2
rra-P3HT	O-IDTBR	90 ± 1	110 ± 2
rra-P3HT	ICBA	58 ± 2	130 ± 3
RR-P3HT	IDFBR	67 ± 2	63 ± 1
RR-P3HT	O-IDTBR	113 ± 3	127 ± 4
RR-P3HT	ICBA	70 ± 2	74 ± 2

Notably, the light sensitivity of rra-P3HT, resulting in flocculation, is strong. Therefore, no additional light source is used for the nanoprecipitation of RR-P3HT to enable a comparison between the two P3HTs. This results in slightly increased average nanoparticle sizes and sedimentation in the blends with RR-P3HT, as depicted in Figure 7.7 a for rra-P3HT and in Figure 7.7 b for RR-P3HT.

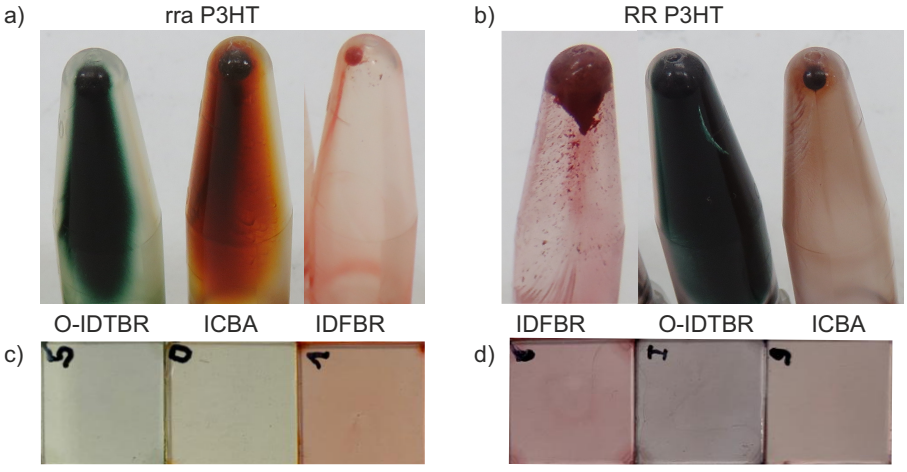

Figure 7.7: Nanoprecipitation of a) rra-P3HT and b) RR-P3HT, with different acceptor materials, resulting in a sedimentation of the acceptor after reduction. However, from the final dispersion, layers of the blends from c) rra-P3HT and d) RR-P3HT could be fabricated, with a distinct color impression.

While a huge amount of NFA is lost for the blend with RR-P3HT, in combination with rra-P3HT, the material loss is reduced. Dispersion of rra-P3HT:IDFBR show almost no material

loss during reduction. The fabrication of layers on glass substrates, as shown in Figure 7.7 c-d, results in smooth layers with a distinct color impression, indicating that some acceptor remains inside the dispersions. Otherwise, the layers would remain bright orange for the blends of rra-P3HT and dark red for the blends of RR-P3HT. From these dispersions, solar cells in inverted architecture are fabricated, with a light-harvesting layer thickness of around 45 nm. The results are summarized in Table 7.11. The *J*-*V* curves of the respective blends are shown in Figure 7.8.

Table 7.11: Solar cell key parameters of different blends, with rra-P3HT or RR-P3HT. The light-harvesting layers were thermal annealed at 150 °C.

Donor	Acceptor	V_{OC} [mV]	J_{SC} [mA/cm^2]	FF [%]	PCE [%]
rra-P3HT	IDFBR	381 ± 84	0.1 ± 0.1	25 ± 1	0.01 ± 0.01
rra-P3HT	O-IDTBR	671 ± 13	1.1 ± 0.1	31 ± 1	0.2 ± 0.1
rra-P3HT	ICBA	131 ± 38	0.1 ± 0.1	26 ± 1	0
RR-P3HT	IDFBR	707 ± 38	1.9 ± 0.1	35 ± 3	0.5 ± 0.1
RR-P3HT	O-IDTBR	533 ± 18	6.4 ± 0.1	44 ± 1	1.5 ± 0.1
RR-P3HT	ICBA	865 ± 3	6.3 ± 0.1	57 ± 1	3.1 ± 0.1

With rra-P3HT, only the combination of O-IDTBR results in solar cells with a significant PCE, with a V_{OC} that is comparable to the V_{OC} of solar cells from RR-P3HT:$PC_{71}BM$. The rather low J_{SC} of the blends with rra-P3HT could result from the amorphous domains of rra-P3HT, leading to a poor charge carrier transport.

Solar cells with a light-harvesting layer fabricated from dispersions containing RR-P3HT delivered a decent PCE. However, it should be noted that only two solar cells with O-IDTBR were not shorted due to the rough layers. The solar cells with IDFBR have a V_{OC} of 700 mV, while they lack in J_{SC} and FF, resulting in a PCE of only 0.5 %. The solar cells with ICBA are too thin, which results in a decreased J_{SC}, compared to the results of the 'hero devices' from section 6.3.

These results show that the use of rra-P3HT does not lead to efficient solar cells. Nevertheless, they also show that rra-P3HT enables the incorporation of NFAs into the nanoparticles, resulting in dispersion that are stable enough to fabricate smooth layers. The combination of rra-P3HT and RR-P3HT could enable the synthesis of dispersions with an NFA such as O-IDTBR, that can be used for the light-harvesting layers of solar cells. From solution, the blends of P3HT:O-IDTBR deliver solar cells with a PCE of 6.4 %.[127] Therefore, different NFAs are invesitaged, at a total concentration of 2 g/L. While stable nanoparticle dispersions could be achieved for

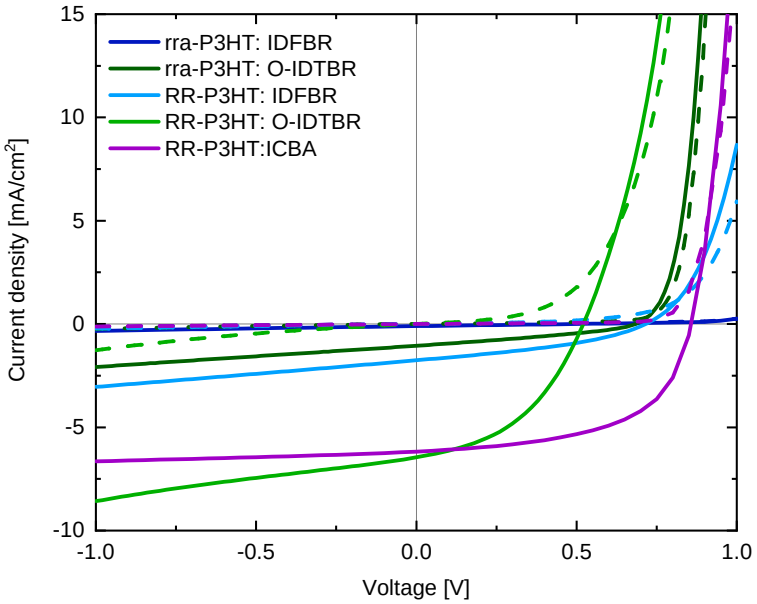

Figure 7.8: *J-V* curves of solar cells with either RR-P3HT or rra-P3HT as donor and IDFBR, O-IDFBR or $IC_{60}BA$ as acceptor.

the P3HT-blends with IDFBR and O-IDTBR, as shown in Table 7.12, the use of CO_i8DFIC, Y6 and ITIC leads to flocculation.

By increasing the concentration to 5 g/L and further decreasing the ratio of RR-P3HT:rra-P3HT to 0.8:0.2, dispersions of the P3HT-mix in combination with O-IDTBR are synthesized, with an average nanoparticle size of 88 nm after nanoprecipitation and 93 nm after reduction. These dispersions are used for the fabrication of inverted solar cells at four different layer thicknesses, as summarized in Table 7.13. The *J-V* curves are shown in Figure 7.9. With the P3HT-mix, solar cells with O-IDTBR and a PCE of 2.4 % could be achieved. However, due to the use of

Table 7.12: Average nanoparticle sizes of different blends at a concentration c_D of 2 g/L (ratio P3HT:NFA 1:1 by weight), after nanoprecipitation and after reduction.

Donor	Acceptor	*d* [nm] after nanoprecipitation	*d* [nm] after reduction
P3HT-mix[a)]	IDFBR	45 ± 1	49 ± 1
P3HT-mix[a)]	O-IDTBR	110 ± 4	110 ± 2
P3HT-mix[a)]	CO_i8DFIC	1000 ± 500[b)]	-[c)]
P3HT-mix[a)]	Y6	1000 ± 500[b)]	-[c)]
P3HT-mix[a)]	ITIC	260 ± 100	-[c)]

[a)] RR-P3HT:rra-P3HT ratio 0.66:0.33, by weight; [b)] growth during measurement; [c)] flocculated.

Table 7.13: Solar cell key parameters of solar cells from the ternary blend of RR-P3HT:rra-P3HT: O-IDTBR (ratio 0.8:0.2:1 by weight, c_D = 5 g/L), at different light-harvesting layer thicknesses t. The light-harvesting layer was thermal annealed at 150 °C.

t [nm]	V_{OC} [mV]	J_{SC} [mA/cm^2]	FF [%]	PCE [%]	Yield[a)]
40	529 ± 33	5.2 ± 0.1	48 ± 1	1.3 ± 0.1	4/8
60	705 ± 14	5.7 ± 0.1	50 ± 2	2.0 ± 0.1	7/8
80	757 ± 10	5.9 ± 0.1	52 ± 1	2.3 ± 0.1	6/8
100	736 ± 25	5.8 ± 0.1	48 ± 2	2.0 ± 0.2	6/8
80 [b)]	726 ± 1	6.9 ± 0.1	52 ± 1	2.6 ± 0.1	8/8

[a)] statistic of working solar cells; [b)] RR-P3HT:rra-P3HT ratio 0.9:0.1, by weight

20 % rra-P3HT, some J_{SC} is missing. In addition, the scattering between the different solar cells is high, resulting in many non-working solar cells. The non-working solar cells were excluded from the results in Table 7.13.

Therefore, the amount of rra-P3HT is further reduced to 10 %, which results in an average nanoparticle size of 100 nm after nanoprecipitation and 110 nm after reduction. While slightly more acceptor material is lost during the reduction step, the remaining RR-P3HT:rra-P3HT:O-IDTBR ratio of the ternary blend is 0.9:0.07:0.72 (initial ratio: 0.9:0.1:1). With this dispersion,

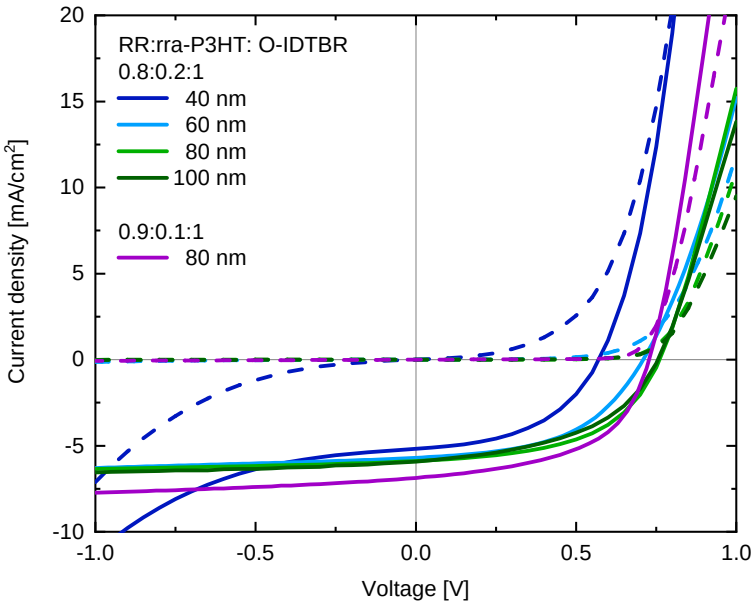

Figure 7.9: J-V curves of solar cells with a nanoparticulate light-harvesting layer from two different dispersions with different blend ratios of RR-P3HT:rra-P3HT:O-IDTBR, at different light-harvesting layer thicknesses.

solar cells with a light-harvesting layer thickness of approx. 80 nm are fabricated, as shown in the last row of Table 7.13, with a 'hero device' PCE of 2.6 %. With this process, a higher fraction of working solar cells was achieved. A further optimization of the layers by reducing the thermal annealing temperature from 150 °C to 120 °C, which is the optimum known from literature for solution processed solar cells from RR-P3HT:O-IDTBR, resulted in shorted solar cells.[183]

7.4 Résumé

In this chapter, the conditions for the formation of nanoparticles from a ternary blend were discussed. By adding a material that forms stable dispersions in combination with P3HT, such as the fullerene $PC_{71}BM$ or the polymer rra-P3HT, to a RR-P3HT:acceptor blend that does not form stable dispersions, the unstable blend can be stabilized. To achieve mixed nanoparticles, the miscibility of the different materials has to be good, resulting in an incorporation into the nanoparticles, as shown for the different fullerene derivatives. Up to a certain extent, fullerenes that do not form stable dispersions in combination with P3HT, such as $PC_{61}BM$, can be stabilized to remain inside the dispersions, while an excess again results in sedimentation.
In current high-efficient solution-processed solar cells, instead of a fullerene acceptor, an NFA is used. However, when nanoprecipitating a blend of NFA and P3HT, this always results in material separation due to sedimentation of the NFA. By using fullerenes such as $PC_{71}BM$ that form stable nanoparticle dispersions in combination with P3HT, P3HT:NFA blends are investigated. Nevertheless, this concept could not be adapted to nanoparticle formation. Instead, the NFA sediments, resulting in a P3HT:fullerene dispersion or a total collapse of the dispersion. Presumably, the miscibility between fullerene and NFA is too low to achieve a stabilizing effect. To increase the miscibility, instead of a second acceptor, a second donor is further examined. A promising candidate is rra-P3HT, which only differs from RR-P3HT by the absence of regioregularity, resulting in amorphous structures instead of semi-crystalline domains. With the idea that acceptor material could be incorporated inside these amorphous polymer domains, a reduced loss of material during nanoprecipitation could be achieved. Before using the blend of rra-P3HT and RR-P3HT, the two donors were separately combined with different acceptor materials. While the combination of RR-P3HT and NFA resulted in a huge material sedimentation of NFA , in the blends of rra-P3HT and NFA, more acceptor remained in dispersion. However, as shown with rra-P3HT, a good miscibility is not sufficient to create efficient solar cells. Charge carrier separation and transport to the respective electrodes are crucial as well. By blending both rra-P3HT and RR-P3HT in different ratios together with O-IDTBR, the NFA could be incorporated into the nanoparticles. Slightly more O-IDTBR sedimented by reducing

the amount of rra-P3HT, but also solar cells with a higher PCE of 2.6 % due to an increase in J_{SC} could be fabricated.
This demonstrates the possibility of stabilizing blends that do not form stable dispersions by using a third component which otherwise forms stable dispersions with P3HT.

8 Conclusion

In this work, knowledge was gained on the formation of organic nanoparticles and their utillization in the fabrication of thin-film solar cells. The two main goals were the implementation of a reproducible, scalable production of dispersions with consistent quality and nanoparticle size as well as the development and optimization of a nanoparticle-based fabrication route of organic solar cells containing P3HT.

Starting with the well-known blend of P3HT and $IC_{60}BA$, a continuous process for the synthesis of nanoparticle dispersions was developed. After the installation of the microfluidic setup and the identification of the influencing parameters on the continuous flow nanoprecipitation, these parameters were optimized to find a controllable process that enables a highly reproducible synthesis of nanoparticle dispersions. For the nanoprecipitation, the microfluidic micromixer chip was chosen and a preconditioning before the synthesis was developed. A flow rate of Q = 3 mL/min at a nonsolvent-fraction of φ_{NS} = 75 % enabled a reproducible process. After the identification of irradiation as the most important parameter, dispersions with a variable nanoparticle size were achieved and a shelf-stability of over one year was reached. Using these dispersions, it is possible to actively tailor the thickness of the light-harvesting layers. While the nanoparticle size did not directly influence the solar cell performance, the light-harvesting layer thickness did. One of the most crucial results was achieving a smooth and closed light-harvesting layer by combining small nanoparticles with several spin coating steps and an annealing temperature above 120 °C. With this, a PCE of over 4 % was achieved. Solar cells from this process were compared to solar cells fabricated from dispersion made by the common batch nanoprecipitation. While solar cells from both nanoprecipitation processes achieved a PCE of approximately 4 %, solar cells with light-harvesting layers deposited from nanoparticle dispersions by microfluidics exhibited a slightly better performance. With this, the goal of developing a scalable process for the reproducible production of non-toxic inks for the fabrication of organic solar cells was achieved.

While P3HT and $IC_{60}BA$ form stable dispersions, blend dispersions of P3HT combined with many other acceptors flocculate. The second part of this thesis identified and evaluated the crucial requirements for the nanoparticle formation of P3HT:acceptor blends. To further investigate the effect of the acceptor on the formation of stable nanoparticle dispersions from P3HT, eight

different acceptors from the group of fullerene derivatives were selected. The polymer P3HT was chosen because of its ability of forming stable nanoparticles in ethanol. First, the residual solubility of the fullerenes was determined, followed by an examination of the miscibility between the different fullerenes and P3HT. While blends of either of the four fullerene derivatives $PC_{71}BM$, $ThC_{71}BM$, $IC_{60}BA$, and $IC_{70}BA$ with P3HT led to stable nanoparticle dispersions, neither of the four fullerene derivatives $PC_{61}BM$, $ThC_{61}BM$, bis-$PC_{62}BM$, and bis-$PC_{72}BM$ remained inside the dispersion at a ratio of 1:1 (by weight). The main reasons are the different miscibilities, residual solubilities, demixing and interactions between the materials.

Afterwards, the influence of the fullerene concentration on the nanoparticle size was investigated. Initially, at a concentration below the residual solubility of the fullerene derivatives, an increase of the concentration results in a decreased nanoparticle size through an increased colloidal stability. A small residual solubility can support the displacement of the negative counter charge to the fullerene in solution. Above the residual solubilities, more fullerene was incorporated into the nanoparticles, resulting in an increased nanoparticle size, until an excess of fullerene resulted in sedimentation. The combination of P3HT and the respective fullerene derivatives resulted in a stable nanoparticle dispersion with a difference in the concentration of the fullerenes. Even with reduced acceptor concentrations, a successful fabrication of solar cells was possible.

With the blend of P3HT:$PC_{61}BM$, which typically does not form stable dispersions, a PCE of 2 % was achieved. This result is remarkable, considering that the ratio of P3HT to $PC_{61}BM$ is only 1:0.4, which is well below the optimum known from literature for conventional deposition routes. The V_{OC} is similar to the V_{OC} of the blend of P3HT and $PC_{71}BM$, but the J_{SC} is decreased, due to the low fullerene concentration that results in hampered charge carrier transport. Solar cells with a light-harvesting layer from the blend of P3HT:$IC_{70}BA$ achieved the best PCE of 4.5 %.

With the miscibility as one of the most important influencing parameters for the successful fabrication of nanoparticle dispersions, the concept of stabilizing a blend that did not form a stable dispersion by applying a third component was examined. If the third component formed stable nanoparticles in combination with P3HT and if the third component and the acceptor were miscible, then a stabilizing effect could be observed.

To achieve mixed nanoparticles, the miscibility between all compounds has to be good, resulting in an incorporation into the nanoparticles. Up to a certain extent, by using a third component, stabilization of otherwise unstable dispersions such as P3HT:$PC_{61}BM$ could be achieved, while an excess resulted in sedimentation.

In current high-efficient solution-processed solar cells, instead of a fullerene acceptor, an NFA is used. However, in this work, the combination of NFA and P3HT always resulted in a separa-

tion of donor and acceptor due to sedimentation of the acceptor material. By using a fullerene like $PC_{71}BM$ that forms stable dispersions with P3HT, the P3HT:NFA blends were investigated, resulting in either the sedimentation of the NFA and a remaining P3HT:fullerene dispersion or the total collapse of the dispersion. Presumably, the miscibility between fullerene and NFA was too low to achieve a stabilizing effect. To increase the miscibility, instead of a second acceptor, a second donor was further examined. A promising candidate was rra-P3HT, which only differed from RR-P3HT by the absence of regioregularity, resulting in amorphous structures instead of semi-crystalline domains. Before using the blend of rra-P3HT and RR-P3HT, the two donors were separately combined with different acceptors. The combination of RR-P3HT and NFA resulted in a huge material loss of the NFA via sedimentation, while in the blends of rra-P3HT and NFA, more acceptor remained inside the dispersion. However, as shown with rra-P3HT, a good miscibility is not sufficient to create efficient solar cells. Charge carrier separation and transport to the respective electrodes are crucial as well. The blend of rra-P3HT and RR-P3HT in different ratios with O-IDTBR resulted in an incorporation of the NFA into the nanoparticles. At an amount of rra-P3HT of 10 %, some O-IDTBR sediments, but solar cells with a higher PCE of 2.6 % due to decent J_{SC} could be achieved, demonstrating the possibility of the stabilizing effect by using a third material.

In summary, this work achieved both of its primary goals by identifying the relevant factors for nanoparticle size as well as designing a continuous, scalable, stable and reproducible manufacturing process for nanoparticle dispersions. With this deeper understanding of the role of the acceptor in the nanoparticle formation process, the design of new materials that form nanoparticles in combination with P3HT will be possible. The modification of highly efficient acceptors by the addition of side chains could allow the incorporation of acceptor material inside the P3HT domains due to an increased miscibility. In a ternary system, the modification of the acceptor to increase the miscibility with the third component could enable the stabilization of the dispersion and hence fabrication of highly efficient organic solar cells from nanoparticle dispersions. After the synthesis of stable dispersions from a highly efficient blend and slight modifications of the microfluidic process, upscaling of ink production by parallelization of several microfluidic setups for the fabrication of solar cells from roll-to-roll printing processes could be accomplished, enabling an eco-friendly printable solar cell fabrication process.

A List of abbreviations

Abbreviation

$_1$H NMR	Proton nuclear magnetic resonance spectroscopy
A	Acceptor
a.u.	Arbitrary unit
AFM	Atomic force microscopy
AM	Air mass
Ann	Annealing
Bis-PC$_{62}$BM	Bis(1-[3-(methoxycarbonyl)propyl]-1-phenyl)-[6,6]C$_{62}$
BT	(1,2,3-benzothiadiazole)
C_{60}	Buckminster fullerene with 60 carbon atoms
$CHCl_3$	Chloroform
CNT	Classical nucleation theory
CO$_i$8DFIC	2,2-[[4,4,11,11-tetrakis(4-hexylphenyl)-4,11-dihydrothieno[2,3:4,5]-thieno[2,3-d]thieno[2,3:4,5]thienov[2,3:4,5]pyrano[2,3:4,5]thieno-[2,3:4,5]thieno[3,2-b]pyran-2,9-diyl]bis[methylidyne(5,6-difluoro)]]
CT	Charge transfer
COB	Chip on board
D	Donor
DLS	Dynamic light scattering
DLVO	Derjaguin-Landau-Verwey-Overbeek (-Theory)
DUT	Device under test
EA	Electron affinity
EQE	External quantum efficiency
ETL	Electron transport layer
EtOH	Ethanol

FF	Fill factor
H	Head
HOMO	Highest occupied molecular orbital
HTL	Hole transport layer
$IC_{60}BA$	Indene-C_{60} bisadduct
IDFBR	(5Z,5'Z)-5,5'-((7,7'-(6,6,12,12-tetraoctyl-6,12-dihydroindeno[1,2-b]fluorene-2,8-diyl)bis(benzo[c][1,2,5]thiadiazole-7,4-diyl))bis-(methanylylidene))bis(3-ethyl-2-thioxothiazolidin-4-one)
IDT	s-indaceno[1,2-b:5,6-b']dithiophene
IDTBR	(5Z,5'Z)-5,5'-((7,7'-(4,4,9,9-tetraoctyl-4,9-dihydro-s-indaceno[1,2-b:5,6-b']dithiophene-2,7-diyl)bis(benzo[c][1,2,5]thiadiazole-7,4-diyl))bis(methanylylidene))bis(3-ethyl-2-thioxothiazolidin-4-one)
IP	Ionisation potential
IPR	Isolated pentagon rule
IQE	Internal quantum efficiency
ITIC	3,9-bis(2-methylene-((3-(1,1-dicyanomethylene)-6,7-dichloro)-indanone))-5,5,11,11-tetrakis(4-hexylphenyl)-dithieno[2,3-d:2',3'-d']-s-indaceno [1,2-b:5,6-b']dithiophene
ITO	Indium tin oxide
J71	Poly[[5,6-difluoro-2-(2-hexyldecyl)-2H-benzotriazole-4,7-diyl]-2,5-thiophenediyl[4,8-bis[5-(tripropylsilyl)-2-thienyl]benzo[1,2-b:4,5-b']dithiophene-2,6-diyl]-2,5-thiophenediyl]
LCAO	Linear combination of atomic orbitals
LDA	Lithium diisopropylamide
LED	Light emitting diode
LUMO	Lowest unoccupied molecular orbital
$MgBr_2 \cdot Et_2O$	Magnesium bromide diethyl etherate
MO	Molecular orbital
MPP	Maximum power point
MW	Molecular weight
NFA	Nonfullerene acceptor
$Ni_2(dppe)Cl_2$	Nickel-based catalyst
$Ni_2(dppp)Cl_2$	Nickel-based catalyst
norm	Normalized

NP	Nanoparticle
NS	Nonsolvent
OSC	Organic solar cell
P3HT	Poly(3-hexylthiophene-2,5-diyl)
$PC_{61}BM$	[6,6]-phenyl-C_{61}-butyric acid methyl ester.
PCE	Power conversion efficiency
PDI	Polydispersity index
PEDOT:PSS	Poly(3,4-ethylenedioxythiophene):Polystyrene sulfonate
PESA	Photoelectron spectroscopy in air
PLQY	Photoluminescence quantum yield
PTFE	Polytetrafluoroethylene
Ref	Reference
RGB	Red green and blue
RR	Regioregular
rra	regiorandom
RT	Room temperature
S	Solvent
SMCF	Spectral mismatch calculation factor
SMU	Source meter unit
SolSim	Solarsimulator
SR	Spectral response
T	Tail
tech-PCBM	PCBM with a technical grade
$ThC_{61}BM$	Thienyl-C_{61}-butyric acid methyl ester.
THF	Tetrahydrofuran
UV	Ultra violet
UV-vis-NIR	Ultra violet - visible - near infrared
Y6	2,2'-((2Z,2'Z)-((12,13-bis(2-ethylhexyl)-3,9-diundecyl-12,13--dihydro-[1,2,5]thiadiazolo[3,4-e]thieno[2",3":4',5']thieno[2', 3':-4,5]pyrrolo[3,2-g]thieno[2',3':4,5]thieno[3,2-b]indole-2,10-diyl)bis-(methanylylidene))bis(5, 6-difluoro-3-oxo-2,3-dihydro-1H-indene-2,1-diylidene))dimalononitrile), also known as BTP-4F
Zn*	Rieke-zinc
ZnO	Zinc oxide

Symbol

A	Absorbance
B	Baseline for DLS calculation
β	Instrument constant for DLS calculation
c	Concentration
c_{D}	Concentration of the disperion
c_{D}	Concentration of the solution
c_0	Vacuum light velocity
d	Diameter of the nanoparticles
d_{H}	Nanoparticle diameter
D	Diffusion coefficient
e	Elementary charge
E_{Opt}	Optical band gap
E_{Ref}	Emission spectrum of the reference
E_{S}	Emission spectrum of the sample
E_{Solar}	Solar spectral irradiance
$E_{\mathrm{transport}}$	Transport energy
E_{Vac}	Vacuum energy
ε_λ	Molar absorption coefficient
η	Viscosity
η	Power conversion efficiency
g_2	Autocorrelation function of the DLS
h	Planck's constant
I	Current
I	Intensity
I_{M}	Correction of the monitor diode
I_{SC}	Short-circuit current
J	Current density
J_{MPP}	Current density at the maximum power point
J_{SC}	Short-circuit current density

k_B	Bolzmann constant
λ	Wavelength
l	Optical path length
L	Characteristic linear dimension, here: channel width
M_w	Number average molar mass
M_w	Weight average molar mass
μ	Mobility
μ	Flow speed
n	Charge carrier density of electrons
n	Refractive index
ν	Kinematic viscosity
p	Charge carrier density of holes
P	Power density
ϕ	Work function
q	Dispersion coefficient
Q	Total flow rate
R_P	Parallel resistance
R_S	Serial resistance
Re	Reynolds number
ρ	Density of the liquid
S_{Ref}	Scatter spectrum of the reference
S_S	Scatter spectrum of the sample
S_0	Ground state
S_1	First excited state
σ	Electrical conductivity
τ	Time
τ_{Ann}	Annealing time
t	Time
t	Layer thickness
T	Temperature
T_{Ann}	Annealing temperature
T_λ	Transmission

θ	Scatter angle
v_{M}	Vibrational state
V	Voltage
V_{MPP}	Voltage at the maximum power point
V_{OC}	Open-circuit voltage
φ_{NS}	Volume fraction of the nonsolvent

Bibliography

[1] Watson. Den Winter überstehen: Frankreich macht die Lichter aus. *https://www.watson.ch/international/energie/301765276-den-winter-ueberstehen-frankreich-macht-nachts-die-lichter-aus*. Accessed: 8.1.2023.

[2] SWR Aktuell. Überhitzter Rhein - Folgen der Wassererwärmung und was dagegen hilft. *https://www.swr.de/swraktuell/rheinland-pfalz/ludwigshafen/ueberhitzter-rhein-fischsterben-droht-basf-ludwigshafen-und-atomkraftwerke-in-frankreich-gefragt-100.html*. Accessed: 8.1.2023.

[3] Deutschlandfunk. Strom gegen Gas: Die deutsch-französische Energiefreundschaft. *https://www.deutschlandfunk.de/frankreich-deutschland-energieversorgung-100.html*. Accessed: 11.1.2023.

[4] Bundesnetzagentur 2023 (SMARD). Electricity market topics: The electricity market in 2022. *https://www.smard.de/page/en/topic-article/207552/209668*. Accessed: 08.1.2023.

[5] A.J. Moulé. Power from plastic. *Current Opinion in Solid State and Materials Science*, 14, 2010.

[6] C.J. Brabec, J.A. Hauch, P. Schilinsky, and C. Waldauf. Production aspects of organic photovoltaics and their impact on the commercialization of devices. *MRS Bulletin*, 30, 2005.

[7] A. Colsmann, H. Röhm, and C. Sprau. Shining light on organic solar cells. *Solar RRL*, 4, 2020.

[8] S. Gärtner, M. Christmann, S. Sankaran, H. Röhm, E.-M. Prinz, F. Penth, A. Pütz, A.E. Türeli, B. Penth, B. Baumstümmler, and A. Colsmann. Eco-Friendly Fabrication of 4% Efficient Organic Solar Cells from Surfactant-free P3HT: ICBA Nanoparticle Dispersions. *Advanced Materials*, 26, 2014.

[9] S. Sankaran, K. Glaser, S. Gärtner, T. Rödlmeier, K. Sudau, G. Hernandez-Sosa, and A. Colsmann. Fabrication of polymer solar cells from organic nanoparticle dispersions by doctor blading or ink-jet printing. *Organic Electronics*, 8, 2016.

[10] L. D'Olieslaeger, G. Pirotte, I. Cardinaletti, J. D'Haen, J. Manca, D. Vanderzande, W. Maes, and A. Ethirajan. Eco-friendly fabrication of PBDTTPD: $PC_{71}BM$ solar cells reaching a PCE of 3.8% using water-based nanoparticle dispersions. *Organic Electronics*, 42, 2017.

[11] C. Xie, X. Tang, M. Berlinghof, S. Langner, S. Chen, A. Späth, N. Li, R.H. Fink, T. Unruh, and C.J. Brabec. Robot-based high-throughput engineering of alcoholic polymer: fullerene nanoparticle inks for an eco-friendly processing of organic solar cells. *ACS Applied Materials & Interfaces*, 10, 2018.

[12] C. Xie, A. Classen, A. Späth, X. Tang, J. Min, M. Meyer, C. Zhang, N. Li, A. Osvet, R.H. Fink, and C.J. Brabec. Overcoming microstructural limitations in water processed organic solar cells by engineering customized nanoparticulate inks. *Advanced Energy Materials*, 8, 2018.

[13] C. Xie, T. Heumüller, W. Gruber, X. Tang, A. Classen, I. Schuldes, M. Bidwell, A. Späth, R.H. Fink, T. Unruh, I. McCulloch, N. Li, and C.J. Brabec. Overcoming efficiency and stability limits in water-processing nanoparticular organic photovoltaics by minimizing microstructure defects. *Nature Communications*, 9, 2018.

[14] F. Manger, K. Fischer, P. Marlow, H. Röhm, C. Sprau, and A. Colsmann. Iodine-Stabilized Organic Nanoparticle Dispersions for the Fabrication of 10% Efficient Non-Fullerene Solar Cells. *Advanced Energy Materials*, 13, 2022.

[15] S. Schubert, J.T. Delaney Jr., and U.S. Schubert. Nanoprecipitation and nanoformulation of polymers: from history to powerful possibilities beyond poly (lactic acid). *Soft Matter*, 7, 2011.

[16] G.M. Whitesides. The origins and the future of microfluidics. *Nature*, 442, 2006.

[17] M. Schwörer and H.C. Wolf. *Organische molekulare Festkörper: Einführung in die Physik von π-Systemen*. John Wiley & Sons, 2012.

[18] A. Köhler and H. Bässler. *Electronic processes in organic semiconductors: An introduction*. John Wiley & Sons, 2015.

[19] D. Wöhrle, M.W. Tausch, and W.-D. Stohrer. *Photochemie: Konzepte, Methoden, Experimente*. John Wiley & Sons, 2012.

[20] J. Buddrus and B. Schmidt. Grundlagen der Organischen Chemie. In *Grundlagen der Organischen Chemie*. de Gruyter, 2014.

[21] G. Li, W.-H. Chang, and Y. Yang. Low-bandgap conjugated polymers enabling solution-processable tandem solar cells. *Nature Reviews Materials*, 2, 2017.

[22] W. Brutting and W. Rieß. Grundlagen der organischen Halbleiter. *Physik Journal*, 7, 2008.

[23] I. Fleming. *Molekülorbitale und Reaktionen organischer Verbindungen*. John Wiley & Sons, 2012.

[24] T. Koopmans. Über die Zuordnung von Wellenfunktionen und Eigenwerten zu den einzelnen Elektronen eines Atoms. *Physica*, 1, 1934.

[25] A.O. Szabo. *NS Modern Quantum Chemistry. Mineola*. New York: Dover Publishing, 1996.

[26] P. Marlow. Organische Solarzellen: Synthese und Stabilisierung tensidfreier organischer Halbleiterdispersionen, Dissertation, Karlsruhe Institut of Technologie (KIT). 2021.

[27] W. Demtröder. *Molecular physics: theoretical principles and experimental methods*. John Wiley & Sons, 2008.

[28] G. Herzberg. *Molecular Spectra and Molecular Structure*. Krieger Publishing Company, 1992.

[29] P.W. Atkins and R.S. Friedman. *Molecular quantum mechanics*. Oxford University Press, 2011.

[30] W. Tress. Organic solar cells. In *Organic Solar Cells*. Springer, 2014.

[31] J.L. Bredas. Mind the gap! *Materials Horizons*, 1, 2014.

[32] C. Brabec, U. Scherf, and V. Dyakonov. *Organic photovoltaics: materials, device physics, and manufacturing technologies*. John Wiley & Sons, 2011.

[33] A.G. MacDiarmid, R.J. Mammone, R.B. Kaner, and L. Porter. The concept of 'doping'of conducting polymers: The role of reduction potentials. *Philosophical Transactions of the Royal Society of London. Series A, Mathematical and Physical Sciences*, 314, 1985.

[34] J.L. Bredas and G.B. Street. Polarons, bipolarons, and solitons in conducting polymers. *Accounts of Chemical Research*, 18, 1985.

[35] J.-L. Brédas, J.E. Norton, J. Cornil, and V. Coropceanu. Molecular understanding of organic solar cells: the challenges. *Accounts of Chemical Research*, 42, 2009.

[36] W. Brütting. Introduction to the physics of organic semiconductors, Physics of organic semiconductors. *Wiley-VCH, Weinheim*, 10, 2006.

[37] T.L. Benanti and D. Venkataraman. Organic solar cells: An overview focusing on active layer morphology. *Photosynthesis Research*, 87, 2006.

[38] C.J. Brabec. Semiconductor aspects of organic bulk heterojunction solar cells. In *Organic Photovoltaics*. Springer, 2003.

[39] S. Ashok and K.P. Pande. Photovoltaic measurements. *Solar Cells*, 14, 1985.

[40] D. Bahro. Externe Quanteneffizienzmessungen an organischen Tandemsolarzellen, Dissertation, Karlsruhe Institut of Technologie (KIT). 2017.

[41] N.K. Elumalai and A. Uddin. Open circuit voltage of organic solar cells: an in-depth review. *Energy & Environmental Science*, 9, 2016.

[42] M.C. Scharber, D. Mühlbacher, M. Koppe, P. Denk, C. Waldauf, A.J. Heeger, and C.J. Brabec. Design rules for donors in bulk-heterojunction solar cells—towards 10% energy-conversion efficiency. *Advanced Materials*, 18, 2006.

[43] B.A. Collins, J.R. Tumbleston, and H. Ade. Miscibility, crystallinity, and phase development in P3HT/PCBM solar cells: toward an enlightened understanding of device morphology and stability. *The Journal of Physical Chemistry Letters*, 2, 2011.

[44] K. Vandewal, S. Himmelberger, and A. Salleo. Structural factors that affect the performance of organic bulk heterojunction solar cells. *Macromolecules*, 46, 2013.

[45] I. Ramirez, M. Causa', Y. Zhong, N. Banerji, and M. Riede. Key tradeoffs limiting the performance of organic photovoltaics. *Advanced Energy Materials*, 8, 2018.

[46] L. Ye, B.A. Collins, X. Jiao, J. Zhao, H. Yan, and H. Ade. Miscibility–function relations in organic solar cells: significance of optimal miscibility in relation to percolation. *Advanced Energy Materials*, 8, 2018.

[47] K. Landfester, R. Montenegro, U. Scherf, R. Güntner, U. Asawapirom, S. Patil, D. Neher, and T. Kietzke. Semiconducting polymer nanospheres in aqueous dispersion prepared by a miniemulsion process. *Advanced Materials*, 14, 2002.

[48] A. Stapleton, B. Vaughan, B. Xue, E. Sesa, K. Burke, X. Zhou, G. Bryant, O. Werzer, A. Nelson, A.L. D. Kilcoyne, L. Thomsen, E. Wanless, W. Belcher, and P. Dastoor. A multilayered approach to polyfluorene water-based organic photovoltaics. *Solar Energy Materials and Solar Cells*, 102, 2012.

[49] J.E. Millstone, D.F.J. Kavulak, C.H. Woo, T.W. Holcombe, E.J. Westling, A.L. Briseno, M.F. Toney, and J.M.J. Fréchet. Synthesis, properties, and electronic applications of size-controlled poly (3-hexylthiophene) nanoparticles. *Langmuir*, 26, 2010.

[50] S. Wu. Bicolored “Janus” Particles with Electrical Anisotropy Synthesized Using a Microfluidic Co-Flow System. *MRS Bulletin*, 31, 2006.

[51] C.-X. Zhao, L. He, S.Z. Qiao, and A.P.J. Middelberg. Nanoparticle synthesis in microreactors. *Chemical Engineering Science*, 66, 2011.

[52] T. Nisisako, T. Torii, T. Takahashi, and Y. Takizawa. Synthesis of monodisperse bicolored janus particles with electrical anisotropy using a microfluidic Co-Flow system. *Advanced Materials*, 18, 2006.

[53] S. Ulum, N. Holmes, M. Barr, A.L.D. Kilcoyne, B.B. Gong, X. Zhou, W. Belcher, and P. Dastoor. The role of miscibility in polymer: fullerene nanoparticulate organic photovoltaic devices. *Nano Energy*, 2, 2013.

[54] N.P. Holmes, K.B. Burke, P. Sista, M. Barr, H.D. Magurudeniya, M.C. Stefan, A.L.D. Kilcoyne, X. Zhou, P.C. Dastoor, and W.J. Belcher. Nano-domain behaviour in P3HT: PCBM nanoparticles, relating material properties to morphological changes. *Solar Energy Materials and Solar Cells*, 117, 2013.

[55] S. Gärtner, A.J. Clulow, I.A. Howard, E.P. Gilbert, P.L. Burn, I.R. Gentle, and A. Colsmann. Relating structure to efficiency in surfactant-free polymer/fullerene nanoparticle-based organic solar cells. *ACS Applied Materials & Interfaces*, 9, 2017.

[56] A. Groisman and S.R. Quake. A microfluidic rectifier: Anisotropic flow resistance at low Reynolds numbers. *Physical Review Letters*, 92, 2004.

[57] C.-Y. Lee, C.-L. Chang, Y.-N. Wang, and L.-M. Fu. Microfluidic mixing: a review. *International Journal of Molecular Sciences*, 12(5), 2011.

[58] R.A.L. Jones. *Soft condensed matter*, volume 6. Oxford University Press, 2002.

[59] S. Karthika, T.K. Radhakrishnan, and P. Kalaichelvi. A review of classical and nonclassical nucleation theories. *Crystal Growth & Design*, 16, 2016.

[60] N.T.K. Thanh, N. Maclean, and S. Mahiddine. Mechanisms of nucleation and growth of nanoparticles in solution. *Chemical Reviews*, 114, 2014.

[61] R.J. Davey, S.L.M. Schroeder, and J.H. Ter Horst. Nucleation of organic crystals—a molecular perspective. *Angewandte Chemie International Edition*, 52, 2013.

[62] S.M. D’Addio and R.K. Prud’homme. Controlling drug nanoparticle formation by rapid precipitation. *Advanced Drug Delivery Reviews*, 63, 2011.

[63] J. Lyklema. *Fundamentals of interface and colloid science: soft colloids*, volume 5. Elsevier, 2005.

[64] A. Nikoubashman, V.E. Lee, C. Sosa, R.K. Prud'homme, R.D. Priestley, and A.Z. Panagiotopoulos. Directed assembly of soft colloids through rapid solvent exchange. *ACS Nano*, 10, 2016.

[65] R.J. Hunter. *Introduction to modern colloid science*. Oxford University Press, 1993.

[66] G. Lagaly, O. Schulz, and R. Zimehl. *Dispersionen und Emulsionen: eine Einführung in die Kolloidik feinverteilter Stoffe einschließlich der Tonminerale*. Springer-Verlag, 2013.

[67] N. Stock. Stabilität von Dispersionen, University Kiel. *http://www.uni-kiel.de/anorg/-bensch/lehre/Dokumente/versuch_k1_stabilitaet_ von_ dispersionen.pdf*. Accessed: 10.01.2020.

[68] A.A. Shvets and A.N. Semenov. Effective interactions between solid particles mediated by free polymer in solution. *The Journal of Chemical Physics*, 139, 2013.

[69] A.N. Semenov and A.A. Shvets. Theory of colloid depletion stabilization by unattached and adsorbed polymers. *Soft Matter*, 11, 2015.

[70] J. Polte. Fundamental growth principles of colloidal metal nanoparticles–a new perspective. *CrystEngComm*, 17, 2015.

[71] W. Geens, S.E. Shaheen, B. Wessling, C.J. Brabec, J. Poortmans, and N.S. Sariciftci. Dependence of field-effect hole mobility of PPV-based polymer films on the spin-casting solvent. *Organic Electronics*, 3, 2002.

[72] S.A. Chen and J.M. Ni. Structure/properties of conjugated conductive polymers. 1. neutral poly (3-alkythiophene) s. *Macromolecules*, 25, 1992.

[73] H. Sirringhaus, P.J. Brown, R.H. Friend, M.M. Nielsen, K. Bechgaard, B.M.W. Langeveld-Voss, A.J.H. Spiering, R.A.J. Janssen, E.W. Meijer, P. Herwig, and D.M. De Leeuw. Two-dimensional charge transport in self-organized, high-mobility conjugated polymers. *Nature*, 401, 1999.

[74] M.-A. Sato, S. Tanaka, and K. Kaeriyama. Soluble conducting polythiophenes. *Journal of the Chemical Society, Chemical Communications*, 1986.

[75] R.L. Elsenbaumer, K.Y. Jen, and R. Oboodi. Processible and environmentally stable conducting polymers. *Synthetic Metals*, 15, 1986.

[76] F. Padinger, R.S. Rittberger, and N.S. Sariciftci. Effects of postproduction treatment on plastic solar cells. *Advanced Functional Materials*, 13, 2003.

[77] Youngkwon Kim, Hyeonjung Park, Jin Su Park, Jin-Woo Lee, Felix Sunjoo Kim, Hyeong Jun Kim, and Bumjoon J Kim. Regioregularity-control of conjugated polymers: from synthesis and properties, to photovoltaic device applications. *Journal of Materials Chemistry A*, 10, 2022.

[78] S. Hugger, R. Thomann, T. Heinzel, and T. Thurn-Albrecht. Semicrystalline morphology in thin films of poly (3-hexylthiophene). *Colloid and Polymer Science*, 282, 2004.

[79] C.H. Woo, B.C. Thompson, B.J. Kim, M.F. Toney, and J.M.J. Fréchet. The influence of poly (3-hexylthiophene) regioregularity on fullerene-composite solar cell performance. *Journal of the American Chemical Society*, 130, 2008.

[80] F. Liu, D. Chen, C. Wang, K. Luo, W. Gu, A.L. Briseno, J.W.P. Hsu, and T.P. Russell. Molecular weight dependence of the morphology in P3HT: PCBM solar cells. *ACS Applied Materials & Interfaces*, 6, 2014.

[81] H. Takeuchi and M. Kobashi. Microparticles and colloidal dispersions of poly (3-hexylthiophene). *Chemistry Letters*, 28, 1999.

[82] H. Shimizu, M. Yamada, R. Wada, and M. Okabe. Preparation and characterization of water self-dispersible poly (3-hexylthiophene) particles. *Polymer Journal*, 40, 2008.

[83] W. Anderson, D. Kozak, V.A. Coleman, Å.K. Jämting, and M. Trau. A comparative study of submicron particle sizing platforms: accuracy, precision and resolution analysis of polydisperse particle size distributions. *Journal of Colloid and Interface Science*, 405, 2013.

[84] J.D. Roehling, I. Arslan, and A.J. Moulé. Controlling microstructure in poly (3-hexylthiophene) nanofibers. *Journal of Materials Chemistry*, 22, 2012.

[85] F.C. Spano and C. Silva. H-and J-aggregate behavior in polymeric semiconductors. *Annual Review of Physical Chemistry*, 65, 2014.

[86] G. Nagarjuna, M. Baghgar, J.A. Labastide, D.D. Algaier, M.D. Barnes, and D. Venkataraman. Tuning aggregation of poly (3-hexylthiophene) within nanoparticles. *ACS Nano*, 6, 2012.

[87] J. Viéville, M. Tanty, and M.-A. Delsuc. Polydispersity index of polymers revealed by DOSY NMR. *Journal of Magnetic Resonance*, 212, 2011.

[88] R.D. McCullough and R.D. Lowe. Enhanced electrical conductivity in regioselectively synthesized poly (3-alkylthiophenes). *Journal of the Chemical Society, Chemical Communications*, 1, 1992.

[89] T.A. Chen and R.D. Rieke. The first regioregular head-to-tail poly (3-hexylthiophene-2, 5-diyl) and a regiorandom isopolymer: nickel versus palladium catalysis of 2 (5)-bromo-5 (2)-(bromozincio)-3-hexylthiophene polymerization. *Journal of the American Chemical Society*, 114, 1992.

[90] R.S. Loewe, P.C. Ewbank, J. Liu, L. Zhai, and R.D. McCullough. Regioregular, head-to-tail coupled poly (3-alkylthiophenes) made easy by the grim method: Investigation of the reaction and the origin of regioselectivity. *Macromolecules*, 34, 2001.

[91] R.D. McCullough, R.D. Lowe, M. Jayaraman, and D.L. Anderson. Design, synthesis, and control of conducting polymer architectures: structurally homogeneous poly (3-alkylthiophenes). *The Journal of Organic Chemistry*, 58, 1993.

[92] T.-A. Chen, X. Wu, and R.D. Rieke. Regiocontrolled synthesis of poly (3-alkylthiophenes) mediated by Rieke zinc: their characterization and solid-state properties. *Journal of the American Chemical Society*, 117, 1995.

[93] A. Marrocchi, D. Lanari, A. Facchetti, and L. Vaccaro. Poly (3-hexylthiophene): synthetic methodologies and properties in bulk heterojunction solar cells. *Energy & Environmental Science*, 5, 2012.

[94] C.J. Brabec, U. Scherf, and V. Dyakonov. *Organic photovoltaics: materials, device physics, and manufacturing technologies*. John Wiley & Sons, 2014.

[95] M.S. Dresselhaus, G. Dresselhaus, and P.C. Eklund. *Science of fullerenes and carbon nanotubes: their properties and applications*. Elsevier, 1996.

[96] A. Graja and J.-P. Farges. Optical spectra of C_{60} and C_{70} complexes: their similarities and differences. *Advanced Materials for Optics and Electronics*, 8, 1998.

[97] M. Lee, O.-K. Song, J.-C.l Seo, D. Kim, Y.D. Suh, S.M. Jin, and S.K. Kim. Low-lying electronically excited states of C_{60} and C_{70} and measurement of their picosecond transient absorption in solution. *Chemical Physics Letters*, 196, 1992.

[98] S. Yamamoto, A. Orimo, H. Ohkita, H. Benten, and S. Ito. Molecular Understanding of the Open-Circuit Voltage of Polymer: Fullerene Solar Cells. *Advanced Energy Materials*, 2, 2012.

[99] R. Sure, A. Hansen, P. Schwerdtfeger, and S. Grimme. Comprehensive theoretical study of all 1812 C 60 isomers. *Physical Chemistry Chemical Physics*, 19, 2017.

[100] T. Došlić. Bipartivity of fullerene graphs and fullerene stability. *Chemical Physics Letters*, 412, 2005.

[101] N. Sivaraman, R. Dhamodaran, I. Kaliappan, T.G. Srinivasan, P.R.V. Rao, and C.K. Mathews. Solubility of C_{60} in organic solvents. *The Journal of Organic Chemistry*, 57, 1992.

[102] C.J. Brabec, S.E. Shaheen, T. Fromherz, F. Padinger, J.C. Hummelen, A. Dhanabalan, R.A.J. Janssen, and N.S. Sariciftci. Organic photovoltaic devices produced from conjugated polymer/methanofullerene bulk heterojunctions. *Synthetic Metals*, 121, 2001.

[103] L.M. Popescu, P. van't Hof, A.B. Sieval, H.T. Jonkman, and J.C. Hummelen. Thienyl analog of 1-(3-methoxycarbonyl) propyl-1-phenyl-[6, 6]-methanofullerene for bulk heterojunction photovoltaic devices in combination with polythiophenes. *Applied Physics Letters*, 89, 2006.

[104] K. Vandewal, A. Gadisa, W.D. Oosterbaan, S. Bertho, F. Banishoeib, I. Van Severen, L. Lutsen, T.J. Cleij, D. Vanderzande, and J.V. Manca. The relation between open-circuit voltage and the onset of photocurrent generation by charge-transfer absorption in polymer: fullerene bulk heterojunction solar cells. *Advanced Functional Materials*, 18, 2008.

[105] J.C. Hummelen, B.W. Knight, F. LePeq, F. Wudl, J. Yao, and C.L. Wilkins. Preparation and characterization of fulleroid and methanofullerene derivatives. *The Journal of Organic Chemistry*, 60, 1995.

[106] C.J. Brabec, U. Scherf, and V. Dyakonov. *Organic photovoltaics: materials, device physics, and manufacturing technologies*. John Wiley & Sons, 2011.

[107] F.B. Kooistra, J. Knol, F. Kastenberg, L.M. Popescu, W.J.H. Verhees, J.M. Kroon, and J.C. Hummelen. Increasing the open circuit voltage of bulk-heterojunction solar cells by raising the LUMO level of the acceptor. *Organic Letters*, 9, 2007.

[108] D. Kronholm and J.C. Hummelen. Fullerene-based n-type semiconductors in organic electronics. *Material Matters*, 2, 2007.

[109] H. Chen, J. Peet, Y.-C. Hsiao, B. Hu, and M. Dadmun. The impact of fullerene structure on its miscibility with P3HT and its correlation of performance in organic photovoltaics. *Chemistry of Materials*, 26, 2014.

[110] M. Lenes, G.-J.A.H. Wetzelaer, F.B. Kooistra, S.C. Veenstra, J.C. Hummelen, and P.W.M. Blom. Fullerene bisadducts for enhanced open-circuit voltages and efficiencies in polymer solar cells. *Advanced Materials*, 20, 2008.

[111] J. Subbiah, P.M. Beaujuge, K.R. Choudhury, S. Ellinger, J.R. Reynolds, and F. So. Combined effects of MoO_3 interlayer and $PC_{70}BM$ on polymer photovoltaic device performance. *Organic Electronics*, 11, 2010.

[112] M. Lenes, S.W. Shelton, A.B. Sieval, D.F. Kronholm, J.C. Hummelen, and P.W.M. Blom. Electron trapping in higher adduct fullerene-based solar cells. *Advanced Functional Materials*, 19, 2009.

[113] D.W. Laird, R. Stegamat, He. Richter, V. Vejins, L. Scott, and T.A. Lada. Organic photovoltaic devices comprising fullerenes and derivatives thereof, wo 2008/018931, *Google Patents*, 2008.

[114] Y. He, H.-Y. Chen, J. Hou, and Y. Li. Indene-C_{60} bisadduct: a new acceptor for high-performance polymer solar cells. *Journal of the American Chemical Society*, 132, 2010.

[115] Y.-H. Lin, Y.-T. Tsai, C.-C. Wu, C.-Hu. Tsai, C.-H. Chiang, H.-F. Hsu, J.-J. Lee, and C.-Y. Cheng. Comparative study of spectral and morphological properties of blends of P3HT with PCBM and ICBA. *Organic Electronics*, 13, 2012.

[116] G. Zhao, Y. He, and Y. Li. 6.5% efficiency of polymer solar cells based on poly (3-hexylthiophene) and Indene-C_{60} bisadduct by device optimization. *Advanced Materials*, 22, 2010.

[117] M.M. Wienk, J.M. Kroon, W.J.H. Verhees, J. Knol, J.C. Hummelen, P.A. Van Hal, and R.A.J. Janssen. Efficient methano [70] fullerene/MDMO-PPV bulk heterojunction photovoltaic cells. *Angewandte Chemie*, 115, 2003.

[118] A. Wadsworth, Z. Hamid, M. Bidwell, R.S. Ashraf, J.I. Khan, D.H. Anjum, C. Cendra, J. Yan, E. Rezasoltani, A.A.Y. Guilbert, and M. Azzouzi. Progress in Poly (3-hexylthiophene) Organic Solar Cells and the Influence of Its Molecular Weight on Device Performance. *Advanced Energy Materials*, 8, 2018.

[119] E. Morvillo, P.and Bobeico. Bisadducts of C_{70} as electron acceptors for bulk heterojunction solar cells: A theoretical study. *Fullerenes, Nanotubes, and Carbon Nanostructures*, 19, 2011.

[120] P.A. Troshin, H. Hoppe, A.S. Peregudov, M. Egginger, S. Shokhovets, G. Gobsch, N.S. Sariciftci, and V.F. Razumov. [70] fullerene-based materials for organic solar cells. *ChemSusChem*, 4, 2011.

[121] Y. He, G. Zhao, B. Peng, and Y. Li. High-yield synthesis and electrochemical and photovoltaic properties of indene-C_{70} bisadduct. *Advanced Functional Materials*, 20, 2010.

[122] X. Fan, S. Li, S. Guo, and G. Fang. Understanding the phase separation evolution in efficient P3HT: $IC_{70}BA$-based bulk-heterojunction polymer solar cells. *Journal of Physics D: Applied Physics*, 46, 2013.

[123] P. Cheng, G. Li, X. Zhan, and Y. Yang. Next-generation organic photovoltaics based on non-fullerene acceptors. *Nature Photonics*, 12, 2018.

[124] S. Holliday, R.S. Ashraf, C.B. Nielsen, M. Kirkus, J.A. Rohr, C.-H. Tan, E. Collado-Fregoso, A.-C. Knall, J.R. Durrant, J. Nelson, and I. McCulloch. A rhodanine flanked nonfullerene acceptor for solution-processed organic photovoltaics. *Journal of the American Chemical Society*, 137, 2015.

[125] D. Baran, R.S. Ashraf, D.A. Hanifi, M. Abdelsamie, N. Gasparini, J.A. Röhr, S. Holliday, A. Wadsworth, S. Lockett, M. Neophytou, C.J. Emmott, J. Nelson, C.J. Brabec, A. Amassian, A. Salleo, T. Kirchartz, J.R. Durrant, and I. McCulloch. Reducing the efficiency–stability–cost gap of organic photovoltaics with highly efficient and stable small molecule acceptor ternary solar cells. *Nature Materials*, 16, 2017.

[126] S. Li, W. Liu, C.-Z. Li, M. Shi, and H. Chen. Efficient organic solar cells with non-fullerene acceptors. *Small*, 13, 2017.

[127] S. Holliday, R.S. Ashraf, A. Wadsworth, D. Baran, S.A. Yousaf, C.B. Nielsen, C.-H. Tan, S.D. Dimitrov, Z. Shang, N. Gasparini, and M. Alamoudi. High-efficiency and air-stable P3HT-based polymer solar cells with a new non-fullerene acceptor. *Nature Communications*, 7, 2016.

[128] H. Li, Z. Xiao, L. Ding, and J. Wang. Thermostable single-junction organic solar cells with a power conversion efficiency of 14.62%. *Science Bulletin*, 63, 2018.

[129] Z. Xiao, X. Jia, and L. Ding. Ternary organic solar cells offer 14% power conversion efficiency. *Science Bulletin*, 62, 2017.

[130] Z. Xiao, X. Jia, D. Li, S. Wang, X. Geng, F. Liu, J. Chen, S. Yang, T.P. Russell, and L. Ding. 26 mA cm- 2 Jsc from organic solar cells with a low-bandgap nonfullerene acceptor. *Science Bulletin*, 62, 2017.

[131] M. Zhang, Z. Xiao, W. Gao, Q. Liu, K. Jin, W. Wang, Y. Mi, Q. An, X. Ma, X. Liu, Y Chuluo, L. Ding, and F. Zhang. Over 13% efficiency ternary nonfullerene polymer solar cells with tilted up absorption edge by incorporating a medium bandgap acceptor. *Advanced Energy Materials*, 8, 2018.

[132] Y. Lin, J. Wang, Z.-G. Zhang, H. Bai, Y. Li, D. Zhu, and X. Zhan. An electron acceptor challenging fullerenes for efficient polymer solar cells. *Advanced Materials*, 27, 2015.

[133] W. Zhao, D. Qian, S. Zhang, S. Li, O. Inganäs, F. Gao, and J. Hou. Fullerene-free polymer solar cells with over 11% efficiency and excellent thermal stability. *Advanced Materials*, 28, 2016.

[134] Malvern Zetasizer Nano User Manual. Malvern instruments limited, 2013.

[135] S. Bhattacharjee. DLS and zeta potential–what they are and what they are not? *Journal of Controlled Release*, 235, 2016.

[136] P. Rademeyer, D. Carugo, J.Y. Lee, and E. Stride. Microfluidic system for high throughput characterisation of echogenic particles. *Lab on a Chip*, 15, 2015.

[137] J. Stetefeld, S.A. McKenna, and T.R. Patel. Dynamic light scattering: a practical guide and applications in biomedical sciences. *Biophysical Reviews*, 8, 2016.

[138] M. Naiim, A. Boualem, C. Ferre, M. Jabloun, A. Jalocha, and P. Ravier. Multiangle dynamic light scattering for the improvement of multimodal particle size distribution measurements. *Soft Matter*, 11, 2015.

[139] F. Manger. Organische Solarzellen: Kolloidale Stabilisierung von organischen Nanopartikeldispersionen durch elektrische Dotierung, Dissertation, Karlsruhe Institut of Technologie (KIT). 2022.

[140] F. Manger, P. Marlow, K. Fischer, M. Nöller, C. Sprau, and A. Colsmann. Organic Solar Cells: Electrostatic Stabilization of Organic Semiconductor Nanoparticle Dispersions by Electrical Doping. *Advanced Functional Materials*, 2022.

[141] A. Distler, P. Kutka, T. Sauermann, H.-J. Egelhaaf, D.M. Guldi, D. Di Nuzzo, S.C.J. Meskers, and R.A.J. Janssen. Effect of PCBM on the photodegradation kinetics of polymers for organic photovoltaics. *Chemistry of Materials*, 24, 2012.

[142] W.C. Tsoi, S.J. Spencer, L. Yang, A.M. Ballantyne, P.G. Nicholson, A. Turnbull, A.G. Shard, C.E. Murphy, D.D.C. Bradley, J. Nelson, and J.S. Kim. Effect of crystallization on the electronic energy levels and thin film morphology of P3HT: PCBM blends. *Macromolecules*, 44, 2011.

[143] V. Meunier and P. Lambin. Theory of scanning probe microscopy. In *Scanning Probe Microscopy*. Springer, 2007.

[144] B. Voigtländer. Electronics for scanning probe microscopy. In *Scanning Probe Microscopy*. Springer, 2015.

[145] Nanosurf. How afm works - dynamic modes. 2022. *https://www.nanosurf.com/en/support/afm-operating-principle*. Accessed: 30.12.2022.

[146] H. Ohshima. A simple expression for henry's function for the retardation effect in electrophoresis of spherical colloidal particles. *Journal of Colloid and Interface Science*, 168, 1994.

[147] K. Fischer, P. Marlow, F. Manger, C. Sprau, and A. Colsmann. Microfluidics: Continuous-Flow Synthesis of Nanoparticle Dispersions for the Fabrication of Organic Solar Cells. *Advanced Materials Technologies*, 7, 2022.

[148] K. Hu, K. Chakrabarty, and T.-Y. Ho. *Computer-aided design of microfluidic very large scale integration (mVLSI) biochips*. Springer, 2017.

[149] M.T. Breckenridge, T.T. Egelhoff, and H. Baskaran. A microfluidic imaging chamber for the direct observation of chemotactic transmigration. *Biomedical Microdevices*, 12, 2010.

[150] Y.K. Suh and S. Kang. A review on mixing in microfluidics. *Micromachines*, 1, 2010.

[151] P. Marlow, F. Manger, K. Fischer, C. Sprau, and A. Colsmann. Eco-friendly fabrication of organic solar cells: electrostatic stabilization of surfactant-free organic nanoparticle dispersions by illumination. *Nanoscale*, 14, 2022.

[152] S. Gärtner. Organische Nanopartikel zum Aufbau photoaktiver Schichten Organischer Solarzellen, Dissertation, Karlsruhe Institut of Technologie (KIT). 2017.

[153] L. Xue, X. Gao, K. Zhao, J. Liu, X. Yu, and Y. Han. The formation of different structures of poly (3-hexylthiophene) film on a patterned substrate by dip coating from aged solution. *Nanotechnology*, 21, 2010.

[154] U. Bielecka, K. Janus, and W. Bartkowiak. Nanoaggregation of P3HT in chloroform-anisole solution: relationship between morphology and electrical properties. In *Organic Field-Effect Transistors XIII; and Organic Semiconductors in Sensors and Bioelectronics VII*, volume 9185. SPIE, 2014.

[155] P. Tabeling. *Introduction to microfluidics*. Oxford University Press on Demand, 2005.

[156] P.-P. Cheng, L. Zhou, J.-A. Li, Y.-Q. Li, S.-T. Lee, and J.-X. Tang. Light trapping enhancement of inverted polymer solar cells with a nanostructured scattering rear electrode. *Organic Electronics*, 14, 2013.

[157] S.-H. Lin, S. Lan, J.-Y. Sun, and C.-F. Lin. Influence of mixed solvent on the morphology of the P3HT: Indene-C_{60} bisadduct (ICBA) blend film and the performance of inverted polymer solar cells. *Organic Electronics*, 14, 2013.

[158] I.D.C. Bartesaghi, D.and Pérez, J. Kniepert, S. Roland, M. Turbiez, D. Neher, and L. Koster. Competition between recombination and extraction of free charges determines the fill factor of organic solar cells. *Nature Communications*, 6, 2015.

[159] F. Monestier, J.-J. Simon, P. Torchio, L. Escoubas, F. Flory, S. Bailly, R. de Bettignies, S. Guillerez, and C. Defranoux. Modeling the short-circuit current density of polymer solar cells based on P3HT: PCBM blend. *Solar Energy Materials and Solar Cells*, 91, 2007.

[160] E. Verploegen, R. Mondal, C.J. Bettinger, S. Sok, M.F. Toney, and Z. Bao. Effects of thermal annealing upon the morphology of polymer–fullerene blends. *Advanced Functional Materials*, 20, 2010.

[161] H. Machrafi. Universal relation between the density and the viscosity of dispersions of nanoparticles and stabilized emulsions. *Nanoscale*, 12, 2020.

[162] K. Fischer, P. Marlow, F. Manger, J. Armleder, C. Sprau, and A. Colsmann. On the formation of polymer:fullerene nanoparticle dispersions: The role of miscibility. in preparation.

[163] B.A. Collins, E. Gann, L. Guignard, X. He, C.R. McNeill, and H. Ade. Molecular miscibility of polymer- fullerene blends. *The Journal of Physical Chemistry Letters*, 1, 2010.

[164] F. Machui, S. Rathgeber, N. Li, T. Ameri, and C.J. Brabec. Influence of a ternary donor material on the morphology of a P3HT: PCBM blend for organic photovoltaic devices. *Journal of Materials Chemistry*, 22, 2012.

[165] H. Chen, R. Hegde, J. Browning, and M.D. Dadmun. The miscibility and depth profile of PCBM in P3HT: thermodynamic information to improve organic photovoltaics. *Physical Chemistry Chemical Physics*, 14, 2012.

[166] X. Cao, Q. Zhang, K. Zhou, X. Yu, J. Liu, Y. Han, and Z. Xie. Improve exciton generation and dissociation by increasing fullerene content in the mixed phase of P3HT/fullerene. *Colloids and Surfaces A: Physicochemical and Engineering Aspects*, 506, 2016.

[167] M. Campoy-Quiles, T. Ferenczi, P.G. Agostinelli, T.and Etchegoin, Y. Kim, T.D. Anthopoulos, P.N. Stavrinou, D.D.C. Bradley, and J. Nelson. Morphology evolution via self-organization and lateral and vertical diffusion in polymer: fullerene solar cell blends. *Nature Materials*, 7, 2008.

[168] M.A. Faist, P.E. Keivanidis, S. Foster, P.H. Wöbkenberg, T.D. Anthopoulos, D.D.C. Bradley, J.R. Durrant, and J. Nelson. Effect of multiple adduct fullerenes on charge

generation and transport in photovoltaic blends with poly (3-hexylthiophene-2, 5-diyl). *Journal of Polymer Science Part B: Polymer Physics*, 49, 2011.

[169] H.-W. Liu, D.-Y. Chang, W.-Y. Chiu, S.-P. Rwei, and L. Wang. Fullerene bisadduct as an effective phase-separation inhibitor in preparing poly (3-hexylthiophene)–[6, 6]-phenyl-C 61-butyric acid methyl ester blends with highly stable morphology. *Journal of Materials Chemistry*, 22, 2012.

[170] A.A.Y. Guilbert, L.X. Reynolds, A. Bruno, A. MacLachlan, S.P. King, M.A. Faist, E. Pires, J.E. Macdonald, N. Stingelin, S.A. Haque, and J. Nelson. Effect of multiple adduct fullerenes on microstructure and phase behavior of P3HT: fullerene blend films for organic solar cells. *ACS Nano*, 6, 2012.

[171] P. Westacott, N.D. Treat, J. Martin, J.H. Bannock, J.C. de Mello, M. Chabinyc, A.B. Sieval, J.J. Michels, and N. Stingelin. Origin of fullerene-induced vitrification of fullerene: donor polymer photovoltaic blends and its impact on solar cell performance. *Journal of Materials Chemistry A*, 5, 2017.

[172] D.I. Kutsarov, I. Rašović, A. Zachariadis, A. Laskarakis, M.A. Lebedeva, K. Porfyrakis, C.A. Mills, M.J. Beliatis, B. Fisher, K. Bruchlos, S. Ludwigs, S. Logothetidis, and S. R. P. Silva. Achieving 6.7% efficiency in P3HT/Indene-C_{70} bisadduct solar cells through the control of vertical volume fraction distribution and optimized regio-isomer ratios. *Advanced Electronic Materials*, 2, 2016.

[173] L.M. Andersson, Y.-T. Hsu, A.B. Vandewal, K.and Sieval, M.R. Andersson, and O. Inganäs. Mixed C_{60}/C_{70} based fullerene acceptors in polymer bulk-heterojunction solar cells. *Organic Electronics*, 13, 2012.

[174] Y. Santo, I. Jeon, K. Sheng Yeo, T. Nakagawa, and Y. Matsuo. Mixture of [60] and [70] PCBM giving morphological stability in organic solar cells. *Applied Physics Letters*, 103, 2013.

[175] A.D. de Zerio and C. Müller. Glass forming acceptor alloys for highly efficient and thermally stable ternary organic solar cells. *Advanced Energy Materials*, 8, 2018.

[176] P. Cheng, C. Yan, Y. Wu, J. Wang, M. Qin, Q. An, J. Cao, L. Huo, F. Zhang, L. Ding, Y. Sun, W. Ma, and X. Zhan. Alloy acceptor: superior alternative to pcbm toward efficient and stable organic solar cells. *Advanced Materials*, 28, 2016.

[177] S. Savagatrup, D. Rodriquez, A.D. Printz, A.B. Sieval, J.C. Hummelen, and D.J. Lipomi. [70] PCBM and incompletely separated grades of methanofullerenes produce bulk heterojunctions with increased robustness for ultra-flexible and stretchable electronics. *Chemistry of Materials*, 27, 2015.

[178] Y. Chen, Y. Qin, Y. Wu, C. Li, H. Yao, N. Liang, X. Wang, W. Li, W. Ma, and J. Hou. From binary to ternary: Improving the external quantum efficiency of small-molecule acceptor-based polymer solar cells with a minute amount of fullerene sensitization. *Advanced Energy Materials*, 7, 2017.

[179] W. Zhao, S. Li, S. Zhang, X. Liu, and J. Hou. Ternary polymer solar cells based on two acceptors and one donor for achieving 12.2% efficiency. *Advanced Materials*, 29, 2017.

[180] W. Xu and F. Gao. The progress and prospects of non-fullerene acceptors in ternary blend organic solar cells. *Materials Horizons*, 5, 2018.

[181] H.B. Naveed and W. Ma. Miscibility-driven optimization of nanostructures in ternary organic solar cells using non-fullerene acceptors. *Joule*, 2, 2018.

[182] W. Li, D. Yan, F. Liu, T. Russell, C. Zhan, and J. Yao. High-efficiency quaternary polymer solar cells enabled with binary fullerene additives to reduce nonfullerene acceptor optical band gap and improve carriers transport. *Science China Chemistry*, 61, 2018.

[183] E. Pascual-San-José, X. Rodríguez-Martínez, R. Adel-Abdelaleim, M. Stella, E. Martínez-Ferrero, and M. Campoy-Quiles. Blade coated P3HT: non-fullerene acceptor solar cells: a high-throughput parameter study with a focus on up-scalability. *Journal of Materials Chemistry A*, 7, 2019.

Danksagung

Auf diesen letzten Seiten möchte ich mich bei allen bedanken, die mich während meiner Promotion unterstützt haben. Da ich sowohl am KIT als auch an der Universität in Melbourne (UoM) eingeschrieben war, war bei mir alles immer etwas komplizierter, daher: Danke, das ihr nicht mit mir verzweifelt seid.
Zuerst einmal möchte ich apl. Prof. Dr. Alexander Colsmann für das entgegengebrachte Vertrauen und die Betreuung der Arbeit danken. Ich danke ihm für die freundliche Aufnahme in die OPV-Gruppe und die Möglichkeit, meine Promotion im Rahmen eines Joint PhD mit der Universität Melbourne durchzuführen. Er stand mir stets mit seinem ungemeinen Erfahrungsschatz zu Seite. In zahlreichen spannenden Diskussionen konnte ich viel über die organische Photovoltaik und die Nanopartikel lernen. Ich weiß, durch den bürokratischen Wirrwarr des Joint-PhD mit Melbourne war es nicht immer einfach, was die Diskrepanzen mit der Fakultät bezüglich des Cotutelle-Vertrags nicht verbessert haben. Zu wissen, dass ich mich jederzeit auf ihn verlassen kann und er mir immer die Wahrheit sagt, war in dieser Zeit essentiell für mich.
Ich möchte mich ebenfalls bei assoc. Prof. Dr. David Jones bedanken, der mich für das Joint PhD von australischer Seite aus betreut hat. Auch wenn es durch Corona und den Abbruch meines einjährigen Forschungsaufenthaltes in Melbourne nach zwei Wochen deutlich anders gekommen ist als geplant, haben wir das Beste aus der Situation gemacht.
Auch assoc. Prof. Wallace Wong, meinem Co-Betreuer von australischer Seite, und Prof. Uta Wille, die die Rolle der Vorsitzenden des Ausschusses übernommen hat, gilt mein Dank. Die jährlichen Review Meetings, die von australischer Seite vorgeschrieben waren, waren sehr aufschlussreich, vielen Dank für das Feedback.
Ein besonderer Dank geht an Prof. Dr. Thomas Heiser von der Universität Straßbourg, der sehr spontan die Rolle des zweiten Korreferenten/ Third Examiner übernommen hat. Danke, dass du dir für mich Zeit genommen hast.
Mein Dank gilt ebenfalls der Gradiertenschule für Klima und Umwelt (GRACE) des KIT, die meine Promotion mit einem Stipendium finanziell ermöglicht hat. Vor allem Dr. Andreas Schenk von GRACE und Anne Houston vom Climate Energy College, dem australischen Pendant zu GRACE, die für die Kommunikation zwischen GRACE und dem Climate Energy College zuständig waren, gilt mein Dank.

Meinem „Team Nanopartikel“, das zu Beginn meiner Promotion aus Dr. Philipp Marlow und Dr. Felix Manger bestand, möchte ich dafür danken, dass sie mich in ihr Team aufgenommen haben und mich vom Verzweifeln abgehalten haben. Gerade zu Beginn, als alle Ergebnisse so willkürlich waren und wir nicht einmal stabile Dispersionen in Ethanol erreichen konnten, als die Solarzellen kaum über 2% kamen, wir selbst beim Kaffee trinken von Sedimentation verfolgt wurden und einfach zwischenzeitlich gar nichts mehr funktioniert hat, da habt ihr mich immer aufgemuntert. Wenn ich heute zurückschaue, bin ich absolut fasziniert, was wir alles geschafft haben und welche „Geheimnisse“ der Nanopartikel wir mittlerweile gelüftet haben. Ich danke euch für die produktiven Gespräche an der Kaffeemaschine und die stundenlangen Diskussionen über Grundlagen der Kolloidchemie, die mir als Elektrotechnikerin zu Beginn so fremd waren und die ihr mir nähergebracht habt. Mit der Zeit hat sich unser Team verändert, mit Dr. Christian Sprau und Jonas Armleder habe ich nun zwei neue Kollegen in diesem Thema, die mich tatkräftig unterstützen. Christian, vielen Dank dafür, dass du immer ein offenes Ohr für mich hast.

Ich möchte ebenfalls meinem „Stammtisch Organik“ danken, den wir während Corona eingerichtet haben, um wenigstens einmal wöchentlich mit jemandem über unsere Ergebnisse sprechen zu können. Danke an Dr. Lorenz Graf von Reventlow, Andreas Tangemann, Lukas Jäger, Dr. Christian Sprau und Dr. Felix Manger für die unzähligen Diskussionen zum Thema Organik.

Vielen Dank an Malte Martens, Alexander Schulz und Dr. Tobias Leonhard für die Topographiemessungen an meinen Proben am AFM. Ich weiß, die Messungen von nanopartikulären Schichten waren am Anfang eine Herausforderung und haben euch ganz schön Zeit gekostet.

Ich möchte mich bei all meinen Kollegen aus der OPV-Gruppe bedanken, die mich bei meiner Promotion begleitet haben: Dr. Joshua Fragoso, Dr. Bernd Ebenhoch, Dr. Christian Sprau, Dr. Holger Röhm, Dr. Bing Guo, Dr. Philipp Marlow, Dr. Tobias Leonhard, Dr. Lorenz Graf von Reventlow, Dr. Felix Manger, Malte Martens, Alexander Schulz, Simon Petrick, Moritz Braun, Andreas Tangemann, Jonas Armleder und Marcel Habrik. Durch die freundschaftliche und immer hilfsbereite Art habt ihr eine angenehme Arbeitsatmosphäre geschaffen. Unsere zahlreichen spannenden Diskussionen, Kaffeepausen, Ausflüge und das gemeinsame Beisammensitzen nach der Arbeit waren einfach super. Ich werde unseren traditionellen Currywurst-Donnerstag weiterhin in Ehren halten.

Auch meinen Studenten Ayse Ardelt, Florian Mintel, Kilian Bitsch, Peer Große Hokamp und Hanna Bletzinger möchte ich für ihren Arbeitseinsatz danken. Auch wenn einigen von ihnen gar nicht so bewusst war, wie wichtig die Ergebnisse eurer Arbeit waren, beim Zusammenschreiben dieser Arbeit ist es mir wieder bewusstgeworden. Ich danke euch für euer Interesse und euren Tatendrang. Jeder von euch hat einen einzigartigen Anteil an dieser Arbeit, dafür

möchte ich euch herzlich danken.
Ein besonderer Dank geht an das LTI, zu dem die AG OPV immer noch gehört, auch wenn wir am MZE sitzen. Vielen Dank an Mario Sütsch, Hans Vögele und Klaus Ochs von der Werkstatt des LTI, Felix Geislhöringer, Astrid Henne, Claudia Holeisen und Nicole Klöfer für die gute elektrotechnische und administrative Unterstützung und Prof. Uli Lemmer für die Hilfe mit dem Cotutelle-Vertrag.

Für die Unterstützung während der Promotion und vor allem in der Endphase dieser Arbeit danke ich meinen Freunden Marie, Ruben, Ebru, Leonie, Karin und Fabi sowie meiner Schwester Steffi, meinen Eltern und meinem Freund Manuel. Ich weiß, ihr seid in letzter Zeit viel zu kurz gekommen, vor allem über Weihnachten, wo ich vor lauter Schreibwahn kaum ansprechbar war. Ihr habt mir das Unmögliche möglich gemacht, und dafür bin ich dankbar. Vielen Dank für euer offenes Ohr und dass ich mich regelmäßig bei euch auskotzen durfte. Das hat mich vor der Verzweiflung bewahrt. Vielen Dank an alle Korrekturleser, die sich teils fachfremd durch meine Arbeit gekämpft haben. Mir wird erst jetzt bewusst, wie schwer das zum Teil für euch gewesen sein muss. Ohne eure Unterstützung hätte ich das nicht geschafft.

Vielen, vielen Dank euch allen.

Karen